INTRACELLULAR ICE FORMATION IN TISSUE CONSTRUCTS AND THE EFFECTS OF MASS TRANSPORT ACROSS THE CELL MEMBRANE

A Dissertation
Presented to
The Academic Faculty

by

Adam Zachary Higgins

In Partial Fulfillment
of the Requirements for the Degree
Doctor of Philosophy in the
Coulter School of Biomedical Engineering

Georgia Institute of Technology
April 2008

INTRACELLULAR ICE FORMATION IN TISSUE CONSTRUCTS AND THE EFFECTS OF MASS TRANSPORT ACROSS THE CELL MEMBRANE

Approved by:

Dr. Jens Karlsson, Advisor
Department of Mechanical Engineering
and Mechanics
Drexel University

Dr. Robert Nerem, Co-Advisor
School of Mechanical Engineering
Georgia Institute of Technology

Dr. Cheng Zhu
School of Mechanical Engineering
Georgia Institute of Technology

Dr. Mark Prausnitz
School of Chemical and Biomolecular
Engineering
Georgia Institute of Technology

Dr. Jeff Sands
Department of Medicine
Emory University

Dr. Paolo Meda
Department of Cell Physiology and
Metabolism
University of Geneva

Date Approved: November 27, 2007

ACKNOWLEDGEMENTS

I'm indebted to many individuals for their support over the last five years. First, I wish to thank my PhD. mentor, Jens Karlsson, who took in a young and enthusiastic student, and created a researcher capable of designing and carrying out experiments and critically analyzing data. To top it off, I'm still enthusiastic about research, which is quite an accomplishment in my mind. I also owe him thanks for his help with editing this document. I wish to acknowledge my committee members Mark Prausnitz, Cheng Zhu, Jeff Sands, Paolo Meda and Robert Nerem for their helpful suggestions. Special thanks are owed to Paolo Meda, who provided the genetically modified MIN6 cell that enabled the research presented in Chapter 7.

The members of the Karlsson lab deserve acknowledgement for their helpful discussions about research, and for their friendship. I'm especially indebted to Shannon Stott, who spent a huge amount of effort training me in the micropatterning technique and high-speed video cryomicroscopy system that I used in my research. Shannon also provided the "Blessed Music Thingy", which brightened my spirits on long days in the lab. Jonathan Barletta, Neel Bagchi, Megan Dickherber and Kevin Carnevale also deserve acknowledgement for their role in the research, and for making the Karlsson lab a fun place to work.

I'd also like to acknowledge my family for their unwavering support, albeit from the other side of the country. My parents never failed to offer to pay for my plane tickets home, despite my constant reminders that I was getting paid to go to school (my dad had a difficult time wrapping his mind around that concept), so I could afford to buy some things for myself. I appreciate the care packages and phone calls and visits over the last five years. I owe much of the success I have achieved thus far in life to the love and support of my family.

Finally, I'd like to thank the many friends who have made graduate school a fun experience, despite the inevitable obstacles encountered in the lab. Not only do I owe much of my personal growth throughout the last five years to the influence of my friends, I probably also owe them my sanity. The immense focus required for research and the solitary nature of lab work can cause one starts to lose perspective with reality after a while. There's nothing like a good Halloween party to remind you that a world does exist outside the lab.

I wish to acknowledge fellowship support from the following sources: the National Science Foundation, the Howard Hughes Medical Institute, the Medtronic Foundation, and the George Family Foundation. I acknowledge grant funding from the NSF EEC-9731643 and BES-0541530.

TABLE OF CONTENTS

LIST OF TABLES

LIST OF FIGURES

SUMMARY

Long-term storage of tissue by cryopreservation is necessary for the efficient mass production of tissue engineered products, and for reducing the urgency and cost of organ transplantation procedures. The goal of this work was to investigate the physical processes thought result in damage during tissue cryopreservation towards development of tissue cryopreservation strategies. Although mathematical models of cell dehydration and intracellular ice formation (IIF) have been successfully used to optimize cryopreservation procedures for cell suspensions, it is not currently possible to use this approach with tissue because of the lack of tissue-specific permeability parameters for prediction cell dehydration during tissue freezing, and because of the increased complexity of the IIF process in tissue. We have measured the membrane permeability properties of tissue comprising a cell monolayer using a fluorescence quenching technique, and compared the results to the corresponding cell suspensions, revealing significant differences in the membrane transport kinetics between monolayers and suspensions. These data enabled the prediction cell dehydration during freezing of cell monolayers, representing a significant step toward developing cryopreservation strategies for tissue. Whereas the mechanisms of IIF are relatively well understood in cell suspensions, tissue is susceptible to new IIF mechanisms. In particular, cell-cell interactions have been shown to increase the IIF probability by enabling the propagation of ice between neighboring cells. We investigated the effect of cell-cell interactions on IIF using genetically modified cells expressing different levels of intercellular junction proteins, revealing that tight junctions may have a protective effect during freezing. A new IIF mechanism was observed associated with penetration of extracellular ice into the paracellular space at the cell-cell interface, suggesting that IIF is caused by mechanical interaction with the extracellular ice. In addition, we investigated the effect of cytoplasm composition, which changes during freezing because of cell dehydration, on the kinetics of IIF in tissue. We found that increasing the viscosity or decreasing the supercooling significantly decreased the rates of independent IIF and intercellular ice propagation, suggesting that IIF protocols for tissue can be optimized by modulating the cytoplasm supercooling and viscosity. Together, these data represent an important step towards developing cryopreservation strategies for tissue.

CHAPTER 1

INTRODUCTION

The ultimate objective of this research is to develop strategies for the cryopreservation of tissue. Whereas the two main factors governing survival of cell suspensions during cryopreservation are cellular dehydration and intracellular ice formation (IIF, Mazur et al., 1972), progress towards developing successful cryopreservation strategies for tissue is significantly hindered by the paucity of the membrane permeability data necessary for predicting cellular dehydration in tissue, and by inadequate understanding of the IIF mechanisms in tissue. Thus, the emphasis of the present study is on cellular dehydration and IIF in tissue.

The ability to successfully cryopreserve tissue would have important implications in tissue banking, organ transplantation and tissue engineering. For example, long term storage by cryopreservation would eliminate the necessity to rush donor organs to the operating room for transplantation, which would significantly reduce the cost of these procedures. In addition, the ability to cryopreserve tissue would enable the efficient mass production of tissue engineered products by facilitating stockpiling, quality control and product distribution. Despite the need for effective cryopreservation strategies for tissue, previous attempts have been largely unsuccessful. This lack of success is striking since suspensions of various cell types have been effectively cryopreserved, and the physical processes that occur during cryopreservation of cell suspensions are relatively well understood. Thus, with the goal of presenting the current understanding of tissue cryopreservation, the biophysical response of suspended cells to cryopreservation will first be discussed. This will be followed by an assessment of previous studies investigating tissue cryopreservation, which will highlight the differences between cryopreservation of cell suspensions and tissues and the mechanisms of tissue damage during cryopreservation.

Cryopreservation of Cell Suspensions

Cryopreservation is advantageous because it has the potential to allow storage of living material for an indefinite period of time by placing samples in a state of suspended animation at extremely cold temperatures. Generally, cryopreserved specimens are stored in liquid nitrogen (-196°C); under these conditions molecular motion is slowed to such an extent that thermally driven chemical reactions, which can be deleterious, essentially do not occur (Mazur, 1984). Cryopreserved samples have been stored for over a decade without loss of viability (Mazur, 1984). Rather, damage has been shown to occur as cells are cooled to -196°C, as well as during warming back to ambient temperature. Thus, it is important to understand the physical environment of the cells during cooling and warming. Cells are exposed to changes in their thermal and chemical environments during freezing. As cells are cooled below the melting temperature, ice forms in the extracellular solution, which depletes water molecules from the liquid fraction and increases the extracellular solute concentration. This increase in solute concentration causes an osmotic pressure imbalance across the cell membrane, which drives efflux of water from the cells. In the limit of extremely slow cooling rates, cell dehydration will maintain chemical equilibrium between the intracellular and extracellular solutions. However, for fast cooling rates, cell dehydration is too slow to maintain chemical equilibrium and intracellular supercooling occurs, which may lead to IIF. This interplay between cell dehydration and IIF is thought to determine the fate of the cell during freezing. Mazur et al. (1972) proposed the two-factor hypothesis of cryoinjury, which postulates that cell damage results from “solution effects” at slow cooling rates, whereas damage results from IIF at fast cooling rates. This hypothesis explains the common observation of an optimum cooling rate. Solution effects, which are dominant at slow cooling rates, are believed to result from excessive dehydration, prolonged exposure to high solute concentrations, and/or mechanical deformation of the cell (Mazur et al., 1972). At fast cooling rates, the magnitude of damage caused by solution effects diminishes, as a result of reduced cell dehydration and shorter exposure time to high solute concentration. However, fast cooling causes intracellular supercooling and concomitant IIF, which has been correlated with cell damage for various cell types (Toner, 1993).

Cryoprotectant chemicals (CPAs) such as glycerol or dimethyl-sulfoxide are thought to protect cells during freezing by mitigating damage due to solution effects and IIF. For example, it has been proposed that CPAs protect cells from solution damage by reducing the temperature at which cells are exposed to damaging electrolyte concentrations (Lovelock, 1953), or by limiting the extent of cell volume changes during freezing (Merryman, 1968). The incidence of IIF is also affected by permeable CPAs because of their effect on the intracellular supercooling and viscosity. Because of the protective effect of CPAs, they are used in nearly every cryopreservation procedure for cell suspensions. Thus, practical theoretical descriptions of cell damage during cryopreservation must account for the effect of CPAs.

Mathematical models of cell dehydration and IIF have been useful for the analysis of the cryopreservation of cell suspensions. In the 1990s, models of intracellular ice nucleation were developed that accurately predicted IIF in various cell types in the absence of CPAs (Toner, 1990) and improvements to these models allowed the prediction of both ice nucleation and subsequent crystal growth in the presence of CPAs (Karlsson et al., 1993, Karlsson and Cravalho, 1994). These models allowed prediction of IIF kinetics as a function of temperature, intracellular viscosity and supercooling. The supercooling and viscosity were computed from the temperature and composition of the intracellular solution, which was modeled as a ternary solution of water, salt and CPA. Since cell dehydration during freezing changes the intracellular composition by loss of water, the IIF models were coupled to a model of cell dehydration (Mazur, 1963). Using these coupled models of ice nucleation and cell dehydration, it has been possible to mathematically optimize cryopreservation procedures for cell suspensions (Karlsson et al., 1996).

Cryopreservation of Tissue

Although mathematical models of IIF have been successful for designing cryopreservation procedures for cell suspensions, progress towards rational design of cryopreservation procedures for tissue has been hindered for several reasons. In particular, it may not be possible to directly apply mathematical models of IIF, which were developed for cell suspensions, directly to tissue systems since there is evidence to suggest that alternative mechanisms for IIF may exist in tissue. In addition, the development of predictive models of IIF for tissue freezing is also contingent on an appropriate model of cell dehydration. It is likely that cell dehydration in tissue can be described by conventional membrane transport models; however, experimental techniques for measuring the necessary permeability parameters in tissue are lacking.

Although various techniques are available for measurement of cellular water transport in cell suspensions (reviewed in McGrath, 1997), these techniques are not valid for tissue. The general strategy with these techniques is to expose cells to a change in extracellular osmotic pressure, and then monitor kinetics of the resulting cell volume change by methods such as optical cell size measurement or electrical sensing of cell size. These techniques rely on the assumption of spherical cell geometry, which is generally valid for suspended cells, but not for adherent cells or tissue. In addition, there is experimental evidence that suggests that the membrane permeability of adherent cells may be altered by the process of detaching the cells to form a cell suspension. For example, Yarmush et al. (1992) measured the membrane water permeability and activation energy of rat hepatocytes cultured between two collagen layers by fitting IIF data to coupled models of IIF and cell dehydration. They found that the permeability and activation energy of these cells were significantly different from the permeability parameters of both freshly isolated hepatocytes and cell suspensions created by dissociating the hepatocyte cultures. Although the literature data suggests that intact tissue and suspensions may have different permeability properties, the effect of tissue disaggregation to form a suspension on the permeability is unclear. To clarify this issue, improved techniques for measuring the membrane permeability in tissue are needed.

Recently, a technique has been reported for measuring osmotically induced volume changes in adherent cells based on the cell-volume-dependent fluorescence quenching of intracellular calcein (Solenov et al., 2004). Although this technique has been used with a few cell types, the general applicability of the fluorescence quenching response has not been established. In addition, the error associated with solution exchange kinetics has not been adequately investigated. Although the calcein quenching technique is a promising approach for determining the membrane permeability in adherent tissue, further work is necessary to optimize the technique.

In addition to the necessity for tissue-specific cell dehydration parameters, our understanding of the response of tissue to cryopreservation is hindered by an inadequate understanding of the mechanisms of IIF in tissue. In particular, the presence of cell-cell interactions has been shown to increase the probability of IIF, which suggests a new mechanism of IIF in tissue associated with cell-cell connections. It has been suggested that this increase in the probability of IIF is a result of propagation of intracellular ice between adjacent cells (Acker et al., 1999; Berger and Uhrik; 1996). The existence of a propagative mechanism of IIF was confirmed by Irimia and Karlsson (2002) by measuring IIF events in hepatic cells micropatterned in cell pairs, which allowed the decoupling of intercellular ice propagation from non-propagative IIF mechanisms. Although the exact mechanism of IIP is unclear, gap junction inhibitors have been shown to reduce the propagation rate, indicating that gap junctions are involved in IIP (Irimia and Karlsson, 2002; Berger and Uhrik; 1996). Thus, there is a need for clarification of the mechanism of IIP and the role of gap junctions in this process.

Whereas cryopreservation protocols are generally optimized by adjusting the cooling rate and the concentration of CPAs, the effect of these factors on IIF in tissue is unknown since most investigations of IIF in tissue are performed for high cooling rates in the absence of CPA. The cooling rate and CPA concentration are thought to affect IIF by modulating the temperature and composition of the cell cytoplasm during freezing. Thus, determination of the kinetics of IIF in tissue as a function of the temperature and composition of the intracellular solution represents an important step towards the development of mathematical models for IIF that can be used to design cryopreservation procedures for tissue.

Thesis Outline

This thesis aims to lay the groundwork for developing strategies for tissue cryopreservation by investigation of two important physical processes that occur during cryopreservation: cellular dehydration and IIF. Cellular dehydration was investigated in Chapters 2-6, with the goal of establishing protocols for measuring the membrane permeability in adherent tissue, and obtaining the permeability parameters necessary to predict cellular dehydration during tissue cryopreservation in the presence of CPAs. The membrane permeability properties were first determined in cell suspensions using an electronic cell sizing technique, as a basis for comparison with subsequent permeability data in tissue comprising cell monolayers. Chapters 2-4 describe novel strategies for analyzing electronic sizing data, resulting in improved estimates for the permeability parameters. In Chapter 5, the recently reported fluorescence quenching technique for measuring the membrane permeability in adherent tissue was optimized for a new cell type, with an emphasis on the potential error resulting from limitations in the solution exchange kinetics. Chapter 6 compares the permeability properties in monolayers and suspensions, and presents permeability data for monolayers in the presence of CPA, enabling prediction of cellular dehydration during tissue cryopreservation. The kinetics and mechanisms of IIF in tissue were investigated in Chapters 7 and 8. In Chapter 7, genetically modified cells expressing different levels of intercellular junction proteins were used to explore the role of cell-cell interactions on IIF. In Chapter 8, the effect of the cytoplasm supercooling and viscosity on the kinetics of IIF in tissue was studied by measuring IIF for various cooling protocols in the presence of CPA.

CHAPTER 2

DYNAMIC RANGE ERROR IN ELECTRONIC CELL SIZING EXPERIMENTS: OSMOTICALLY INACTIVE VOLUME FRACTION

Introduction

The ability to predict the cellular response to a change in extracellular osmotic strength is important for designing cryopreservation procedures, in which cells are exposed to a changing osmotic environment during both freezing and thawing. Electronic cell sizing instruments (e.g., Coulter counters) have been used extensively to measure the necessary cellular osmotic properties (e.g., Agca, Liu et al., 2005, Agca, Mullen et al., 2005, Gao et al., 1998, McGann et al., 1988, Woods et al., 1999). These instruments work by measuring the change in voltage as cells are drawn through a small aperture under a constant electrical current. As a cell passes through the aperture, there is a transient increase in electrical resistance, which is manifested as a voltage pulse with a magnitude proportional to the cell volume. The steady-state cellular osmotic response is characterized by the osmotically inactive volume fraction ($\overline{V_b}$), which can be determined by measuring the cell volume in solutions of varying osmotic strength. The cell volume (normalized to the isotonic volume) is typically assumed to vary linearly with the inverse of osmotic strength, approaching $\overline{V_b}$ in the limit of infinite osmotic strength, as predicted from the Boyle-van't Hoff relationship.

Experimental cell populations often exhibit a broad range of volumes (Elmoazzen et al., 2005; Muldrew et al., 2001), which introduces the potential that dynamic range limitations will exclude a portion of the cell population from calculation of the mean volume, affecting estimates for $\overline{V_b}$. The dynamic range upper limit can be chosen to exclude cell clusters (Liu et al., 1997; Woods et al., 1999), or is defined by the Coulter counter settings (gain, current), whereas the lower limit is typically chosen to exclude small volume noise resulting from cell debris. Small volume noise has been shown to interfere with measurement of the cell volume distribution for astrocytes (Olson et al., 1986), keratocytes (Armitage and Juss, 1996), spermatozoa (Petrunkina and Topfer-Petersen, 2000), leukocytes (Weiser, 1987), and islet cells (Liu et al., 1997), and the exclusion of small volume data is evidently common practice for other cell types as well (Woods et al., 1999; McGann et al., 1988; Lewis et al, 1989; Gao et al., 1998; Agca et al., 2005a,b; Fedorow et al., 2001; Gilmore et al., 1995; Acker et al., 1999).

Although it is evident that dynamic range limitations can exclude a portion of the cell population from calculation of the mean cell volume, the error associated with dynamic range limitations has not been thoroughly investigated. Dynamic range limitations are expected to cause underestimation of the magnitude of the steady-state volume change upon exposure to anisotonic solution. For instance, exposure to hypotonic solution causes larger cells to cross the upper volume limit, excluding them from analysis, while smaller cells enter the dynamic range by crossing the lower volume limit. This results in an apparent mean volume that is lower than expected. This phenomenon has the net effect of reducing the slope in the Boyle-van't Hoff plot (cell volume vs. reciprocal osmotic strength), resulting in overestimation of $\overline{V_b}$. Evidence of this type of error has been observed in the literature. For example, Petrunkina et al. (2000) observed a two-fold higher value of $\overline{V_b}$ using the mean volume within the dynamic range, than using the modal volume, which is consistent with overestimation of $\overline{V_b}$ because of dynamic range limitations. Armitage and Juss (1996) observed similar results when comparing the use of the mode diameter and mean diameter in the Boyle-van't Hoff plot, suggesting error due to dynamic range limitations in this case as well. Thus, the conventional method of excluding data outside the dynamic range in calculation of the mean volume in the Boyle-van't Hoff plot is expected to yield erroneously high estimates for $\overline{V_b}$.

Since the conventional method is susceptible to error due to dynamic range limitations, we devised a new method that is expected to be insensitive to dynamic range, based on fitting the experimental volume distribution to the sum of a lognormal distribution, representing the cell population, and an exponential distribution, representing the cell debris. The new method is not expected to be sensitive to the dynamic range because a lower volume limit is not needed (since we are accounting for cell debris in the exponential distribution fit), and because the lognormal distribution fit allows extrapolation beyond the upper volume limit. To determine $\overline{V_b}$ by the new method, the mean volume of the best-fit lognormal distribution is used in the Boyle-van't Hoff plot. The new method is expected to yield improved estimates for $\overline{V_b}$ compared with the conventional method, especially when dynamic range limitations are significant.

The present study compares the new method for determining $\overline{V_b}$ to the conventional method, using theoretical simulations, as well as experimental data for mouse insulinoma (MIN6) cells. We will show that the conventional method can yield significant error in $\overline{V_b}$ because of dynamic range limitations, whereas the new method results in very little error.

Background

Conventional Method

For the conventional method, $\overline{V_b}$ was determined from a Boyle-van't Hoff plot of the mean cell volume, excluding volume data outside the dynamic range. Selection of the dynamic range volume limits was not discussed in detail in the literature, although in many cases it was clear from plots of the volume data that volume limits were used. Thus, it is unclear whether researchers typically choose consistent limits to be used for all osmotic solutions, or if different, "optimal", limits were chosen for each solution concentration. Consistent volume limits were used in the current study for several reasons. In a few cases, sufficient methodological detail was given to ascertain that consistent limits were used for analysis of the steady-state data (Gao et al., 1998, Petrunkina and Topfer-Petersen, 2000). In addition, the fact that the value of $\overline{V_b}$ determined from the steady-state data is often used in analysis of transient data provides evidence that consistent volume limits are typically used. Analysis of transient data requires the use of consistent volume limits for the initial condition (usually isotonic) and the final condition (usually anisotonic). Thus, if different volume limits are used to analyze the steady-state data for the initial and final conditions, then the steady-state results are not expected to be consistent with transient results. Additionally, the conventional method is expected to yield results for $\overline{V_b}$ equivalent to the common practice of fitting transient data for the membrane water permeability and $\overline{V_b}$

simultaneously (Elmoazzen et al., 2005, Liu et al., 1997, McGann et al., 1988, Muldrew et al., 2001). This is because of the constant volume limits employed during the transient volume change, which yields the fit for $\overline{V_b}$ (i.e., the fit for $\overline{V_b}$ is essentially determined by the initial mean isotonic volume and the final mean anisotonic volume, both of which are subject to the same dynamic range volume limits). Thus, the dynamic range was defined using consistent volume limits.

For the conventional method, $\overline{V_b}$ was determined using the typical modeling approach. The variation in cell volume with osmotic strength was described using the Boyle-van't Hoff relationship, which assumes an ideal and dilute intracellular solution and no solute transport across the cell membrane:

$$\frac{V_f}{V_0} = \frac{\Pi_0}{\Pi_f}\left(1-\overline{V_b}\right)+\overline{V_b} \qquad [1]$$

where *V* is the cell volume and the subscripts "0" and "*f*" refer to initial and final conditions, respectively. As is commonly done, it was assumed that the mean cell volume (μ) could be substituted for *V* in Eq. 1, yielding:

$$\frac{\mu_f}{\mu_0} = \frac{\Pi_0}{\Pi_f}\left(1-\overline{V_b}\right)+\overline{V_b} \qquad [2]$$

The mean volume (excluding data outside the dynamic range) was normalized to isotonic conditions and plotted against the inverse of the normalized osmotic pressure, and $\overline{V_b}$ was determined by fitting the data to Eq. 2. This approach will not result in error if the entire cell population is considered, but exclusion of a portion of the population because of dynamic range limitations is expected to cause error (see Appendix for details).

New Method

Since the conventional method is susceptible to error because of dynamic range limitations, a new method was devised that is expected to be insensitive to dynamic range. The new method consists of a simultaneous fit to a lognormal distribution, representing the cell population, and an exponential distribution, representing the cell debris. To determine $\overline{V_b}$, the arithmetic mean of the best-fit lognormal distribution was used in the Boyle-van't Hoff plot. This approach does not require the use of a lower volume limit, since the cell debris is accounted for in the exponential distribution fit. In addition, the mean of the lognormal distribution fit is expected to be insensitive to the upper volume limit since the fit extrapolates to large volumes. Thus, consistent values for $\overline{V_b}$ are expected, regardless of the dynamic range.

A lognormal distribution was chosen to represent the cell population based on the shape of cell volume distributions observed in the literature. In many cases, cell volume distributions were observed to be positively skewed (Acker et al., 1999, Anderson et al., 1970, Armitage and Juss, 1996, Bell et al., 1967, Ben-Sasson et al., 1974, Elmoazzen et al., 2005, Fedorow et al., 2001, Gilmore et al., 1995, Liu et al., 1995, Liu et al., 1997, McGann et al., 1982, Muldrew et al., 2001, Olson et al., 1986, Petrunkina and Topfer-Petersen, 2000, Rosenberg and Gregg, 1969, Sinclair and Ross, 1969, Sipe et al., 1966, Weiser, 1987, Westring et al., 1969, Wu et al., 2005). In fact, the positive skew of the cell volume distribution has been predicted from mathematical models of cell growth (Bell et al., 1967, Sinclair and Ross, 1969). Several authors suggested that the cell volumes follow a lognormal distribution, which exhibits the expected positive skew (Rosenberg and Gregg, 1969, Sipe et al., 1966, Westring et al., 1969). Ben-Sasson et al.

(1974) fit volume data for lymphocytes to both normal and lognormal distributions, but had more success with the lognormal distribution fit. Thus, we selected the lognormal distribution to represent the cell population, which is defined as follows:

$$P_l(V) = \frac{1}{S\sqrt{2\pi}V}\exp\left[-\frac{(\ln V - M)^2}{2S^2}\right] \qquad [3]$$

where P_l is the probability density for the lognormal distribution, V is the volume, and M and S are the mean and standard deviation of the logarithm of the volume, respectively.

An exponential distribution was chosen to represent the small volume noise resulting from cell debris. The selection of this distribution was based on personal observations with mouse insulinoma (MIN6) cells and bovine pulmonary artery endothelial cells, as well as published volume data for rabbit corneal keratocytes (Armitage and Juss, 1996), canine and feline leukocytes (Weiser, 1987) and canine pancreatic islet cells (Liu et al., 1997). The exponential distribution is defined as:

$$P_e(V) = \frac{1}{\mu_e}\exp\left(-\frac{V}{\mu_e}\right) \qquad [4]$$

where P_e is the probability density for the exponential distribution and μ_e is the arithmetic mean of the exponential distribution.

The experimental volume data were fit simultaneously with a lognormal distribution and an exponential distribution as follows. Since the experimental volume data were divided into bins, the fitting algorithm minimized the error squared between the predicted count (y) in a given bin and the observed count (n). For the k^{th} bin, the predicted count was calculated using the following equation:

$$y_k = N_e P_e(V_k) + \left[\sum_{j=1}^{N} n_j - N_e P_e(V_j) \right] \frac{\int_{V_k - w/2}^{V_k + w/2} [P_l(V)] dV}{\int_{0}^{V_N + w/2} [P_l(V)] dV} \quad [5]$$

where N_e is the total count for the exponential distribution, N is the total number of bins, and w is the bin width. In Eq. 5, the first term represents the count in the k^{th} bin due to the exponential distribution, and the second term represents the count in the k^{th} bin resulting from the lognormal distribution. Four parameters were adjusted to minimize the error squared between y and n: N_e and m_e, which characterize the exponential distribution, and M and S, which characterize the lognormal distribution.

The value of $\overline{V_b}$ was then determined using the arithmetic mean of the best-fit lognormal distribution, defined as:

$$\mu_l = \exp\left(M + \frac{S^2}{2} \right) \quad [6]$$

This mean volume was used to create a Boyle-van't Hoff plot, which was subsequently fit to Eq. 2 to determine $\overline{V_b}$.

Methods

Osmotic Test Solutions

Hypotonic and hypertonic solutions were prepared by addition of either purified water or sucrose to isotonic (300 mOsm/kg) phosphate buffered saline (Ca^{2+} and Mg^{2+} free). The osmolality of all solutions was measured with a freezing point depression osmometer to be within 1% of the reported value. To remove particles, solutions were filtered with 0.2 μm filters before use.

Experimental Setup

The raw voltages from the Coulter counter (Z2 series, 100 μm aperture) were accessed via a custom installed BNC connection, and peak voltage signals were digitized and sent to a computer using a Cell Size Analyzer (CSA) interface (McGann et al., 1982). Temperature was controlled to within ± 0.5°C by circulating liquid from a refrigerated water bath through the jacket of a custom designed 10 ml jacketed beaker. Mixing of the sample solution was accomplished using a small magnetic stirrer attached to the base of the beaker holder, and a 1/2 x 5/16” stir bar. Copper wire was inserted into the jacket of the beaker and grounded to the base of the Coulter counter, creating a Faraday shield and essentially eliminating contaminating electrical noise. To enhance the effectiveness of the Faraday shield, a conductive liquid (i.e., Sodium Chloride solution) was used as the circulating liquid in the beaker jacket. Peak voltage signals were converted to volume by calibration with spherical latex beads of known size. The Coulter counter was drained and refilled with the appropriate osmotic solution before initiating calibration experiments. Calibration was performed for each osmotic solution on the day of the experiment using 10 μm diameter beads. The Coulter counter settings were chosen such that the maximum measurable volume was 3400 fL (gain = 32, current = 0.5, preamplifier gain = 179.2).

Cell Culture

Mouse insulinoma cells (MIN6, generously provided by Paolo Meda, M.D.) were cultured in DMEM (high glucose) supplemented with 15% v/v heat inactivated FBS and β-mercaptoethanol (0.07 mM) at 37ºC in a 5% CO_2 environment. Media was changed every 3 days and passages were performed weekly. Cell suspensions (96% single cells, 93% viability) were created by exposure to 0.2% trypsin solution at 37°C for 15 min, followed by trituration in culture medium 20 times with a 20G needle (see Chapter 4). Suspensions were used in osmotic experiments within 5 minutes.

Steady-State Osmotic Response

Steady-state volume measurements were performed for MIN6 cell suspensions in isotonic (300 mOsm/kg), hypotonic (200 mOsm/kg) and hypertonic (430 mOsm/kg, 600 mOsm/kg, 1000 mOsm/kg) solutions at 21°C. A volume of 100 μL of cell suspension (1-2x10^6 cells/ml) in isotonic cell culture medium was injected into 10 mL of osmotic test solution in the Coulter counter sample beaker. At this concentration, the cell suspension (96% single cells) is expected to yield < 6% error due to coincidence (see Chapter 4). Steady-state was assumed to occur 3 min after exposure to anisotonic solution. The validity of this assumption was confirmed using transient measurements of MIN6 cell volume changes (see Chapter 3). For each osmotic solution, four replicates were performed, each representing cell suspensions created from different cultures.

Simulated Experiments

Simulated experiments were performed by applying the Boyle-van't Hoff relationship to a theoretical isotonic cell volume distribution. Two approaches were taken. In the first approach, the isotonic volume distribution was constructed from the experimental volume data for suspended MIN6 cells. Since small volume noise obscured cell volume measurements below 450 fL, and the maximum measurable volume was 3400 fL, the experimental volume data was used in this range, whereas outside this range, the best-fit lognormal distribution was used. For simulations, 10^4 cells were chosen at random from this isotonic distribution, the Boyle-van't Hoff relationship (Eq. 1) was applied, small volume noise was introduced to match experimental observations, and the data was binned using the experimental bin widths. In the second approach, an isotonic lognormal distribution was assumed (Eq. 3 with $M = M_0$ and $S = S_0$), and the resulting cell volume distribution in anisotonic solution was determined by combining Eq. 3 with Eq. A2 (see appendix), yielding:

$$P(V_f) = \frac{1}{S_0\sqrt{2\pi}V_f}\exp\left[-\frac{(\ln V_f - \ln\alpha - M_0)^2}{2S_0^2}\right] \qquad [7]$$

where $\alpha = \frac{\Pi_0}{\Pi_f}\left(1-\overline{V_b}\right)+\overline{V_b}$

The mean volume within the dynamic range was then computed from this probability density function (Eq. 7).

Statistical Analysis

Data are reported as averages and standard error of the mean. Values of $\overline{V_b}$ determined from Boyle-van't Hoff plots were compared using two-tailed t-tests, and differences were considered significant at a 95% confidence level (i.e., $p < 0.05$).

Results

Fig. 1 shows representative steady-state volume distributions for MIN6 cell suspensions in hypertonic, isotonic and hypotonic solutions. The distributions exhibit a typical bimodal shape, which is commonly attributed to cell debris and the cell population. As expected, the shape of the volume distribution is dependent on the solution osmotic strength, with smaller volumes in hypertonic solution than in hypotonic solution. For the conventional method, volume data outside the dynamic range (450 fL to 3400 fL, indicated by arrows in Fig. 1B) was excluded from analysis, yielding a mean

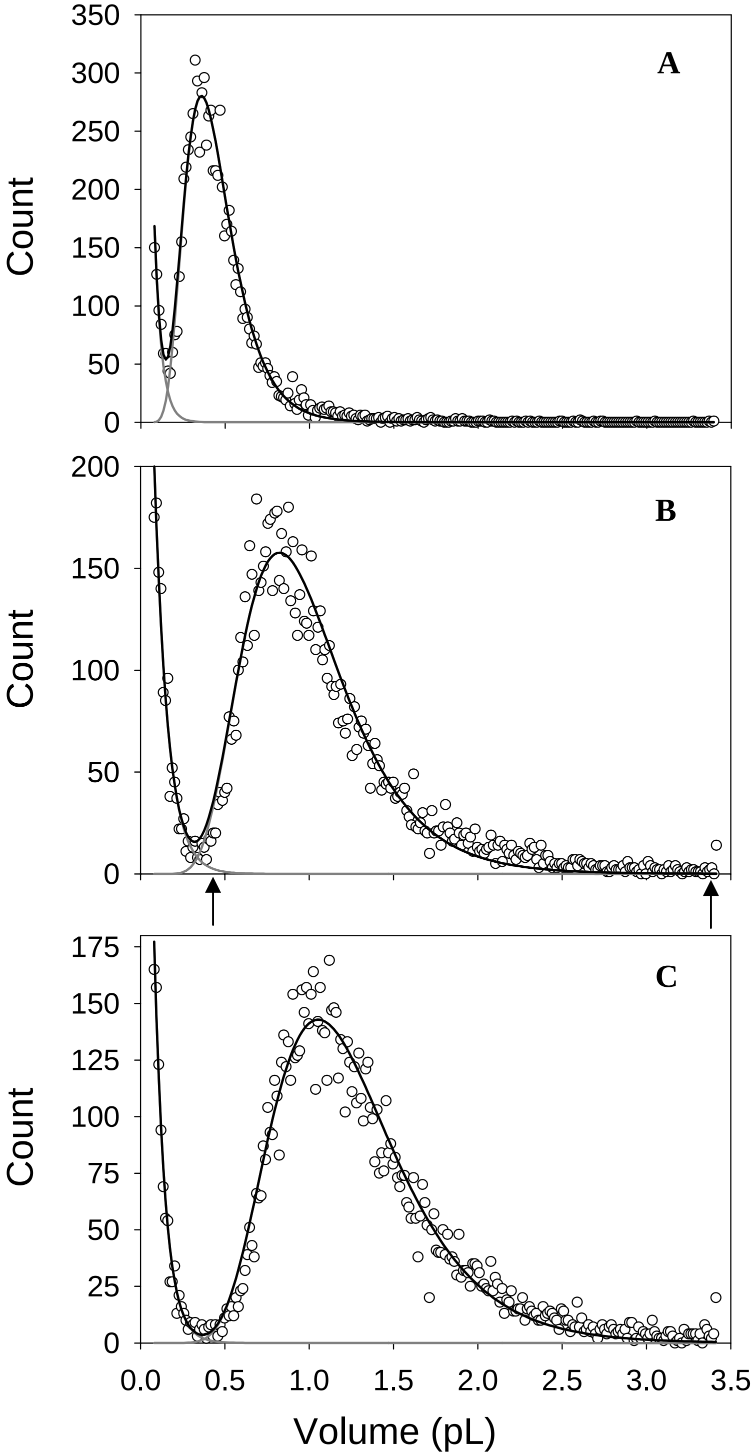

FIGURE 2.1. Experimental volume distributions for MIN6 cells. Volume distributions are shown for hypertonic (A), isotonic (B), or hypotonic (C) conditions ($\Pi_0/\Pi_f = 0.3$, 1.0 and 1.5, respectively). To illustrate the new method, the best-fit lognormal distributions and exponential distributions are shown (lines). The dynamic range for the conventional method (450 fL to 3400 fL) is indicated by the arrows in (B).

isotonic volume of 1096 ± 12 fL. For the new method, the volume data were fit to the sum of an exponential distribution and a lognormal distribution, representing the small volume noise and the cell volumes, respectively. As is evident from Fig. 1, the best-fit curves adequately describe the shape of the experimental volume distributions. The new method yielded a best-fit lognormal distribution in isotonic solution with an arithmetic mean and standard deviation of 1025 ± 14 fL and 385 ± 3 fL, respectively.

The steady-state volume distributions for MIN6 cell suspensions were used to generate Boyle-van't Hoff plots using either the conventional method or the new method, as shown in Fig. 2. The conventional method yielded $\overline{V_b} = 0.37 \pm 0.02$, whereas the new method yielded $\overline{V_b} = 0.15 \pm 0.01$. The difference between these $\overline{V_b}$ values was statistically significant ($p < 0.05$).

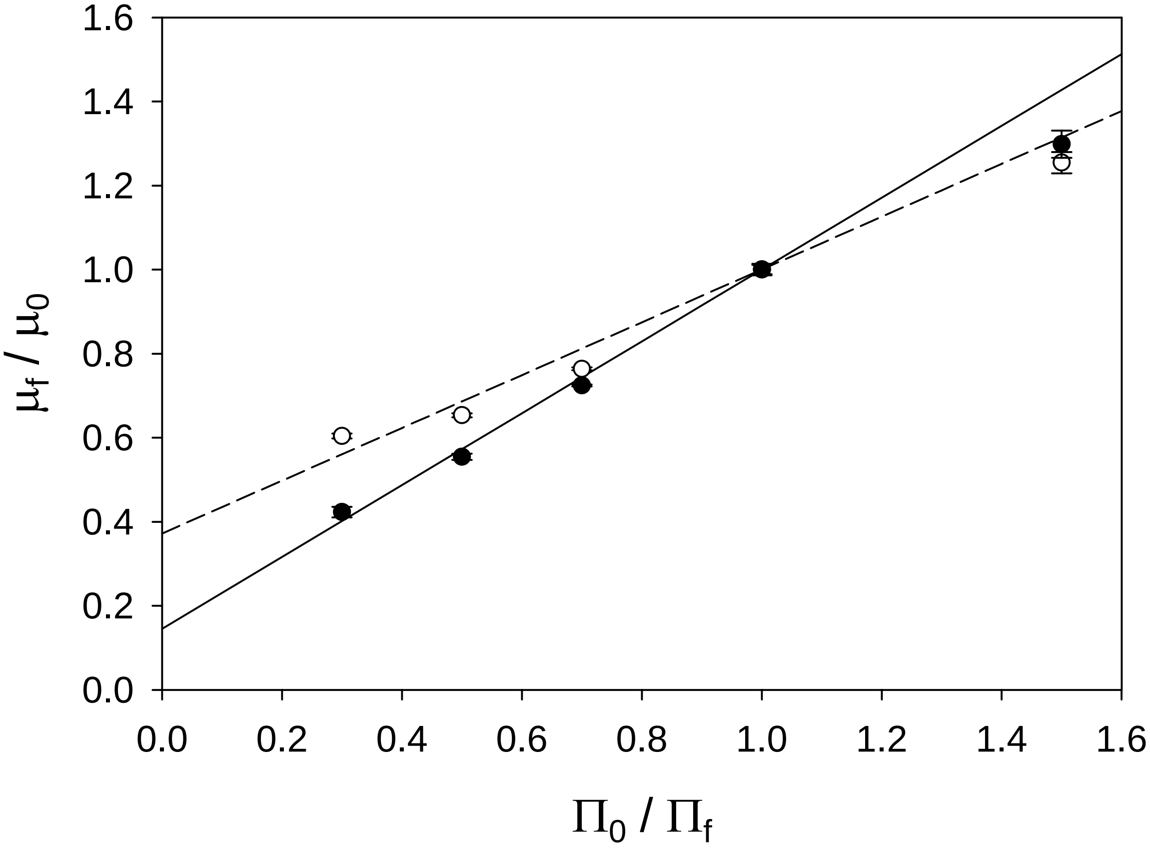

FIGURE 2.2. Boyle-van't Hoff plot for MIN6 cells. The mean volume in the Boyle-van't Hoff plot (normalized to isotonic conditions) was determined using the new method (closed symbols) or the conventional method (open symbols). The value of $\overline{V_b}$ was determined by fitting Eq. 2 to the data, yielding $\overline{V_b} = 0.15$ for the new method (solid line), and $\overline{V_b} = 0.37$ for the conventional method (dashed line). The hypotonic data was excluded for determination of the best-fit lines.

To explore the basis for the difference in the measured values of $\overline{V_b}$ for the conventional method and the new method, a simulated Boyle-van't Hoff experiment was performed to emulate the experiments with MIN6 cells. Fig. 3A shows Boyle-van't Hoff plots of the mean steady-state volumes predicted using the Boyle-van't Hoff relationship (Eq. 1) with $\overline{V_b} = 0.15$ (the value determined by the new method for MIN6 cells). The isotonic volume distribution used in the simulations was derived from MIN6 cell volume data, as shown in the inset for Fig. 3A. The conventional method resulted in overestimation of $\overline{V_b}$ by 150% ($\overline{V_b} = 0.37$), whereas the new method yielded less than 5% error ($\overline{V_b} = 0.16$). It is noteworthy that the apparent $\overline{V_b}$ determined from the simulated data using the conventional method matches the apparent $\overline{V_b}$ determined from experiments with MIN6 cells (Fig. 2), which suggests that the $\overline{V_b}$ used in the simulations ($\overline{V_b} = 0.15$) matches the $\overline{V_b}$ for MIN6 cells (i.e., the new method yielded the correct $\overline{V_b}$). Since it is possible that the use of $\overline{V_b} = 0.15$ in the simulations biased the results, simulations were also performed for a range of $\overline{V_b}$ values, as shown in Fig. 3B. The conventional method yielded error ranging from 8% to more than 500%. In contrast, the error resulting from the new method was less than 5% for the entire range of $\overline{V_b}$ values, which provides further evidence that the value of $\overline{V_b}$ determined by the new method for MIN6 cells ($\overline{V_b} = 0.15$) is accurate.

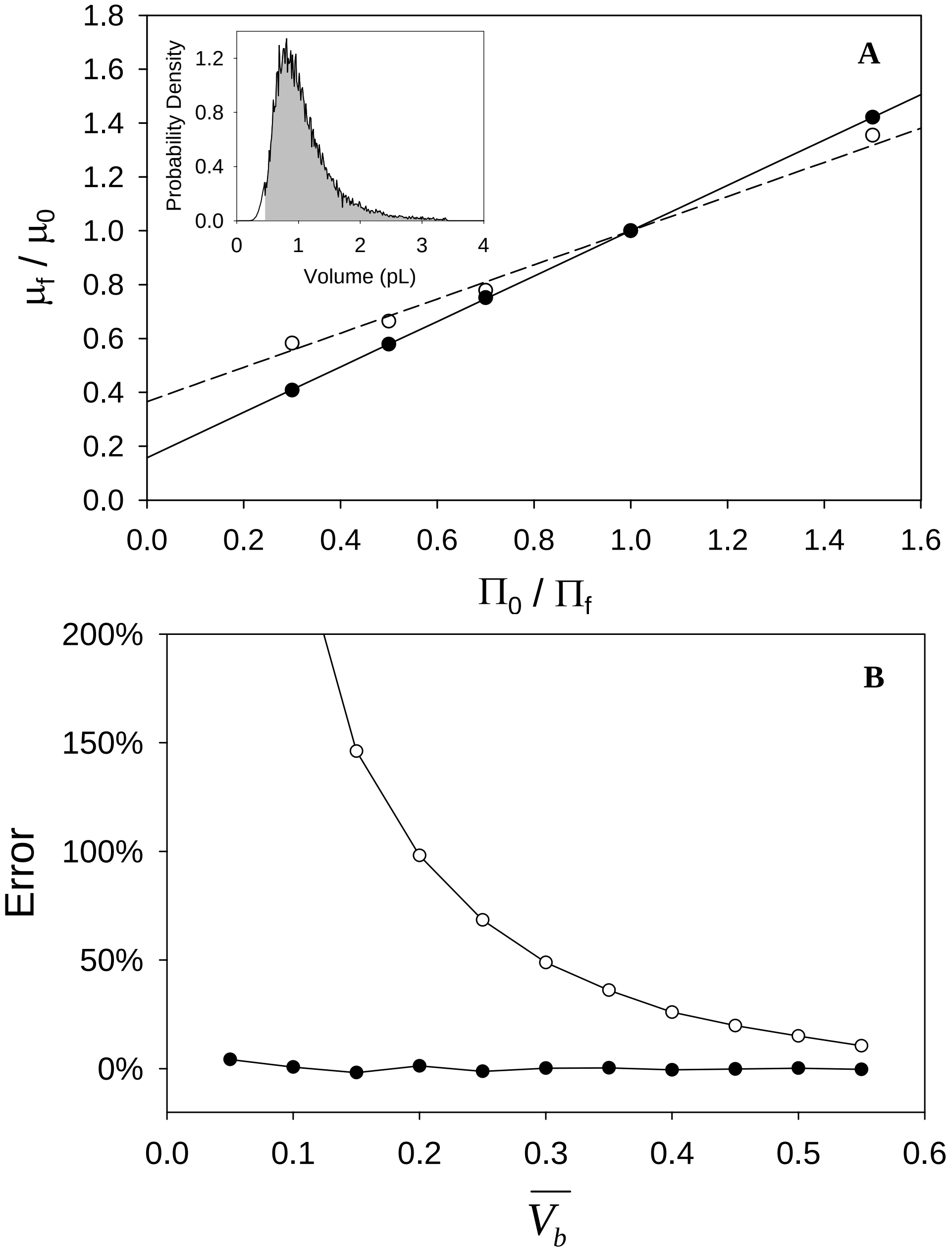

FIGURE 2.3. Comparison of conventional method (open symbols) and new method (closed symbols) using simulated experiments. (A) A simulated Boyle-van't Hoff experiment was performed using $\overline{V_b} = 0.15$, and best-fit lines were determined from the resulting volume data for the conventional method (dashed line) and the new method (solid line). (B) The error in estimation of $\overline{V_b}$ was determined from simulations for a range of $\overline{V_b}$ values. The inset in (A) shows the isotonic volume distribution used in the simulations, comprising the MIN6 volume data between 450 fL and 3400 fL and the best-fit lognormal distribution outside this range.

Since the experiments with MIN6 cells and the simulated Boyle-van't Hoff experiments both indicated that the conventional method results in error because of dynamic range limitations, the factors affecting dynamic range error were systematically investigated using simulations of the steady-state osmotic response for several representative lognormal cell volume distributions, the results of which are shown in Figs. 4 and 5. To facilitate presentation of the data, the standard deviation of the isotonic volume, the upper volume limit, and the lower volume limit were all normalized to the mean isotonic volume ($\overline{\sigma}$, $\overline{U}$, and $\overline{L}$, respectively), which rendered the results independent of the value of the mean isotonic volume. Representative Boyle-van't Hoff plots from the simulations are shown in Fig. 4 for several dynamic ranges. For a large dynamic range (low $\overline{L}$, high $\overline{U}$), the simulated data matches the predictions from the Boyle-van't Hoff relationship, as expected. However, for smaller dynamic range, deviations from this predicted line were observed. For a restrictive lower volume limit (high $\overline{L}$, high $\overline{U}$), the deviations from the Boyle-van't Hoff predictions were most pronounced in hypertonic solution, whereas a restrictive upper volume limit (low $\overline{L}$, low $\overline{U}$) yielded the largest deviations in hypotonic solution. For a small dynamic range (high $\overline{L}$, low $\overline{U}$), large deviations from the expected Boyle-van't Hoff line were observed in both hypertonic and hypotonic solutions. However, despite the observed deviations from the expected Boyle-van't Hoff line, the plots remained approximately linear as is predicted by the Boyle-van't Hoff relationship, particularly under hypertonic conditions.

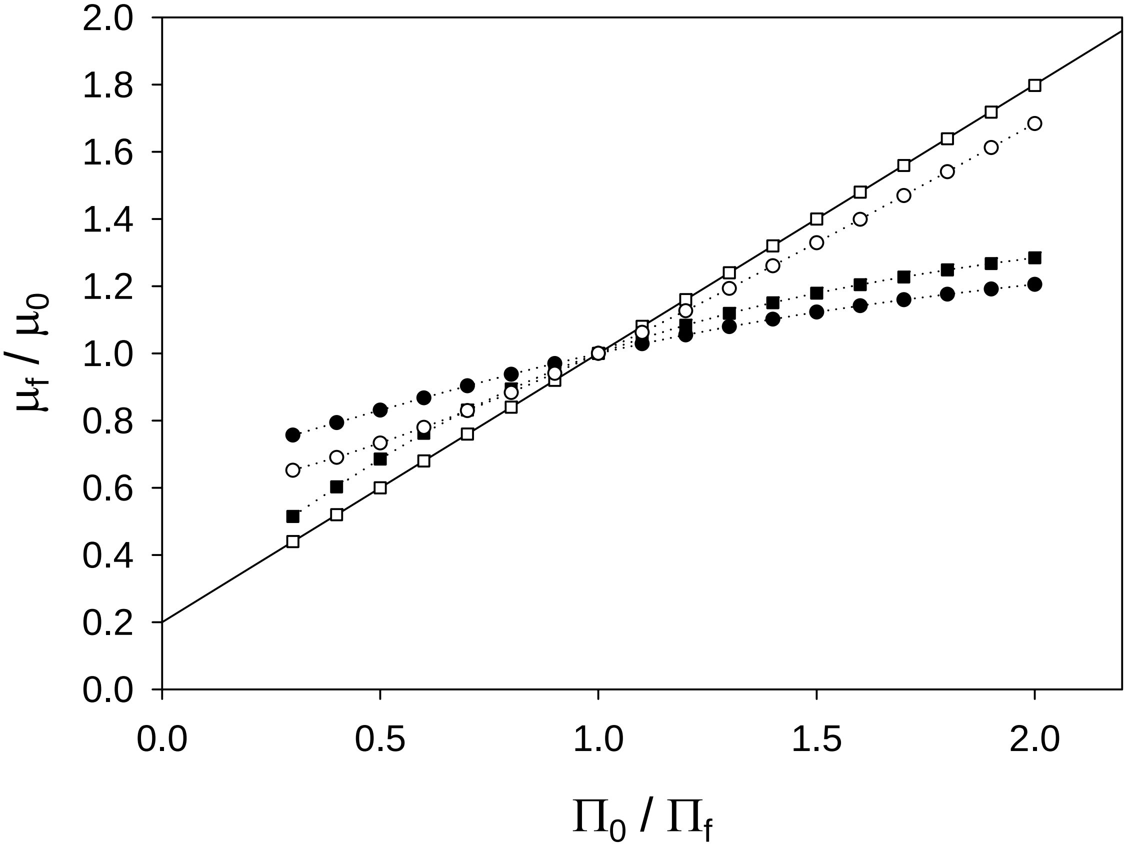

FIGURE 2.4. Boyle-van't Hoff plots for the conventional method from simulations using an isotonic lognormal distribution with $\overline{\sigma} = 0.5$ and $\overline{V_b} = 0.2$. Simulations were performed for $\overline{L}$ values of 0.001 (squares) or 0.5 (circles), and $\overline{U}$ values of 1.5 (closed symbols) or 8.0 (open symbols). The line represents the predicted Boyle-van't Hoff plot using Eq. 2 with $\overline{V_b} = 0.2$.

The Boyle-van't Hoff plots generated from the simulations (e.g., Fig. 4) were fit with Eq. 2 to determine the error in estimation of $\overline{V_b}$ by the conventional method. This error is illustrated in Fig. 5 for several representation cell populations. Because of the common practice of excluding hypotonic data in experimental Boyle-van't Hoff plots (Acker et al., 1999, Fedorow et al., 2001, Liu et al., 1995, Liu et al., 1997, Woods et al., 2000), the error in $\overline{V_b}$ for the conventional method was determined using either hypertonic data only, or both hyper- and hypotonic data (Π_0/Π_f between 0.3 and 2.0). The lesser of these two errors is displayed on the contours in Fig. 5. As indicated by the shaded area, excluding hypotonic data generally results in less error, particularly for low $\overline{L}$ and low $\overline{U}$, which is consistent with the shape of the simulated Boyle-van't Hoff plots in Fig. 4. The effect of $\overline{\sigma}$, $\overline{V_b}$ and the dynamic range (i.e., $\overline{L}$ and $\overline{U}$) on the error is also shown in Fig. 5. As expected, the error increases as the dynamic range decreases. For a typical cell population ($\overline{\sigma} = 0.5$ and $\overline{V_b} = 0.2$), more than 200% error was observed when the dynamic range was small ($\overline{L} = 0.6$ and $\overline{U} = 1.5$, e.g., Petrunkina and Topfer-Petersen, 2000), whereas a large dynamic range ($\overline{L} = 0.2$ and $\overline{U} = 2.7$, e.g., Fedorow et al., 2001) resulted in 20% error. Error was strongly dependent on $\overline{\sigma}$, with a difference in error between $\overline{\sigma} = 0.25$ and $\overline{\sigma} = 1.0$ of more than an order of magnitude (e.g., 6% and 200%, respectively for $\overline{V_b} = 0.2$ and a typical dynamic range of $\overline{L} = 0.3$, $\overline{U} = 2.3$). The value of $\overline{V_b}$ also had a large effect on error. The error was nearly an order of magnitude higher for $\overline{V_b} = 0.2$ than for $\overline{V_b} = 0.6$, illustrating that it is particularly difficult to obtain accurate estimates for $\overline{V_b}$ using the conventional method when the true value of $\overline{V_b}$ is low (e.g., for MIN6 cells).

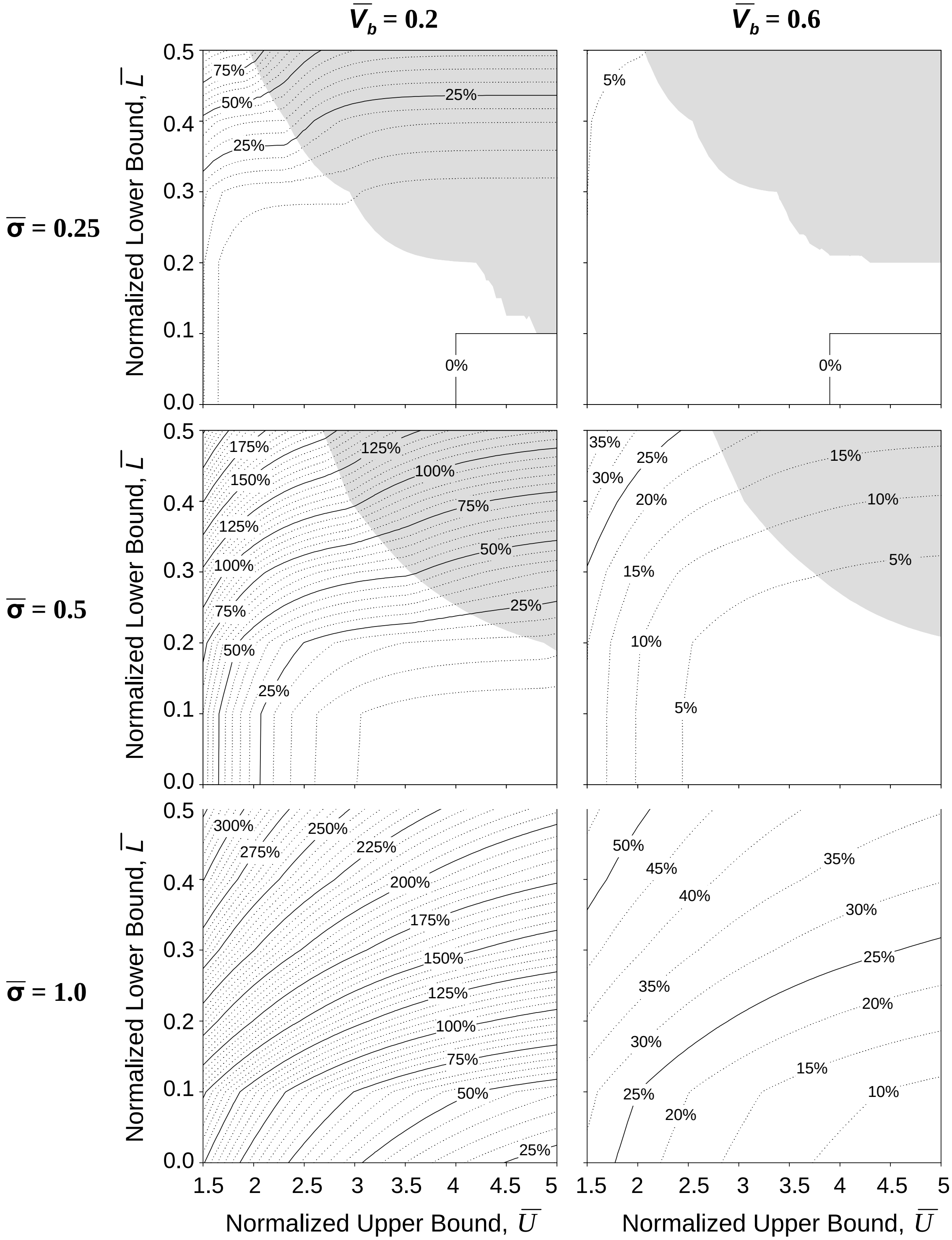

FIGURE 2.5. Error in estimation of $\overline{V_b}$ by the conventional method. The shaded area represents the region in which use of both hyper- and hypotonic data (Π_0/Π_f between 0.3 and 2.0) resulted in less error than using only hypertonic data. The contour labels represent the approach that resulted in the least error (i.e., in the shaded region, hyper- and hypotonic data was used; outside the shaded region, only hypertonic data was used).

Discussion

Since dynamic range limitations can cause error in the value of $\overline{V_b}$ estimated by the conventional method, a new method was devised that is theoretically insensitive to the dynamic range. Using experimental data for MIN6 cell suspensions and theoretical simulations, we have shown that the new method yields better estimates for $\overline{V_b}$ than the conventional method, and that the conventional method can lead to significant error in many cases because of dynamic range limitations.

The finding that the conventional method can lead to significant error in estimation of $\overline{V_b}$ is supported by literature evidence. Although most studies do not discuss the effect of dynamic range on estimates for $\overline{V_b}$, the error in published $\overline{V_b}$ estimates can be obtained using Fig. 5 in conjunction with plots of the isotonic cell volume distribution and the values of the dynamic range volume limits. Table 1 shows a comparison of $\overline{\sigma}$, $\overline{L}$, and $\overline{U}$ observed in the literature. For MIN6 cells, the conventional method yielded $\overline{V_b}$ = 0.37, which is expected to be more than two-fold higher than the true $\overline{V_b}$. The values of $\overline{L}$, $\overline{U}$, and $\overline{\sigma}$ observed in the literature were comparable to the values for MIN6 cells, which suggests comparable error in the estimation of $\overline{V_b}$. Although Liu et al. (1997) used the median volume in the Boyle-van't Hoff plot, rather than the mean, the median volume is expected to yield similar error in estimation of $\overline{V_b}$. In fact, for MIN6 cells, the value of $\overline{V_b}$ determined using mean volumes (0.37) was nearly identical to the value of $\overline{V_b}$ determined from using median volumes (0.36, data not shown). Although both median and mean volumes are expected to result in error, the mode is independent of the dynamic range limitations (as long as the mode falls within the volume limits). Armitage and Juss (1996) compared Boyle-van't Hoff plots generated from mode diameter and the mean diameter. For calculation of the mean diameter, a lower volume limit was chosen to exclude cell debris. They found that the value of $\overline{V_b}$ was 30% higher using the mean than the mode. This result is consistent with the conclusions of the current study about the error associated with dynamic range limitations. Further support is provided by Petrunkina and Topfer-Petersen (2000), who compared $\overline{V_b}$ for boar spermatozoa determined from Boyle-van't Hoff plots of both mean and mode cell volumes. They observed a two-fold higher $\overline{V_b}$ using the mean volume (0.6) than the mode (0.3), which is indicative of error due to dynamic range limitations. The erroneous value of $\overline{V_b}$ determined using the mean volume (i.e., conventional method) was strikingly similar to a previously published value of $\overline{V_b}$ for boar spermatozoa (Gilmore et al., 1996), suggesting error due to dynamic range limitations in this case as well.

TABLE 2.1. Literature values for the dynamic range volume limits and standard deviation of the cell volume distribution

Cell Type	Normalized Standard Deviation ($\bar{\sigma}$)	Normalized Lower Volume Limit ($\bar{L}$)	Normalized Upper Volume Limit ($\bar{U}$)
MIN6 cells	0.38	0.44	3.3
Canine islet cells[a*]	0.4	0.5	1.7
Pig islet cells[b*]	0.5	0.2	2.7
Hamster islet cells[c*]	0.3	0.4	2.1
Human keratinocytes[d*]	0.5	0.2	2.5
MDCK cells[e*]	0.6	0	2.2
Boar spermatozoa[f*]	0.4	0.6	1.5

[*] The normalized parameters were estimated from plots of the isotonic cell volume distribution
[a] Liu et al, 1997; [b] Fedorow et al, 2001; [c] Liu et al, 1995; [d] Acker et al, 1999; [e] Elmoazzen et al, 2005; [f] Petrunkina and Topfer-Petersen, 2000

Examination of the shape of the Boyle-van't Hoff plot may also provide evidence for dynamic range error. For example, the common observation of a lower-than-expected volumetric response upon exposure to hypotonic solution (Acker et al., 1999, Fedorow et al., 2001, Liu et al., 1995, Liu et al., 1997, Woods et. al., 2000) may be attributed to dynamic range error (see Fig. 4, closed squares). However, the deviation from the Boyle-van't Hoff line observed for MIN6 cells in hypotonic solution does not appear to be caused by dynamic range limitations, for the following reasons: (1) the normalized hypotonic volume was nearly the same for the new method and the conventional method (see Fig. 2), suggesting that the normalized volume determined by the conventional method is accurate, and (2) the normalized hypotonic volume predicted for the conventional method in simulated experiments (1.35, see Fig. 3) was higher than the experimental value for MIN6 cells (1.25, see Fig. 2). Although in some cases dynamic range limitations can cause nonlinearity in the Boyle-van't Hoff plot (as described above), it is also possible to observe a linear Boyle-van't Hoff plot despite deviation from the true Boyle-van't Hoff line and significant error in estimation of $\overline{V_b}$ (see Fig. 4, closed circles). For example, approximately linear Boyle-van't Hoff plots were reported by Petrunkina and Topfer-Petersen (2000) in spite of a narrow dynamic range (high $\overline{L}$ and low $\overline{U}$) and the concomitant expectation for error in the $\overline{V_b}$ estimate.

Although the conventional method resulted in significant error for MIN6 cells because of dynamic range limitations, the new method was shown to yield an accurate estimate for $\overline{V_b}$. The new method is theoretically insensitive to the dynamic range since the best-fit lognormal distribution is extrapolated beyond the dynamic range volume limits. However, error in estimation of $\overline{V_b}$ may result from differences between the experimental cell volume distribution and the best-fit lognormal distribution. Error was shown to be less than 5% for MIN6 cells (see Fig. 7), which exhibit a cell volume distribution that is qualitatively similar to many other cell types (Acker et al., 1999; Elmoazzen et al., 2005; Muldrew et al., 2001; Sipe et al., 1966; Westring et al., 1969). Thus, it is expected that the error in estimation of $\overline{V_b}$ by the new method would yield comparable error (i.e., < 5%) for most cell types.

For MIN6 cells (a mouse pancreatic β-cell line), $\overline{V_b}$ was determined to be 0.15 using the new method, which is lower than most values of $\overline{V_b}$ reported in the literature (Table 2). In particular, the $\overline{V_b}$ values determined using the Coulter counter technique for islet cells from dog, pig and hamster were 0.36, 0.35, and 0.4, respectively, which is more than two-fold higher than the $\overline{V_b}$ for MIN6 cells. It is interesting to note that the $\overline{V_b}$ for

MIN6 cells determined by the conventional method ($\overline{L}$ = 0.44, $\overline{U}$ = 3.3) was 0.37, which is comparable to the values of $\overline{V_b}$ determined by the Coulter counter technique reported in the literature for islet cells. It is also noteworthy that microscopic measurement of cell volume, which is not susceptible to dynamic range errors, yielded $\overline{V_b}$ = 0.22 for hamster islet cells (Benson et al., 1993) and $\overline{V_b}$ = 0.16 for canine β-cells, both of which are comparable to the value of $\overline{V_b}$ for MIN6 cells determined by the new method presented here. Taken together, these findings suggest that the value of $\overline{V_b}$ for MIN6 cells determined using the new method is accurate.

TABLE 2.2. Literature values of $\overline{V_b}$ for pancreatic islet cells

Cell Type	$\overline{V_b}$	**Experimental Technique**
MIN6 cells[a]	0.15	Electronic cell sizing, new method
Canine islet cells[b]	0.36	Electronic cell sizing, conventional method
Pig islet cells[c]	0.35	Electronic cell sizing, conventional method
Hamster islet cells[d]	0.4	Electronic cell sizing, conventional method
Hamster islet cells[e]	0.22	Microscopic volume measurement
Canine β-cells[f]	0.16	Microscopic volume measurement

[a]Current study; [b]Liu et al, 1997; [c]Fedorow et al, 2001; [d]Liu et al, 1995; [e]Benson et al., 1993; [f]Aggarwal et al., 1986

In summary, we have established that the conventional method for determining $\overline{V_b}$ can result in significant error because of dynamic range limitations, and that the new method presented herein, which is not susceptible to dynamic range error, provides improved estimates for $\overline{V_b}$. Although the new method can lead to error because of deviation between the best-fit lognormal distribution and the experimental cell volume distribution, this error was shown to be < 5% for MIN6 cells, which exhibit a cell volume distribution that is qualitatively similar to many other cell types. Thus, it expected that, in general, the new method will yield more accurate estimates for $\overline{V_b}$ than the conventional method.

Appendix

Theoretical Derivation of Dynamic Range Error

Although the Boyle-van't Hoff relationship (Eq. 1) is expected to describe the steady-state osmotic response for a cell with initial volume V_0, experimental cell populations exhibit a distribution of cell volumes, confounding analysis of experimental volume distributions using the Boyle-van't Hoff relationship. In analysis of Coulter counter data, it is generally assumed that the cell volume (V) can be replaced with the mean cell volume (μ) in the Boyle-van't Hoff relationship (as in Eq. 2), regardless of the shape of the volume distribution or the presence of dynamic range limitations. To examine this assumption, we have first analyzed the osmotic response of the mean cell volume in the absence of dynamic range limitations. Under isotonic conditions, the mean cell volume is defined as:

$$\mu_0(0,\infty) = \int_0^\infty V_0\left[P_{V_0}(V_0)\right]dV_0 \qquad \text{[A1]}$$

where V_0 is the isotonic cell volume and $P_{V_0}(V_0)$ is the probability density function for the isotonic cell volume. If V_0 is a continuous random variable, then the rules for transformations of univariate random variables can be used in conjunction with the Boyle-van't Hoff relationship (Eq. 1) to determine the probability density function for the final cell volume, $P_{V_f}\left(V_f\right)$. Since the Boyle-van't Hoff relationship describes V_f as monotonically increasing function of V_0, it follows that:

$$P_{V_f}\left(V_f\right)=\frac{d\left(\alpha^{-1}V_f\right)}{dV_f}P_{V_0}\left(V_0=V_f\alpha^{-1}\right)=\alpha^{-1}P_{V_0}\left(V_0=V_f\alpha^{-1}\right) \qquad \text{[A2]}$$

where $\alpha=\frac{\Pi_0}{\Pi_f}\left(1-\overline{V_b}\right)+\overline{V_b}$

Making use of the Boyle-van't Hoff relationship (Eq. 1), the final mean volume can be determined from Eq. A2:

$$\mu_f\left(0,\infty\right)=\int_0^\infty V_f\left[P_{V_f}\left(V_f\right)\right]dV_f=\int_0^\infty \alpha V_0\left[\alpha^{-1}P_{V_0}\left(V_0\right)\right]\alpha dV_0=\alpha\int_0^\infty V_0\left[P_{V_0}\left(V_0\right)\right]dV_0 \qquad \text{[A3]}$$

The relationship between the initial and final mean cell volume in the absence of dynamic range limitations can be determined by substituting Eq. A1 into Eq. A3:

$$\frac{\mu_f\left(0,\infty\right)}{\mu_0\left(0,\infty\right)}=\frac{\Pi_0}{\Pi_f}\left(1-\overline{V_b}\right)+\overline{V_b} \qquad \text{[A4]}$$

The above equation shows that, if the entire cell population is considered, the mean cell volume is expected to follow the Boyle van't Hoff relationship (i.e., no error in the apparent $\overline{V_b}$ is expected if the mean volume is used in the Boyle-van't Hoff plot). However, when dynamic range limitations are considered, this convenient result no longer applies. The definition of the mean isotonic volume within the dynamic range with lower volume limit (*L*) and upper volume limit (*U*) is given by:

$$\mu_0\left(L,U\right)=\frac{\int_L^U V_0\left[P_{V_0}\left(V_0\right)\right]dV_0}{\int_L^U\left[P_{V_0}\left(V_0\right)\right]dV_0} \qquad \text{[A5]}$$

Using the same approach as in the derivation of Eq. A3, and being careful to appropriately adjust the bounds of the integral, it can be shown that:

$$\mu_f(L,U) = \alpha\left(\frac{\int_{L/\alpha}^{U/\alpha} V_0\left[P_{V_0}(V_0)\right]dV_0}{\int_{L/\alpha}^{U/\alpha}\left[P_{V_0}(V_0)\right]dV_0}\right) = \alpha\mu_0(L/\alpha, U/\alpha) \qquad \text{[A6]}$$

Thus, the final mean volume within the dynamic range defined by *L* and *U* is proportional to the initial mean volume within the range *L*/α to *U*/α. Combining Eq. A5 with Eq. A6 yields:

$$\frac{\mu_f(L,U)}{\mu_0(L,U)} = \left(\frac{\Pi_0}{\Pi_f}\left(1-\overline{V_b}\right)+\overline{V_b}\right)\left(\frac{\mu_0(L/\alpha, U/\alpha)}{\mu_0(L,U)}\right) \qquad \text{[A7]}$$

By comparison of Eq. A7 with Eq. A4, it can be seen that the mean cell volume within the dynamic range (*L* to *U*) does not follow the Boyle-van't relationship because of the extra term at the right representing the dynamic range error. This error depends the location of the volume limits (*L* and *U*), the value of α (i.e. the magnitude of the osmotic volume change), and the shape of the isotonic cell volume distribution. As expected, for large dynamic range, $\mu_0(L/\alpha,U/\alpha) = \mu_0(L,U) = \mu_0(0,\infty)$, and Eq. A4 is recovered from Eq. A7.

Boyle-van't Hoff Plot for Cell Debris

Since we observed in Fig. 1A-C that the small volume noise (i.e., cell debris) is affected by the solution osmotic strength, we constructed a Boyle-van't Hoff plot from the mean of the best-fit exponential distribution, as shown in Fig. 6. The data showed a linear trend ($R^2 = 0.91$), yielding $\overline{V_b} = 0.36 \pm 0.03$ for the small volume noise. The mean of the best-fit exponential distribution to the isotonic data was 72 fL.

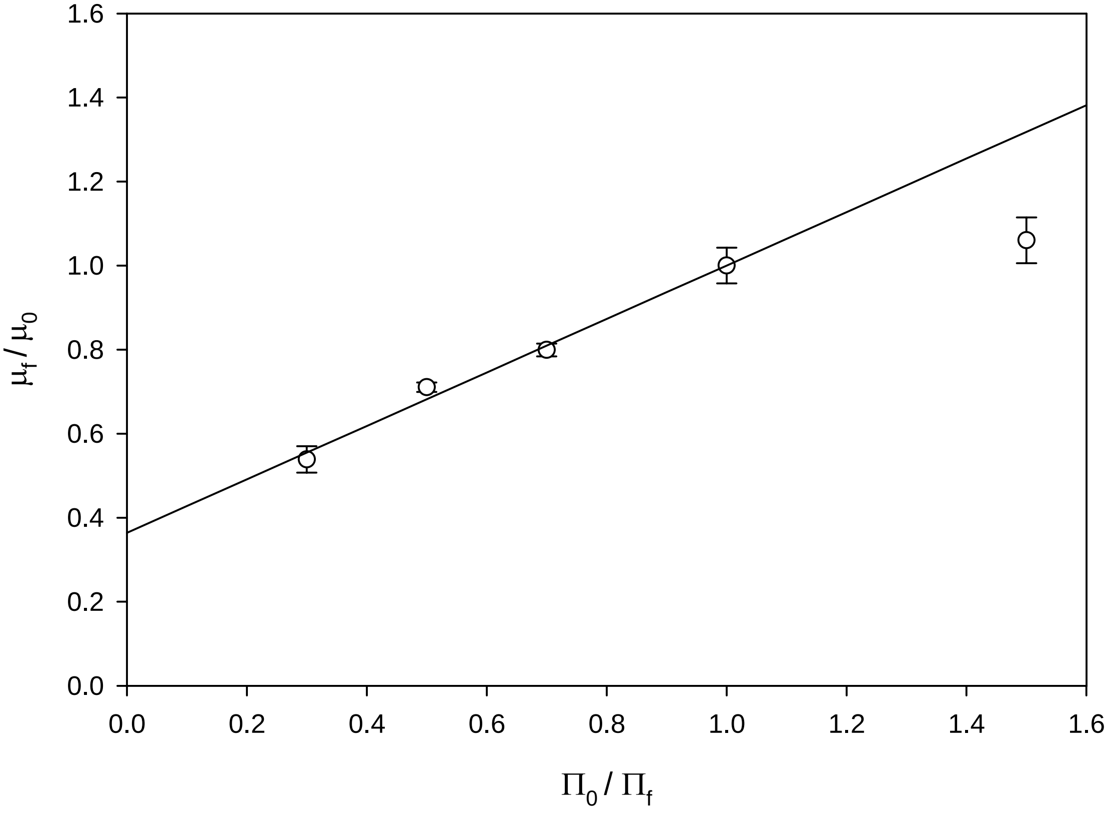

FIGURE 2.6. Boyle-van't Hoff plot for cell debris constructed using the mean of the best-fit exponential distribution. The hypotonic data point was excluded for determination of the best-fit line.

CHAPTER 3

DYNAMIC RANGE ERROR IN ELECTRONIC CELL SIZING EXPERIMENTS: MEMBRANE WATER PERMEABILITY

Introduction

Survival of cryopreservation is linked to intracellular water content, which changes during freezing as a result of osmotic efflux of water upon formation of extracellular ice: excessive removal of water during freezing leads to "solution damage," whereas insufficient removal of water leads to damage due to intracellular ice formation (Mazur et al., 1972). Thus, the cell membrane water permeability (L_p), which controls the rate of osmotic water transport during freezing, is an important cell-specific parameter for designing cryopreservation procedures. The membrane water permeability is generally determined by measuring the change in cell volume after exposure to anisotonic solution, and fitting the resulting data to a mathematical model of osmotic water transport. Electronic cell sizing instruments (e.g., Coulter counters), which measure the cell-volume-dependent change in the electrical resistance as suspended cells pass through a small aperture, are commonly used to perform these experiments (e.g., Agca, Liu et al., 2005, Agca, Mullen et al., 2005, Gao et al., 1998, McGann et al., 1988, Woods et al., 1999).

In electronic cell sizing experiments, it is common to exclude a portion of the volume data because of dynamic range limitations. The dynamic range lower volume limit (i.e., the volume below which data is discarded when determining cellular osmotic properties) is typically chosen to exclude small volume data attributed to cell debris

(Agca, Liu et al., 2005, Agca, Mullen et al., 2005, Lewis et al., 1989, Liu et al., 1997, McGann et al., 1988, Woods et al., 1999), whereas the dynamic range upper volume limit is either determined by the limits of the electronic sizing instrument, or is chosen to exclude cell clumps (Agca, Liu et al., 2005, Agca, Mullen et al., 2005, Liu et al., 1997, Woods et al., 1999). Although the exclusion of data outside the dynamic range is advantageous in that it removes unwanted data due to cell debris and cell clumps, it may also exclude useful cell volume measurements. This is because cell populations exhibit a broad range of cell volumes (Elmoazzen et al., 2005, Muldrew et al., 2001). We have recently shown that exclusion of cell volume data outside the dynamic range can result in significant error in estimates for the osmotically inactive volume fraction, the cell property that characterizes the steady-state osmotic response (Chapter 2), which suggests that dynamic range limitations may also lead to error in estimates for L_p. However, the effect of dynamic range limitations on estimates for L_p has not been investigated.

In the present study, we examine the effect of dynamic range limitations on the error in estimates for L_p obtained using conventional approaches. In addition, we present two new methods for determining L_p that are not expected to be sensitive to dynamic range limitations: the lognormal extrapolation method and the volume limit adjustment method.

Background

Conventional Method

For the conventional method, the value of the membrane water permeability was determined by fitting a membrane water transport model to transient cell volume data, while excluding volumes outside the dynamic range. Although dynamic range volume limits are commonly used in experiments to measure the transient osmotic response (Agca, Mullen et al., 2005, Liu et al., 1997, Woods et al., 1999), there does not appear to be a consistent method for selecting the volume limits. In the present study, we chose a lower volume limit of 450 fL based on the isotonic volume distribution for MIN6 cells, which exhibited cell debris below this volume (see Chapter 2). For the dynamic range upper volume limit, we used the maximum measurable volume for the experimental Coulter counter settings (3400 fL).

The change in cell volume (*V*) after exposure to an anisotonic solution containing only membrane impermeable solutes can be described by the well-known equation:

$$\frac{dV}{dt} = L_p A(\Pi_i - \Pi_e) \qquad [1]$$

where L_p is the hydraulic permeability, Π is the osmotic pressure, *A* is the cell membrane surface area, and the subscripts "*i*" and "*e*" refer to intracellular and extracellular conditions, respectively. For an ideal and dilute intracellular solution, the intracellular osmotic pressure can be expressed in terms of the isotonic osmotic pressure using the Boyle-van't Hoff relationship:

$$\Pi_i = \frac{\Pi_0\left(1 - \overline{V_b}\right)}{V/V_0 - \overline{V_b}} \qquad [2]$$

where $\overline{V_b}$ is the osmotically inactive volume fraction and the subscript "0" refers to isotonic conditions. Combining Eqs. 1 and 2, and assuming a step-change in extracellular osmotic pressure to Π_f at $t = 0$ (i.e., for $t > 0$, $\Pi_e = \Pi_f$), one obtains:

$$\frac{dV}{dt} = L_p A \Pi_0 \left(\frac{1 - \overline{V_b}}{V/V_0 - \overline{V_b}} - \frac{\Pi_f}{\Pi_0} \right) \qquad [3]$$

For the conventional method, Eq. 1 was fit to the experimental volume data by a least-squares method using L_p as the variable parameter. The isotonic cell volume (V_0) was replaced by the mean isotonic cell volume within the dynamic range (μ_0) and A was replaced by $(36\pi)^{1/3}\mu_0^{2/3}$ (i.e., the area of a sphere with a volume of μ_0), as is commonly done (Adams et al., 2003, Rule et al 1980, Scheiwe and Korber, 1983). To determine the best-fit L_p, we used the apparent value of $\overline{V_b}$ in Eq. 3, which was determined by noting that at steady-state Eq. 3 reduces to

$$\overline{V_b} = \frac{\Pi_0 / \Pi_f - \mu_f / \mu_0}{\Pi_0 / \Pi_f - 1} \quad [4]$$

where μ_f is the mean steady-state volume within the dynamic range. Although the use of the apparent $\overline{V_b}$ in the fit for L_p is less common than using $\overline{V_b}$ determined from a Boyle-van't Hoff plot over a range of solution osmotic strengths, the use of the apparent $\overline{V_b}$ is expected to yield less ambiguous results. As shown in Chapter 2, estimates for $\overline{V_b}$ obtained from Boyle-van't Hoff plots can be affected by dynamic range limitations, resulting in an estimate for $\overline{V_b}$ that depends on the specific osmotic strengths used for generation of the Boyle-van't Hoff plot. In contrast, determination of L_p using the apparent value of $\overline{V_b}$ (Eq. 2) requires a single measurement of the transient osmotic response, and does not require construction of a Boyle-van't Hoff plot. In addition, the use of the apparent $\overline{V_b}$ is expected to yield results that are equivalent to the common practice of fitting for $\overline{V_b}$ and L_p simultaneously (McGann et al., 1988, Elmoazzen et al., 2005, Muldrew et al., 2001, Liu et al., 1997).

New Method 1: Lognormal Extrapolation Method

Since the conventional method for determining the best-fit L_p does not account for dynamic range limitations, we designed a new method for determining L_p based on extrapolation of the best-fit lognormal distribution beyond the dynamic range volume limits, as illustrated in Fig. 1. This new approach for determining L_p (lognormal extrapolation method) was motivated by the observation that the steady-state volume data for MIN6 cells is adequately described by a lognormal distribution (see Chapter 2). The best-fit isotonic lognormal distribution and $\overline{V_b}$ are required as inputs to the lognormal extrapolation algorithm, and can be determined from steady-state cell volume measurements, as described in Chapter 2. In the first step of the lognormal extrapolation method, the transient response of the best-fit isotonic lognormal distribution is predicted using Eq. 3 with an initial guess for $L_p\Pi_0$ and known values for Π_0/Π_f and $\overline{V_b}$. As shown in Fig. 1, the transient predictions include volume data outside the dynamic range, and permit accounting for cells that cross the dynamic range volume limits. In the second step, the volume data outside the dynamic range is removed, and the mean volume is calculated as a function of time. In the third step, the sum of the error squared is computed between the predicted mean volume and the experimental data, and a revised guess for $L_p\Pi_0$ is returned to step 1. The process is repeated until the sum of the error squared is minimized, yielding a best-fit $L_p\Pi_0$.

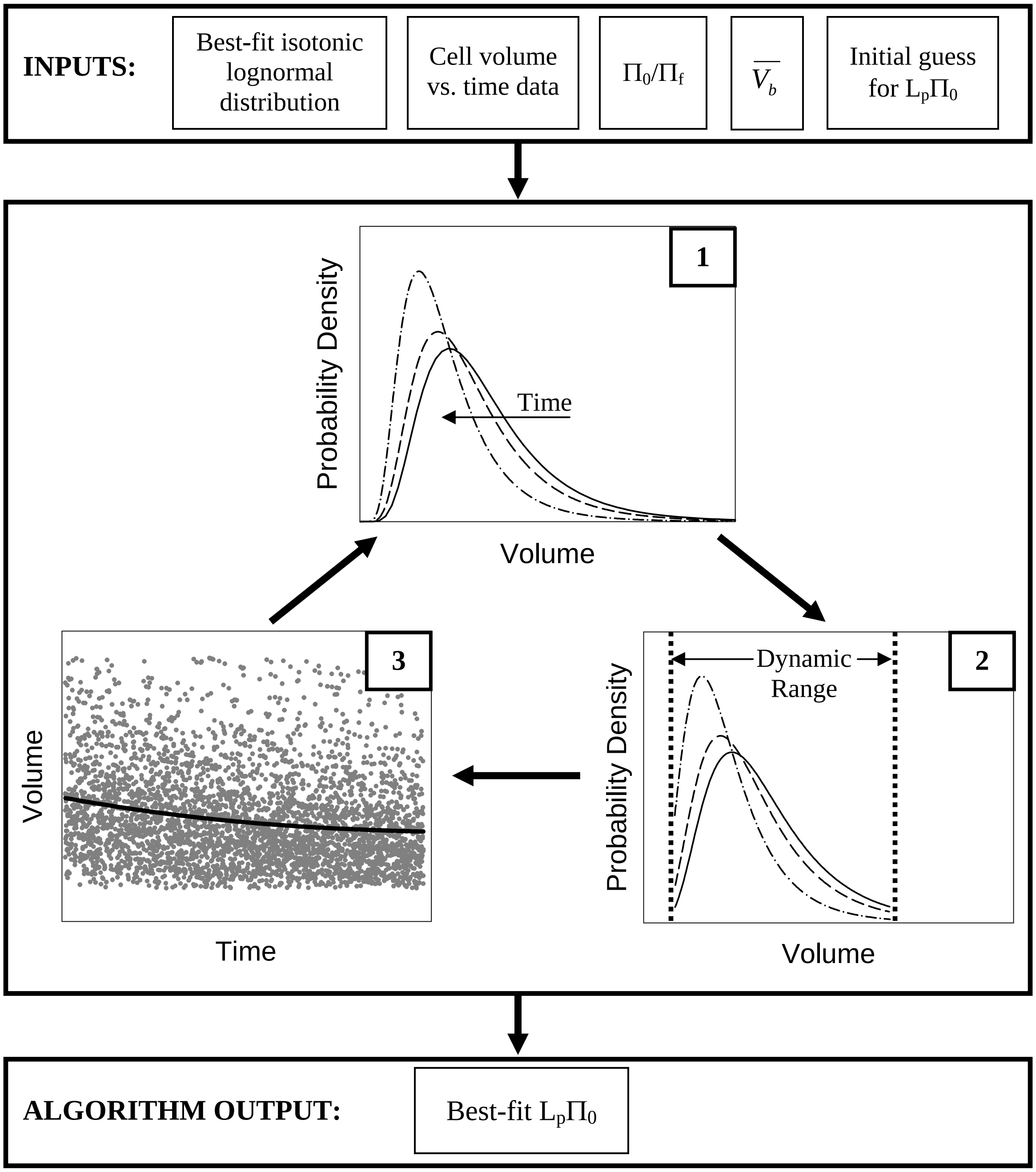

FIGURE 3.1. Schematic of lognormal extrapolation method for determining L_p. See text for details.

New Method 2: Volume Limit Adjustment Method

Although examination of the steady-state volume data for MIN6 cells suggests that a lognormal distribution adequately describes the cell population (Chapter 2), it is possible that determining L_p using predictions of the transient osmotic response for the best-fit isotonic lognormal distribution (lognormal extrapolation method) will lead to error in the estimate for L_p because of deviations between the experimental volume data and the best-fit lognormal distribution. Therefore, we designed an additional algorithm for determining L_p that is not sensitive to dynamic range limitations or the quality of the lognormal distribution fit. This new method, which we call the volume limit adjustment method, consists of three steps, and is illustrated for exposure to hypertonic solution (i.e., cell shrinkage) in Fig. 2.

As shown in Fig. 2, the first step in the algorithm is to predict the transient volume change of the isotonic cell population (which comprises cell volume measurements within the dynamic range) using Eq. 3 with an initial guess for $\mathrm{L_p}\Pi_0$ and known values of $\overline{V_b}$ and Π_0/Π_f. The isotonic cell volume data and the value of $\overline{V_b}$ can be obtained from steady-state Coulter counter experiments, as previously described (Chapter 2). As can be seen in Fig. 2, the isotonic cell volumes fall within the dynamic range (i.e., the lowest and highest cell volumes correspond with the dynamic range lower and upper volume limits, L and U, respectively). Whereas one expects large cells ($V > U$) to cross U during shrinkage, it is not possible to account for these cells since experimental volume measurements are not available for volumes greater than U.

Therefore, in the second step of the algorithm, the dynamic range is adjusted (i.e., U is lowered to U^*) such that isotonic cell volume data can be used to predict cells crossing the upper volume limit, and the mean volume within this adjusted dynamic range is calculated as function of time. The value of U^* is taken as the steady-state volume for a cell with an initial volume of U, which is given as:

$$U^* = U\left[\overline{V_b} + \frac{\Pi_0}{\Pi_f}\left(1 - \overline{V_b}\right)\right]$$

In the third step of the algorithm, the sum of the error-squared is computed between the predicted change in the mean volume (determined in step 2) and the experimental data. The entire process (steps 1-3) is repeated for a new value of $L_p\Pi_0$ until the sum of the error squared is minimized, yielding a best-fit $L_p\Pi_0$.

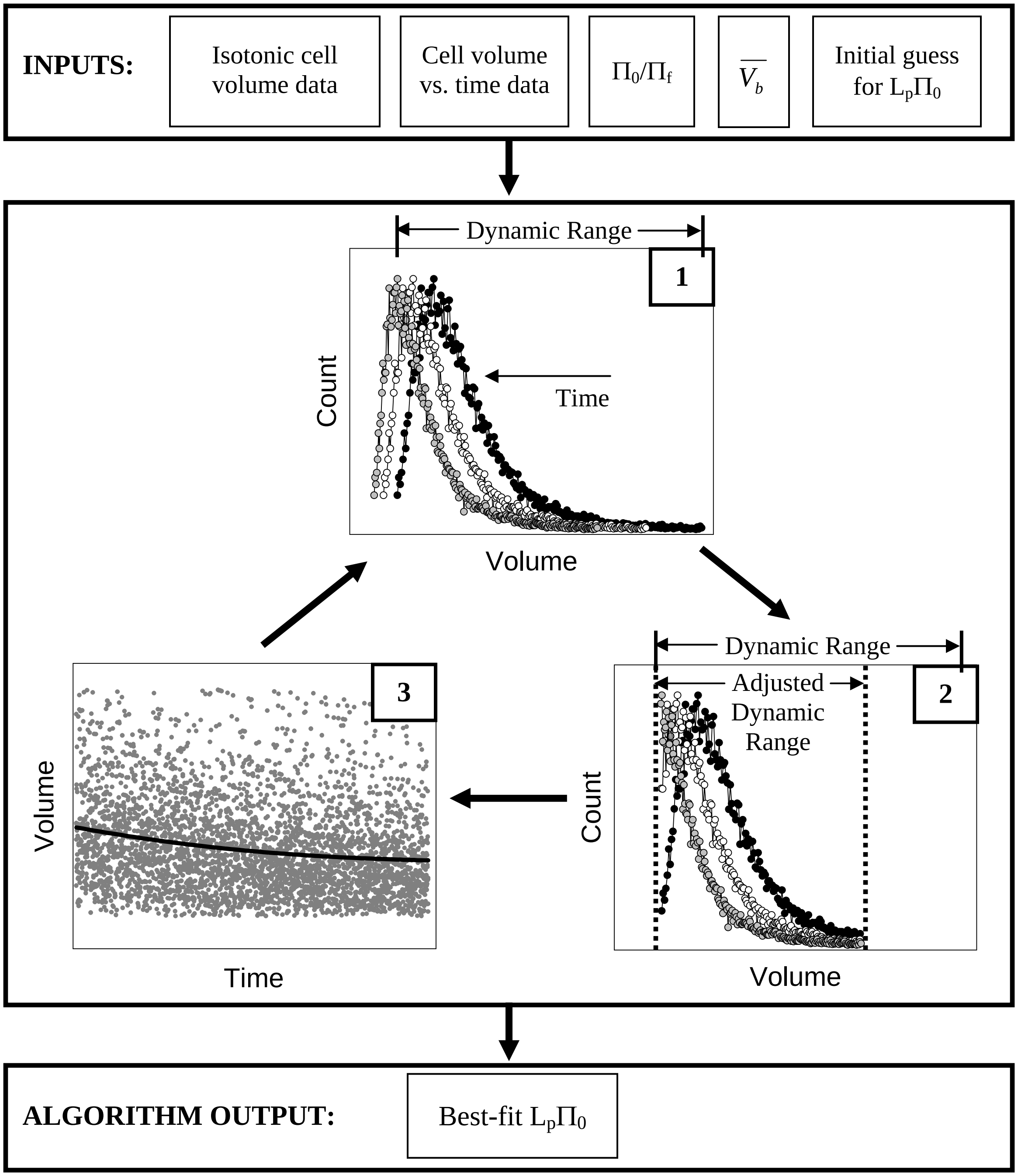

FIGURE 3.2. Schematic of volume limit adjustment method for determining L_p. See text for details.

Materials and Methods

Osmotic Test Solutions

Hypertonic solutions were prepared by addition of sucrose to isotonic (300 mOsm/kg) phosphate buffered saline (Ca^{2+} and Mg^{2+} free). The osmolality of all solutions was measured with a freezing point depression osmometer to be within 1% of the reported value. Solutions were filtered with 0.2 μm filters before use.

Cell Culture

Mouse insulinoma cells (MIN6, generously provided by Paolo Meda, M.D.) were cultured in DMEM (high glucose) supplemented with 15% v/v heat inactivated FBS and β-mercaptoethanol (0.07 mM) at 37ºC in a 5% CO_2 environment. Media was changed every 3 days and passages were performed weekly. Cell suspensions (96% single cells, 93% viability) were created by exposure to 0.2% trypsin solution at 37°C for 15 min, followed by trituration in culture medium 20 times with a 20G needle (see Chapter 4). Suspensions were used in osmotic experiments within 5 minutes.

Transient Osmotic Response

A volume of 100 μL of cell suspension (1-2 x 10^6 cells/ml) in isotonic cell culture medium was injected into 10 mL of well-mixed osmotic test solution (430 mOsm/kg, 600 mOsm/kg, or 1000 mOsm/kg) in the Coulter counter sample beaker. At this cell concentration, the cell suspension (96% single cells) is expected to yield < 6% error due to coincidence (see Chapter 4). For each osmotic solution, four replicates were performed, each representing cell suspensions created from different cultures. Mixing of the sample solution was accomplished using a small magnetic stirrer attached to the base of the beaker holder, and a 1/2 x 5/16” stir bar (see Appendix for a discussion of mixing in the sample beaker). Temperature was maintained at 21 ± 0.5°C by circulating liquid from a refrigerated water bath through the jacket of the sample beaker. The raw voltages from the Coulter counter (Z2 series) were accessed via a custom installed BNC connection, and peak voltage signals were digitized and sent to a computer using a Cell Size Analyzer (CSA) interface (McGann et al., 1982). To reduce electrical noise, copper wire was inserted into the jacket of the beaker and grounded to the base of the Coulter counter, creating a Faraday shield (see Chapter 2). Peak voltage signals were converted to volume by calibration with spherical latex beads of known size, as described previously (Chapter 2). The Coulter counter settings were chosen such that the maximum measurable volume was 3400 fL (gain = 32, current = 0.5, preamplifier gain = 179.2).

Although it is common in electronic sizing experiments to pool volume data over time intervals (i.e., compute the mean, mode or median volume for each time increment) before determining the best-fit L_p, the effect of this practice on the apparent L_p is unclear. For example, Elmoazzen et al. (2005) point out that the mean, median and mode follow different kinetics during osmotic volume changes, and recommend using the mean volume, whereas other authors suggest that the mode is a better measure of central tendency (Armitage and Juss, 1996, Hunt et al., 2003). To avoid the potential error introduced by pooling the data, we used all of the volume data to determine the best-fit L_p. Since the CSA software (v. 3.0) automatically pools the data over time increments and does not give access to the unpooled data, the entire data set (without pooling) was extracted from the CSA files using MATLAB.

Whereas the initiation of recording of the volume data occurred at an arbitrary time, it was necessary to determine the time at which the cell sample was injected into the sample beaker and exposed to a step change in osmotic strength (i.e., $t = 0$ in Eq. 3). As shown in Fig. 3, this was accomplished by fitting a four-parameter logistic function to the rate at which voltage pulses were recorded (count rate), defined as:

$$X = X_0 + \frac{\left(X_f - X_0\right)}{1 + e^{-(t - t^*)/m}}$$

where X is the count rate, t is the time, and the remaining parameters (X_f, X_0, t^* and m) are constants. The time for the step change in osmotic strength ($t = 0$ in Eq. 3) was taken as t^*, the half time for the change in the count rate from X_0 to X_f.

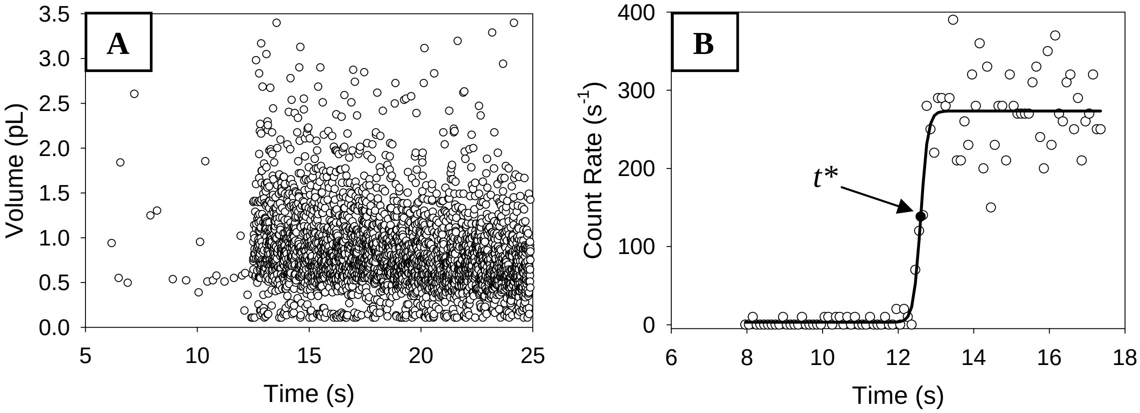

FIGURE 3.3. The location of the start time ($t = 0$) for the transient osmotic response was determined from the raw volume vs. time data (A) by pooling over 0.1 sec intervals to determine the count rate, and fitting the resulting data to a logistic function (B). The start time was taken as the time to achieve one half of the final count rate (arrow).

The best-fit value of L_p was then determined from the transient volume data using the conventional method, the lognormal extrapolation method and the volume limit adjustment method. For the conventional method, the mean isotonic volume within the dynamic range was used (1096 fL, see Chapter 2). As inputs for the lognormal extrapolation method, and the best-fit isotonic lognormal distribution (arithmetic mean and standard deviation of 1025 fL and 385 fL, respectively) and $\overline{V_b}$ = 0.15 were used (see Chapter 2). For the volume limit adjustment method, the inputs to the algorithm were $\overline{V_b}$ = 0.15 and the isotonic cell volume measurements within the dynamic range (see Chapter 2).

Simulated Experiments

A simulated experiment was designed to test the accuracy of the conventional method, lognormal extrapolation method and volume limit adjustment method for determining L_p from transient osmotic data. For a given value of L_p, the transient osmotic response was predicted using Eq. 1 for a simulated isotonic cell population, which was randomly generated from a cell volume distribution consisting of MIN6 cell volume data within the dynamic range, and the best-fit lognormal distribution outside the dynamic range (see Chapter 2, Fig. 3A, inset). Small volume noise (i.e., cell debris) was then introduced to match experimental observations, and the experimental dynamic range volume limits (450 fL and 3400 fL) were applied. The best-fit L_p was determined from the resulting volume vs. time data using either the conventional method, the lognormal extrapolation method or the volume limit adjustment method, and compared with the original L_p value to determine the error.

To further characterize the error in the best-fit L_p for the conventional method, another set of simulated experiments was performed. For these experiments, an initial cell population was randomly generated from a given lognormal distribution, and the transient volume change of this cell population was predicted for a given L_p using Eq. 1. The resulting data was subjected to various dynamic ranges (i.e., volume data outside the dynamic range was removed), and the best-fit L_p was determined by the conventional method.

Statistical Analysis

Data are reported as averages and standard error of the mean. Data were analyzed by ANOVA, followed by Tukey's test for pairwise comparisons. Differences were considered to be significant at the 95% confidence level (i.e., $p < 0.05$).

Results

Figure 4 shows the best-fit L_p values for MIN6 cells determined by the conventional method, lognormal extrapolation method and volume limit adjustment method. Analysis of the data by 2-way ANOVA revealed a statistically significant effect of the method used to determine L_p ($p < 0.05$), but the effect of osmotic strength on L_p was not significant ($p = 0.25$). The new methods for determining L_p (i.e., lognormal extrapolation method, volume limit adjustment method) yielded best-fit L_p values that were significantly different from the conventional method, and significantly different from each other ($p < 0.05$). The average value of L_p after pooling the data across all osmotic strengths was $(3.8 \pm 0.2) \times 10^{-14}$ m Pa^{-1} s^{-1}, $(2.8 \pm 0.2) \times 10^{-14}$ m Pa^{-1} s^{-1} and $(4.7 \pm 0.3) \times 10^{-14}$ m Pa^{-1} s^{-1} for the conventional method, lognormal extrapolation method and volume limit adjustment method, respectively. This represents a reduction in the value of the best-fit L_p of 19% and 40% for the conventional method and lognormal extrapolation method, respectively, compared with the volume limit adjustment method (which is expected to yield the most accurate results).

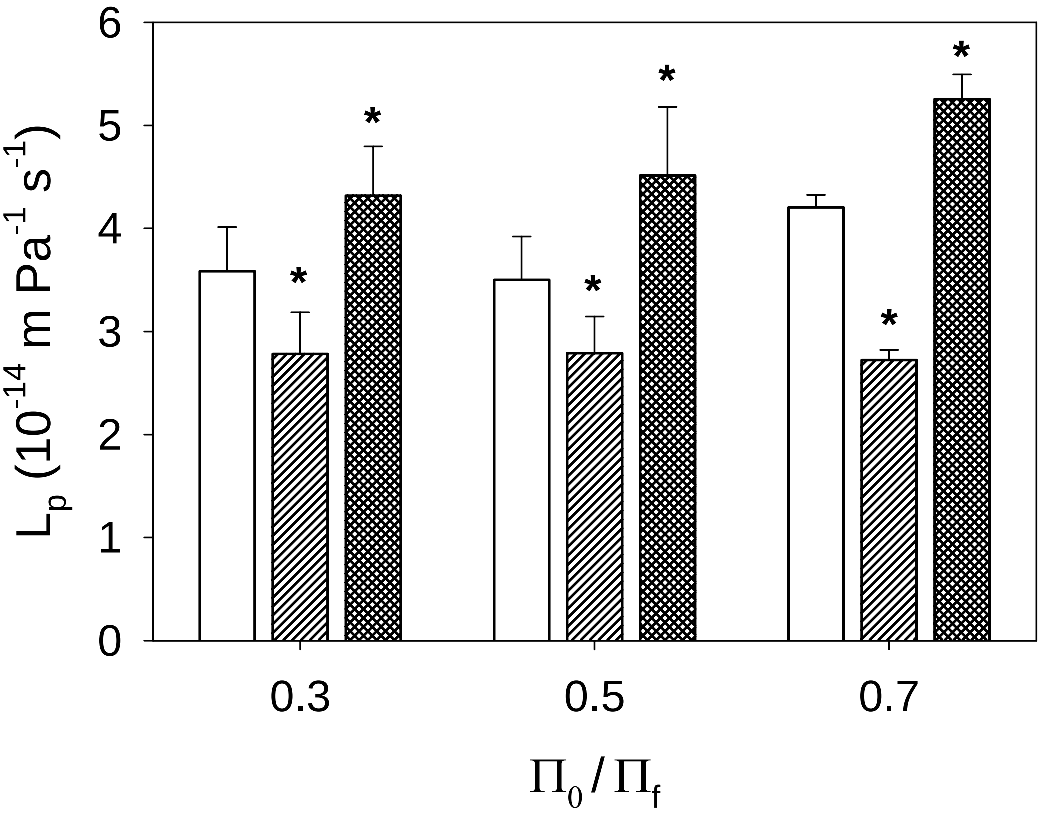

FIGURE 3.4. Membrane water permeability (L_p) for MIN6 cells at 21°C determined using the conventional method (open bars), lognormal extrapolation method (hatched bars) and the volume limit adjustment method (cross-hatched bars). Data is represented as averages and standard error of the mean ($n = 4$). Asterisks indicate a statistically significant difference from the conventional method ($p < 0.05$).

To explore the reasons for the differences in the best-fit L_p determined by the different methods, we simulated the transient osmotic response using a range of L_p values for a cell population derived from the isotonic volume distribution for MIN6 cells, and excluded volume data outside the experimental dynamic range (i.e., 450 fL to 3400 fL). The error in the best-fit L_p to the resulting data is shown in Fig. 5. For all of the methods used to determine the best-fit L_p, the true value of L_p (i.e., the value used to predict the transient osmotic response) had very little effect on the error (however, this effect was significant, $p = 0.04$). In contrast, the method used to determine the best-fit L_p had a dramatic effect on the error ($p < 0.001$). The volume limit adjustment method, which is expected to be insensitive to both dynamic range and the quality of the lognormal distribution fit, yielded very little error in the best fit L_p over a wide range of L_p values (< 3%). In fact, the overall error for the volume limit adjustment method was not significantly different from zero ($p = 0.25$). However, the conventional method, which is expected to be susceptible to dynamic range error, underestimated L_p by 20%, a value that was statistically different from the error associated with the lognormal extrapolation method and the volume limit adjustment method ($p < 0.001$). Surprisingly, the lognormal extrapolation method, which is not expected to exhibit dynamic range error, resulted in greater error than the conventional method, underestimating L_p by 28%, suggesting that the best-fit lognormal distribution does not adequately describe the cell population. These simulated results (20% and 28% error for the conventional method and the lognormal extrapolation method, respectively) are consistent with the results of experiments with MIN6 cells (19% and 40% reduction in L_p for the conventional method and the lognormal extrapolation method, respectively, compared with the volume limit adjustment method).

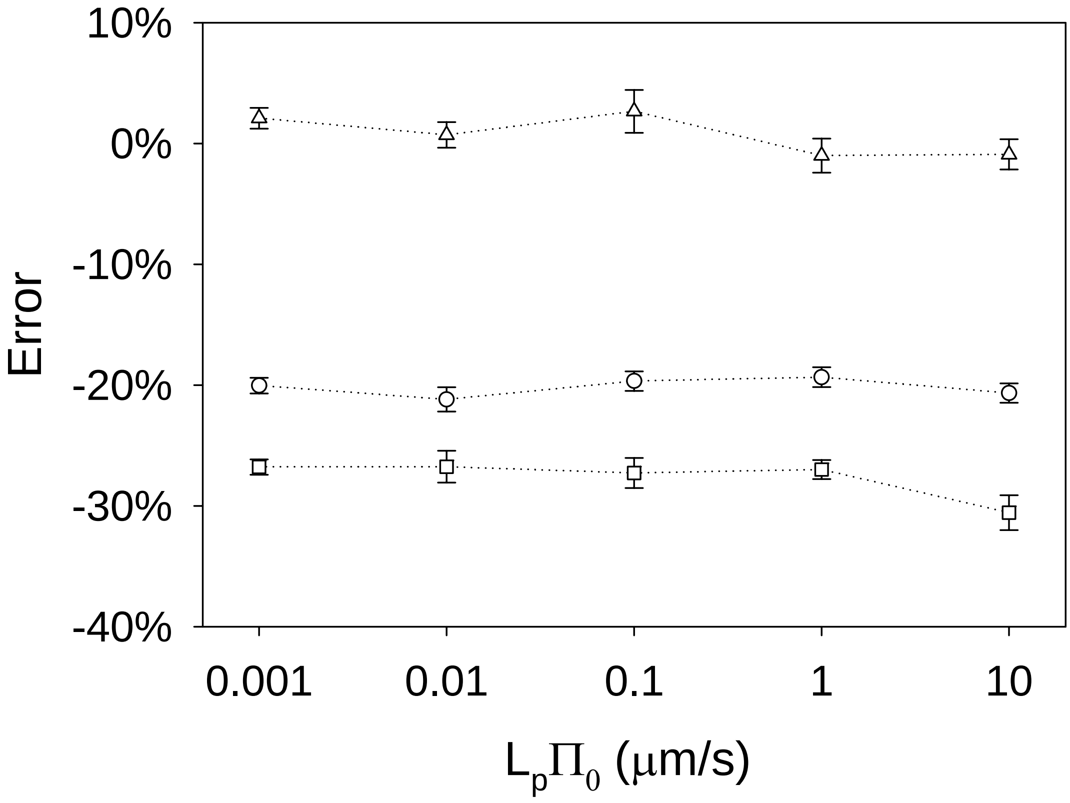

FIGURE 3.5. Error in L_p for the conventional method (circles), lognormal extrapolation method (squares) and the volume limit adjustment method (triangles), determined for a simulated experiment with $\Pi_0/\Pi_f = 0.5$ and $\overline{V_b} = 0.15$. Simulated data sets were created by predicting the transient volume change for a cell population generated at random from the isotonic cell volume distribution for MIN6 cells. The data are represented as averages and standard error of the mean (n = 6).

To investigate the source of the error associated with the conventional method and the lognormal extrapolation method, a simulated experiment was performed for various dynamic ranges, using an isotonic cell population generated from a lognormal distribution. The error for the lognormal extrapolation method was negligible (i.e., average error < 0.1%), indicating that this method is accurate when the isotonic cell population exhibits a lognormal distribution. However, the conventional method resulted in significant error, particularly when the dynamic range was narrow, as shown in Figs. 6 and 7. To facilitate presentation of the data, the standard deviation of the isotonic volume, the upper volume limit, and the lower volume limit were all normalized to the mean isotonic volume ($\overline{\sigma}$, $\overline{U}$, and $\overline{L}$, respectively). The error was independent of the mean isotonic volume when presented in terms of these normalized parameters.

Fig. 6 illustrates the effect of the standard deviation of the isotonic cell volume distribution on the error caused by dynamic range limitations for the conventional method. For all values of $\overline{\sigma}$ that we considered, the conventional method underestimated L_p, and the magnitude of error increased as the dynamic range decreased (i.e., $\overline{U}$ decreased or $\overline{L}$ increased). The standard deviation of the volume distribution had a dramatic effect on the error observed for a given dynamic range, increasing by approximately an order of magnitude between $\overline{\sigma}$ = 0.25 and $\overline{\sigma}$ = 1. For example, for a typical dynamic range of $\overline{L}$=0.4 and $\overline{U}$ = 2.3, the magnitude of the error was 10-fold higher for $\overline{\sigma}$ = 1 than for $\overline{\sigma}$ = 0.25 (70% and 7%, respectively).

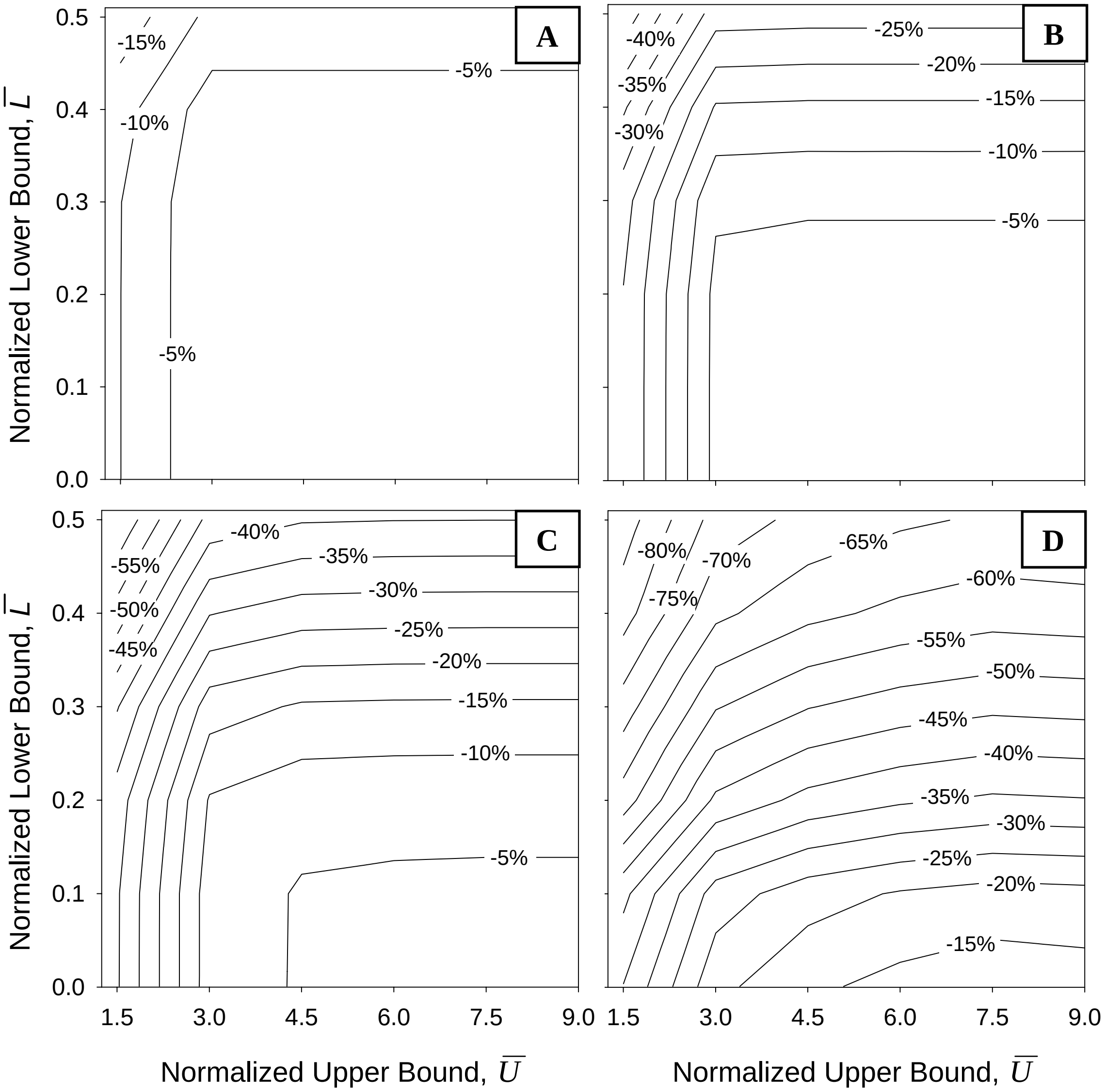

FIGURE 3.6. Effect of standard deviation of cell volumes on error associated with dynamic range limitations for the conventional method. The error in L_p was determined for an initial isotonic lognormal cell volume distribution with normalized standard deviation of 0.25 (A), 0.375 (B), 0.5 (C) and 1.0 (D), with $\overline{V}_b = 0.3$ and $\Pi_0/\Pi_f = 0.5$.

The effect of Π_0/Π_f and $\overline{V}_b$ on the error caused by dynamic range limitations is shown in Fig. 7 for a typical cell population ($\overline{\sigma} = 0.375$). Comparison between Fig. 7A ($\overline{V}_b = 0.15$, $\Pi_0/\Pi_f = 0.3$) and Fig. 7C ($\overline{V}_b = 0.45$, $\Pi_0/\Pi_f = 0.3$) and comparison between Fig. 7B ($\overline{V}_b = 0.15$, $\Pi_0/\Pi_f = 0.7$) and Fig. 7D ($\overline{V}_b = 0.45$, $\Pi_0/\Pi_f = 0.7$) reveals very little effect of $\overline{V}_b$ on the error. Similarly, comparison between Fig. 7A and Fig. 7B and comparison between Fig. 7C and Fig. 7D shows very little effect of Π_0/Π_f on the error. In fact, the error in Fig. 6B ($\overline{\sigma} = 0.375$, $\overline{V}_b = 0.3$, $\Pi_0/\Pi_f = 0.5$) is comparable to Fig. 7A-D, which provides further evidence that the error is insensitive to both $\overline{V}_b$ and Π_0/Π_f. However, the dynamic range is shown to have a major effect on the error: for $\overline{L} < 0.2$ and $\overline{U} > 3$, error was less than 5%, whereas for a typical dynamic range of $\overline{L}=0.4$ and $\overline{U} = 2.3$, L_p was underestimated by 25%.

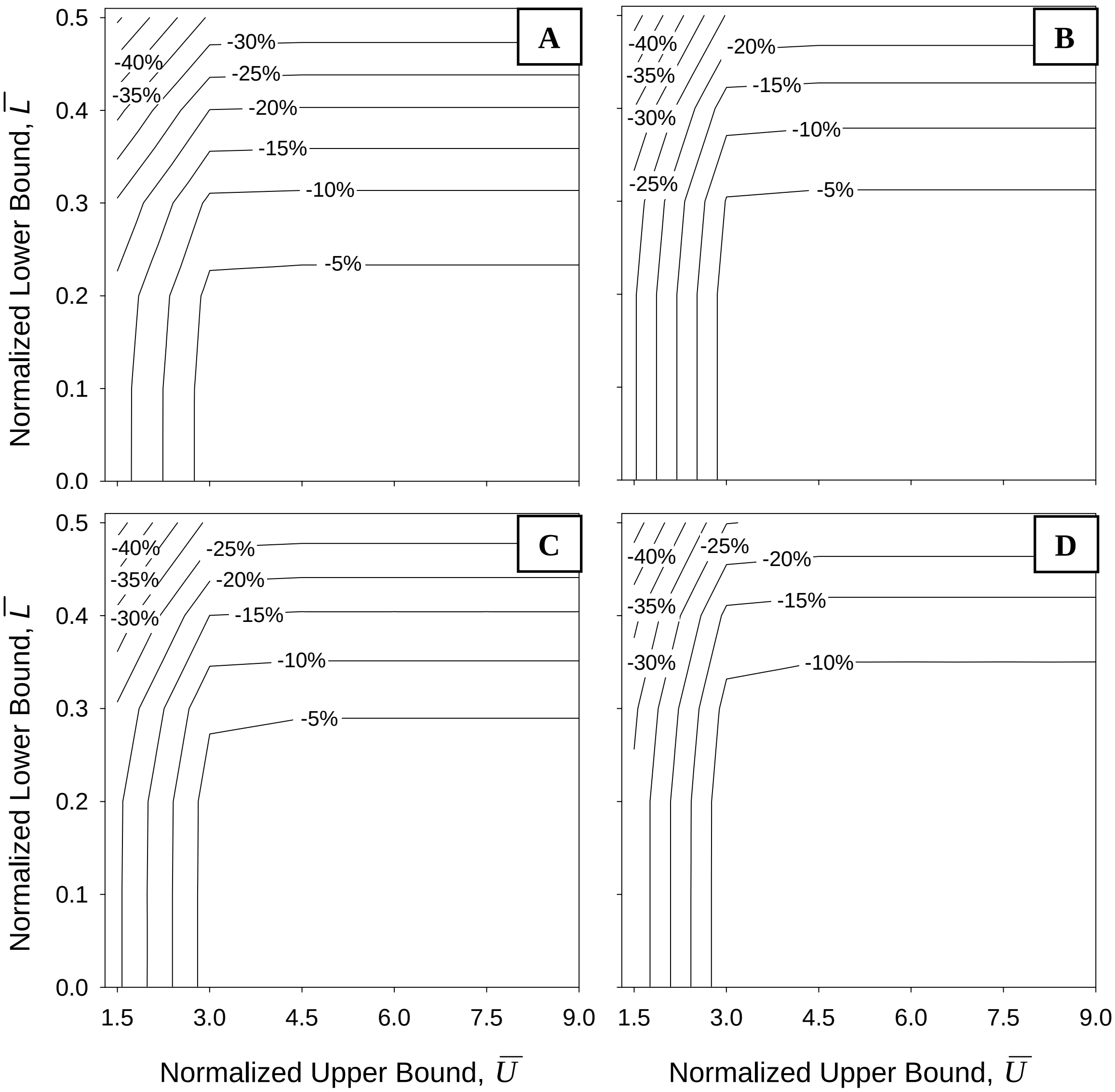

FIGURE 3.7. Effect of Π_0/Π_f and $\overline{V_b}$ on error associated with dynamic range limitations for the conventional method. The error in L_p was determined for an initial isotonic lognormal cell volume distribution with $\overline{\sigma} = 0.375$, $\overline{V_b} = 0.15$ (A, B) or $\overline{V_b} = 0.45$ (C, D) and $\Pi_0/\Pi_f = 0.3$ (A, C) or $\Pi_0/\Pi_f = 0.7$ (B, D).

Discussion

The present study investigated the effect of dynamic range limitations on estimates for L_p obtained using the conventional method, and presented two new methods for determining L_p: the lognormal extrapolation method and the volume limit adjustment method. We found that the conventional method can lead to significant error because of dynamic range limitations, particularly for cell populations that exhibit a large range of cell volumes (i.e., large $\overline{\sigma}$) and for small dynamic range (i.e., large $\overline{L}$, small $\overline{U}$). The lognormal extrapolation method was shown to be insensitive to dynamic range, but significant error resulted because of deviation between the experimental volume data and the best-fit lognormal distribution. The best estimates for L_p were obtained with the volume limit adjustment method, which is insensitive to the dynamic range and does not require isotonic cell volume data that obeys a lognormal distribution.

As shown in Table 1, the cell volume distributions (characterized by $\overline{\sigma}$) and dynamic ranges (characterized by $\overline{L}$ and $\overline{U}$) reported in the literature are similar to our observations for MIN6 cells, which suggests similar error in estimates for L_p. For MIN6 cells, which exhibited $\overline{\sigma} = 0.38$, $\overline{L} = 0.44$ and $\overline{U} = 3.3$, the conventional method underestimated L_p by approximately 20%. Using Fig. 6 in conjunction with the values of $\overline{\sigma}$, $\overline{L}$ and $\overline{U}$ in Table 1, the typical error in L_p associated with the conventional method was estimated to be between -15% and -45%.

Also shown in Table 1 are literature values for L_p at room temperature (20-22°C). The values of L_p that we determined for MIN6 cells (a mouse pancreatic β-cell line) using the volume limit adjustment method ($4.7\text{x}10^{-14}$ m Pa^{-1} s^{-1}) and the conventional method ($3.8\text{x}10^{-14}$ m Pa^{-1} s^{-1}) are both similar to published L_p values for pancreatic islet cells from different sources, such as dog (3.1×10^{-14} m Pa^{-1} s^{-1}, Liu et al., 1997), pig (4.9×10^{-14} m Pa^{-1} s^{-1}, Fedorow et al., 2001) and hamster (4.1×10^{-14} m Pa^{-1} s^{-1}, Liu et al., 1995). Interestingly, the study that reported the lowest value of L_p (Liu et al., 1997) is also the study with highest expected error (-45%), suggesting that dynamic range error may have led to underestimation of L_p in this case.

TABLE 3.1. Literature values for the dynamic range volume limits, standard deviation of the cell volume distribution, and L_p measured at 20-22°C. The approximate error in L_p was estimated using Fig. 6.

Reference	Cell Type	$\overline{\sigma}$	$\overline{L}$	$\overline{U}$	Error	L_p[#]
Present study	MIN6 cells	0.38	0.44	3.3	n/a	4.7[a]
Present study	MIN6 cells	0.38	0.44	3.3	-20%	3.8[b]
Liu et al., 1997[*]	Canine islet cells	0.4	0.5	1.7	-45%	3.1
Fedorow et al., 2001[*]	Pig islet cells	0.5	0.2	2.7	-15%	4.9
Liu et al., 1995[*]	Hamster islet cells	0.3	0.4	2.1	-15%	4.1
Elmoazzen et al., 2005[*]	Human keratinocytes	0.5	0.2	2.5	-20%	3.1
Acker et al., 1999[*]	MDCK cells	0.6	0	2.2	-15%	5.5

[*] The parameters $\overline{\sigma}$, $\overline{L}$ and $\overline{U}$ were estimated from plots of the isotonic cell volume distribution

[#] 10^{14} m Pa^{-1} s^{-1}

[a] Volume limit adjustment method

[b] Conventional method

In summary, we have demonstrated that the conventional method for determining L_p results in underestimation by approximately 20% because of dynamic range limitations (for a typical cell volume distribution and dynamic range). To address the error associated with the conventional method, we presented two alternative approaches for determining L_p (i.e., lognormal extrapolation method, volume limit adjustment method) that are insensitive to dynamic range. The lognormal extrapolation method did not exhibit dynamic range error, but did result in error when the isotonic cell volume data deviated from a lognormal distribution. The volume limit adjustment method, however, does not require that the isotonic cell volume data obey a lognormal distribution, and yielded accurate results for L_p under all of the conditions that we investigated. Thus, we recommend using the volume limit adjustment method to determine L_p.

Appendix

Although a step-change in osmotic strength is commonly assumed in Coulter counter measurement of transient cell volume changes, this assumption is rarely rigorously justified with experimental data. We have thoroughly analyzed the step-change assumption for our experimental system.

The time to achieve complete mixing (mixing time, t_{mix}) was estimated in our experimental system by observing injection of 10 μl of Napthol Green dye solution (0.5 g/mL) into 10 mL of water in the sample beaker. High-speed video images were acquired at 1000 fps and the light intensity was monitored at several locations in the beaker. Mixing was assumed to be complete when the intensity stabilized to a constant value. For our experimental system, the mixing time was found to be ~0.5 sec.

Another factor that may affect transient volume measurements is the lag between addition of cell suspension and detection of the injected cells (lag time, t_{lag}). The lag time was determined using an oscilloscope connected to an electronic pressure switch on the syringe plunger, which indicated initiation of injection, and the raw Coulter counter voltages. After injection of 100 μL of latex particles, voltage data was recorded at rate of

10^5 Hz over 0.1 second intervals, and the number of voltage peaks was counted. Fig. 8 shows the results of these experiments, which yielded a lag time of ~1 sec.

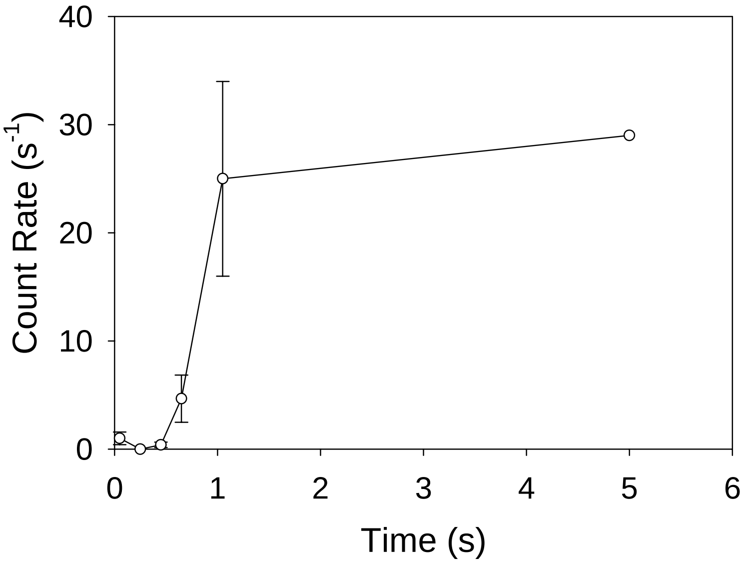

FIGURE 3.8. Oscilloscope measurement of lag time. The lag time was determined by monitoring the rate at which voltage pulses were measured (count rate) following injection of latex particles into the sample beaker.

The error associated with neglecting the mixing time and lag time was estimated using theoretical simulations. The half-time of the osmotic response can be determined from Eq. 3 to be

$$t_{1/2} = \frac{V_0\left(1-\overline{V}_b\right)}{AL_p\Pi_0}\left(\frac{\Pi_0}{\Pi_f}\right)\left[\left(\ln 2 - 0.5\right)\frac{\Pi_0}{\Pi_f} + 0.5\right] \qquad [5]$$

Combining Eq. 3 with Eq. 5 one obtains

$$\frac{d\tilde{V}}{dt} = \frac{\left[{}^{\Pi_0}\!\big/_{\Pi_f}\left(\ln 2 - 0.5\right) + 0.5\right]\left(1-\tilde{V}\right)}{t_{1/2}\left[\tilde{V}\left({}^{\Pi_0}\!\big/_{\Pi_f} - 1\right) + 1\right]} \qquad [6]$$

where $\tilde{V}$ is the non-dimensional cell volume, defined as

$$\tilde{V} \equiv \frac{V - V_0}{V_f - V_0} \qquad [7]$$

Simulated data were generated using Eq. 6 for given values of $t_{1/2}$ and Π_0/Π_f. A step-change in osmolality was assumed at t_{mix} after injection of cell suspension into the sample beaker, and acquisition of volume data was assumed to begin at t_{lag} after injection of cell suspension. The simulated data were fit with Eq. 6 using a least squares method, assuming that $t = 0$ corresponded to the beginning of volume data acquisition (t_{lag} after injection of cell suspension), and the apparent volume equilibration half time ($t_{1/2}^a$) was determined.

Fig. 8 illustrates the error associated with neglecting the lag time and mixing time in analysis of the transient osmotic response. This plot can be used to approximate the error in the measured value of $t_{1/2}^a$ if the mixing time and lag time are known. Using the membrane permeability measurements for MIN6 cells at 21°C ($L_p = 4.7\text{x}10^{-14}$ m Pa^{-1} s^{-1}), we can calculate $t_{1/2}^a$ using Eq. 5 to be in the range 3 s to 86 s for highly hypertonic ($\Pi_0/\Pi_f = 0.1$) to highly hypotonic ($\Pi_0/\Pi_f = 2$) solutions, respectively. For the range of solution concentrations used in the present study ($\Pi_0/\Pi_f = 0.3$ to $\Pi_0/\Pi_f = 0.7$) the expected $t_{1/2}^a$ is 8 s to 22 s. Noting that the difference between t_{lag} and t_{mix} is ~0.5 s for our experimental system, we can approximate the error using Fig. 8 to be to be < 5%, indicating that the assumption of a step-change in osmotic strength is valid for transient osmotic experiments with MIN6 cells. Additional evidence for the validity of the step-change assumption is provided by fact that the measured values of L_p for MIN6 cells did not depend on the solution osmotic strength in the range $\Pi_0/\Pi_f = 0.3$ to $\Pi_0/\Pi_f = 0.7$ (see Fig. 4), despite a 3-fold difference in the expected $t_{1/2}$ (Eq. 5).

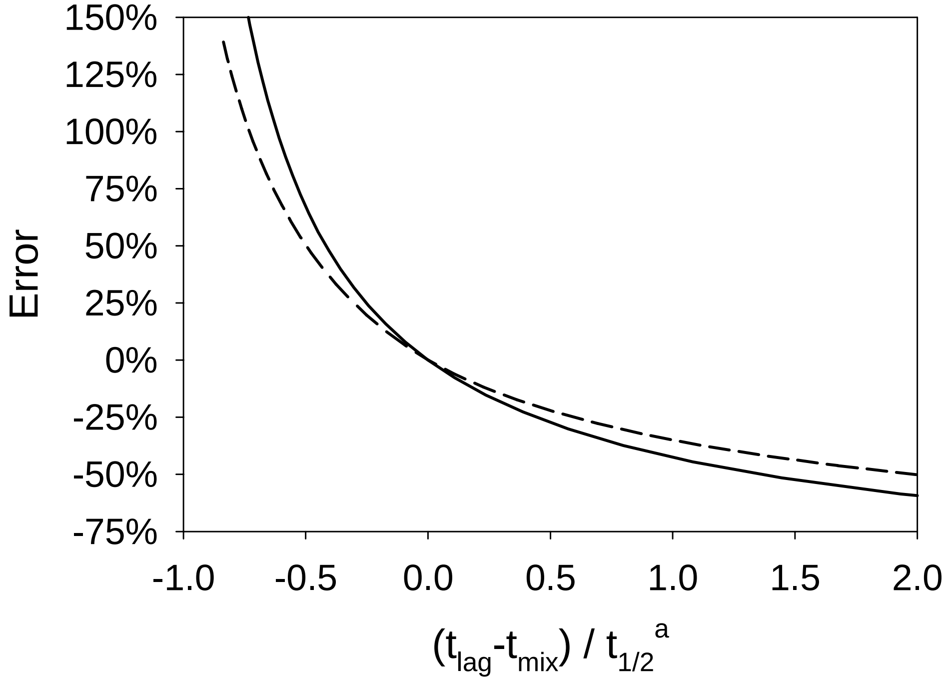

FIGURE 3.9. Simulated effect of mixing and lag on the error associated with the apparent equilibration half-time for 10x (solid line) and 0.5x isotonic conditions (dashed line).

CHAPTER 4

COINCIDENCE ERROR DURING MEASUREMENT OF CELLULAR OSMOTIC PROPERTIES BY ELECTRONIC CELL SIZING

Introduction

The cellular response to changes in the extracellular osmotic environment has important implications for understanding cell membrane biology, and for designing procedures for cryopreservation, in which cells are exposed to a changing osmotic environment during both freezing and thawing. Electronic cell sizing instruments (e.g., Coulter counters) are commonly used to measure cellular osmotic properties by monitoring the cell volume after exposure to anisotonic solution. These instruments pump suspended cells through a small aperture under a constant electrical current, resulting in a voltage pulse that is proportional to the cell volume.

Although coincidence has been a known source of error in electronic counting and sizing measurements for decades (Adams et al., 1967; Berg, 1992; Helleman, 1990; Helleman and Benjamin, 1969; Lewis and England, 1989; Pisani and Thomson, 1971; Sikdar and Webster, 1980; Wynn and Hounslow, 1997), the effects of coincidence are generally neglected in experiments to measure cellular osmotic properties, often without explicit justification. Coincidence occurs when more than one cell passes through the sensing volume of an electronic sizing instrument at the same time, resulting in a single voltage pulse. This phenomenon results in a reduction in the observed count, and an increase in the observed mean volume. In a suspension of single cells, coincidence becomes more significant as the cell concentration increases. Although the error associated with concentration coincidence can be predicted using existing mathematical models (Pisani and Thomson, 1971; Wynn and Hounslow, 1997), these models are not generally used to estimate coincidence error in experiments to measure cellular osmotic properties. In addition to concentration coincidence, error can result from the presence of cell aggregates in the cell suspension. Existing mathematical models assume a suspension of single cells, and as such do not account for this form of coincidence.

In the present study, we investigate the effect of coincidence error on the measurement of cellular osmotic properties. A new model for coincidence is presented that accounts for the presence of cell aggregates, and model predictions are compared against experimental data for suspensions of mouse insulinoma cells (MIN6). In addition, we explore the effect coincidence error on the measurement of cellular osmotic properties using computer simulations.

Theory

Coincidence

Coincidence occurs when more than one cell passes through the sensing zone of the Coulter counter simultaneously. This results in a single voltage pulse measurement, with a corresponding volume that is larger than the volume of a single cell (Fig. 1).

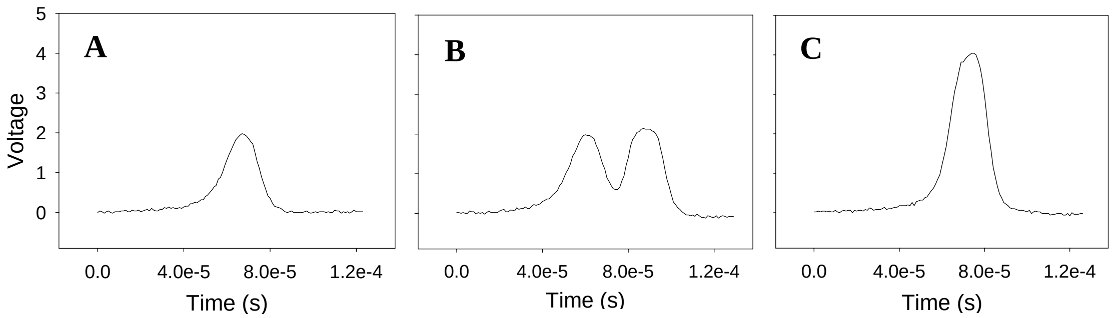

FIGURE 4.1. Coulter counter voltage pulses measured for 10 μm latex calibration particles using an oscilloscope. Most pulses corresponded to single particles (A), but some pulses partially overlapped (B), or entirely overlapped (C), resulting in an increased peak voltage.

Coincidence can occur because of multiple single cells passing through the sensing zone simultaneously, or because of the presence of cell aggregates. Although coincidence due to simultaneous passage of single cells through the sensing zone (concentration coincidence) has been extensively investigated in the literature (Adams et al., 1967; Berg, 1992; Helleman, 1990; Helleman and Benjamin, 1969; Lewis and England, 1989; Pisani and Thomson, 1971; Sikdar and Webster, 1980; Wynn and Hounslow, 1997), the effect of cell aggregates on coincidence error has received little attention. Thus, we have adapted the theory of Wynn and Hounslow (1997), which describes concentration coincidence, to include the effect of cell aggregates on coincidence error.

For a cell suspension, which may contain cell aggregates of different sizes, the total particle concentration can be described as follows:

$$C = \sum_{i=1}^{\infty} C_i \qquad [1]$$

where C_i is the concentration of cell aggregates containing i cells. It is evident from Eq. 1 that C is the number of “particles” in a unit volume, where a particle can be a single cell, or a cell aggregate. The effect of C coincidence can be predicted as follows. If the sensing zone volume (z) is divided into E small elements, the probability that an element will contain a particle is given by:

$$P = C\left(\frac{z}{E}\right) \qquad [2]$$

To determine the probability that n particles are contained in the sensing zone (P_n), the binomial probability formula is used:

$$P_n = \left(\frac{E!}{(E-n)!n!}\right)P^n(1-P)^n \qquad [3]$$

After taking the limit as E approaches infinity, one obtains:

$$P_n = \frac{(Cz)^n}{n!}\exp(-Cz) \qquad [4]$$

This gives the probability that, at a given instant, the sensing volume contains n particles. However, this expression includes the possibility that $n = 0$, for which case no electrical pulse would be recorded. The probability that an observed pulse is due to n particles is obtained by normalization of P_n to the probability of measuring a pulse:

$$\overline{P_n} = \frac{P_n}{1-P_0} \qquad [5]$$

The probability given in Eq. 5 can be used to relate the apparent count (number of observed pulses, N_a) to the underlying count of particles ($N_{u,p}$), as follows:

$$N_{u,p} = N_a\sum_{n=1}^{\infty} n\overline{P_n} \qquad [6]$$

Combining Eqs. 4, 5 and 6, and substituting e^{Cz} for its infinite series yields:

$$N_a = \frac{V_m}{z}\left[1-\exp\left(-\frac{N_{u,p}z}{V_m}\right)\right] \qquad [7]$$

where V_m is the volume of cell suspension that is drawn through the sensing volume (metered volume). Eq. 7 relates the apparent count to the total concentration of particles ($C = N_{u,p} / V_m$), and is commonly used to predict the error due to concentration coincidence. For a suspension of single cells the underlying cell count (N_u) is equal to the underlying count of particles ($N_{u,p}$), and Eq. 7 can easily be used to determine N_u from N_a. However, if cell aggregates are present, $N_{u,p}$ will be lower than N_u, since passage of a cell aggregate (> 1 cell) through the sensing volume will result in a single voltage pulse. The underlying count of cells (N_u) is then given by:

$$N_u = N_{u,p} \sum_{i=1}^{\infty} i \frac{C_i}{C} \qquad [8]$$

Combining Eqs. 7 and 8, it is a simple matter to determine the underlying cell count from the apparent count. To determine the effect of coincidence on the apparent mean volume (μ_a), it is first necessary to make an assumption about the effect of coincidence on the measured volume. The simplest assumption is that multiple particles in the sensing volume will have an additive effect on the measured volume, such that the total volume of particles remains unaffected by coincidence (Wynn and Hounslow, 1997). This assumption leads to a simple relationship between the underlying mean cell volume (μ_u) and the apparent mean volume:

$$\mu_u = \mu_a \frac{N_a}{N_u} \qquad [9]$$

The value of μ_u can be calculated using the experimentally measured values of μ_a and N_a, as well as the value of N_u predicted from Eq. 7 and 8.

The theoretical framework presented here can also be used to determine the effect of coincidence on the observed probability density function for cell volume, as shown in the appendix.

Cellular Osmotic Response

The steady-state cell volume after exposure to a solution of non-permeating solutes can be determined from the Boyle-van't Hoff relationship:

$$V_f = \frac{\Pi_0}{\Pi_f}\left(V_0 - V_b\right) + V_b \qquad [10]$$

where V is the cell volume, V_b is the osmotically inactive volume, Π is the osmotic pressure, and *0* and *f* refer to initial and final conditions, respectively. This expression is a statement of the constancy of intracellular solute content, assuming that the intracellular solution is ideal and dilute. If we assume a population of uniformly sized cells, the cell volume can be replaced by the underlying mean volume, yielding:

$$\mu_{u,f} = \frac{\Pi_0}{\Pi_f}\left(\mu_{u,0} - V_b\right) + V_b \qquad [11]$$

Combining Eq. 9 with Eq. 11, one obtains

$$\mu_{a,f} = \frac{\Pi_0}{\Pi_f}\left(\mu_{a,0} - \frac{N_u}{N_f}V_b\right) + \frac{N_u}{N_f}V_b \qquad [12]$$

It is clear from Eq. 12 that the apparent value of V_b under conditions that result in coincidence error is overestimated by the factor N_u / N_f. We also note that the osmotically inactive volume fraction ($\overline{V_b} = V_b / \mu_{u,0}$) is not affected by coincidence error.

The transient cell volume change after exposure to an anisotonic solution of non-permeating solutes can be described as follows:

$$\frac{dV}{dt} = L_p A \Pi_0 \left(\frac{V_0 - V_b}{V - V_b} - \frac{\Pi_f}{\Pi_0} \right) \qquad [13]$$

where L_p is the hydraulic permeability and A is the cell membrane surface area, which is assumed to be the area of a sphere with the isotonic cell volume, $(36\pi)^{1/3}V_0^{2/3}$. The above expression assumes that the intracellular solution is ideal and dilute (i.e., the Boyle-van't Hoff relationship applies), and that a step-change in extracellular osmotic strength is introduced at $t = 0$. If we assume a population of uniformly sized cells, Eq. 13 can be expressed in terms of the underlying mean volume as follows:

$$\frac{d\left(\mu_u / \mu_{u,0} \right)}{dt} = \frac{(36\pi)^{1/3} L_p \Pi_0}{\mu_{u,0}^{1/3}} \left(\frac{1 - \overline{V}_b}{\mu_u / \mu_{u,0} - \overline{V}_b} - \frac{\Pi_f}{\Pi_0} \right) \qquad [14]$$

Combining Eq. 9 with Eq. 14, one obtains

$$\frac{d\left(\mu_a / \mu_{a,0} \right)}{dt} = \left(\frac{N_u}{N_a} \right)^{1/3} \frac{(36\pi)^{1/3} L_p \Pi_0}{\mu_{a,0}^{1/3}} \left(\frac{1 - \overline{V}_b}{\mu_a / \mu_{a,0} - \overline{V}_b} - \frac{\Pi_f}{\Pi_0} \right) \qquad [15]$$

Comparison of Eq. 14 and Eq. 15 reveals that coincidence error changes the apparent value of L_p by a factor of $(N_u / N_a)^{1/3}$.

Methods

Determination of the Sensing Volume

The first experiment was designed to determine the sensing volume (z), which can be used to predict the error resulting from concentration coincidence. For the Z2 series Coulter counter with a 100 μm aperture tube, the value of z was determined by fitting Eq. 7 to measurements of the particle count in a metered volume of 1 ml for various dilutions of 10 μm latex beads. We assumed that the latex particles did not aggregate, such that $N_u = N_{u,p}$ (see Eq. 8). The Coulter counter displays the number of voltage pulses counted (uncorrected count) as well as the count after applying an internal correction for coincidence (corrected count). The corrected count was assumed to represent the underlying particle count (N_u). This assumption is supported by the observation of a straight line in a plot of the corrected count against the latex particle dilution ($R^2 > 0.99$, data not shown). The apparent particle count (N_a) was either taken as the uncorrected Coulter counter count, or was determined using a Cell Size Analyzer (CSA) interface, which is a commonly used Coulter counter attachment that allows transient measurement of voltage pulses for experiments to measure cellular osmotic properties (McGann et al., 1982). The value of z determined from the particle count data was used to predict the apparent mean volume as a function of particle concentration (Eq. 7, 8, and 9). Theoretical predictions were then compared against the mean volume measured using the CSA interface for various concentrations of latex beads.

Coincidence in Cell Suspensions

The effect of coincidence was investigated using suspensions of mouse insulinoma cells (MIN6). MIN6 cells were cultured in DMEM (high glucose) supplemented with 15% v/v heat inactivated FBS and β-mercaptoethanol (0.07 mM) at 37ºC in a 5% CO_2 environment. Media was changed every 3 days and passages were performed weekly. Since coincidence error can result from passage of cell aggregates through the sensing volume, several sample preparation procedures were investigated for generation of a suspension of single cells. Cell suspensions were created by exposure to 0.2% trypsin solution at 37ºC for 5, 10, 15 and 20 min, followed by trituration in culture medium 20 times with a 20G needle. After preparation of cell suspensions, viability was evaluated by automated measurement of trypan blue exclusion in a ViCell instrument. The probability of observing a single cell or larger cell aggregate was determined from bright field images of the cell suspension on a hemacytometer. The mean volume for these cell suspensions was measured using the Coulter counter, and the result was compared against predictions using Eqs. 7-9. A volume of 100 μL of cell suspension (1-2x10^6 cells/ml) in isotonic (300 mOsm/kg) cell culture medium was injected into 10 mL of well-mixed isotonic phosphate buffered saline (without Ca^{2+}, Mg^{2+}) in the Coulter counter sample beaker. The isotonic buffer was filtered (0.2 μm) to remove particles, and the osmolality was determined using a freezing point depression osmometer. Coulter counter measurements were initiated 3 min after injecting the cells into the sample beaker.

Theoretical Simulations of Coincidence Error

The effect of coincidence error on the observed osmotic response was investigated using theoretical simulations. The Boyle-van't Hoff relationship (Eq. 12) was used to predict the apparent equilibrium volume for various levels of coincidence error. In addition, transient changes in μ_a after exposure to hypertonic solution (Π_0/Π_f = 0.3) were predicted using Eq. 15 for various levels of coincidence error, and the resulting data were fit to Eq. 15 assuming N_u / N_a = 0 (i.e., coincidence error was neglected in the fit) using a least squares method to determine the best-fit value of L_p. The parameters used in the simulations are given in Table 1.

TABLE 1. Parameters used in simulations

Parameter	Symbol	Value	Units
Underlying isotonic cell volume	$\mu_{u,0}$	10^{-15}	m^3
Osmotically inactive volume fraction	$\overline{V_b}$	0.2	N/A
Hydraulic Permeability	L_p	10^{-13}	$m\ Pa^{-1}\ s^{-1}$
Isotonic osmotic pressure	Π_0	736000	Pa

Statistical Analysis

Data are reported as averages and standard error of the mean. Data were analyzed by ANOVA, followed by Tukey's test for pairwise comparisons. Differences were considered to be significant at the 95% confidence level (i.e., $p < 0.05$).

Results and Discussion

To determine the volume of the Coulter counter sensing zone, the apparent count was determined for various dilutions of latex particles. The results of these experiments are shown in Fig. 2. As expected, the apparent particle count (either the uncorrected count in the Coulter counter display, or the count determined using the CSA interface), exhibited negative concavity because of coincidence error, resulting in an increasing magnitude of coincidence error with increasing particle concentration. The error in the apparent count was more pronounced for the CSA interface than for the Coulter counter, suggesting inferior processing of voltage pulses by the CSA interface. To determine the volume of the sensing zone, these data were fit with Eq. 7, yielding $z = 14$ nL and $z = 2$ nL for the CSA interface and Coulter counter, respectively. Since z is a physical property of the Coulter counter aperture, and Coulter counter and CSA measurements were taken using the same aperture, the larger value of *z* determined using CSA interface must not represent the true volume of the sensing zone. The most likely explanation for the larger value of *z* observed using the CSA interface is that a portion of the voltage pulses are not recorded due to the 25 μs analog-to-digital conversion time in the CSA hardware (McGann et al., 1982). Thus, for analysis of the effect of coincidence on the observed volume, the value of *z* determined from the uncorrected Coulter counter count was used.

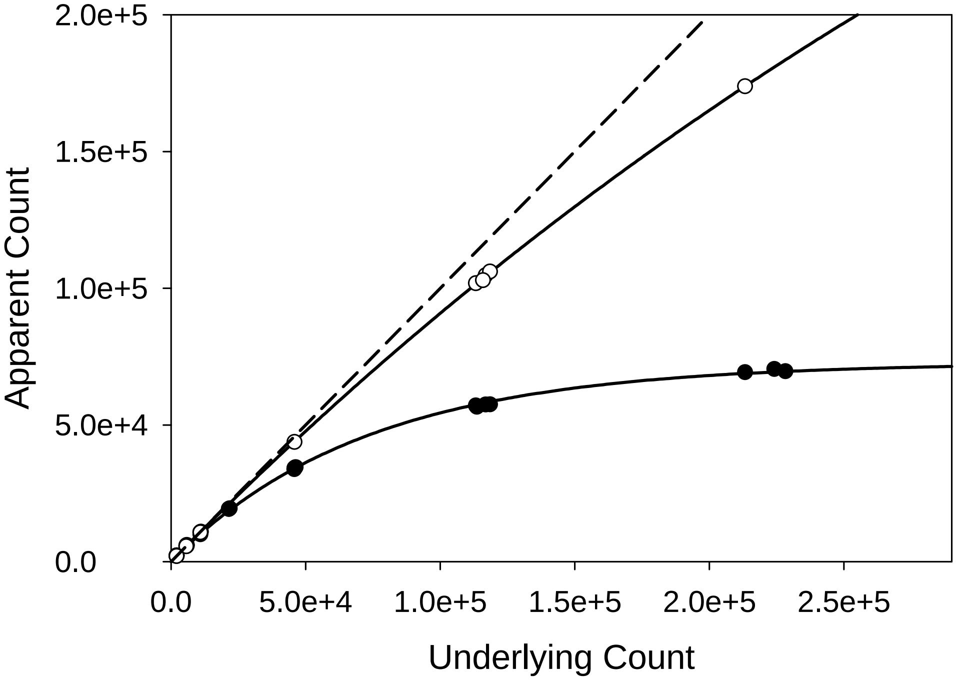

FIGURE 4.2. Effect of particle concentration on coincidence error. The apparent count was measured for various dilutions of 10 μm latex particles using the Coulter counter (open circles), and the CSA interface (closed circles). The sensing volume was determined from the best-curve to Eq. 7 (solid lines). The dashed line shows the expected count in the absence of coincidence error.

Fig. 3 illustrates the error in the apparent mean volume measured using the CSA interface, as well as theoretical predictions of the error using Eq. 9 in conjunction with the value of *z* determined in Fig. 2. The model predictions adequately describe the experimental data over the entire range of particle concentrations considered (up to 2.3 x 10^5 particles/ml), indicating that Eq. 9 can be used to accurately predict the effect of coincidence error on the measured volume. The error in the apparent volume increased approximately linearly with the particle concentration, yielding an error of approximately 10% for a particle concentration of 10^5 particles/ml.

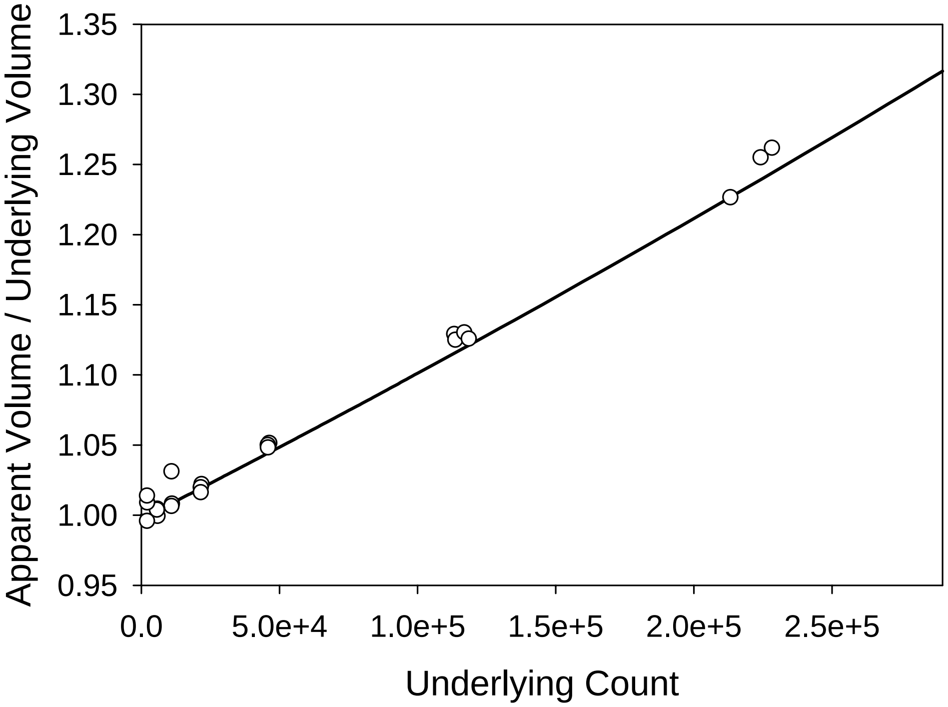

FIGURE 4.3. Effect of coincidence on volume measurements. The mean volume measured using the CSA hardware was normalized to the underlying mean volume (determined by linear extrapolation to an underlying count of 0) for various particle concentrations (open symbols). These data were compared with theoretical predictions using Eq. 9 with a sensing volume of 2 nL (line).

Whereas the predictions of the coincidence model in Fig. 3 accurately describe the apparent mean volume for a suspension of single latex particles (i.e., no aggregates), biological cells tend to stick to one another and form aggregates. Since the presence of aggregates is expected to increase coincidence error, we assessed the quality of suspensions of MIN6 cells after various sample preparation protocols by microscopically counting the number of single cells and cell aggregates. Table 2 shows the probabilities of observing a single cell or larger cell aggregate for the MIN6 cell suspensions. The probability of observing a single cell (i.e., C_1/C) was significantly affected by the incubation time in trypsin solution (ANOVA, $p = 0.005$). Trypisinization times of 5 and 10 min resulted in a significantly lower probability of observing a single cell than 20 min ($p < 0.05$), whereas no significant difference was observed between 15 and 20 min ($p = 1.00$). Although the duration of trypsinization affected the number of cell aggregates, trypsinization time did not have a statistically significant effect on cell viability (ANOVA, $p = 0.34$), yielding an average viability of 93.5% ± 0.4.

TABLE 4.2. Probability of observing a single cell or larger aggregate for suspensions of MIN6 cells (mean ± standard error).

Duration of Trypsinization	**C_1/C**	**C_2/C**	**C_3/C**	**C_4/C**	**C_5/C**
5 min*	0.84 ± 0.02	0.11 ± 0.01	0.03 ± 9e-3	0.01 ± 4e-3	3e-3 ± 5e-4
10 min*	0.85 ± 0.04	0.12 ± 0.04	0.02 ± 6e-3	4e-3 ± 1e-3	2e-3 ± 9e-4
15 min*	0.96 ± 4e-3	0.04 ± 3e-3	2e-3 ± 9e-4	3e-4 ± 3e-4	0
20 min#	0.96 ± 0.01	0.04 ± 9e-3	3e-3 ± 1e-3	0	0

*Each mean represents 4 replicates
#Each mean represents 5 replicates

After obtaining the necessary physical data (i.e., z, C_1/C, C_2/C, etc.), the coincidence model was used to predict the error in the apparent volume for suspensions of MIN6 cells and model predictions were compared against Coulter counter volume measurements. For trypsinization of 15 min and a cell concentration of 1-2x10^4 cells/ml, the error in the apparent cell volume can be estimated from Eq. 7, 8 and 9 to be < 6%, whereas sample preparation by trypsinization for 5 min is expected to result in 18-20% error. Despite the expected differences in the magnitude of coincidence error for cell suspensions prepared by 5 and 15 min trypsinization, the difference between the measured mean cell volumes was not statistically significant. The reason for this discrepancy is likely due to additional dissociation of cell aggregates as a result of mixing in the Coulter counter sample beaker. It is interesting to note that the majority of the predicted coincidence error results from the presence of cell aggregates. If cell aggregates are neglected, the error in mean volume resulting from concentration coincidence is < 3% for a cell concentration of 1-2x10^4 cells/ml.

The effect of coincidence error on the observed cellular osmotic response was investigated using theoretical simulations of cell volume changes upon exposure to anisotonic solution, as shown in Fig. 4. First, the steady-state response was examined. In Fig. 4A, the apparent equilibrium cell volumes are displayed in Boyle-van't Hoff plots for coincidence error of 0%, 10% and 20%. As expected, the plots remain linear for all levels of coincidence error, with a slope that is proportional to the magnitude of the error (Eq. 12). The value of V_b determined from the y-intercept also increases in proportion to the coincidence error (Eq. 12), whereas $\overline{V_b}$ is not affected by coincidence error. Next, the transient osmotic response was examined. As shown in Fig. 4B, coincidence error causes the curves to shift toward larger volumes. As expected from Eq. 15, the value of the best-fit L_p was higher than the true L_p by 3% and 6%, for 10% and 20% coincidence error, respectively.

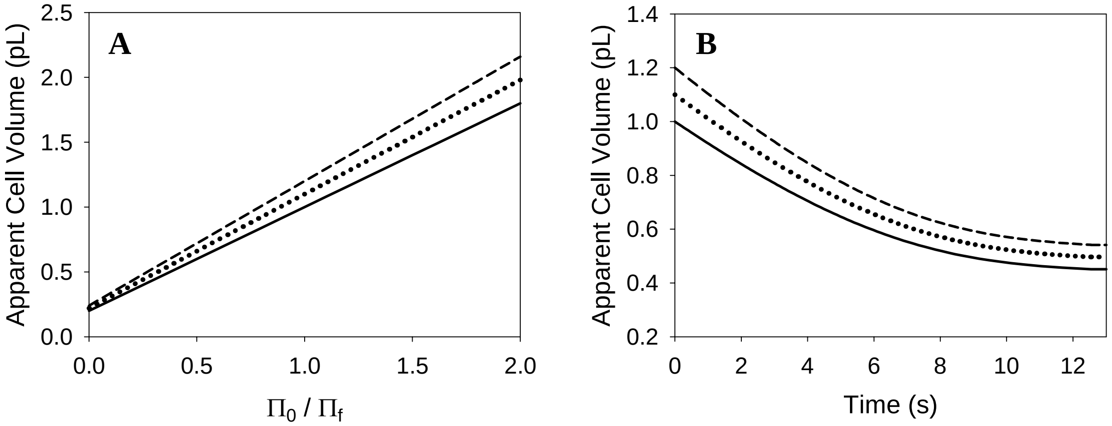

FIGURE 4.4. Effect of coincidence error on the observed equilibrium (A) and transient (B) osmotic responses. Osmotic responses were predicted for 0% coincidence error (solid line), 10% coincidence error (dotted line), and 20% coincidence error (dashed line).

The coincidence model was then used to estimate the magnitude of coincidence error in typical experiments to measure cellular osmotic properties in the literature, as shown in Table 3. For the cell concentration in the present study, coincidence is expected to result in an error of 2% and 1% for V_b and L_p, respectively. However, many authors use higher cell concentrations, which may yield higher coincidence errors. Using the value of z determined in the present study, we predicted the coincidence error in several published investigations of the cellular osmotic response, yielding an error of up to 82%

and 22% for V_b and L_p, respectively (Agca, Mullen et al., 2005). Whereas the effect of cell aggregates was neglected in the calculation of the error in Table 3, the actual error could be even higher for cell suspensions that contain aggregates. However, in most cases, the error in L_p due to coincidence is expected to be < 10%, suggesting that coincidence may not be an significant source of error in most experiments to determine L_p. It is important to point out that we used z = 2 nL to estimate the error, which is an attribute of the 100 μL aperture tube used in the present study. Since previous studies did not measure z, the estimates for error in Table 3 should be treated as approximate values.

TABLE 4.3. Predicted coincidence error using literature values for cell concentration.

Reference	**Cell Concentration**[*] **(cells/ml)**	**Error in V_b**[#]	**Error in L_p**[#]
Present study	2e+4	2%	1%
Agca, Mullen et al., 2005	6.7e+5	82%	22%
Hempling, 1977	1e+5	11%	3%
Liu et al., 1995	2e+5	22%	7%
Rule et al., 1980	1e+4	1%	<1%
Woods et al., 1999	6e+4	6%	2%

[*] If a range of concentrations was reported, the maximum bound is shown in the table.
[#] Error was estimated for z = 2 nL; cell aggregates were neglected.

Conclusions

We have presented a new model for coincidence that accounts for cell aggregates, which allows prediction of error in the measured cell volume. Although $\overline{V_b}$ was shown to be unaffected by coincidence, V_b and L_p are both overestimated because of coincidence error. Using the modeling approach presented here, the magnitude of the error in L_p and V_b can be predicted given the value of the sensing volume (specific to the instrument aperture tube) and the characteristics of the cell suspension (i.e., concentration of single cells and cell aggregates). Although most studies in the literature are expected to yield coincidence errors of < 25% for V_b and < 10% for L_p, it is possible to observe much greater error. Therefore, it is recommended that coincidence error be considered carefully when designing experiments to measure cellular osmotic properties.

Appendix

The modeling approach presented above can be extended to include the effect of coincidence on the apparent cell volume distribution. If only electrical pulses corresponding to single clusters are examined, then the underlying probability density function for cell clusters ($\rho_{u,c}$) would be observed. However, if 2 clusters are contained in the sensing volume, then the probability density function (ρ_2) would be given by the convolution of the $\rho_{u,c}$

$$\rho_2 = \int_0^{v^*} \rho_{u,c}\left(v^* - v\right)\rho_{u,c}(v)dv = \rho_{u,c} * \rho_{u,c} \qquad [A1]$$

This is easily extended to the general case for n clusters in the sensing volume (n convolutions of the $\rho_{u,c}$). The observed probability density function is thus

$$\rho_o = \sum_{n=1}^{\infty} \overline{P_n}\rho_n \qquad [A2]$$

After taking the Fourier transform and applying the convolution theorem, it can be shown that

$$\hat{\rho}_{u,c} = \frac{\ln\left(\frac{x-1}{x}\hat{\rho}_o + 1\right)}{\ln\left(\frac{1}{x}\right)} \qquad \text{[A3a]}$$

$$x = \exp(-Cz) \qquad \text{[A3b]}$$

where the superscript ^ denotes the Fourier transform. It is possible to determine $\rho_{u,c}$ from the ρ_o by taking the Fourier transform of the ρ_o, applying the above equation, and taking the inverse Fourier transform of the result (Wynn and Hounslow, 1997). The volume probability density function for single cells (ρ_u) can be determined from the above expression, assuming that the volume distribution for cell clusters containing *i* cells is equal to *i* convolutions of ρ_u, as described above, which yields

$$\rho_{u,c} = \sum_{i=1}^{\infty} P_{c,i}\rho_i \qquad \text{[A4]}$$

where ρ_i is the volume distribution for a cluster with *i cells, given by i* convolutions of ρ_u.

CHAPTER 5

MEMBRANE WATER PERMEABILITY IN ADHERENT PANCREATIC BETA-CELLS MEASURED BY FLUORESCENCE QUENCHING

Introduction

During cryopreservation cells are exposed to extreme changes in the osmotic environment, resulting in osmotically driven transport of water across the cell membrane. The fate of the cell is dependent on the kinetics of this membrane water transport: insufficient removal of intracellular water leads to supercooling and concomitant intracellular ice formation, whereas excessive removal of water leads to cell damage caused by "solution effects" (Mazur et al., 1972). Thus, the membrane water permeability is an important parameter for designing cryopreservation procedures.

Whereas membrane water permeability data are available for many cell types in suspension, there is a paucity of membrane permeability data for intact tissue, mainly because of the relative lack of convenient techniques for measuring membrane water transport (Bischof, 2000). In addition, prediction of water transport in tissue based on permeability properties derived from cell suspensions is problematic since there is evidence that the membrane permeability of tissue is different than that of the corresponding cell suspensions created by tissue disaggregation (Balasubramanian et al., 2006; Devireddy et al., 1998; Smith et al., 1997; Smith, Pham et al., 1998; Smith, Schulte et al., 1998; Yarmush et al., 1992). These observed differences in permeability properties may be caused by membrane changes incurred during disaggregation process, mass transport limitations in the interstitial space, and/or tethering to the extracellular matrix and adjacent cells (Bischof, 2000). Thus, convenient techniques for *in situ* measurement of membrane water transport in tissue are needed to facilitate design of tissue cryopreservation procedures.

Several techniques have been proposed for measuring membrane water transport in tissue comprising a cell monolayer, including light scattering (Echevarria and Verkman, 1992; Srinivas et al., 2003), interferometry (Farinas and Verkman, 1996), light microscopy with spatial filtering (Farinas et al., 1997), total internal reflection microfluorimetry (Farinas et al., 1995) and dilution of an intracellular fluorophore (Crowe et al., 1995; Muallem et al., 1992; Raat et al., 1996; Sonnentag et al., 2000; Tauc et al., 1990; Zelenina and Brismar, 2000). In addition, membrane water transport during freezing can be estimated by the differential scanning calorimetry method (Devireddy et al., 1999), by measuring intracellular ice formation kinetics (Yarmush et al., 1992; Balasubramanian et al., 2006), or by two-step freezing followed by microscopic cell volume measurement (Pazhayannur and Bischof, 1997). However, none of these techniques is ideal, due to the requirement for complicated equipment or data analysis, or because of uncertainties introduced by indirect measurement of water transport.

Recently, a convenient technique for measuring membrane water transport in adherent cells was reported based on the fluorescence quenching of intracellular calcein (Hamann et al., 2002; Solenov et al., 2004). The fluorescence intensity was shown to increase upon cell swelling and decrease upon shrinkage because of the quenching of calcein fluorescence by a molecule present in the cytoplasm (Solenov et al., 2004), yielding a linear relationship between the cell volume and the fluorescence intensity. This linear relationship was used to convert transient fluorescence intensity data to transient volume data, enabling determination of the membrane water permeability. Although fluorescence quenching behavior has been observed for epithelial cells (Capo-Aponte, 2006; Hamann et al., 2002, 2003, 2005; Levin and Verkman, 2004), astrocytes (Solenov et al., 2004), Chinese hamster ovary cells (Solenov et al., 2004) and endothelial cells (Saadoun et al., 2005), it is unclear whether this behavior can be expected in all cell types. Farinas et al. (1995) did not observe a change in fluorescence intensity after exposing calcein-loaded Sf-9 insect cells to anisotonic solution, suggesting that the fluorescence quenching technique cannot be used with this cell type, and further evidence that fluorescence quenching behavior may not occur in all cell types is provided by common use of calcein in dye-dilution studies (Crowe et al., 1995; Sonnentag et al., 2000; Zelenina and Brismar, 2000), in which the opposite effect of cell volume on fluorescence intensity is observed (i.e., swelling results in a reduction in fluorescence intensity). Thus, to establish the utility of the fluorescence quenching technique for measuring the membrane water permeability in adherent cells, further studies are necessary to determine the generality of the fluorescence quenching response.

Although it is common to assume a step-change in osmotic strength in experiments designed to measure water transport, the validity of this assumption is unclear in many cases. Several researchers have observed mixing kinetics with a similar time scale to the observed cell volume changes (Hamann et al., 2005; Berner and Gervais, 1993; Marañon et al., 1997; Takamatsu et al., 2004), in which case the step-change assumption is expected to cause error in estimates for the membrane permeability, by more than an order of magnitude in some cases (Marañon et al., 1997). However, even in studies with mixing kinetics that appear to be adequate, the step-change assumption may not be valid, since common methods of measuring mixing, such as measuring the light transmittance after addition of a dye-containing solution (Berner and Gervais, 1993; Marañon et al., 1997; Hing et al., 2000), can be associated with error. Since flow chambers are commonly used in experiments to measure the membrane water permeability in adherent cells, a critical analysis of mixing in flow chambers would clarify the validity of the step-change assumption, and lead to more accurate permeability estimates.

In the present study, we have evaluated the fluorescence quenching technique for measuring the membrane water permeability in new cell type: mouse insulinoma (MIN6) cells. The water permeability was measured by examining the transient change in fluorescence intensity after exposure of MIN6 monolayers to anisotonic solution in a flow chamber. In addition, we thoroughly analyzed mixing in the flow chamber using confocal microscopy experiments to determine the mixing time, and theoretical simulations to predict both the mixing kinetics and the error associated with common methods of measuring.

Theoretical Background

Membrane Water Transport

The cell volume after exposure to anisotonic solution containing only impermeable solutes can be described using the Boyle-van't Hoff relationship:

$$\frac{V_w}{V_{w0}} = \frac{\Pi_0}{\Pi_i} \qquad [1]$$

where V_w is the osmotically active cell volume (i.e., the volume of cellular water that can be removed in the limit of infinite osmotic strength), Π is the osmotic pressure and the subscripts “0” and “i” denote isotonic and intracellular conditions, respectively. The Boyle-van’t Hoff relationship is essentially a statement of the constancy of the intracellular solute content, assuming that intracellular solution is dilute and ideal.

The transient change in cell volume after exposure to anisotonic solution can be described using the following equation:

$$\frac{d\left(V_w \big/ V_{w0}\right)}{dt} = \frac{L_p A}{V_{w0}}\left(\Pi_i - \Pi_e\right) \qquad [2]$$

where A is the cell surface area, the subscript “e” denotes extracellular conditions, and L_p (the membrane water permeability) is the proportionality constant relating the volumetric flux of water to the difference between the intra- and extracellular osmotic pressures. Combining Eqs. 1 and 2, and assuming a step-change in extracellular osmotic pressure at $t = 0$, an analytical solution to the differential equation can be obtained:

$$t = \frac{V_{w0}}{L_p A \Pi_e}\left[\widetilde{V}_w\left(1 - \frac{\Pi_0}{\Pi_e}\right) - \frac{\Pi_0}{\Pi_e}\ln\left(1 - \widetilde{V}_w\right)\right] \qquad [3a]$$

where the nondimensional osmotically active cell volume ($\widetilde{V}_w$) is defined in terms of the initial and final volumes (V_{w0} and V_{wf}, respectively):

$$\widetilde{V}_w = \frac{V_w - V_{w0}}{V_{wf} - V_{w0}} \qquad [3b]$$

Using Eq. 3, one obtains the following expression for the rise time for the cell volume change (i.e., the time between $\widetilde{V}_w = 0.1$ and $\widetilde{V}_w = 0.9$):

$$t_{rise} = \frac{V_{w0}}{L_p A \Pi_e}\left[\left(\ln 9 - 0.8\right)\frac{\Pi_0}{\Pi_e} + 0.8\right] \qquad [4]$$

Eq. 4 allows calculation of the time required for the cell volume change given the initial and final osmotic pressure, and the value of the lumped water transport parameter L_pA/V_{w0}.

Flow Chamber Solution Exchange Kinetics

Because accurate determination of membrane transport requires a well-defined change in solute concentration at the flow chamber wall (i.e., where the cells are attached), an analysis of mixing in the chamber was undertaken. The majority of flow chambers employ a thin channel (on the order of 0.1 to 1 mm) with a small aspect ratio (width and length much larger than the height), which permits modeling of the chamber as a 2D volume bounded by parallel plates of infinite width. The Reynolds number in these chambers is generally small ($\mathrm{Re} \sim O(1) < 1400$) resulting in laminar flow with a fully-developed velocity profile described by the Poiseuille equation (Munson et al., 1998):

$$u_x = u_{\max}\left[1-\left(\frac{y}{h}\right)^2\right] \qquad [5]$$

where y is the distance from the center of the channel, u_{max} is the maximum flow velocity, and h is the distance from the center of the channel to the wall. Flow becomes fully developed after a distance l^* from the entrance of the channel, defined by (Brodkey, 1995):

$$l^* \approx 0.08h\,\mathrm{Re} \qquad [6]$$

Due to the low Reynold's numbers and low channel heights used with most flow chambers, the entry length (l^*) is small compared to the length of the channel and the deviations from Poiseuille flow in the entry region can be neglected. Thus, mass transfer of solute in the flow chamber after a step-change in concentration at the chamber entrance from $C = C_0$ to $C = C_\infty$ can be described using the following diffusion-convection model:

$$\frac{\partial \tilde{C}}{\partial \tilde{t}} = -Pe\left(1-\tilde{y}^2\right)\frac{\partial \tilde{C}}{\partial \tilde{x}} + \frac{\partial^2 \tilde{C}}{\partial \tilde{x}^2} + AR^2\frac{\partial^2 \tilde{C}}{\partial \tilde{y}^2} \qquad [7a]$$

where the nondimensional concentration is defined as

$$\tilde{C} \equiv \frac{C - C_0}{C_\infty - C_0}, \qquad [7b]$$

the nondimensional time is defined as

$$\tilde{t} \equiv \frac{tD}{x_c^2}, \qquad [7c]$$

the nondimensional y-coordinate is defined as

$$\tilde{y} \equiv \frac{y}{h}, \qquad [7d]$$

the nondimensional distance from the channel entrance is defined as

$$\tilde{x} \equiv \frac{x}{x_c}, \qquad [7e]$$

and the constants Pe and AR are the Peclet number and aspect ratio, defined as $\frac{u_{\max} x_c}{D}$ and x_c/h, respectively. In the above equations, D is the solute diffusivity, and x_c is the distance of interest from the flow chamber entrance (i.e., where the kinetic measurements are made). The following initial and boundary conditions were assumed:

$$\tilde{C} = 0 \text{ at } \tilde{t} = 0, \text{all } \tilde{x}, \tilde{y} \qquad [8a]$$

$$\frac{d\tilde{C}}{d\tilde{y}} = 0 \text{ at } \tilde{y} = 0 \qquad [8b]$$

$$\frac{d\tilde{C}}{d\tilde{y}} = 0 \text{ at } \tilde{y} = 1 \qquad [8c]$$

$$\tilde{C} = 1 \text{ at } \tilde{t} > 0, \tilde{x} = 0 \qquad [8d]$$

$$\tilde{C} \to 0 \text{ as } \tilde{x} \to \infty \qquad [8e]$$

Using Eqs. 7 and 8, the solute concentration can be predicted at any location in the chamber as a function of time.

The kinetics of the concentration change in flow chambers used for transport experiments have previously been estimated using experimental techniques that rely on an integrated property across the thickness of the chamber, which may result in error for the kinetics of the concentration change at the flow chamber wall. Therefore, we also investigated common methods of measuring mixing. The mixing time has been estimated by monitoring the light transmittance after dye addition (Berner, J. and Gervais, P., 1993; Marañon et al., 1997; Hing et al., 2000) or dye removal (Solenov, E., et al., 2004), by measuring the absorbance after dye addition (Echevaria, M., and Verkman, A., 1992), and by measuring the index of refraction after changing the concentration of sodium chloride (Takamatsu et al., 2004). Both absorbance and index of refraction are expected to be linearly related to the concentration of the absorbing molecule, resulting in the following expression when the concentration may vary across the height of the chamber:

$$\Theta = 2\int_0^h \varepsilon C dy \qquad [9]$$

where Θ is the index of refraction or the absorbance and ε is a proportionality constant between concentration and Θ (e.g., the extinction coefficient). This equation can be expressed in nondimensional form as follows:

$$\tilde{\Theta} = \int_0^1 \left(\tilde{C}\right) d\tilde{y} \qquad [10a]$$

where the nondimensional value of Θ is defined as

$$\tilde{\Theta} \equiv \left(\frac{\Theta - \Theta_0}{\Theta_\infty - \Theta_0} \right), \qquad [10b]$$

and the subscripts "0" and "∞" denote initial and final conditions, respectively. In contrast to index of refraction and absorbance, light transmittance (γ) has an exponential dependence on concentration, which results in

$$\gamma = \exp\left(2\int_0^h \varepsilon C dy \right). \qquad [11]$$

This equation can be written in nondimensional form as follows:

$$\tilde{\gamma} = \frac{\left(\gamma_\infty / \gamma_0 \right)^{\tilde{\Theta}} - 1}{\left(\gamma_\infty / \gamma_0 \right) - 1} \qquad [12a]$$

where the nondimensional transmittance is defined as

$$\tilde{\gamma} = \left(\frac{\gamma - \gamma_0}{\gamma_\infty - \gamma_0} \right), \qquad [12b]$$

and the subscripts "0" and "∞" denote initial and final conditions, respectively.

Materials and Methods

Theoretical Analysis of Solution Exchange Kinetics

The diffusion-convection equation (Eq. 7) was solved numerically using an upwind finite differencing scheme (Morton, 1996), expressed mathematically as

$$\begin{aligned}\tilde{C}(n+1,i,j) = \tilde{C}(n,i,j) &- \frac{Pe\Delta\tilde{t}}{\Delta\tilde{x}}\left[1-\tilde{y}_j^2\right]\left[\tilde{C}(n,i,j)-\tilde{C}(n,i-1,j)\right] \\ &+ \frac{\Delta\tilde{t}}{\Delta\tilde{x}^2}\left[\tilde{C}(n,i+1,j)-2\tilde{C}(n,i,j)+\tilde{C}(n,i-1,j)\right] \\ &+ \frac{AR^2\Delta\tilde{t}}{\Delta\tilde{y}^2}\left[\tilde{C}(n,i,j+1)-2\tilde{C}(n,i,j)+\tilde{C}(n,i,j-1)\right]\end{aligned} \quad [13]$$

where *n*, *i* and *j* refer to the $\tilde{t}$, $\tilde{x}$, and $\tilde{y}$ grid points, respectively. To facilitate expression of the boundary conditions in discretized form, we define the final grid points in the $\tilde{x}$ and $\tilde{y}$ directions as the I^{th} and the J^{th} grid points, respectively, and we note that the chamber wall ($\tilde{y}$ = 1) and the centerline ($\tilde{y}$ = 0) correspond with the grid coordinates $j = J - 1$ and $j = 2$, respectively. Given the above discretization scheme, the initial and boundary conditions (Eqs 8a-e) can be expressed as

$$\tilde{C}(n=1, i>1, j) = 0 \quad [14a]$$

$$\tilde{C}(n,i,j=1) = \tilde{C}(n,i,j=3) \quad [14b]$$

$$\tilde{C}(n,i,j=J-2) = \tilde{C}(n,i,j=J) \quad [14c]$$

$$\tilde{C}(n,i=1,j) = 1 \quad [14d]$$

$$\tilde{C}(n,i=I,j) = 0 \quad [14e]$$

To apply the boundary condition described in Eqs. 8e and 14e, which describes the limiting value of $\tilde{C}$ as $\tilde{x}$ approaches infinity, we increased the value of the final boundary in the $\tilde{x}$-direction until the result at $\tilde{x}$ = 1 no longer changed (Hoffman, 2001), resulting in a maximum value of $\tilde{x}$ that ranged between 2 and 20. The grid spacing in the $\tilde{x}$ and $\tilde{y}$ directions was fixed at 0.01, whereas the time spacing was chosen to ensure stability of the numerical simulations, using the following criteria (Morton, K.W., 1996):

$$\Delta\tilde{t} < 0.5\Delta\tilde{y}^2 \quad [15a]$$

$$\Delta\tilde{t} < \left(\frac{AR}{Pe}\right)^2 \left(2 + Pe\Delta\tilde{x}\right) \qquad [15b]$$

$$\Delta\tilde{t} < \frac{AR^2 \Delta\tilde{x}^2}{2 + Pe\Delta\tilde{x}} \qquad [15c]$$

The most restrictive of these criteria was used to select the value of $\Delta\tilde{t}$.

The resulting numerical predictions of the solute concentration in the flow chamber were used to quantify the kinetics of solution exchange. To characterize the mixing kinetics, we used the nondimensional rise time ($\tilde{t}_{rise}$), which is defined as the time required for $\tilde{C}$ to pass between 0.1 and 0.9 at $\tilde{x}$=1 and $\tilde{y}$=1.

The numerical simulations were also used to evaluate common methods of measuring mixing by applying Eq. 10 or 12 to the simulation results at $\tilde{x}$=1, yielding an apparent rise time ($\tilde{t}_{rise}^{a}$), defined as the time for $\tilde{\Theta}$ or $\tilde{\gamma}$ to pass between 0.1 and 0.9. To evaluate the accuracy of the methods of measuring mixing, the error in the apparent rise time was calculated (i.e., 100*($\tilde{t}_{rise}^{a}$ - $\tilde{t}_{rise}$)/ $\tilde{t}_{rise}$).

Whereas the diffusion-convection model presented above assumes a step-change in concentration at the chamber inlet, flow chambers generally require a finite length of tubing to deliver the solution to the chamber, which may result in a more gradual concentration change at the chamber inlet. To estimate the effect of inlet tubing on mixing, the diffusion-convection model (Eq. 7) was adapted for analyzing transport in the inlet tubing, assuming Poiseuille flow in a circular tube, resulting in:

$$\frac{\partial \tilde{C}}{\partial \tilde{t}} = -Pe\left(1 - \tilde{r}^2\right)\frac{\partial \tilde{C}}{\partial \tilde{x}} + \frac{\partial^2 \tilde{C}}{\partial \tilde{x}^2} + AR^2 \frac{\partial^2 \tilde{C}}{\partial \tilde{r}^2} + \frac{AR^2}{\tilde{r}}\frac{\partial \tilde{C}}{\partial \tilde{r}} \qquad [16]$$

where the nondimensional r-coordinate ($\tilde{r}$) is ratio of the radial coordinate to the tube radius (R), and the circular tube aspect ratio (AR) is defined as x_c/R. The initial and boundary conditions were assumed to be equivalent to Eq. 8, with $\tilde{y}$ replaced by $\tilde{r}$. The discretization of Eq. 16 was identical to Eq. 13, with the addition of a central difference approximation for the first derivative in $\tilde{r}$, and the discretized boundary conditions were equivalent to Eq. 14, with the $\tilde{r}$ grid points denoted by j.

Experimental Measurement of Solution Exchange Kinetics

The kinetics of the concentration change in the flow chamber was investigated experimentally using confocal microscopy (LSM 510, Carl Zeiss, Inc.). The concentration change at the chamber wall was determined by measuring the change in fluorescence intensity after addition of solution containing the fluorescent probe fluoresceinamine (M_w = 347 g/mol), which is representative of the molecule used in osmotic test solutions for experiments to measure cell membrane transport (i.e., sucrose, M_w = 342 g/mol). As shown in Figure 1, the chamber dimensions were 0.1, 3, and 24 mm for the height, width, and length, respectively, and the fluorescence intensity measurements were made at a distance of approximately 12 mm from the chamber inlet. The fluorescence intensity was determined from confocal microscope images acquired in spot mode (i.e., a single voxel was imaged) at a rate of 7-23 kHz using a 20x objective (0.75 NA), an argon laser (illumination at 488 nm) and a pinhole diameter of 200 μm. The focal plane was selected by locating the channel center in a z-stack across the height of the chamber, and then moving the microscope stage 50 μm from the center. The flow rate was varied between 2 and 200 ml/hr using a syringe pump. The tubing from the syringes was combined at a y-connector, which was connected to the flow chamber inlet by approximately 25 mm of 1.5 mm ID tubing. For comparison of the confocal microscopy results with numerical simulations, a diffusivity of 0.52×10^{-5} cm^2/sec was assumed, which is the diffusivity of sucrose at 25°C (CRC Handbook, 1996).

Cell Culture

Mouse insulinoma (MIN6) cells (Miyazaki et al., 1990) were generously provided by Paolo Meda, M.D. (University of Geneva, Switzerland). MIN6 cells were cultured in tissue culture flasks containing culture media (DMEM with high glucose supplemented with 15% v/v heat inactivated FBS and 0.07 mM β-mercaptoethanol) at 37ºC in a 5% CO_2 environment. Media was changed every 3 days and passages were performed weekly. For fluorescence quenching experiments, cells were seeded onto 40 mm diameter glass coverslips in 60 mm Petri dishes and cultured for 3-4 days.

Fluorescence Quenching Experiments

The membrane water permeability for monolayers of MIN6 cells was determined by measuring the fluorescence quenching of intracellular calcein during exposure to anisotonic solution in a flow chamber (illustrated in Figure 1). Cell monolayers were first rinsed with 4 ml of isotonic phosphate buffered saline solution with Ca^{2+} and Mg^{2+} (PBS), and incubated in PBS containing 1.25 μg/ml calcein-AM for 15-20 min at 37°C. The cell monolayers were then assembled into the flow chamber unit (FCS2, Bioptechs, Butler, PA USA) with chamber dimensions of 0.1 mm, 3 mm and 24 mm (height, width and length, respectively), being careful to avoid introduction of bubbles. Perfusion with isotonic PBS was immediately initiated at a flow rate of 20 ml/hr using a syringe pump. The flow chamber was then mounted onto an upright microscope (Eclipse ME600, Nikon) using a custom stage adapter. After 10 min of perfusion at 20 ml/hr, the flow rate was changed to 200 ml/hr, and time-lapse image acquisition was initiated at a rate of 1 Hz (camera exposure time 100 ms) using a cooled CCD camera (SensiCam, Cooke Corporation, Romulus, Michigan USA). The camera shuttering was synchronized with exposure of the cells to blue light (FITC filter) using a high speed shutter placed in the epifluorescence light path (VS25, Uniblitz, Rochester, NY USA) and IP lab software (BD Biosciences, Rockville, MD USA). To ensure stable light output from the mercury lamp (Nikon), the lamp was turned 45 min prior to fluorescence quenching experiments. A neutral density filter was placed in the light path (ND4) to reduce photobleaching. After approximately 5 min of image acquisition, the perfusion solution was changed from isotonic to anisotonic by switching the syringe in the syringe pump. Anisotonic solutions were prepared by addition of either sucrose or purified water to isotonic PBS, and the osmolality of all solutions was measured with a freezing point depression osmometer. The cell monolayers were exposed to anisotonic solution for 3 min, and then perfusion was changed to isotonic solution, and video acquisition was continued for an additional 5 minutes. The temperature was measured to be 21±1°C using a thermocouple inserted into the outlet tubing.

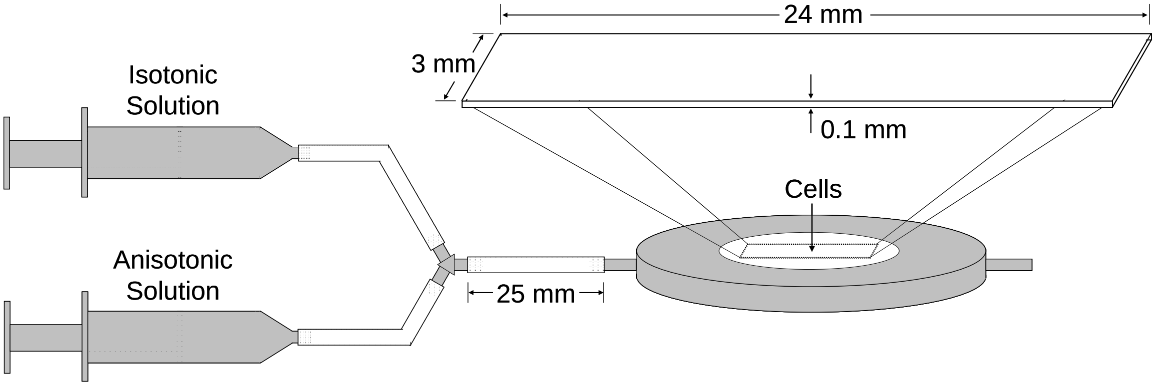

FIGURE 5.1. Schematic of flow chamber.

The resulting fluorescence intensity data was first corrected for the effects of fading (e.g., photobleaching, leakage of intracellular calcein) by fitting an exponential decay model to the data (Hamman et al., 2002; Muallem et al., 1992; Srinivas and Bonanno, 1997; Tauc et al., 1990). For the exponential decay fit, we used data corresponding with isotonic conditions (i.e., the initial exposure to isotonic solution and the steady-state data after return to isotonic conditions following the anisotonic solution exposure). To analyze the corrected fluorescence intensity data, we assumed a linear relationship between relative fluorescence intensity and relative osmotically active cell volume (Hamman et al., 2002; Solenov et al., 2004):

$$\frac{F}{F_0} = a\frac{V_w}{V_{w0}} + 1 - a \qquad [17]$$

In the above equation, *F* is the fluorescence intensity, *a* is a constant and the subscript “0” denotes isotonic conditions. Combining Eqs 1, 2 and 17 one obtains the following expression for the transient change in fluorescence intensity:

$$\frac{d\left(F/F_0\right)}{dt}=\frac{L_pA}{V_{w0}}\left(\frac{a^2\Pi_0}{F/F_0+a-1}-a\Pi_e\right) \qquad [18]$$

The fluorescence intensity data were fit for a and L_pA/V_{w0} simultaneously by minimizing the error squared between the data and the numerical solution of Eq. 18, assuming a step-change in extracellular osmotic pressure at $t = 0$. The steady-state fluorescence intensity in anisotonic solution was calculated using the best-fit value of a.

Statistical Analysis

Unless otherwise noted, the data are reported as averages and the standard error of the mean. For normally distributed data and equal variances, the data were analyzed by ANOVA, followed by Tukey's tests. When either of these criteria was not met (i.e., normal distribution, equal variances), the data were analyzed using a nonparametric ANOVA (Kruskal-Wallis), followed by Dunn's method for pairwise comparisons.

Results

Figure 2 illustrates the numerical predictions of the solution exchange kinetics in the flow chamber. The effect of the parabolic velocity profile is evident in Figure 2, which results in a more rapid change in solute concentration at the center of the chamber than at the chamber wall. The effect of diffusion is also evident in the blurring of the interface between the solute concentration introduced at the inlet (black) and the initial solute concentration in the chamber (white).

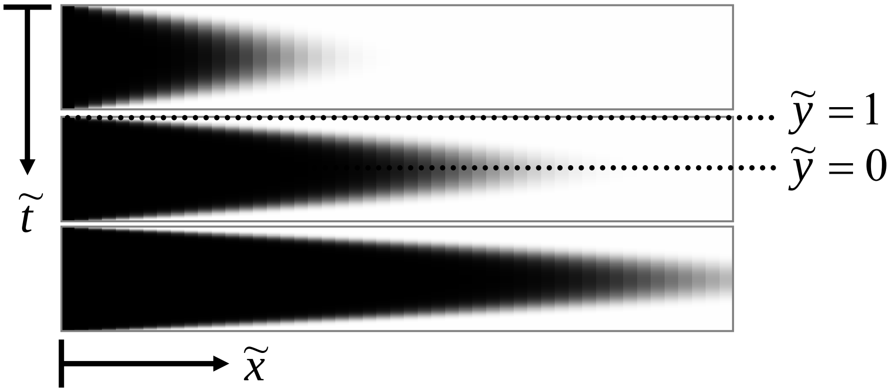

FIGURE 5.2. Numerical simulation of solution exchange kinetics. A step-change in concentration from $\tilde{C} = 0$ (white) to $\tilde{C} = 1$ (black) was assumed at the flow chamber inlet ($\tilde{x} = 0$). The flow chamber wall corresponds with $\tilde{y} = 1$.

These numerical simulations were used to determine the kinetics of solution exchange at the chamber wall. The effect of *Pe* and *AR* on the rise time ($\tilde{t}_{rise}$) is shown in Figure 3. In general, the value of $\tilde{t}_{rise}$ decreased as *Pe* increased and as *AR* increased, which is indicative of more rapid mixing for high flow velocities and thin chambers. For low *Pe* the data converged to a constant value of $\tilde{t}_{rise}$ (dashed line), as can be predicted by examination of the governing equations. As *Pe*→0, Eq. 7 reduces to

$$\frac{\partial \tilde{C}}{\partial \tilde{t}} = \frac{\partial^2 \tilde{C}}{\partial \tilde{x}^2} + AR^2 \frac{\partial^2 \tilde{C}}{\partial \tilde{y}^2}, \qquad [19]$$

which is subject to the boundary conditions given in Eq. 8. The above equation can be further simplified by noting the symmetry in the $\tilde{y}$-direction, yielding:

$$\frac{\partial \tilde{C}}{\partial \tilde{t}} = \frac{\partial^2 \tilde{C}}{\partial \tilde{x}^2} \qquad [20]$$

with boundary conditions:

$$\tilde{C} = 0 \text{ at } \tilde{t} = 0, \text{all } \tilde{x} \qquad [21a]$$

$$\tilde{C} = 1 \text{ at } \tilde{t} > 0, \tilde{x} = 0 \tag{21b}$$

$$\tilde{C} \to 0 \text{ as } \tilde{x} \to \infty \tag{21c}$$

Eq. 20 describes diffusion into a semi-infinite medium and has the well-known analytical solution

$$\tilde{C} = 1 - erf\left(\frac{\tilde{x}}{2\sqrt{\tilde{t}}}\right) \tag{22}$$

which results in a $\tilde{t}_{rise}$ of 31.6, indicating that $\tilde{t}_{rise}$ is independent of both *Pe* and *AR* for low *Pe*.

The solution exchange kinetics when both *Pe* and when *AR* are large can approximated by the dotted lines shown in Figure 3, which were determined from a fit to the data in the high *Pe* and *AR* regime. For large values of *Pe* and *AR*, one can neglect diffusion in the $\tilde{x}$-direction, yielding

$$\frac{\partial \tilde{C}}{\partial \tilde{t}} = -Pe\left(1 - \tilde{y}^2\right)\frac{\partial \tilde{C}}{\partial \tilde{x}} + AR^2 \frac{\partial^2 \tilde{C}}{\partial \tilde{y}^2}, \tag{23}$$

which can be rewritten as

$$\frac{\partial \tilde{C}}{\partial\left(AR^2 \tilde{t}\right)} = -\frac{Pe}{AR^2}\left(1 - \tilde{y}^2\right)\frac{\partial \tilde{C}}{\partial \tilde{x}} + \frac{\partial^2 \tilde{C}}{\partial \tilde{y}^2} \tag{24}$$

Eq. 24 shows that $\tilde{t}_{rise}*AR^{2}$ is a function of $Pe*AR^{-2}$ when diffusion in the $\tilde{x}$-direction is negligible. Thus, for $Pe > 10^2$ and $AR > 10$, a power function was fit to a plot of $\tilde{t}_{rise}*AR^{2}$ against $Pe*AR^{-2}$ (R^2=0.998), yielding

$$\tilde{t}_{rise} = 0.79 Pe^{-0.64} \varepsilon^{-0.72} \tag{25}$$

The above equation yields accurate estimates for the rise time even for smaller *AR* values. For example, Eq. 25 is accurate for *AR* = 1 as long as *Pe* > 100.

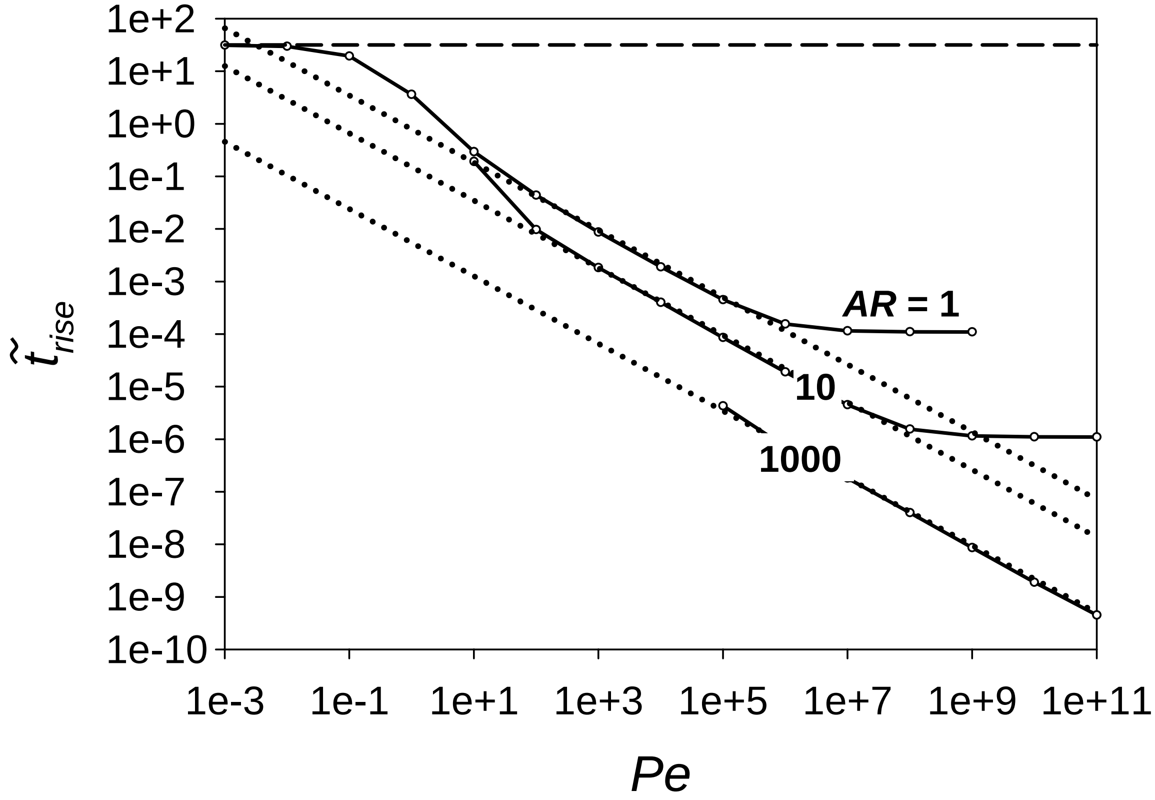

FIGURE 5.3. Numerical and analytical prediction of the flow chamber mixing kinetics. The nondimensional rise time was determined by numerically solving Eq. 7 for several values of *AR* and *Pe* (solid lines). The dashed line shows the analytical solution to Eq. 7 in the limit of vanishing Pe. The dotted lines show the best-fit equation (Eq. 25) determined in the high *Pe* (*Pe* > 100) and high AR (*AR* > 10) regime.

Common methods of measuring mixing were also investigated using the numerical model, and the error associated with using these techniques is illustrated in Figure 4. Measurement of Θ (i.e., absorbance or index of refraction) or light transmittance after dye addition is expected to result in underestimation of the rise time, particularly for small *AR* and large *Pe*, indicating that high flow rates and large channel heights can lead to significant underestimation of the rise time. In the limit of low *Pe*, error in the mixing time estimated using Θ vanishes, because there is no variation in concentration in the $\tilde{y}$-direction as Pe approaches zero (see Eq. 20). However, visualization of light transmittance after introduction or removal of a dye exhibits more complicated behavior, with an apparent rise time that is dependent on the ratio of final transmittance to initial transmittance (Eq. 12). As a result, addition of dye generally yields a larger underestimation of the true rise time than does dye removal. For the limiting case of $Pe << 1$, the error in the mixing time estimated using the light transmittance was calculated using Eqs. 10, 12 and 22 to be -87.6% and +499% for dye addition and removal, respectively, which matches the results of numerical simulations.

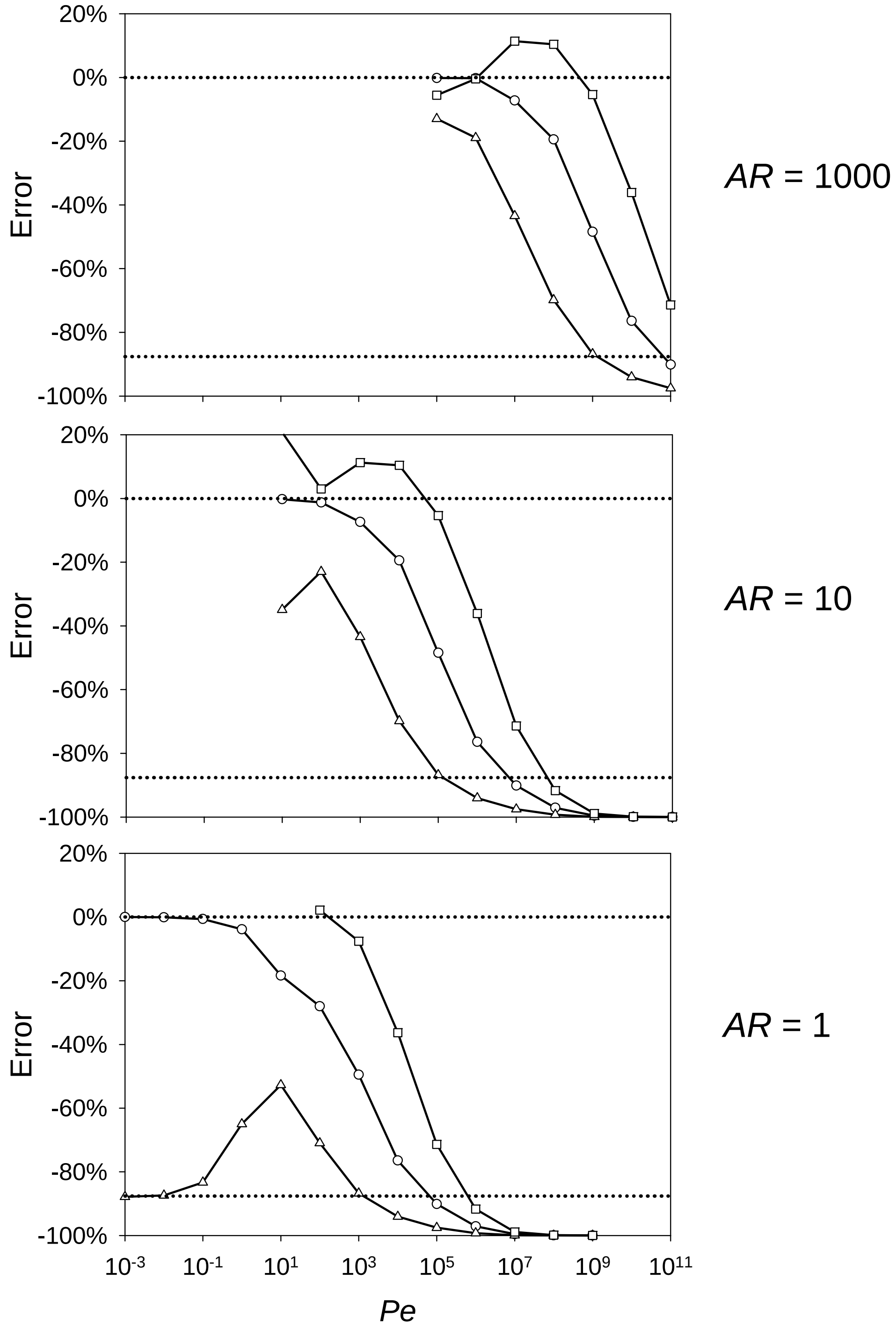

FIGURE 5.4. Error associated with common methods of measuring mixing in flow chambers. The error in the mixing time was determined for measurement of Θ (circles, i.e., any property that is linearly related to concentration, such as absorbance, or index of refraction), or light transmittance upon dye addition (triangles, γ_f / γ_i = 0.1) or removal (squares, γ_f / γ_i = 10).

The results of confocal microscopy experiments to determine kinetics of mixing at the flow chamber wall are shown in Figure 5. As expected, the rise time decreased as the flow rate increased. However, the rise time for mixing in the chamber is much larger than expected based on theoretical predictions for the chamber alone. Analysis of transport in the inlet tubing revealed that the assumption of a step-change in solute concentration at the chamber entrance is not valid for our system, and that the kinetics of mixing in the chamber is expected to be significantly slowed as a result of the inlet tubing. For low flow rates, the concentration change at the center of the inlet tubing (where the flow velocity is at a maximum) is predicted to be slower than the expected concentration change at the wall of the chamber – the step change assumption is clearly not valid in this regime. However, even for the higher flow rates, a step-change in concentration is not introduced at the chamber inlet, as evidenced by the slow concentration change at the wall of the inlet tubing. Despite the mixing limitations in the inlet tubing, a rise time of less than 1 sec was achieved for a flow rate of 200 ml/hr, which is sufficiently fast for measurement of the cellular osmotic response for many cell types.

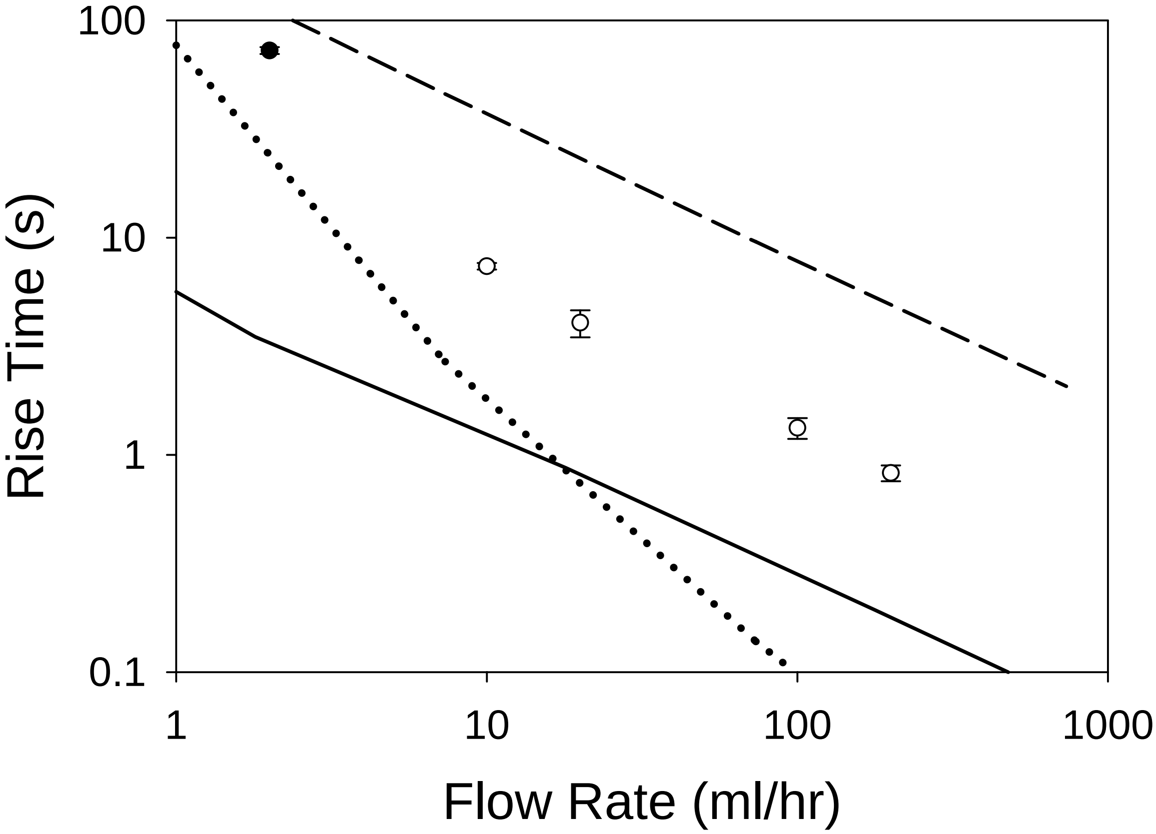

FIGURE 5.5. Comparison of mixing kinetics measured by confocal microscopy (symbols) and theoretical predictions of mixing at the chamber wall (solid line), at the tubing wall (dashed line) and at center of the tubing (dotted line). The rise time was determined from confocal microscopy data as the time to pass between 10% and 90% of the equilibrium fluorescence intensity (open symbols), or by multiplying the time to pass between 10% and 36.7% of equilibrium by 3 (closed symbol).

After examining the kinetics of mixing in the flow chamber, we investigated cell membrane water transport in adherent cultures of MIN6 cells using the fluorescence quenching technique. Since the fluorescence intensity decreased over the course of the experiments, we accounted for this fading phenomenon by fitting the data to an exponential decay model, as shown in Figure 6. After correcting the fluorescence intensity data for the effects of fading using the best-fit exponential function, the fluorescence intensity was approximately constant under isotonic conditions, indicating that changes in the corrected fluorescence intensity after exposure to anisotonic solution can be attributed to the resulting change in cell volume.

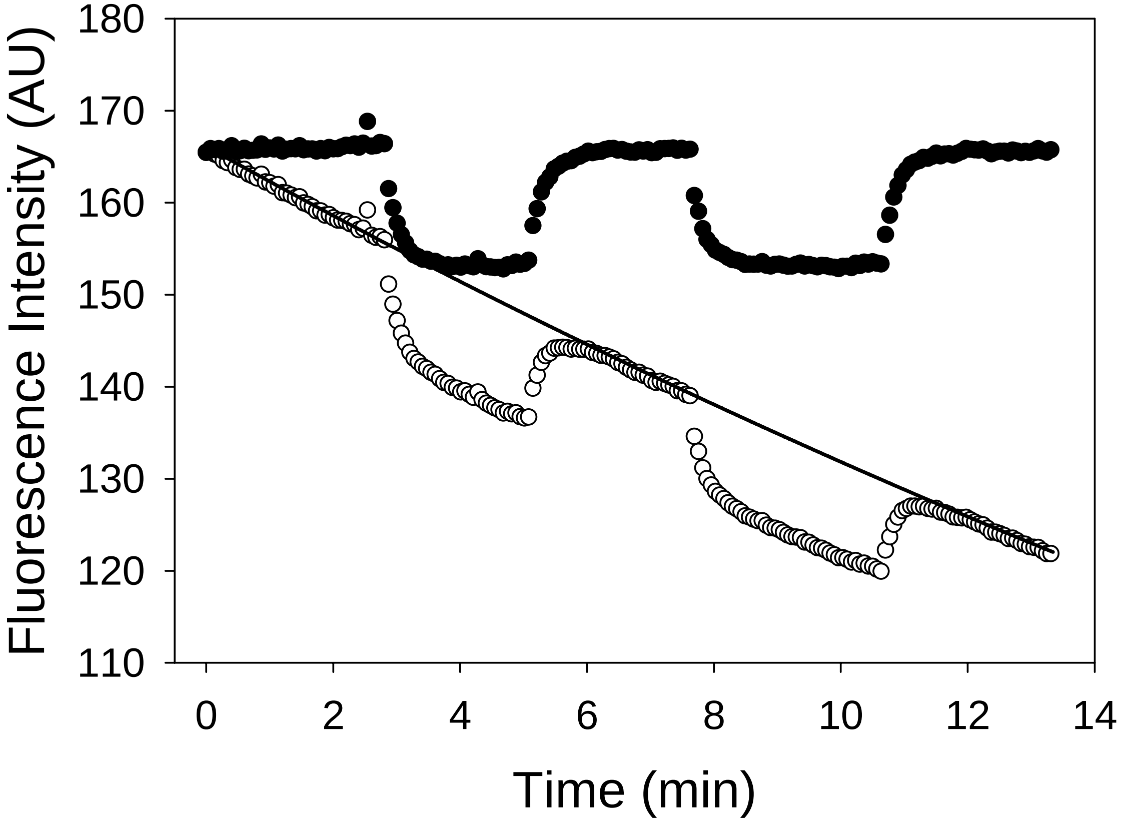

FIGURE 5.6. Correction for fading of fluorescence in monolayers of MIN6 cells initially in isotonic solution (0.3 osmoles/kg), and then alternately exposed to hypertonic (0.5 osmoles/kg) and isotonic solutions. The resulting fluorescence intensity data (open symbols) corresponding with isotonic conditions were fit to an exponential decay model (line), and the corrected fluorescence intensity (closed symbols) was calculated.

Figure 7 illustrates the effect of osmotic strength on the magnitude of the resulting fluorescence intensity change. Exposure to hypotonic solution (i.e., swelling) resulted in an increase in the fluorescence intensity, whereas exposure to hypertonic solution (i.e., shrinkage) yielded a decrease in the fluorescence intensity, as expected for fluorescence quenching behavior. The effect of osmotic strength on the fluorescence intensity was significant ($p < 0.001$), and pairwise comparisons yielded significant differences for all combinations ($p < 0.05$). To characterize the fluorescence quenching response, we fit a linear model to the data, revealing a remarkably linear relationship between the normalized fluorescence intensity and the osmotic strength under hypertonic conditions. Whereas experiments with suspensions of MIN6 cells yielded linear osmometric behavior (i.e., agreement with the Boyle-van't Hoff predictions, Eq. 1) under hypertonic conditions (Chapter 2), this result suggests that the normalized fluorescence intensity is proportional to the normalized osmotically active cell volume, and justifies the use of Eq. 17.

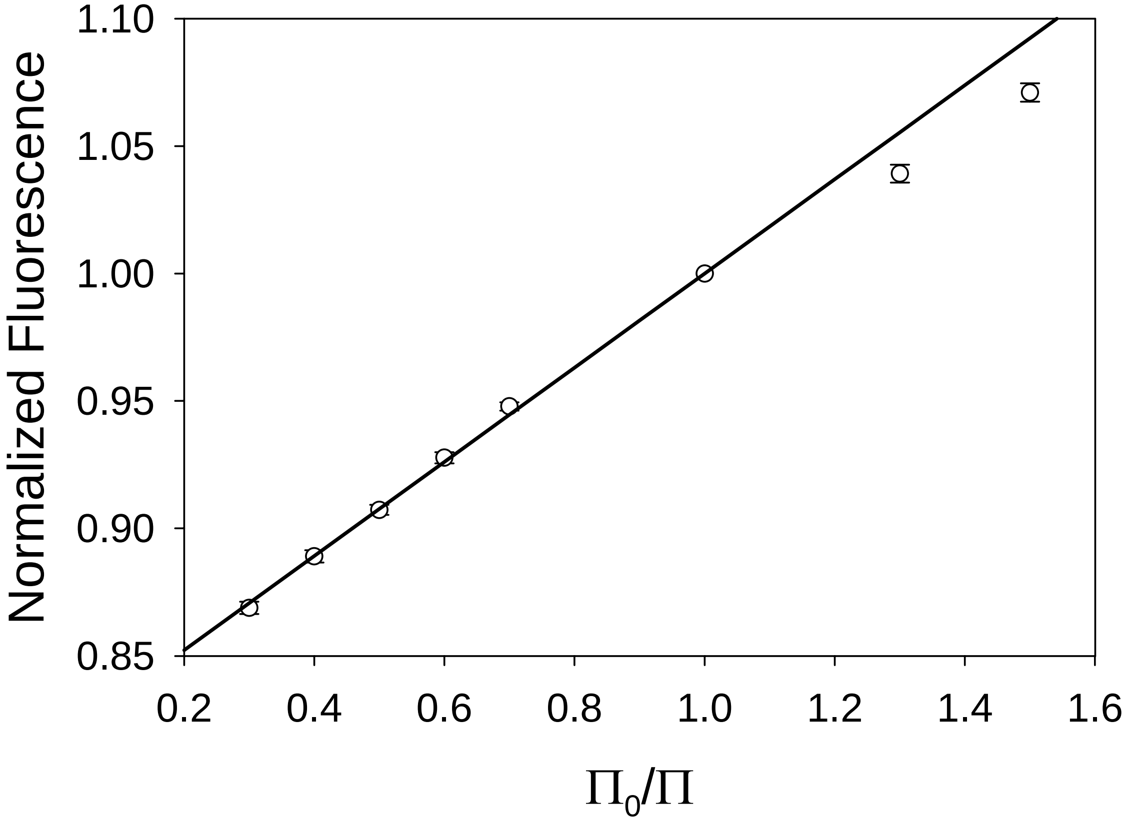

FIGURE 5.7. Effect of solution osmotic strength on the fluorescence intensity for monolayers of MIN6 cells. The reciprocal osmotic pressure and the fluorescence intensity were normalized to isotonic conditions, and a best-fit line was obtained using the hypertonic data. Each anisotonic data point represents the mean of 6 replicates. The best-fit line to the hypertonic data was forced through the point 1,1.

Since a linear relationship was observed between fluorescence intensity and osmotically active cell volume, we used Eq. 17 to convert the transient response of fluorescence intensity to the transient response of the osmotically inactive volume, as illustrated in Figure 8. The best-fit predictions adequately reflect the transient volume data over a wide range of hyper- and hypotonic conditions. The value of the lumped water transport parameter L_pA/V_{w0} was determined from these transient data, as shown in Table 1. Under hypertonic conditions, the osmotic strength did not significantly affect L_pA/V_{w0} ($p = 0.45$), yielding an average L_pA/V_{w0} of $(4.4\pm0.1) \times 10^{-8}\ \mathrm{Pa}^{-1}\ \mathrm{s}^{-1}$.

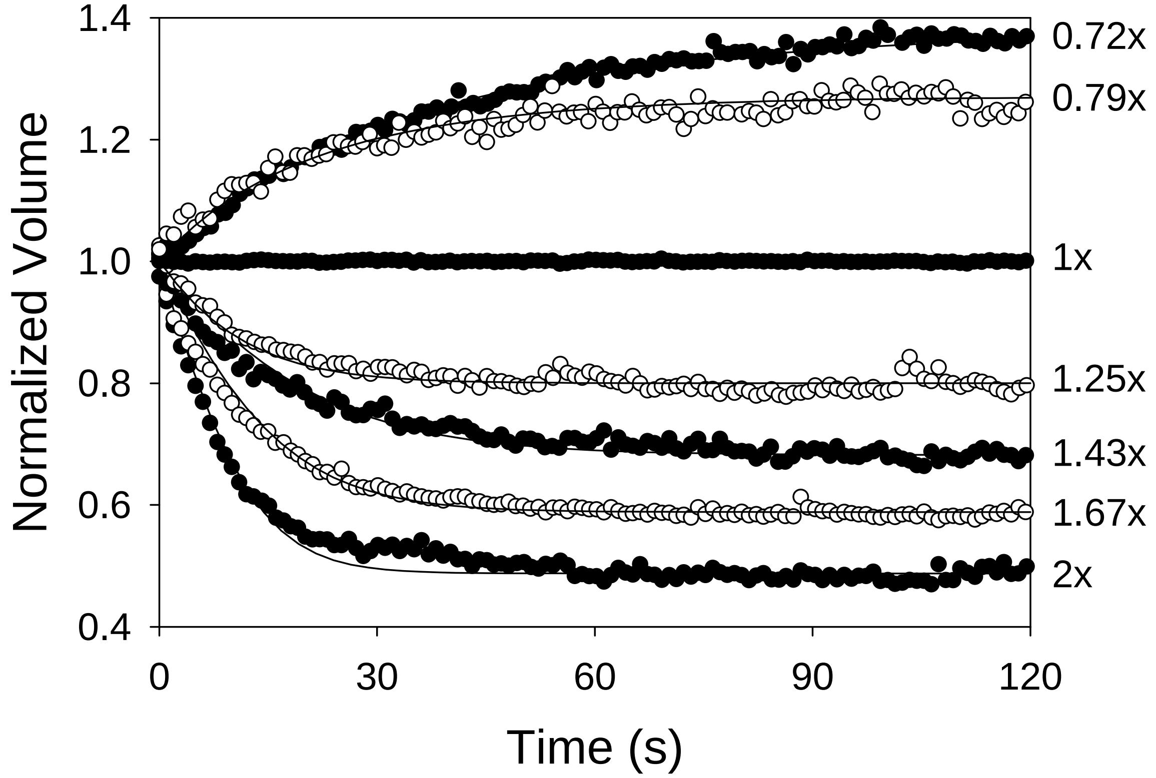

FIGURE 5.8. Transient response of the osmotically active cell volume after exposure to anisotonic conditions. Monolayers of MIN6 cells initially in isotonic solution (0.3 osmoles/kg) were exposed anisotonic solutions ranging from 0.72x to 2x the isotonic osmotic strength.

TABLE 5.1. Membrane water transport kinetics in MIN6 monolayers

Π_0/Π	**0.3**	**0.4**	**0.5**	**0.6**	**0.7**	**1.3**	**1.5**
L_pA/V_{w0} $(10^{8}\ \mathrm{Pa}^{-1}\ \mathrm{s}^{-1})$	4.0±0.5	4.6±0.7	4.4±0.9	4.4±0.9	4.8±0.8	8.5±3.3	5.8±1.9

To compare the results of the fluorescence quenching experiments to the analysis of flow chamber mixing kinetics, we calculated the rise time for the change in the osmotically active cell volume using the best-fit values of L_pA/V_{w0} in conjunction with Eq. 4, as illustrated in Figure 9. The rise time decreased as the solution osmolality increased, as predicted by Eq. 4, resulting in a statistically significant effect of osmolality on the rise time ($p < 0.001$). As indicated by the dashed line, the rise time for the concentration change at the chamber wall measured by confocal microscopy was much smaller than the rise time for the change in osmotically active cell volume, which shows that mixing in the flow chamber is adequate for measuring membrane water transport in MIN6 cells. As indicated by the solid lines, the kinetics of mixing in the flow chamber is expected to by adequate under hypotonic conditions for L_pA/V_{w0} as high as 10^{-6} Pa^{-1} s^{-1}, and over a wide range of osmolalities for $L_pA/V_{w0} \leq 10^{-7}$ Pa^{-1} s^{-1}.

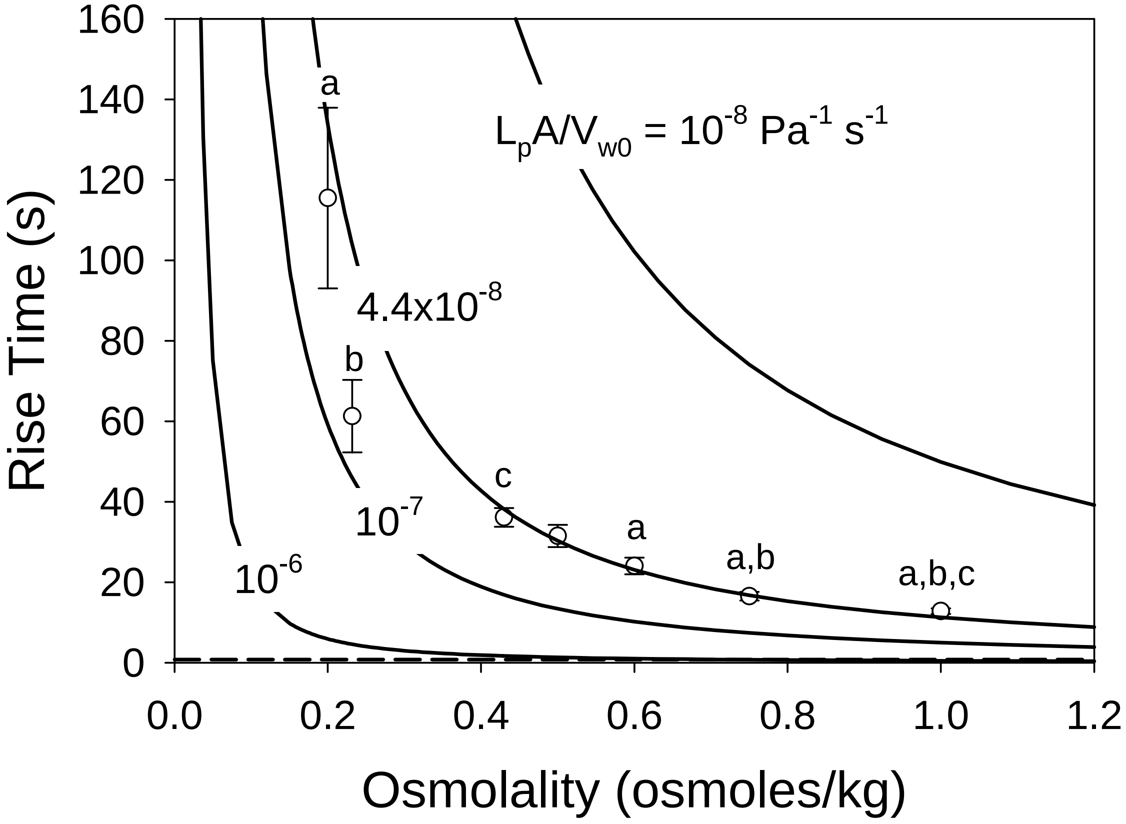

FIGURE 5.9. Rise time for the change in osmotically active cell volume after exposure anisotonic solution for MIN6 monolayers initially in isotonic solution (0.3 osmoles/kg). Significant differences are denoted by like superscript letters ($p < 0.05$). The dashed line shows the mixing time at the flow chamber wall measured by confocal microscopy, and the solid lines show rise time predictions using Eq. 4 for the given values of L_pA/V_{w0}.

Discussion

The purpose of this study was to evaluate the general utility of the fluorescence quenching technique for measuring the membrane water permeability in adherent cells, and to provide a thorough analysis of solution exchange kinetics in flow chambers, which is critical for interpretation of transient fluorescence quenching data. Using theoretical simulations of diffusion and convection in the flow chamber, we predicted the solution exchange kinetics as a function of important flow chamber design parameters, revealing that mixing is more rapid for thin channels and for fast flow velocities. The results of the numerical simulations were also used to evaluate common methods of measuring solution exchange kinetics (i.e., light transmittance after addition of a dye-containing solution), indicating that these methods can result in significant underestimation of the mixing kinetics. To evaluate the general utility of the fluorescence quenching technique, we measured fluorescence quenching in MIN6 cells, a pancreatic β-cell line that has not previously been studied using the fluorescence quenching technique. MIN6 cells exhibited typical fluorescence quenching behavior, with a linear relationship between fluorescence intensity and cell volume, indicating that the fluorescence quenching technique can be used to measure the membrane water permeability in these cells.

Although in many cases insufficient methodological detail is reported to critically examine flow chamber solution exchange kinetics, the results of the theoretical simulations presented here appear to be consistent with the literature. The large majority of studies that employ flow chambers to study the cellular osmotic response have $Pe > 10^4$, and as a consequence, Eq. 25 should approximate the mixing kinetics if a step-change in solute concentration can be assumed at the flow chamber inlet (see Figure 3). Table 2 summarizes the results of previous studies alongside predictions using Eq. 25. In some cases, the measured rise time for mixing was slower than the predicted rise time (Berner & Gervais, 1993; Maranon et al., 1997; Takamatsu et al., 2004), which suggests that the step-change assumption is not valid because of mixing limitations in the inlet tubing. Of these studies, only Takamatsu et al. (2004) reported sufficient information to estimate the effect of the inlet tubing. Theoretical simulations yielded a rise time at the entrance to the flow chamber of approximately 20 seconds for both the wall and the center of the inlet tubing, which is similar to the measured rise time of 15 seconds. Whereas a measured mixing time that is greater than the predicted mixing time suggests mixing limitations in the inlet tubing, a measured mixing time that is lower than the predicted mixing time may indicate error caused by the method of measuring mixing. Since measurement of mixing using absorbance or light transmittance can cause significant underestimation of the solution exchange time (see Figure 4), it is not surprising that the mixing time reported by Echevarria and Verkman (1992) and Solenov et al. (2004) is lower than the predicted mixing time. Although absorbance and light transmittance tend to underestimate the mixing kinetics, measurement of mixing at the flow chamber wall by techniques such as total internal reflection microfluorimetry (Farinas et al., 1995) or pH measurement (Kaplan et al., 1996) is expected to yield more accurate results, as evidenced by the similarity between the measured and predicted mixing times for these studies.

TABLE 5.2. Flow chamber mixing kinetics reported in the literature.

Reference	**Mixing Measurement Method**	***Pe*** **$*10^{-5}$**	***AR***	**Measured t_{rise} (s)**	**Predicted t_{rise} (s)[d]**
Berner and Gervais, 1993	Transmittance, dye addition	5.3	380	7	1.7
Marañon et al., 1997	Transmittance, dye addition	5.9	380	5[c]	1.5
		21	380	1.4	0.69
		9500	380	0.4[c]	0.014
Echevarria and Verkman, 1992[a]	Absorbance	13	15	1	6
Solenov et al., 2003[b]	Transmittance, dye removal	6.0	8	0.4	4.4
Takamatsu et al., 2004	Index of refraction	0.34	800	15	6.3
Kaplan et al., 1996	pH at flow chamber wall	140	50	1.5	1.5
		1100	50	0.25	0.41
Farinas et al., 1995	Total internal reflection fluorimetry	11	6	1	3
Current study	Confocal microscopy	64	240	0.82	0.19

[a] The length of the flow chamber was not reported. A length of 30 mm was assumed for calculation of *Pe* and *AR*.

[b] The chamber was circular rather than rectangular. The diameter of the chamber was used for both the width and length.

[c] The rise time was estimated from the time to achieve 63% of equilibrium.

[d] The rise time was predicted using Eq. 25 with $D = 0.52\text{x}10^{-5}$ cm^2/sec, which is the diffusivity of sucrose at 25°C (CRC Handbook, 77th Ed., 1996, p. 6-220).

The theoretical simulations of solution exchange kinetics presented here provide framework for designing flow chambers with rapid solution exchange kinetics. Whereas it is not surprising that more rapid mixing is achieved for higher flow velocities, the dependence of mixing kinetics on the channel height is less intuitive. We found that the thin channels yield more rapid mixing kinetics than thick channels, a result that seems to be poorly utilized in the literature. For example, several flow chambers that were designed for rapid solution exchange (Echevarria and Verkman, 1992; Farinas et al., 1995; Kaplan et al., 1996; Solenov et al., 2004) had chamber heights at least an order of magnitude larger than that used in the present study. Since the mixing time measured by conventional methods is more significantly underestimated for thicker channels (Figure 4), it is possible that thicker chambers were chosen because of erroneous mixing data. Another important outcome of the theoretical simulations presented here is that the inlet tubing can have a profound effect on the flow chamber mixing kinetics. For our experimental setup, the kinetics of mixing was dominated by the inlet tubing, indicating that altering the inlet tubing (e.g., decreasing the length, decreasing the inner diameter) could potentially improve the mixing kinetics. However, despite the importance of the inlet tubing, the dimensions of the inlet tubing are generally not even given in the literature (Berner and Gervais, 1993; Echevarria and Verkman, 1992; Farinas et al., 1995; Marañon et al., 1997; Solenov et al., 2004). In the flow chamber that achieved the fastest mixing kinetics (Kaplan et al., 1996), the test solution was brought directly to the chamber entrance (i.e., no inlet tubing), which further emphasizes the importance of considering mixing limitations in the inlet tubing when designing flow chambers for rapid solution exchange.

Despite the observation of fluorescence quenching behavior in several cell types loaded with calcein, there are conflicting data in the literature that call into question the generality of the fluorescence quenching response. Solenov et al. (2004) observed fluorescence quenching behavior (i.e., an increase in fluorescence intensity upon swelling and a decrease in fluorescence intensity upon shrinkage) in Chinese hamster ovary cells over a broad range of intracellular calcein concentrations and for a several depths of field (objective numerical aperture between 0.25 and 1.4), and demonstrated that calcein fluorescence is quenched by both cytosol and albumin, which suggests that calcein quenching is a general response and is not specific to cell type. However, these results are contrary to the observation of a decrease in fluorescence intensity upon swelling in calcein-loaded MDCK cells (Zelenina and Brismar, 2000), parietal cells (Sonnentag et al., 2000) and neuroblastoma cells (Altamirano et al., 1998; Crowe et al., 1995). Although it is possible that this discrepancy is caused by the smaller depth of field used to measure calcein fluorescence in these studies, Solenov et al. (2004) observed a fluorescence quenching response that did not depend on depth of field. In the present study, we observed a linear fluorescence quenching response for MIN6 cells, a previously unstudied cell type. In addition, we have observed behavior indicative of fluorescence quenching (i.e., an increase in fluorescence intensity upon swelling and a decrease in fluorescence intensity upon shrinkage) in human hepatoma cells (HepG2) and bovine pulmonary artery endothelial cells (unpublished observations). Thus, the results of this study further support the view that the fluorescence quenching response is not cell-type specific, as would be expected if calcein fluorsesence were quenched by a ubiquitous intracellular protein (Solenov et al., 2004).

The value of the membrane water permeability measured in this study for adherent cultures of MIN6 cells (a mouse β-cell line) is consistent with water permeability values reported in the literature, as shown in Table 3. Suspensions of pancreatic islet cells derived from the pig (Fedorow et al., 2001), dog (Liu et al., 1997) and hamster (Liu et al., 1995) all exhibited similar water permeability properties to MIN6 monolayers. However, although the membrane permeability parameter L_pA/V_{w0} was similar for suspensions of MIN6 cells (Chapter 3), a significant difference was observed ($p < 0.05$), indicating that suspensions and monolayers have different permeability properties. The value of L_pA/V_{w0} that we determined for MIN6 monolayers was similar to that of monolayers of wild-type Chinese hamster ovary (CHO) cells, but much lower than the L_pA/V_{w0} for CHO monolayers transfected with aquaporin-1 (Farinas et al., 1997) and mouse astrocytes, which are known to express aquaporins (Solenov et al., 2004). These data suggest that MIN6 cells either do not express aquoporins, or express aquaporins at low levels, resulting in a relatively low L_pA/V_{w0}.

TABLE 5.3. Kinetics of cell membrane water transport at 20-24°C.

Reference	**Cell Type**	**Monolayer or Suspension**	**L_pA/V_{w0} (10^8 Pa^{-1} s^{-1})**
Current Study	MIN6	Monolayer	4.4
Chapter 3	MIN6	Suspension	2.6*
Fedorow et al., 2001	Pig islet cells	Suspension	4.3
Liu et al., 1995	Hamster islet cells	Suspensions	3.6
Liu et al., 1997	Canine islet cells	Suspension	2.3
Solenov et al., 2004	Mouse astrocytes	Monolayer	220 31$
Farinas et al., 1997	Chinese hamster ovary cells	Monolayer	4.8 56#

* indicates a statistically significant difference from the current study.
$ cells from a knock-out mouse lacking aquaporin 4.
\# cells transfected with aquaporin 1.

As shown in Figure 9, the kinetics of the cell volume change is highly dependent on the solution osmolality (see Eq. 4), which has important implications in experiments to measure the membrane water permeability. The reason for the trend predicted by Eq. 4 (i.e., the decrease in the response time of the cell volume change with increasing osmolality) can be most easily explained by examining both the driving force for osmotic water transport (i.e., the osmolality difference between intra- and extracellular solutions, see Eq. 2) and the change in cell volume required to establish osmotic equilibrium (see Eq. 1). For exposure to high osmolality (e.g., 1 osmole/kg), osmotic water movement is driven initially by a relatively large osmolality difference (e.g., 0.7 osmoles/kg, if isotonic osmolality is 0.3 osmoles/kg), whereas the resulting volume change is relatively small (e.g., 0.7 x the isotonic osmotically active cell volume), yielding a fast response of the cell volume. In contrast, for exposure to low osmolality (e.g. 0.1 osmoles/kg), the driving force for osmotic water transport is low (e.g., 0.2 osmoles/kg), but the resulting volume change is large (e.g. 3 x the isotonic osmotically active cell volume), yielding a slow response of the cell volume. Although the time-scale for membrane water transport decreases as the osmolality increases, mixing kinetics either does not depend on osmolality (see Eq. 7), or exhibits the opposite trend because of the increase in viscosity associated with increasing the osmolality. Two important conclusions follow from this analysis.

First, one can take advantage of the fact that the cellular osmotic response is expected to be slower for exposure to low osmolality solutions to obtain more accurate membrane permeability measurements in cases where mixing limitations are significant (Farinas et al., 1995). Although this strategy would be of benefit in many cases, it is seldom utilized in the literature. For example, both Hamann et al. (2005) and Marañon et al. (1997) reported that mixing kinetics limited the accuracy estimates for the membrane water permeability, but both groups measured the transient cell volume change after exposure to hypertonic solution. Exposure to lower osmolality solution in these cases would be expected to yield more accurate estimates for the water permeability.

Second, since the response time of the cell volume decreases as the osmolality increases, systems that are limited by mixing kinetics will erroneously yield values for the water permeability that decrease as the osmolality increases. If one assumes that the kinetics of the cell volume change is limited by mixing and that the mixing time is independent of osmolality, the response time of the cell volume is also expected to be independent of osmolality, yielding an apparent permeability in hypotonic solution ($\Pi_0/\Pi_f = 2$) that is approximately 10-fold higher than that for hypertonic solution ($\Pi_0/\Pi_f = 0.5$). This trend of decreasing permeability with increasing osmolality has been observed by several researchers (Armitage, 1986; Farmer and Macey, 1970; Rich et al., 1968; Toupin et al., 1989; Woods et al., 2000), and has generally been attributed to a property of the cell membrane that changes with osmolality or with direction of water flow. A more likely explanation may be that the observed decrease in permeability with increase in osmolality is caused by mixing limitations.

In summary, we provided a thorough analysis of solution exchange kinetics in flow chambers using theoretical model of diffusion and convection, and we demonstrated that the fluorescence quenching technique can be used to determine the membrane permeability in monolayers of MIN6 cells, a previously unstudied cell type. The results of the theoretical simulations provide a framework for designing flow chambers for rapid solution exchange, which is critical for studying rapid osmotic volume changes in experiments to determine membrane permeability parameters. The theoretical simulations were also used to examine common methods of measuring mixing, revealing that these methods can lead to significant underestimation of the mixing time. Comparison of the membrane water permeability of MIN6 monolayers to previously reported data for MIN6 cell suspensions indicated that the permeability is affected by the cell isolation process, which underscores the importance of *in situ* permeability measurement to determine tissue permeability properties. Future studies are necessary to fully characterize the effect of cell isolation on the membrane permeability properties.

CHAPTER 6

MEMBRANE PERMEABILITY PROPERTIES IN CELL SUSPENSIONS AND CELL MONOLAYERS

Introduction

Cell damage during cryopreservation is intimately linked to cellular dehydration since excessive dehydration leads to damage as a result of high solute concentrations, and insufficient dehydration leads to damage due to formation of intracellular ice (Mazur et al., 1972). Thus, the ability to predict cell membrane transport during freezing is crucial for the optimization of cryopreservation protocols (Karlsson et al., 1996).

Whereas the membrane permeability properties in cell suspensions are available for many cell types (e.g., McGrath, 1988), permeability properties for tissue are relatively scarce. In addition, there is evidence in the literature that membrane permeability is affected by processing required to create a cell suspension (Bischof, 2000), indicating that it may not be possible to use permeability properties derived from cell suspensions to predict membrane transport in tissue. For example, Yarmush et al. (1992) observed a decrease in the water permeability at 0°C and an increase in the activation energy of almost an order of magnitude after disaggregation of cultured hepatocytes to form a cell suspension. Balasubramanian et al. (2006) also observed dramatic differences in the permeability properties of cultured fibroblasts and suspensions, but with a decrease in both the water permeability and the activation energy. Other investigators have reported similar permeability properties in intact liver tissue and isolated cells (Devireddy and Bischof, 1998; Pazhayannur and Bischof, 1997; Smith, Schulte et al., 1998), suggesting that cell isolation may not affect the permeability. Thus, the differences, if any, between the permeability properties of intact tissue and cell suspensions are unclear.

Since survival of cryopreservation generally requires the use of cryoprotectants (CPAs, e.g., glycerol), the ability to predict membrane transport in the presence of CPA is critical for developing cryopreservation procedures. Whereas CPAs are generally assumed to reduce the membrane water permeability by approximately a factor of 2 in cell suspensions (Karlsson et al., 1993; Mazur, 1990), a much more dramatic effect has been reported for tissue (Bischof, 2000). For rat liver tissue, a reduction in the water permeability of almost 2 orders of magnitude was observed in the presence of dimethylsulfoxide (Me_2SO) at 1 M and 2 M concentrations (Smith, Pham et al., 1998), in contrast to a 5-6 fold reduction for isolated cells (Smith, Schulte et al., 1998). The effect of CPA on the activation energy was also more extreme in tissue than suspension. It is unclear whether these extreme changes in permeability parameters in the presence of CPA will extend to other tissue types. Further studies are necessary to fully elucidate the effect of CPA on the permeability properties of tissue.

The objective of the present study was to investigate the differences in the membrane permeability of intact tissue and cell suspensions, and to clarify the effect of CPA on tissue permeability properties. We used cells cultured in monolayers as a model tissue system since monolayers exhibit many of the characteristics of tissue, such as an organized cytoskeleton, cell-cell connections, and cell-substrate connections. The membrane permeability in monolayers was measured using a fluorescence quenching technique (Chapter 5), and compared with the permeability properties of cell suspensions measured using electronic cell sizing (Chapters 2, 3 and 4).

Cell Membrane Transport Theory

The change in cell volume resulting from exposure to anisotonic solution containing impermeable solutes and a single permeable solute is governed by two transport processes: membrane water transport and transport of the permeable solute. Assuming an ideal and dilute intracellular solution, the following pair of coupled differential equations (two-parameter model, Kleinhans, 1998) can be used to describe the cell volume change in terms of these transport processes:

$$\frac{d\left(V_w / V_{w0}\right)}{dt} = \frac{L_p A}{V_{w0}} RT\left(M_n^i + \frac{N_s / V_{w0}}{V_w / V_{w0}} - M_n^e - M_s^e \right) \qquad [1]$$

$$\frac{d\left(N_s / V_{w0}\right)}{dt} = \frac{P_s A}{V_{w0}}\left(M_s^e - \frac{N_s / V_{w0}}{V_w / V_{w0}} \right) \qquad [2]$$

where V_w is the osmotically active cell volume (i.e., the volume of cellular water that can be removed in the limit of infinite osmotic strength), A is the cell surface area, L_p is the membrane water permeability, R is the ideal gas constant, T is the absolute temperature, M represents the osmoles of intracellular solute divided by the osmotically active cell volume, N_s is the number of moles of permeable solute per cell, P_s is the solute permeability, the subscript “0” corresponds with an isotonic concentration of impermeable solutes, the superscripts “*i*” and “*e*” denote intracellular and extracellular conditions, respectively, and the subscripts “n” and “s” denote the impermeable solutes and the permeable solute, respectively. In Eqs. 1 and 2, the extracellular osmotic strength can be controlled experimentally (i.e., M_n^e and M_s^e are known quantities), and the intracellular osmotic strength of the permeable solute is given as the ratio of N_s to V_w (i.e., the variables that are predicted by the model), but an additional equation is needed to describe the intracellular osmotic strength of the impermeable solutes in terms of known quantities. This additional equation is obtained by noting that the intracellular content of impermeable solutes is constant, resulting in the Boyle-van't Hoff relationship:

$$\frac{V_w}{V_{w0}} = \frac{M_{n0}^i}{M_n^i} \qquad [3]$$

Whereas Eqs. 1-3 describe the changes in the osmotically active cell volume, in some cases it is desirable to use the total cell volume (*V*). The total cell volume is related to the osmotically active cell volume as follows:

$$\frac{V_w}{V_{w0}} = \frac{V/V_0 - \overline{V}_b}{1 - \overline{V}_b} \qquad [4]$$

where $\overline{V}_b$ is the osmotically inactive volume fraction.

The temperature dependence of the permeability parameters is characterized by the Arrhenius activation energy. For membrane water transport, the Arrhenius relationship is given as

$$L_p = L_{p,ref} \exp\left[\frac{E_{Lp}}{R}\left(\frac{1}{T_{ref}} - \frac{1}{T}\right)\right] \qquad [5]$$

where the $L_{p,ref}$ is the water permeability at the reference temperature, T_{ref}, and E_{Lp} is the activation energy for membrane water transport. For solute transport, the Arrhenius relationship is given as

$$P_s = P_{s,ref} \exp\left[\frac{E_{Ps}}{R}\left(\frac{1}{T_{ref}} - \frac{1}{T}\right)\right] \qquad [6]$$

where $P_{s,ref}$ is the solute permeability at T_{ref}, and E_{Ps} is the activation energy for solute transport.

The cytoplasm composition and intracellular supercooling during freezing can be predicted using the above equations. It is generally assumed that transport of the permeable solute is negligible during freezing, and that the extracellular solution is in equilibrium with ice, resulting in the following differential equation (Karlsson et al., 1993; Mazur, 1963):

$$\frac{d\left(V_w/V_{w0}\right)}{dt} = \frac{L_p A}{V_{w0}}\left[\frac{-RT}{v_w}\ln\left(\frac{V_w/V_{w0}}{V_w/V_{w0} + \nu_w M_{n0}^{i} + \nu_w M_{s0}^{i}}\right) - \frac{\Delta H_f}{v_w}\left(1 - \frac{T}{T_m}\right)\right] \qquad [7]$$

where $\Delta H_f = 6016.5$ J/mol, $T_m = 273.15$ K and $v_w = 1.8 \times 10^{-5}$ m^3/mol are the heat of fusion, melting temperature and molar volume of pure water, respectively. To fully describe membrane transport during freezing, the relationship between the temperature and the time is needed. For a linear cooling rate (B), one obtains

$$\frac{dT}{dt} = -B \qquad [8]$$

Combining Eqs. 7 and 8, it is possible to predict the intracellular water content during freezing, from which the intracellular supercooling can be calculated:

$$\Delta T = \left[\frac{1}{T_m} - \frac{R}{\Delta H_f}\ln\left(\frac{V_w/V_{w0}}{V_w/V_{w0} + \nu_w M_{n0}^{i} + \nu_w M_{s0}^{i}}\right)\right]^{-1} - T \qquad [9]$$

It can be seen from Eqs. 7-9 that predictions for the cell water content and supercooling can be obtained given a single cell-specific parameter, L_pA/V_{w0}, comprising the membrane water permeability (L_p) and the cell surface to volume ratio (A/V_{w0}).

Materials and Methods

Cell Culture

Mouse insulinoma (MIN6) cells (Miyazaki et al., 1990) were generously provided by Paolo Meda, M.D. (University of Geneva, Switzerland). MIN6 cells were cultured at 37ºC in a 5% CO_2 environment in tissue culture flasks containing DMEM (high glucose, Invitrogen) supplemented with 15% v/v heat inactivated FBS (Sigma-Aldrich) and 0.07 mM β-mercaptoethanol (Invitrogen). Media was changed every 3 days and passages were performed weekly. For experiments to determine the membrane permeability in cell monolayers, cells were seeded onto 40 mm diameter glass coverslips in 60 mm Petri dishes and cultured for 3-4 days. For experiments to measure the membrane permeability in cell suspensions, cells were cultured in 35 mm Petri dishes for 3-4 days, and then cell suspensions (96% single cells, 93% viability) were created by exposure to 0.2% trypsin solution (Invitrogen) at 37°C for 15 min, followed by trituration in culture medium 20 times with a 20G needle (see Chapter 4). Suspensions were used in osmotic experiments within 5 minutes.

Bovine pulmonary artery endothelial cells (BPAEC, Cambrex) were cultured in a 5% CO_2 environment at 37°C in tissue culture flasks containing MCDB 131 media (Mediatech) supplemented with 5% v/v fetal bovine serum (Sigma-Aldrich), 2 ng/mL basic human fibroblast growth factor (PeproTech), 10 ng/mL human epithelial growth factor (Invitrogen), 1 ng/mL vascular endothelial growth factor (Sigma-Aldrich), 2 ng/mL insulin-like growth factor-1 (Invitrogen), 0.001 mg/mL hydrocortisone (Sigma-Aldrich), 2 mM L-glutamine (Mediatech), 100 U/mL penicillin and 100 µg/mL streptomycin (Invitrogen), and 50 µg/mL ascorbic acid (Sigma-Aldrich). Media was changed every 2 days and passages were performed when the flasks reached a confluency of approximately 80% by exposure to trypsin-EDTA solution (Cambrex) for 5 min, as recommended by the vendor. For experiments to measure to the membrane permeability in cell monolayers, BPAEC were seeded onto 40 mm diameter glass coverslips in 60 mm Petri dishes, and cultured for 2 days. For experiments to measure the membrane permeability in cell suspensions, BPAEC were cultured in 35 mm Petri dishes for 2 days, and then cell suspensions (97% single cells, 96% viability) were created as follows. The cells were first rinsed in Hepes buffered saline solution (Cambrex). Then the surface of the Petri dish was coated with 0.5 ml of 0.2% trypsin solution (Invitrogen) and excess solution was aspirated. After incubation for 10 min, trypsinization was stopped by addition of 1 ml of BPAEC media, and the resulting suspension was triturated gently 20 times with a 20G needle. The quality of the cell suspension was assayed by counting cells on a hemacytometer and viable cells were identified by exclusion of trypan blue.

Osmotic Test Solutions

For experiments to determine the membrane water permeability in the absence of CPA, osmotic test solutions were prepared by addition of either sucrose or purified water to isotonic (0.3 osmoles/kg) phosphate buffered saline solution (PBS). Whereas the PBS for experiments with cell monolayers contained divalent cations (Mg^{2+} and Ca^{2+}), the PBS used with cell suspensions did not. To examine permeability properties in the presence of CPA, two types of experiments were performed. In the first type of experiment, cells initially in isotonic PBS were exposed to isotonic PBS containing either 5% v/v glycerol (1.04 osmoles/kg) or 5% v/v Me_2SO (1.04 osmoles/kg). The second type of experiment was designed to emulate freezing in the presence of CPA. For these experiments, cells initially in isotonic solution containing CPA were exposed to solutions made hypertonic by addition of both sucrose and CPA such that an equivalent ratio of CPA to impermeable solutes was maintained (i.e., only the relative content of water in the solution was changed). Initial Me_2SO concentrations of 2.5% v/v (0.67 osmoles/kg), 5% v/v and 10% v/v (1.87 osmoles/kg) and initial glycerol concentrations of 2.5% v/v (0.65 osmoles/kg) and 5% v/v were used. The final osmolality of impermeable solutes was varied between 0.43 osmoles/kg ($M_{n0}^{i}/M^{e} = 0.7$) and 1000 osmoles/kg ($M_{n0}^{i}/M^{e} = 0.3$). The osmolality of all solutions was measured using a freezing point depression osmometer. Since the equations describing membrane transport (Eqs. 3 and 4) are expressed in terms of osmoles per osmotically active cell volume (M), the osmolality was converted to M by multiplying by the density of water (1 g/mL).

Measurement of Membrane Permeability in Cell Monolayers

The membrane water permeability for cell monolayers in the absence of CPA was determined by measuring the fluorescence quenching of intracellular calcein during exposure to anisotonic solution in a flow chamber, as described previously (Chapter 5). Briefly, cell monolayers were incubated in PBS containing 1.25 μg/ml calcein-AM (Invitrogen) for 15-20 min at 37°C, assembled into the flow chamber (FCS2, Bioptechs), and mounted onto an upright microscope (Eclipse ME600, Nikon) using a custom stage adapter. To control the temperature in the flow chamber, a refrigerated water bath was used to pump fluid through the flow chamber frame and through a heat exchanger contacting the inlet tubing. The temperature was monitored throughout the experiments using a thermocouple inserted into the outlet tubing, yielding a temperature precision of ±1°C. Cell monolayers were initially bathed in isotonic solution (15 min), exposed to anisotonic solution (3 min), and then returned to isotonic solution (5 min) while recording the fluorescence intensity using a cooled CCD camera (SensiCam, Cooke Corporation). The fluorescence intensity data was corrected for the effects of fading (e.g., photobleaching, dye leakage) by fitting an exponential decay model to the data. To analyze the corrected fluorescence intensity data, we assumed a linear relationship between relative fluorescence intensity and relative osmotically active cell volume:

$$\frac{F}{F_0} = a\frac{V_w}{V_{w0}} + 1 - a \qquad [10]$$

where F is the fluorescence intensity and a is a constant. Combining Eqs 1, 3 and 10 one obtains the following expression for the transient change in fluorescence intensity after exposure to anisotonic solution containing only membrane impermeable solutes:

$$\frac{d\left(F/F_0\right)}{dt} = \frac{L_pA}{V_{w0}}RT\left(\frac{a^2M_{n0}^{i}}{F/F_0 + a - 1} - aM_n^e\right) \qquad [11]$$

The fluorescence intensity data were fit for a and L_pA/V_{w0} simultaneously by minimizing the error squared between the data and the numerical solution of Eq. 11, assuming a step-change in extracellular osmolarity at $t = 0$. The steady-state fluorescence intensity in anisotonic solution was calculated using the best-fit value of a. To determine the temperature dependence of the membrane water permeability, experiments were performed at 4°C, 12°C, 21°C and 37°C.

To determine the apparent membrane water permeability in the presence of CPA we performed fluorescence quenching experiments that emulated the cell freezing process. Cell monolayers were equilibrated in isotonic PBS containing CPA, and then exposed to solution made hypertonic by addition of both sucrose and CPA such that the relative concentration of CPA to impermeable solutes was unchanged. This change in the osmotic environment is similar to that encountered during freezing, in which water is removed from the liquid solution by formation of ice, leaving the relative solute concentrations unchanged. The protocol described above for determination of the water permeability in the absence of CPA was followed here, with the following exceptions. For MIN6 cells, isotonic solution refers to isotonic PBS containing 5% v/v glycerol and for BPAEC, isotonic solution refers to isotonic PBS containing 5% v/v Me_2SO. To allow equilibration with the isotonic CPA solution, MIN6 monolayers were loaded with calcein by incubation in PBS containing 5% v/v glycerol and 1.25 μg/ml calcein-AM for 15-20 min at 37°C, and then exposed to the isotonic glycerol solution for 15 min in the flow chamber prior to exposure to anisotonic solution. Since BPAEC equilibration in 5% v/v DMSO solution was found to be rapid, BPAEC monolayers were not exposed to DMSO solution during the calcein loading, and achieved complete equilibration with the isotonic DMSO solution during the initial 15 min exposure in the flow chamber. CPA transport was neglected to determine the best-fit apparent water permeability using Eq. 11 (i.e., both M_{n0}^{i} and M_{n}^{e} refer to the total osmolarity).

Fluorescence quenching experiments were also used to investigate the membrane permeability to Me_2SO and glycerol. Monolayers initially in isotonic PBS were exposed to either 5% v/v glycerol (MIN6 cells and BPAEC) or 5% v/v Me_2SO (BPAEC) in the flow chamber, and then returned to isotonic conditions. The resulting fluorescence intensity data were corrected for the effects of fading (e.g., photobleaching, dye leakage) as described above, and then converted to the relative osmotically active cell volume using Eq. 10 with the best-fit value of *a* determined from exposure of the monolayers to anisotonic solutions of impermeable solutes. These transient volume data were fit to Eq. 1 and Eq. 2 to determine the solute permeability parameter (P_sA/V_{w0}) and the water permeability parameter (L_pA/V_{w0}).

Measurement of Membrane Permeability in Cell Suspensions

The membrane water permeability in suspensions of BPAEC and MIN6 cells was determined using the Coulter counter method, as previously described (Chapters 2 and 3). A volume of 100 μL of cell suspension (0.5-2 x 10^6 cells/ml) in isotonic cell culture medium was injected into 10 mL of well-mixed osmotic test solution in the Coulter counter sample beaker. At this cell concentration, both BPAEC and MIN6 cell suspensions are expected to yield < 6% error due to coincidence (see Chapter 4). For each osmotic solution, four replicates were performed, each representing cell suspensions created from different cultures. Mixing of the sample solution was accomplished using a small magnetic stirrer attached to the base of the beaker holder, and a 1/2 x 5/16” stir bar. Temperature was controlled to ± 0.5°C by circulating liquid from a refrigerated water bath through the jacket of the sample beaker. The raw voltages from the Coulter counter (Z2 series) were accessed via a custom installed BNC connection, and peak voltage signals were digitized and sent to a computer using a Cell Size Analyzer (CSA) interface (McGann et al., 1982). To reduce electrical noise, copper wire was inserted into the jacket of the beaker and grounded to the base of the Coulter counter, creating a Faraday shield. Peak voltage signals were converted to volume by calibration with spherical latex beads of known size. The Coulter counter settings were chosen such that the maximum measurable volume was 3400 fL (gain = 32, current = 0.5, preamplifier gain = 179.2). The osmotically inactive volume fraction was determined from measurements of the mean cell volume after exposure to solutions of various osmotic strengths. The mean cell volume at steady-state was determined by fitting the volume data to the sum of an exponential distribution and a lognormal distribution to account for the cell debris and cell volumes, respectively (Chapter 2). Steady-state was assumed to occur 3 min after exposure to anisotonic solution. The membrane water permeability was determined by fitting the transient cell volume data to Eq. 3 using the volume limit adjustment method (Chapter 3), which has been shown to yield more accurate results than the conventional method when the range of measurable cell volumes is restricted (e.g., by cell debris).

Statistical Analysis

Unless otherwise noted, the data are reported as averages and the standard error of the mean. For normally distributed data and equal variances, the data were analyzed by ANOVA, followed by Tukey's tests. A logarithmic transformation was used when either of these criteria was not met (i.e., normal distribution, equal variances). If the logarithmic transformation did not yield normally distributed data and equal variances, the data were analyzed using a nonparametric ANOVA (Kruskal-Wallis), followed by Dunn's method for pairwise comparisons.

Results

Since determination of the membrane permeability from measurement of transient cell volume changes requires knowledge of cell-specific equilibrium parameters (e.g., $\bar{V}_b$), we first measured the steady-state response after exposure to anisotonic solution, as shown in Figure 1. As illustrated in the inset, the volume distribution for BPAEC suspensions in isotonic solution is adequately described using an exponential distribution to account for cell debris and a lognormal distribution to account for the cell volumes. The best-fit lognormal distribution to these isotonic data yielded an arithmetic mean and standard deviation of 1380±40 fL and 530±4 fL, respectively. The mean cell volumes in anisotonic solution were normalized to this isotonic value to generate a Boyle-van't Hoff plot, which exhibited linear osmometric behavior after exposure to hyper- and hypotonic solution. The best-fit line to these data ($R^2 = 0.98$) yielded an osmotically inactive volume fraction of 0.29±0.03 for BPAEC suspensions. BPAEC monolayers exhibited a linear response of fluorescence intensity after exposure to anisotonic solution, as evidenced by the quality of the linear fit to the data ($R^2 = 0.94$). Given that suspended BPAEC exhibited linear osmometric behavior, and that BPAEC monolayers exhibited a linear response of fluorescence intensity, the use of Eq. 12 to relate the osmotically active cell volume to the fluorescence intensity is justified. The steady-state response of MIN6 monolayers and suspensions after exposure to anisotonic solution has been reported previously (Chapters 2 and 5).

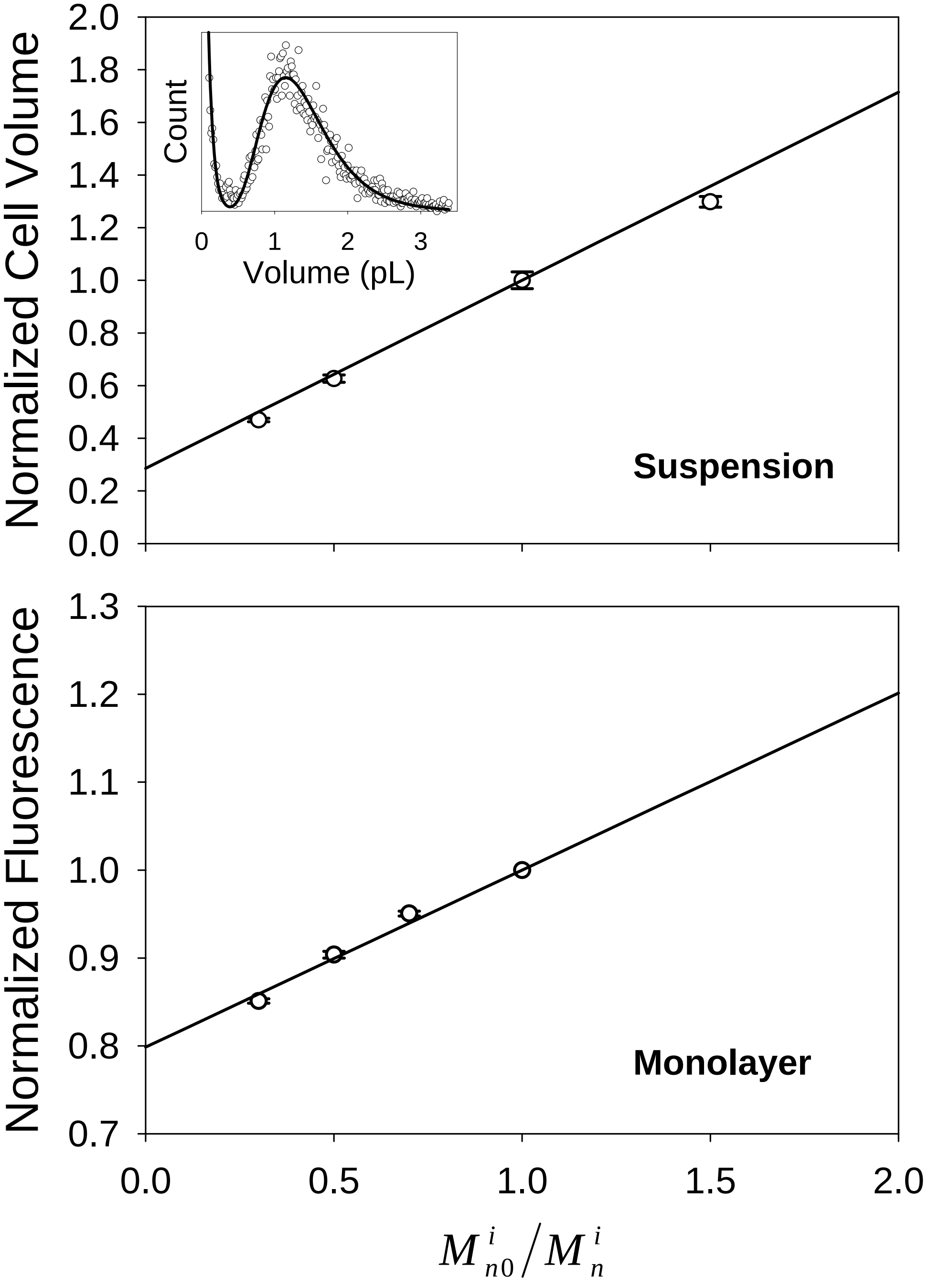

FIGURE 6.1. Equilibrium response of BPAEC suspensions and monolayers after exposure to anisotonic solution containing impermeable solutes. The inset shows the volume distribution for BPAEC suspensions in isotonic solution and the best-fit curve describing the cell debris (exponential distribution) and the cell volume (lognormal distribution). The data represents the mean and standard error of 4 replicates. The best-fit lines were forced through the point 1,1.

The membrane water permeability properties of monolayers and suspensions of BPAEC and MIN6 cells are compared in Figure 2. The water permeability was determined from measurements of the cell volume change after exposure to anisotonic solution at 4°C, 12°C, 21°C and 37°C, an example of which is shown in the inset for BPAEC monolayers. These experiments revealed a statistically significant ($p < 0.001$) effect of cell morphology (cell monolayer vs. suspension) and temperature on L_pA/V_{w0} for both BPAEC and MIN6 cells. The kinetics of membrane water transport was significantly faster in monolayers than suspensions at all temperatures investigated for both BPAEC and MIN6 cells ($p < 0.05$). The activation energy for water transport was determined from the best-fit line, yielding a significantly lower ($p < 0.001$) activation energy for monolayers of BPAEC (49±2 kJ/mol) than for suspensions (69±5 kJ/mol), indicating that the differences in water transport kinetics will become larger as the temperature decreases (i.e., during freezing). The difference between the activation energies for MIN6 suspensions (33±6 kJ/mol) and monolayers (45±4 kJ/mol) was not significant ($p = 0.11$). The water permeability properties for monolayers and suspensions of BPAEC and MIN6 cells are summarized in Table 1.

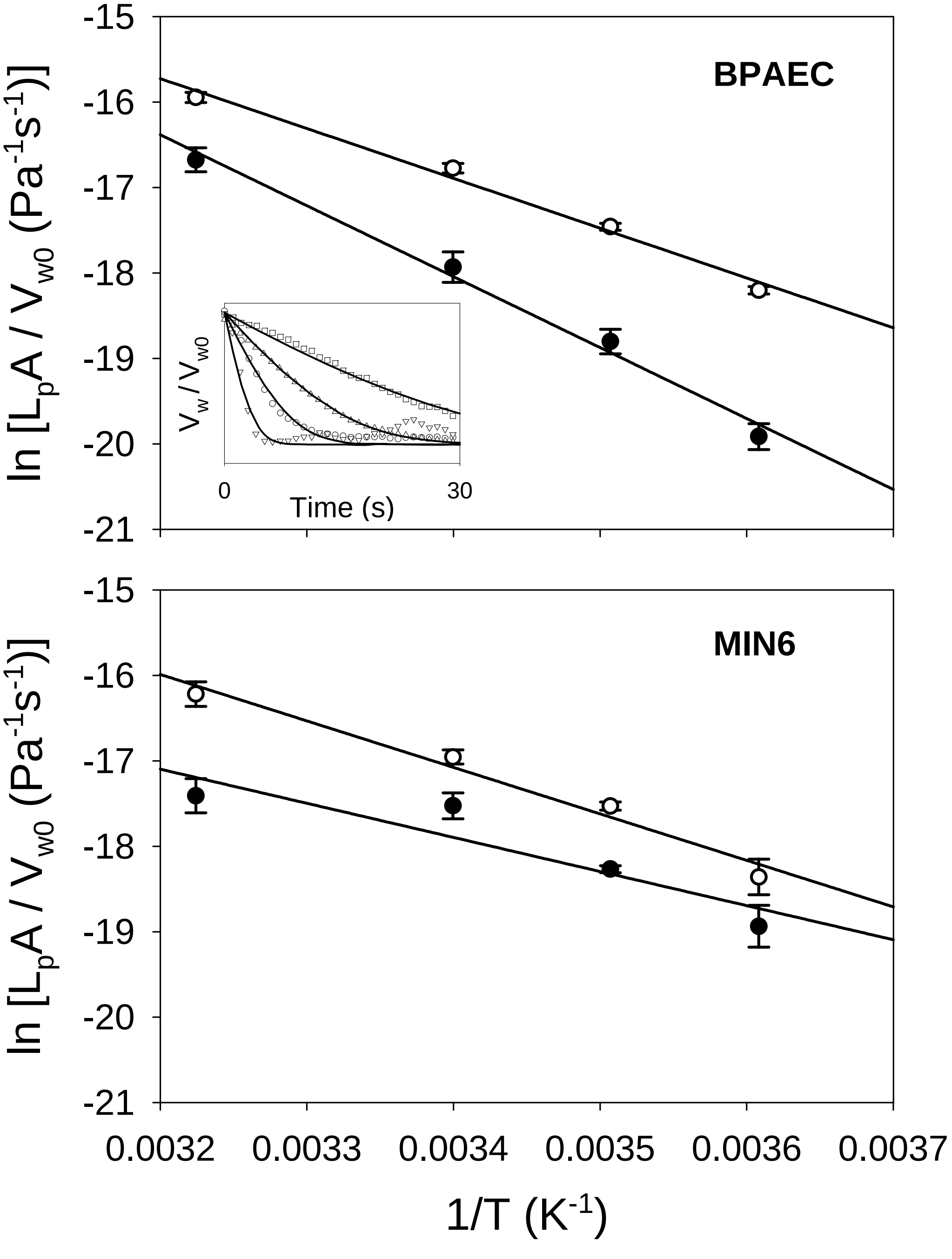

FIGURE 6.2. Arrhenius plots of the water permeability parameter for monolayers (open symbols) and suspensions (closed symbols) of BPAEC and MIN6 cells. The activation energy for membrane water transport was determined from the best-fit lines using Eq. 7. The inset shows an example of the transient response of the cell volume after exposing BPAEC monolayers to hypertonic solution at 4°C, 12°C, 21°C and 37°C. The data either represents 4 replicates (BPAEC, MIN6 suspensions), or 6 replicates (MIN6 monolayers).

Using these membrane water permeability parameters, we next predicted the cell dehydration during freezing of cell monolayers and suspensions using Eq. 9. Since cryopreservation protocols are typically designed to avoid damaging intracellular ice formation (IIF), we used the predictions of cell dehydration to calculate the intracellular supercooling, which is the driving force for IIF. For BPAEC, it is evident that membrane water transport is faster in monolayers than suspensions, resulting less supercooling for a given cooling rate. This is particularly evident for a cooling rate of 10°C/min, for which monolayers exhibited a maximum supercooling of <5°C, whereas suspensions reached a supercooling of >30°C after cooling to -40°C. At this cooling rate, suspensions are expected to undergo IIF, but monolayers may not, indicating that the optimum cooling rate is expected to be higher for monolayers than suspensions of BPAEC and underscoring the importance of *in situ* measurement of the membrane permeability properties in tissue. Although MIN6 monolayers exhibited faster membrane water transport kinetics than suspensions for temperatures above 4°C, a slightly higher supercooling was predicted for monolayers because of the higher activation energy for monolayers. Since the activation energies for monolayers and suspensions of MIN6 cells were not statistically different, these data emphasize the importance of obtaining accurate estimates for the activation energy.

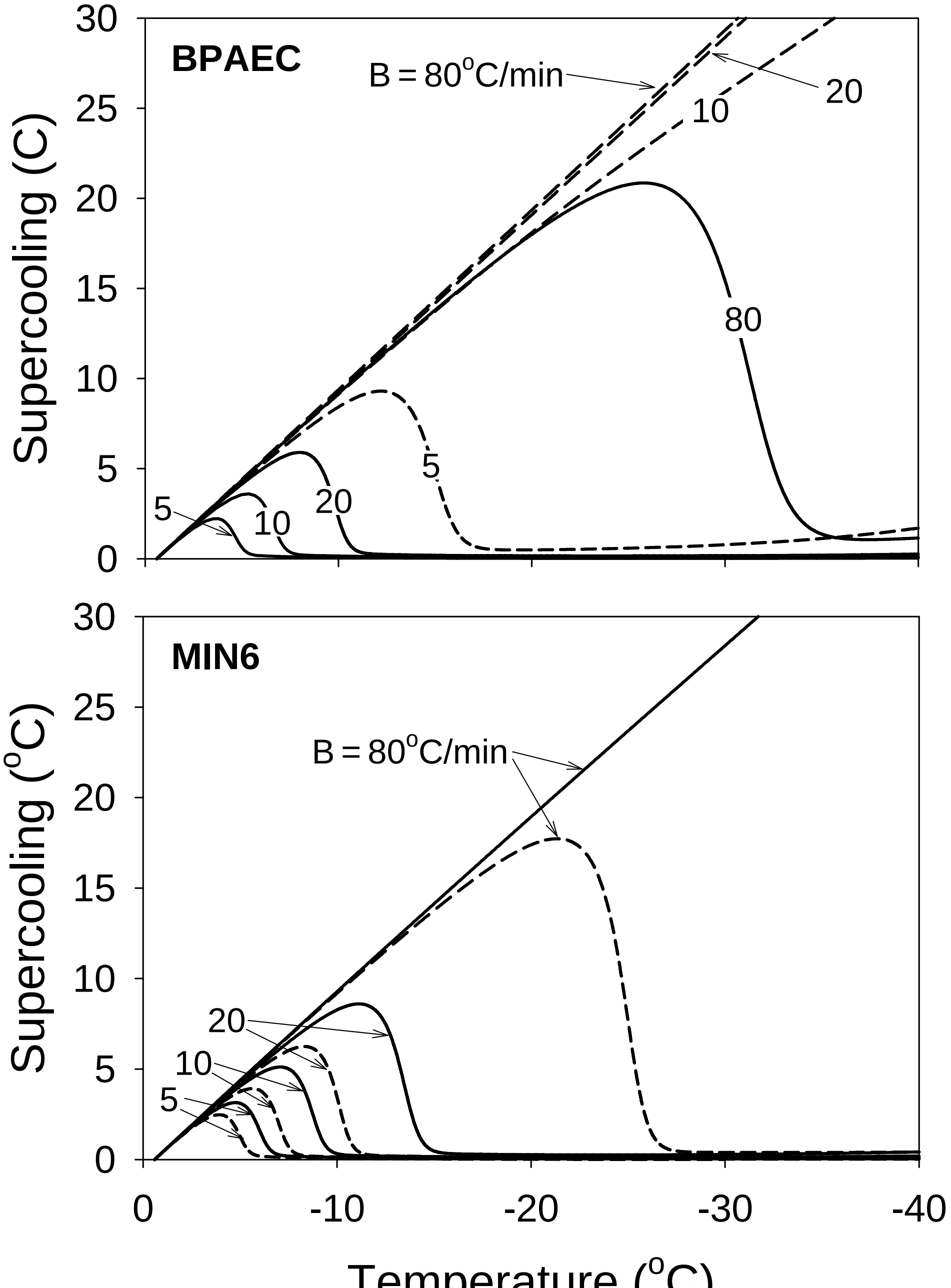

FIGURE 6.3. Theoretical predictions of intracellular supercooling in cell suspensions (dashed lines) and monolayers (solid lines) during cooling in the presence of extracellular ice from -6° to -40°C at the given cooling rate (B).

Since previous studies have reported a dramatic effect of CPAs on the membrane permeability in tissue, we next investigated the membrane permeability properties of cell monolayers in the presence of CPA. Figure 4A illustrates the response of the osmotically active cell volume after exposing BPAEC monolayers to hypertonic solutions containing sucrose (membrane impermeable), glycerol (5% v/v) or Me_2O (5% v/v) at 21°C. Exposure to the sucrose solution resulted in a monotonic reduction in the cell volume due to exosmosis of water, whereas exposure to the CPA solutions resulted in typical shrink-swell responses, in which the volume initially decreased because of water loss, and then increased as both CPA and water entered the cells. As evidenced by the more rapid swelling after exposure to Me_2SO than glycerol, Me_2SO transport is faster than glycerol transport at 21°C. These shrink-swell experiments were performed over a range of temperatures, and the resulting data were fit to Eqs. 3 and 4 to determine the membrane water permeability parameter L_pA/V_{w0} and the CPA permeability parameter P_sA/V_{w0}, which are displayed in Arrhenius plots in Figure 4B. The linear fits to these data yielded activation energies for membrane water transport and Me_2SO transport in BPAEC monolayers of 50 ± 6 kJ/mol and 99 ± 5 kJ/mol, respectively. The membrane permeability parameters determined from shrink-swell experiments are summarized in Table 1, demonstrating that the room temperature water permeability is lower for exposure to CPA solution than for exposure to sucrose solution by about 30%, but the value of E_{Lp} is unchanged.

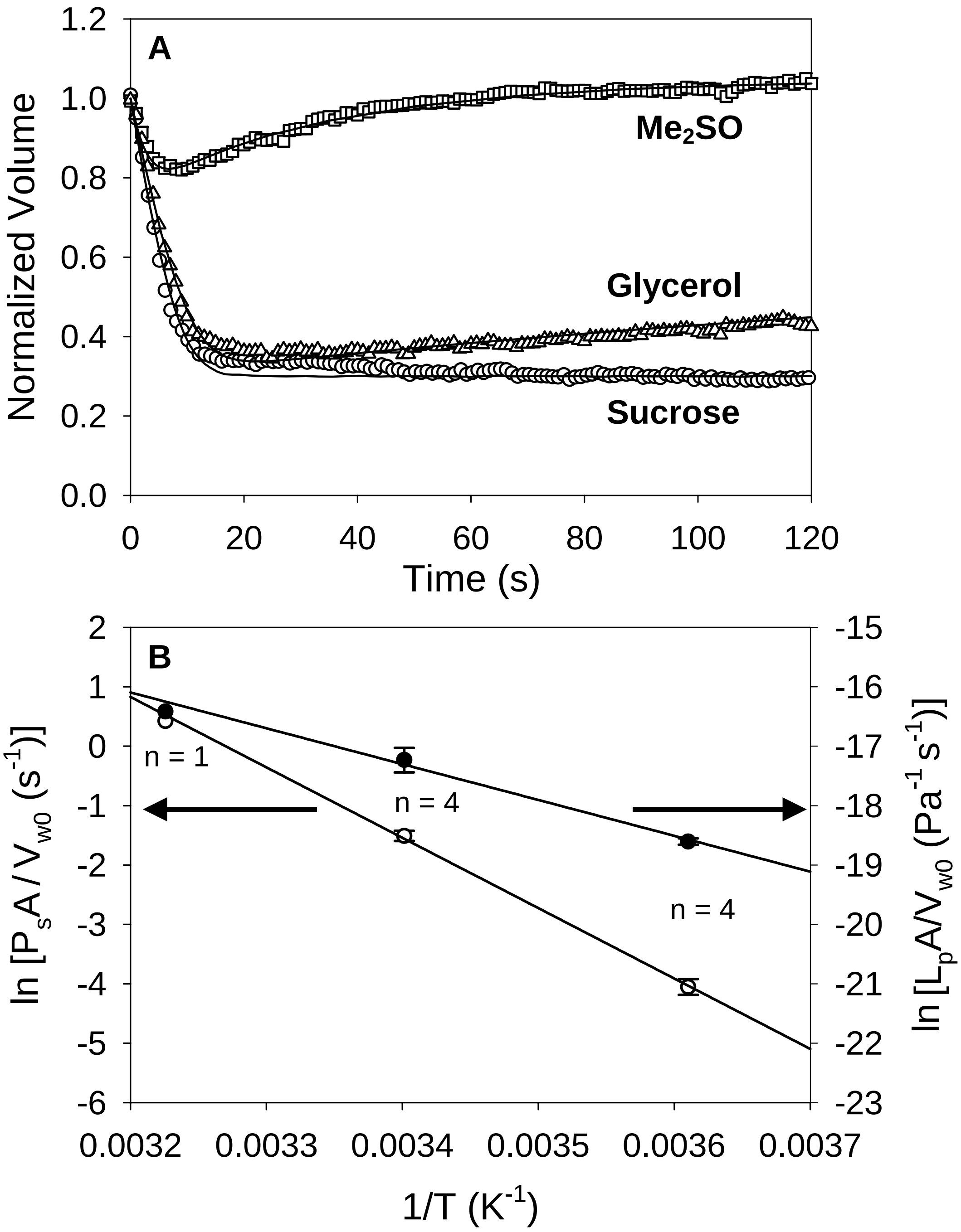

FIGURE 6.4. CPA transport in BPAEC monolayers. (**A**) Representative responses of the osmotically active cell volume (normalized to isotonic conditions) after exposure to hypertonic solution (1.04 osmoles/kg) containing sucrose, glycerol and Me_2SO at 21°C. (**B**) Arrhenius plot of the Me_2SO permeability parameter P_sA/V_{w0} (left axis, open symbols) and the membrane water permeability parameter L_pA/V_{w0} (right axis, closed symbols) for BPAEC monolayers exposed to 5% v/v Me_2SO. The best-fit lines were used to determine the activation energy (Eqs. 7 and 8).

TABLE 6.1. Membrane permeability properties in monolayers and suspensions.

Cell Type	CPA	L_pA/V_{w0} [*] (10^8 Pa^{-1} s^{-1})	E_{Lp} (kJ/mol)	P_sA/V_{w0} [*] (10^3 s^{-1})	E_{Ps} (kJ/mol)
MIN6 suspensions	none	2.5 ± 0.4	33 ± 6	n/a	n/a
MIN6 monolayers	none	4.4 ± 0.4	45 ± 4	n/a	n/a
	5% glycerol	2.6 ± 0.3		7.2 ± 1	
BPAEC suspensions	none	1.7 ± 0.4	69 ± 5	n/a	n/a
BPAEC monolayers	none	5.2 ± 0.3	49 ± 2	n/a	n/a
	5% glycerol	3.8 ± 0.2		2.3 ± 0.3	
	5% Me_2SO	3.5 ± 0.7	50 ± 6	220 ± 20	99 ± 5

[*] Permeability at a reference temperature of 21°C

To investigate the effect of CPAs on the apparent membrane water permeability during freezing, we performed experiments with BPAEC monolayers to emulate the freezing process, in which monolayers were initially equilibrated in isotonic PBS containing CPA, and then exposed to hypertonic solutions similar to those encountered during freezing (i.e., the relative concentrations of CPA and impermeable solutes were constant). Since CPA transport is generally neglected during freezing, we neglected CPA transport while determining the best-fit water permeability from the resulting transient cell volume data. Figure 5A shows the effect of the final solution tonicity on the apparent water permeability for BPAEC monolayers initially in 5% v/v Me_2SO and MIN6 monolayers initially in 5% v/v glycerol. For comparison, the water permeability is shown in the absence of CPA (i.e., monolayers initially in isotonic PBS). The final tonicity did not have a statistically significant effect on the apparent water permeability at 21°C for either cell type ($p > 0.58$), suggesting that a single value for the water permeability can be used to predict cell dehydration in the presence of CPA, even though the CPA concentration changes during the freezing process. However, the effect of CPA on the apparent water permeability was statistically significant ($p < 0.001$), with a reduction in the apparent water permeability in the presence of CPA of 70% and 40% for BPAEC and MIN6 monolayers, respectively.

Since neglecting CPA transport can lead to erroneous estimates for the water permeability, we used theoretical simulations to predict the effect of CPA transport on the apparent water permeability, with the goal of determining whether the observed effect of CPA on the apparent water permeability was real, or an artifact caused by neglecting CPA transport. The results of these theoretical simulations are shown in Figure 5A, revealing that neglecting CPA transport does not result in significant error in the apparent water permeability for MIN6 cells, but does yield significant underestimation of the water permeability for BPAEC. However, the measured water permeability was even lower than the predictions, indicating that the predicted reduction in the water permeability caused by neglecting CPA transport does not entirely account for the reduction in the measured water permeability. Together, these data suggest that the reduction in the water permeability is a real effect for both BPAEC and MIN6 monolayers, and not an artifact of neglecting CPA transport.

Another potential explanation for the observed reduction in the water permeability in the presence of CPA is limitations in the kinetics of solution exchange in the flow chamber, since the osmotic volume change is expected to be 3.5 fold faster in the presence of 5% v/v CPA (Chapter 5, Eq. 4). To explore this possibility, we examined the rise time for the osmotic volume change and compared it to the rise time for solution exchange (Chapter 5), as shown in Figure 5B. For BPAEC and MIN6 monolayers in the presence and absence of CPA, the measured rise time for the osmotic volume change was much higher than the rise time for solution exchange, indicating that the measured water permeability is not affected by mixing limitations. These data further support the idea that the reduction in water permeability in the presence of CPA is the result of a real effect of the CPA on the cell membrane properties.

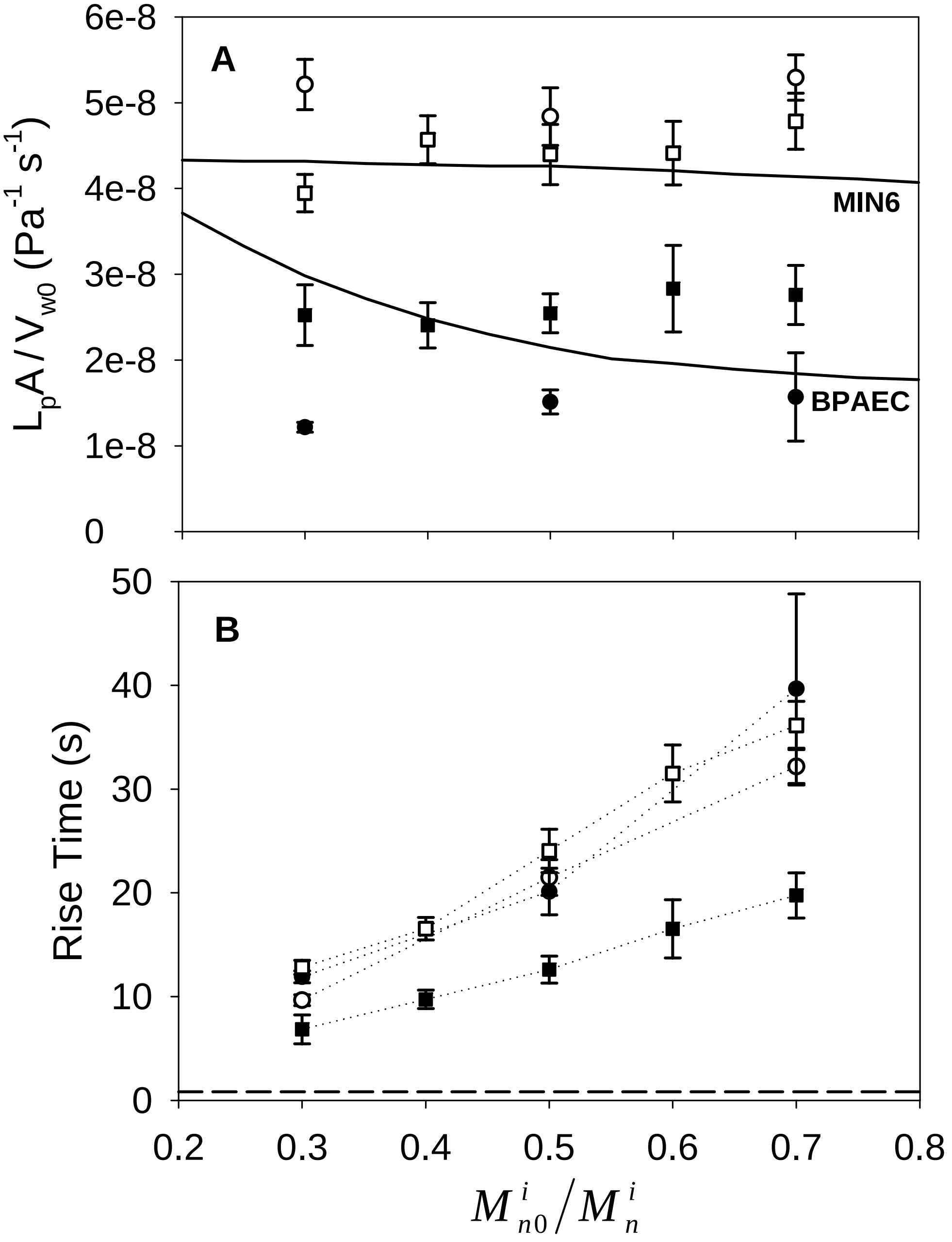

FIGURE 6.5. The apparent water permeability at 21°C for monolayers of MIN6 cells (squares) and BPAEC (circles) depends on the initial CPA concentration, but not on the final concentration. Cell monolayers were equilibrated in isotonic PBS (open symbols) or isotonic PBS containing 5% v/v CPA (closed symbols, glycerol for MIN6, Me_2SO for BPAEC), and the apparent water permeability (neglecting CPA transport) was determined after exposure to hypertonic solution. (**A**) To examine the effect of neglecting CPA transport, the apparent L_pA/V_{w0} was predicted using Eqs. 3 and 4 with P_sA/V_{w0} from shrink-swell experiments (see Table 1) and L_pA/V_{w0} in the absence of CPA (solid lines). (**B**) The dashed line represents the rise time for solution exchange in the flow chamber.

Since experiments with monolayers in 5% v/v CPA revealed a reduction in the water permeability in the presence of CPA, we next investigated the effect of the initial CPA concentration on the water permeability. The apparent water permeability (neglecting CPA transport) is shown in Figure 6 for MIN6 monolayers over a range of glycerol concentrations and for BPAEC monolayers over a range of Me_2SO concentrations. For both cell types, the CPA concentration had a significant effect on the apparent water permeability ($p < 0.05$), resulting in a dose-dependent reduction in L_pA/V_{w0} of more than 60% for BPAEC monolayers exposed to Me_2SO concentrations higher than 2.5% v/v. Since this observed reduction in the water permeability could have been caused by neglecting CPA transport, we also predicted the effect of neglecting CPA transport on the apparent water permeability, as illustrated by the solid lines. Whereas neglecting CPA transport did not appreciably affect the apparent water permeability for MIN6 monolayers (which exhibited a low permeability to glycerol), neglecting CPA transport caused a large reduction in the apparent water permeability for BPAEC monolayers (which exhibited a relatively high permeability to Me_2SO). However, the reduction in the measured water permeability was even greater than the predictions, suggesting that observed effect of CPAs on the water permeability is real. To estimate the effect of Me_2SO on the actual water permeability (i.e., not the apparent permeability) in BPAEC monolayers, we fit the experimental data for L_pA/V_{w0} by inspection using Eqs. 3 and 4 with $P_sA/V_{w0} = 0.22$ s^{-1} (i.e., accounting for Me_2SO transport), yielding a reduction in L_pA/V_{w0} of 35%, 38% and 52% in 2.5%, 5% and 10% Me_2SO, respectively.

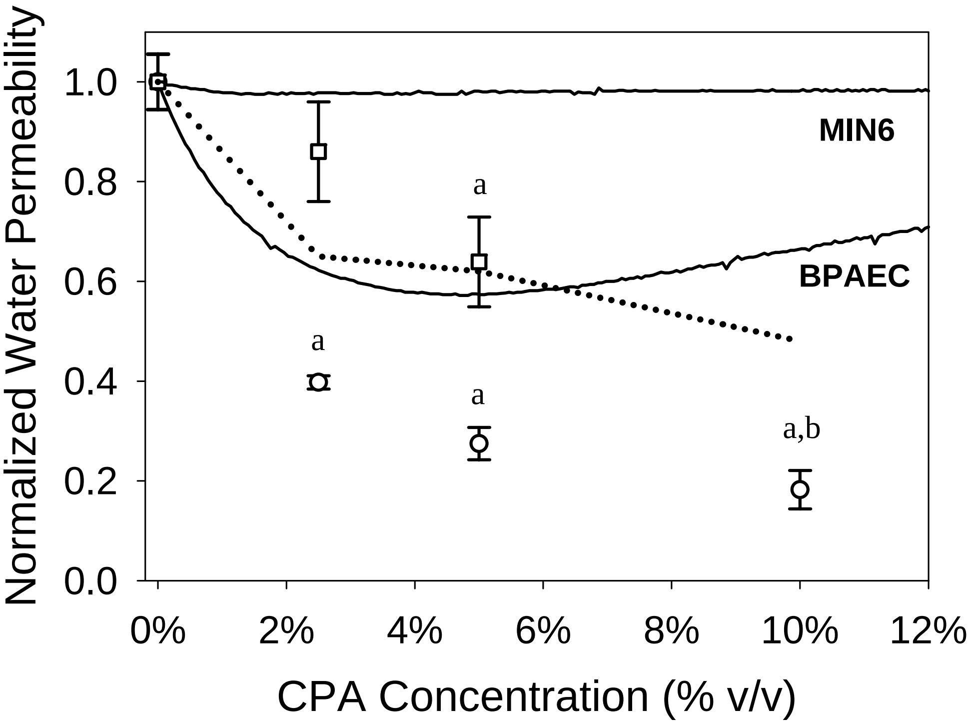

FIGURE 6.6. The water permeability at 21°C for monolayers of MIN6 cells (circles) and BPAEC (squares) is reduced in the presence of CPA (glycerol for MIN6, Me_2SO for BPAEC). The apparent L_pA/V_{w0} (neglecting CPA transport) was normalized to the L_pA/V_{w0} in the absence of CPA. The superscripts "a" and "b" indicate a significant difference from 0% and 2.5% CPA, respectively ($p < 0.05$). To examine the effect of neglecting CPA transport, the apparent L_pA/V_{w0} was predicted using Eqs. 3 and 4 with the P_sA/V_{w0} from shrink-swell experiments (see Table 1) and the L_pA/V_{w0} in the absence of CPA (solid lines). For BPAEC monolayers, we also determined L_pA/V_{w0} by fitting the experimental data to Eqs. 3 and 4 with a fixed $P_sA/V_{w0} = 0.22\ s^{-1}$ (dotted line).

Whereas the results presented in Figures 5 and 6 indicate that the apparent water permeability in cell monolayers is reduced in the presence of CPA at 21°C, the effect of CPA on the water permeability at lower temperatures is needed to predict cell dehydration during freezing. Thus, we determined the apparent water permeability for BPAEC monolayers in 5% v/v Me_2SO over a range of temperatures, as shown in Figure 7. For comparison, the best-fit line in the absence of CPA is also shown (see Figure 2), revealing that the apparent water permeability in the presence of 5% v/v Me_2SO falls well below this line. To investigate the effect of neglecting CPA transport, we predicted the apparent water permeability using P_sA/V_{w0} = 0.22 s^{-1} and E_{Ps} = 99 kJ/mol (see Table 1). As shown by the dashed line, neglecting CPA transport results in a reduction in the apparent water permeability. However, the measured reduction in the water permeability was much greater, indicating that the reduction of water permeability in the presence of CPA is not an artifact of neglecting CPA transport. The dashed line also shows that the error caused by neglecting CPA transport was large for high temperatures, but disappeared for lower temperatures, suggesting that the assumption of negligible CPA transport during freezing is valid for BPAEC monolayers in the presence of Me_2SO. Assuming that the water permeability at the reference temperature (i.e., 21°C) is reduced by 38% in the presence of 5% Me_2SO, and that all other parameters are unchanged (i.e., E_{Lp} = 49 kJ/mol, P_sA/V_{w0} = 0.22 s^{-1}, E_{Ps} = 99 kJ/mol), one obtains the predictions shown in the dotted line, which approximately matches the experimental data. Thus, the experimental data for BPAEC in the presence of 5% Me_2SO are consistent with a reduction in the water permeability of 38% and an unchanged activation energy, suggesting that cell dehydration during freezing of BPAEC monolayers in 5% Me_2SO can be predicted using L_pA/V_{w0} = 3.2 x 10^{-8} Pa^{-1} s^{-1} and E_{Lp} = 49 kJ/mol.

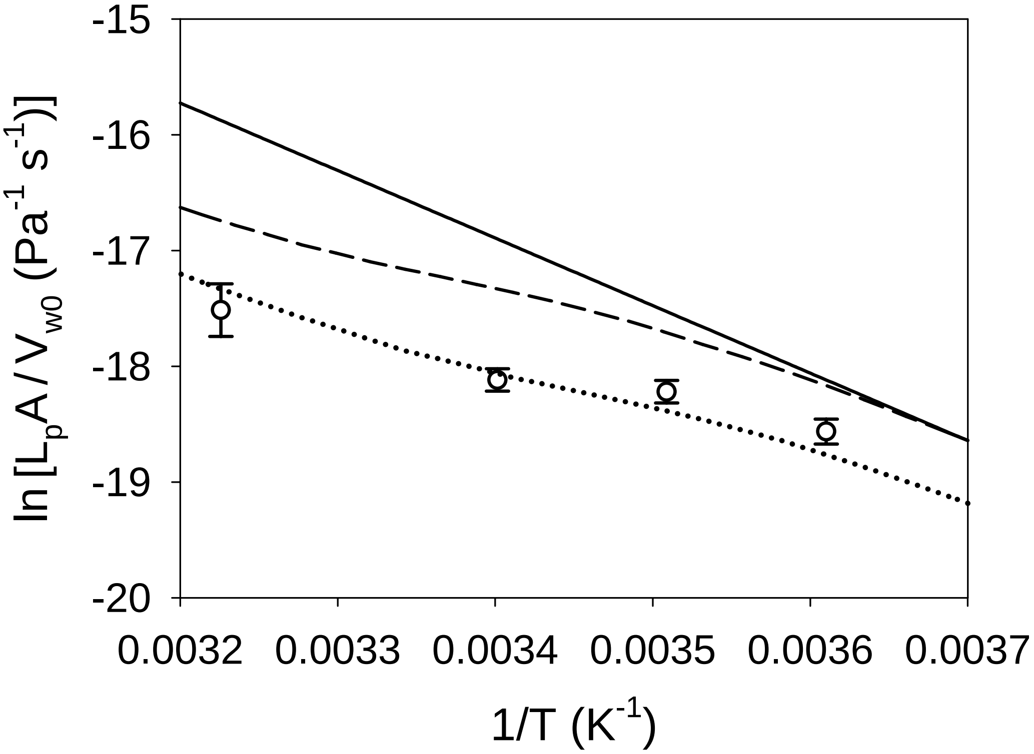

FIGURE 6.7. Temperature dependence of the apparent water permeability in the presence of 5% v/v Me_2SO for BPAEC monolayers. The solid line represents the best-fit line in the absence of CPA (see Figure 2). The dashed line shows theoretical predictions for the apparent water permeability using the activation energies (water and Me_2SO) and reference Me_2SO permeability given in Table 1, and a reference water permeability of $L_pA/V_{w0} = 5.2 \times 10^{-8}$ Pa^{-1} s^{-1} (i.e., in the absence of CPA). The dotted line represents predictions using a reference water permeability of $L_pA/V_{w0} = 3.2 \times 10^{-8}$ Pa^{-1} s^{-1}, and the activation energies and reference Me_2SO permeability given in Table 1.

Discussion

The goal of the current study was to elucidate the differences in membrane permeability properties between intact tissue and cell suspensions, and to determine the effect of CPAs on the membrane permeability in tissue. To determine the differences between tissue and cell suspensions, we compared the membrane permeability properties in cell monolayers and in suspensions created by disaggregation of the monolayers. We found that membrane water transport was faster in monolayers than in suspensions at room temperature for both BPAEC and MIN6 cells. Although there was not a significant difference in the temperature-dependence of the water permeability for suspensions and monolayers of MIN6 cells, the water permeability for BPAEC was more strongly affected by temperature in suspensions than in monolayers, as evidenced by the higher activation energy. To determine the effect of CPAs on the membrane permeability properties of tissue, we measured membrane transport in BPAEC monolayers in the presence of Me_2SO and MIN6 monolayers in the presence of glycerol. Me_2SO and glycerol caused a reduction in the water permeability at room temperature of approximately 40%, and the temperature-dependence of the water permeability was adequately describing using the activation energy determined in the absence of CPA, suggesting that CPA does not affect the activation energy.

The effect of tissue disaggregation on the membrane water permeability for BPAEC and MIN6 cells is compared against the results of previous studies in Table 2. The reference membrane water permeability parameter (L_pA/V_{w0}) was consistently lower for cell suspensions than for intact tissue. Whereas Balasubramanian et al. (2006) observed a reduction in the water permeability of more than 99%, other investigators observed reductions of 71% (Yarmush et al., 1992) and 19% (Smith, Pham et al., 1998), which is consistent with the results of the present study (reduction of 67% and 43% for BPAEC and MIN6 cells, respectively). The effect of tissue disaggregation on the activation energy for water transport is less clear since both increases (Yarmush et al., 1992) and decreases (Balasubramanian et al., 2006) have been reported in the literature.

In the present study, we observed a significant increase in the activation energy for BPAEC, whereas the effect of tissue disaggregation on the activation energy in MIN6 cells was not statistically significant.

TABLE 6.2. Literature values for water permeability of tissue and cell suspensions.

Reference	**Cell Type**	**Relative L_pA/V_{w0}[a]**	**Relative E_{Lp}[a]**
Current study	BPAEC	0.33[b]	1.4
Current study	MIN6 cells	0.57[b]	0.73
Yarmush et al., 1992	Rat hepatocytes	0.29[c,d]	3.1
Smith, Pham, et al., 1998	Rat hepatocytes	0.81[c]	1.1
Balasubramanian et al., 2006	Human fibroblasts	0.03[c]	0.53

[a] ratio of suspension parameter to tissue parameter; [b] 21ºC; [c] 0 ºC; [d] Since the value of A/V_{w0} was not given, we assumed equal values for tissue and suspension

There are several reasons that one might expect to observe differences in membrane transport kinetics between cell suspensions and cell monolayers. One factor is the changes in surface to volume ratio (A/V_{w0}) that occur upon creation of a cell suspension. Since cells in tissue are connected to the matrix and to adjacent cells, the available area for membrane transport is reduced, which should result in slower water transport in tissue than in suspension. However, we observed the opposite result (i.e., slower water transport in suspensions). A potential explanation for this result is the inactivation of water-transporting membrane channels during the enzymatic digestion process (e.g., exposure to trypsin). Inactivation of membrane channels would also explain the higher activation energy in BPAEC suspensions. Changes in membrane permeability could also be attributed to changes in the cytoskeletal organization, since the cytoskeleton is known to directly interact with the cell membrane (Sheetz, 2001). The permeability properties may also be affected by tethering of cells in tissue to the matrix and/or to adjacent cells (Bischof, 2000; Yarmush et al., 1992). Further studies are necessary to elucidate the causes for the differences in permeability properties between suspensions and tissue.

A potential limitation of the current study is that we used two different techniques to measure the membrane permeability in cell suspensions and monolayers (electronic cell sizing and fluorescence quenching, respectively). Because of the physical differences between suspended cells and monolayers, it is difficult to measure the membrane permeability using the same technique. For example, the fluorescence quenching technique that we used for monolayers cannot be used with cell suspensions since suspended cells cannot withstand the high flow rates necessary for rapid solution exchange (unpublished observations). Although we measured the permeability properties using different methods, both techniques were carefully designed to maximize the accuracy of the permeability estimates (Chapters 2-5). Thus, it is unlikely that the observed differences in permeability were caused by differences in the experimental techniques for measuring membrane water transport.

Whereas previous investigations reported a much more dramatic effect of CPA on the water permeability in tissue than cell suspensions (Bischof, 2000, Smith, Pham et al., 1998; Smith, Schulte et al., 1998), we observed a moderate effect of CPA on the membrane water permeability in cell monolayers, which was consistent with previous observations for cell suspensions. In cell suspensions, the water permeability in the presence of CPA has been reported to increase (McGrath et al., 1992; Ebertz and McGann, 2004), decrease (Adams et al., 2003; Hempling and White, 1984; McCaa et al., 1991; Rule et al., 1980; Smith, Schulte et al., 1998) or stay the same (Benson et al., 1998; Ebertz and McGann, 2004; Liu et al., 1997), but the general consensus is that CPAs reduce the water permeability by approximately a factor of two (Karlsson et al., 1993; Mazur, 1990). We observed a reduction in the water transport kinetics by approximately 30% and 38% for MIN6 monolayers in 5% v/v glycerol and BPAEC monolayers in 5% v/v Me_2SO, respectively, which is consistent with the observations for cell suspensions. There is no consensus in the literature regarding the effect of CPAs on the activation energy for water transport. Whereas several authors have reported similar values of E_{Lp} in the presence and absence of CPA (Benson et al., 1998; Ebertz and McGann, 2004; Liu et al., 1997; Rule et al., 1980), others have reported either increases (McCaa et al., 1991) or decreases (Smith, Schulte et al., 1998) in E_{Lp} in the presence of CPA. We determined similar E_{Lp} for BPAEC monolayers after exposure to hypertonic solutions containing sucrose (i.e., no CPA) and hypertonic solutions containing Me_2SO (shrink-swell experiments), suggesting that E_{Lp} is not affected by CPA. Furthermore, we showed that the water permeability over a range of temperatures could be described using the E_{Lp} determined in the absence of CPA and a reduced water permeability to account for the effect of CPA. Together these data suggest that the water permeability at room temperature is reduced in the presence of CPA by approximately a factor of 2, and that the activation energy for water transport is unaffected by CPA.

In summary, we have investigated the differences between the membrane permeability properties of cell monolayers and cell suspensions, and we have characterized the effect of CPAs on the membrane permeability in monolayers. We observed slower membrane water transport kinetics in cell suspensions than in monolayers for two cell types: BPAEC and MIN6 cells. Although there was not a significant difference in the activation energy for water transport in suspensions and monolayers of MIN6 cells, BPAEC suspensions exhibited a higher activation energy than monolayers, indicating that the differences between BPAEC suspensions and monolayers will become more pronounced at lower temperatures (i.e., during cryopreservation), and underscoring the importance of *in situ* measurement of the permeability parameters in tissue. We showed that the water permeability decreased in the presence of CPAs by approximately 30% for MIN6 monolayers exposed to 5% glycerol and 45% for BPAEC monolayers exposed to 5% Me_2SO, and that the activation energy for membrane water transport was not affected by CPA. The approach presented here will enable determination of the tissue-specific permeability parameters necessary for predicting membrane transport during cryopreservation, which may lead to the development of improved cryopreservation procedures for tissue.

CHAPTER 7

EFFECT OF INTERCELLULAR JUNCTION PROTEIN EXPRESSION ON INTRACELLULAR ICE FORMATION

Introduction

Long-term storage of tissue by cryopreservation is necessary for the efficient mass production of tissue engineered products (Karlsson and Toner, 1996), and for reducing the urgency and cost of transplantation procedures, especially when tissue from multiple donors is required (Rajotte, 1999). However, attempts at tissue cryopreservation have met with limited success. Whereas strategies exist for designing cryopreservation procedures for cell suspensions based on avoidance of cell damage mechanisms (e.g., Karlsson et al., 1996; Mazur et al., 1972), the increased complexity of tissue (e.g., cell-cell connections, cell-substrate connections) has made tissue cryopreservation more difficult (Karlsson and Toner, 1996). This is evidenced by the common observation that intact tissue responds differently to cryopreservation than suspended cells, resulting in decreased post-thaw viability and/or function in many cases (Armitage and Juss, 1996; Liu and McGrath, 2006; McGann et al., 1972; Oegema et al., 2000; Yang et al., 1996; Zieger et al., 1996).

One reason for the observed differences between cryopreservation of cells and tissue may be related to differences in the likelihood of intracellular ice formation (IIF[1]), a phenomenon that has been correlated with cell death for many cell types (Toner et al.,

---

[1] Abbreviations used in this study: IIF = intracellular ice formation; IIP = intercellular ice propagation; PIP = paracellular ice penetration; WT = wild-type; AS = WT transfected with antisense for connexin-36; AS+Cx = AS transfected with connexin-36; AS+Ecad = AS transfected with E-cadherin

1993). The differences in IIF probability can be attributed (at least in part) to cell-substrate interactions and cell-cell interactions, since the IIF probability has been shown to be lower for suspended cells than single adherent cells, and lower for single adherent cells than for cell monolayers (Acker and McGann, 2002; Irimia and Karlsson, 2002).

In particular, cell-cell interactions have been shown to increase the probability of IIF, a phenomenon that has been attributed to intercellular ice propagation (IIP). The early evidence for IIP was derived from observations of non-random spatial patterns of IIF, suggesting that internal ice could spread to neighboring cells (Acker et al., 1999; Acker et al., 2001; Berger and Uhrik, 1996; Brown, 1980; Stuckey and Curtis, 1938). Irimia and Karlsson (2002) used micropatterned cell pairs to prove the existence of a propagative IIF mechanism, and developed a mathematical model to describe this phenomenon, which was validated in linear cell arrays (Irimia and Karlsson, 2005). Although there is strong evidence that cell-cell interactions increase the likelihood of IIF by enabling IIP, the mechanism of IIP is unclear. IIP has been suggested to result from ice growth through gap junctions pores, because of the observation of a more random spatial pattern of IIF after treatment with gap junction inhibitors (Berger and Uhrik, 1996) or after culture in low Ca^{2+} media, which has been shown to reduce gap junction expression (Acker et al., 2001). Irimia and Karlsson (2002) showed that treatment with the gap junction blocker 18β-glycyrrhetinic acid reduced the rate of IIP, also implicating gap junctions in IIP. However, ice growth through gap junctions does not entirely explain the IIP phenomenon, since Irimia and Karlsson (2002) still observed IIP after treatment with the gap junction blocker (albeit at a reduced rate), and others have observed non-random spatial patterns of IIF that are indicative of IIP in cell types that are known to lack gap junctions (Acker et al., 2001). Whatever the mechanism of IIP, the architecture of the cell-cell interface is likely to play an important role.

In addition to the enhanced likelihood of IIF due to IIP, attached cells are subject to an additional mechanism of IIF associated with growth of extracellular ice dendrites into the space between the basal cell membrane and the substrate (Stott, 2006). These paracellular ice dendrites frequently colocalized with initiation of IIF in micropatterned endothelial cells, suggesting that paracellular ice penetration (PIP) leads to IIF, possibly as a result of mechanical interaction between the paracellular ice dendrite and the cell membrane. The incidence of PIP was shown to correlate with the number and size of gaps in focal adhesions at the cell periphery, implicating the physical architecture of the cell-substrate attachment in the IIF process. Although it is feasible for paracellular ice to penetrate the space between adjoining cells, the effect of cell-cell interaction on PIP has not been investigated.

The cell-cell interface can contain several types of intercellular junctions that may affect both PIP and IIP. Gap junctions are comprised of connexin proteins that from hydrophilic pores with a diameter of approximately 1.5 nm connecting the cytoplasm of adjoining cells (Sosinsky and Nicholson, 2005). Not only do gap junctions form pores that may enable IIP, but they also associate with proteins involved in adherens junctions and tight junctions, which physically connect adjacent cell membranes and create connections with the cell cytoskeleton (Herve et al., 2004). Tight junctions form an intimate connection between apposing membranes, and contain several proteins, most notably occludin and claudins, whereas adherens junctions form a looser connection between apposing membranes and are comprised of E-cadherins and nectins (Zheng et al., 2006). These physical connections between cells may affect IIP by modulating surface catalyzed nucleation of intracellular ice (Acker and McGann, 1998; Toner et al., 1990; Tsuruta et al., 1998) or by transmitting the mechanical forces that may result from IIF between neighboring cells. In addition, physical connections between cells may affect PIP by modulating interactions between the extracellular ice and the cell-cell interface.

Recently, Calabrese et al. (2003, 2004) used genetic engineering methods to alter the expression of intercellular junction proteins in MIN6 cells (Miyazaki et al., 1990), a mouse pancreatic β-cell line that is a potential cell source for tissue-engineering approaches to treat diabetes (Hayashi et al., 1998). These genetically modified MIN6 cells provide an attractive experimental system for studying the effect of the architecture of the cell-cell interface on IIF. Wild-type MIN6 cells express connexin-36 (gap junctions), E-cadherin (adherens junctions) and occludin (tight junctions), but cells transfected with an antisense construct for connexin 36 exhibited markedly reduced expression of all of these proteins (Calabrese et al., 2003, 2004). These antisense-transfected cells were further modified by transfection with either E-cadherin or connexin-36, restoring expression of these proteins to normal levels (Calabrese et al., 2004). Thus, MIN6 cells are available with altered expression of proteins involved in gap junctions, tight junctions and adherens junctions, all of which may be implicated in IIF.

In the present study, we investigated the effect of intercellular junctions on IIF, with an emphasis on IIP and PIP at the cell-cell interface. We used high-speed video cryomicroscopy to study IIF and PIP in adherent cell pairs comprising genetically modified MIN6 cells expressing different levels of intercellular junction proteins. To analyze the resulting data, we modified the IIF model of Irimia and Karlsson (2002) to account for PIP at the cell-cell interface, allowing us to determine the effect of intercellular junctions on the rates of PIP, independent IIF, and IIP.

Theoretical Background

Since PIP at the cell-cell interface was frequently observed prior to IIF in our cryomicroscopy experiments with MIN6 cell pairs, we modified the mathematical model of Irimia and Karlsson (2002) to account for this phenomenon. As illustrated in Figure 1, the cell pair was assumed to occupy one of four states: the unfrozen state without PIP (state A), the unfrozen state with PIP (state B), the singlet state (i.e., one of the two cells contains intracellular ice) and the doublet state (i.e., both cells contain intracellular ice). Whereas the model of Irimia and Karlsson (2002) accounted for all possible IIF states and state transitions, incorporation of PIP into the model introduces the possibility for several additional states and state transitions. To decrease the complexity of the resulting model, we have assumed that cell pairs in state A can only undergo PIP to form state B, and we have neglected to possibility of IIF in the absence of PIP.

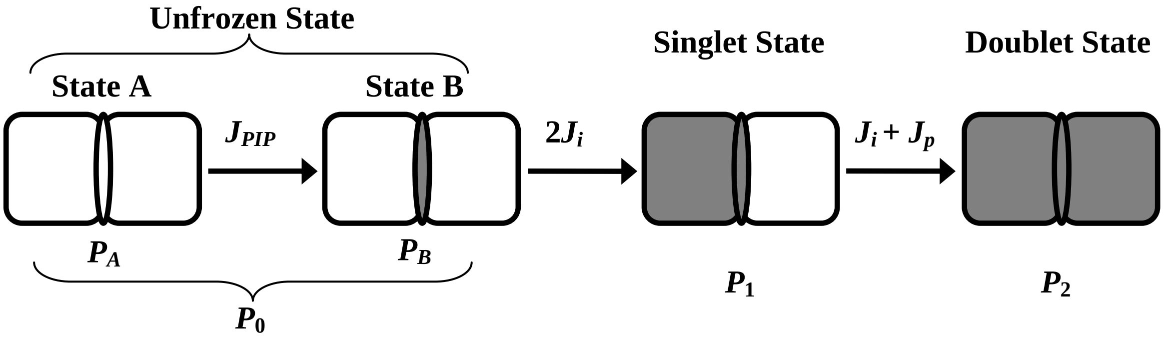

FIGURE 7.1. Schematic illustrating the states of PIP and IIF for a cell pair. Each cell is depicted as a rectangle, and the paracellular space at the cell-cell interface is shown as an ellipse. Internal ice is indicated by the dark gray fill. Transitions between states were modeling as first-order rate processes, with rate coefficients as shown. The probabilities of state A, state B, the singlet state and the doublet state are given by P_A, P_B, P_1 and P_2, respectively. The probability of the unfrozen state, P_0, is equal to $P_A + P_B$.

Transitions between the states were modeled as first-order rate processes, with time-dependent rate coefficients for PIP (J_{PIP}), independent IIF following PIP (J_i) and IIP (J_p). Independent IIF was only considered to be active following PIP, and includes any IIF mechanism that does not depend on the presence of internal ice in an adjoining cell. Intercellular ice propagation, in contrast, describes any mechanism of IIF that *is* dependent on the presence of internal ice in a neighboring cell. The rate of consumption of cell pairs in state A is given as:

$$\frac{dN_A}{dt} = -J_{PIP} N_A \qquad [1]$$

where N_A is the number of cell pairs in state A. Consumption of cell pairs in state B is proportional to twice the independent IIF rate (since there are two unfrozen cells), yielding the following expression for the number of cell pairs in state B (N_B):

$$\frac{dN_B}{dt} = J_{PIP} N_A - 2J_i N_B \qquad [2]$$

The rate of change of the number of cell pairs in the singlet state (N_1) depends on both the propagation rate and the independent IIF rate, yielding the following expression:

$$\frac{dN_1}{dt} = 2J_i N_B - \left(J_i + J_p\right)N_1 \qquad [3]$$

The state of an ensemble of N cell pairs can be more easily described using state probabilities, rather than absolute numbers (i.e., N_A, N_B, etc.). An ensemble of cell pairs is fully described using the probability of state A (P_A), the probability of state B (P_B) and the probability of the singlet state (P_1), which are defined as:

$$P_A \equiv \frac{N_A}{N} \qquad [4]$$

$$P_B \equiv \frac{N_B}{N} \qquad [5]$$

$$P_1 \equiv \frac{N_1}{N} \qquad [6]$$

The probability of the unfrozen state (P_0) and the probability of the doublet state (P_2) are not independent variables since they can be determined from P_A, P_B and P_1:

$$P_0 \equiv \frac{N_0}{N} = P_A + P_B \qquad [7]$$

$$P_2 \equiv \frac{N_2}{N} = 1 - P_A - P_B - P_1 \qquad [8]$$

To facilitate solution of Eqs. 1-3, we define a non-dimensional time based on the rate of PIP:

$$\tau \equiv \int_0^t J_{PIP}\, dt \qquad [9]$$

Combining Eqs. 1-6 and Eq. 9, the state of an ensemble of cell pairs can be described using the following equation:

$$\frac{d}{d\tau}\begin{bmatrix} P_A \\ P_B \\ P_1 \end{bmatrix} \equiv \begin{bmatrix} -1 & 0 & 0 \\ 1 & -2\bar{J}_i & 0 \\ 0 & 2\bar{J}_i & -\left(\bar{J}_i + \bar{J}_p\right) \end{bmatrix} \bullet \begin{bmatrix} P_A \\ P_B \\ P_1 \end{bmatrix} \qquad [10]$$

where the coefficients $\bar{J}_i$ and $\bar{J}_p$ are defined as:

$$\bar{J}_i \equiv \frac{J_i}{J_{PIP}} \qquad [11]$$

$$\bar{J}_p \equiv \frac{J_p}{J_{PIP}} \qquad [12]$$

Eq. 10 can be easily solved to obtain P_A as a function of τ:

$$P_A = e^{-\tau} \qquad [13]$$

However, an analytical solution of Eq. 10 for P_B and P_1 does not exist, since the coefficients $\bar{J}_i$ and $\bar{J}_p$ are, in the most general sense, functions of time. Nonetheless, it is illustrative to examine the solution to Eq. 10 for the special case of constant coefficients. Solving for P_B, one obtains

$$P_B = \left(\frac{1}{2\bar{J}_i - 1}\right)\left(e^{-\tau} - e^{-2\bar{J}_i\tau}\right) \qquad [14]$$

The maximum value of P_B can be determined from Eq. 14, yielding

$$P_{B,\max} = \left(\frac{1}{2\bar{J}_i - 1}\right)\left[\left(2\bar{J}_i\right)^{1/\left(1-2\bar{J}_i\right)} - \left(2\bar{J}_i\right)^{2\bar{J}_i/\left(1-2\bar{J}_i\right)}\right] \qquad [15]$$

Similarly, Eq. 10 can be solved for P_1, yielding

$$P_1 = \left(\frac{2\bar{J}_i}{2\bar{J}_i - 1}\right)\left[\left(\frac{1}{\bar{J}_i + \bar{J}_p - 1}\right)e^{-\tau} + \left(\frac{1}{\bar{J}_i - \bar{J}_p}\right)e^{-2\bar{J}_i\tau} + \left(\frac{2\bar{J}_i - 1}{\bar{J}_p^{\,2} - \bar{J}_p - \bar{J}_i^{\,2} + \bar{J}_i}\right)e^{-\left(\bar{J}_i + \bar{J}_p\right)\tau}\right] \qquad [16]$$

Using Eq. 16, it can be shown that P_1 reaches a maximum value ($P_{1,max}$) when τ is equal to the root of the following of equation:

$$\left(\frac{1}{1-\bar{J}_i-\bar{J}_p}\right)e^{-\tau}+\left(\frac{2\bar{J}_i}{\bar{J}_p-\bar{J}_i}\right)e^{-2\bar{J}_i\tau}+\left(\frac{\left(\bar{J}_i+\bar{J}_p\right)\left(1-2\bar{J}_i\right)}{\bar{J}_p^{\,2}-\bar{J}_p-\bar{J}_i^{\,2}+\bar{J}_i}\right)e^{-\left(\bar{J}_i+\bar{J}_p\right)\tau} \qquad [17]$$

After numerically solving for the root of Eq. 17, Eq. 16 can be used to determine $P_{1,max}$.

It is worth noting that as $\bar{J}_i \rightarrow 0$, the mathematical development presented herein reduces to the simpler case reported by Irimia and Karlsson (2002), which did not consider PIP. In the case of $\bar{J}_i \rightarrow 0$, the formation of state B by PIP is much faster than consumption of state B by independent IIF, such that consideration of state A in the mathematical analysis is unnecessary. In other words, one may assume that the entire ensemble of cell pairs begins in state B, rendering the model schematic presented herein (Figure 1) equivalent to the schematic presented by Irimia and Karlsson (2002, Figure 1). Thus, the predictions for $P_{1,max}$ using Eq. 16 and 17 as $\bar{J}_i \rightarrow 0$ should approach the solution of Irimia and Karlsson (2002, Eq. 20):

$$P_{1,\max}=\left(\frac{1+\alpha}{2}\right)^{(1+\alpha)/(1-\alpha)} \qquad [18]$$

where α is the non-dimensional propagation rate, defined as

$$\alpha \equiv \frac{J_p}{J_i} \qquad [19]$$

Materials and Methods

Cell Lines

Experiments were performed with wild-type (WT) mouse insulinoma cells (MIN6, Miyazaki et al., 1990), and genetically modified MIN6 cells with altered expression of the intercellular junction proteins connexin-36, E-cadherin and occludin (generously provided by Paolo Meda, M.D.). WT cells were stably transfected with antisense mRNA for connexin-36 (Calabrese et al., 2003), resulting in reduced expression of connexin-36, E-cadherin and occludin (AS cells, Calabrese et al., 2004). These AS cells were rescued by restoring expression of either connexin-36 (AS+Cx) or E-cadherin (AS+Ecad) to normal levels (Calabrese et al., 2004).

Cell Culture

MIN6 cells were cultured in tissue culture flasks containing culture media (DMEM with high glucose supplemented with 15% v/v heat inactivated FBS and 0.07 mM β-mercaptoethanol) at 37ºC in a 5% CO_2 environment. Media was changed every 3 days and passages were performed weekly. For cryomicroscopy experiments, cells were seeded onto 12 mm diameter glass coverslips and cultured for 48 hrs.

Sample Preparation

To prepare the MIN6 cultures for cryomicroscopy experiments, samples were incubated in culture media containing the membrane permeable nucleic acid stain SYTO13 (2 μM) and the membrane impermeable stain ethidium homodimer (10 μM) at 37ºC for 10 to 60 min. Immediately prior to freezing, glass coverslips were rinsed with isotonic phosphate buffered saline (with Ca^{2+} and Mg^{2+}), dried by dragging the bottom of the coverslip across a Kimwipe, and inverted onto a 16 mm coverslip on the temperature-controlled microscope stage.

Cryomicroscopy

Samples were observed during cooling using a high-speed video cryomicroscopy system consisting of a temperature-controlled microscope stage (FDCS 196, Linkam

Scientific Instruments, Tadworth, Surrey, UK), an upright microscope (Eclipse ME600, Nikon) and a high-speed digital camera (FastCam-X 512PCI, Photron, Tokyo, Japan or Phantom v4.3 Vision Research, New Jersey, USA). Temperature was calibrated by measuring the melting point of purified water. Samples were visualized under Khöler illumination using a 50x objective with the microscope halogen lamp set to maximum light output. Images were acquired at 3000-4000 Hz with an exposure time of 143 μs, and video acquisition was stopped using the camera trigger after observing IIF. The depression of the camera trigger was detected using the pressure sensor of the temperature controller (TMS 94, Linkam), allowing synchronization of the temperature measurements with the video frames. All samples were subjected to the following freezing protocol: cool to -2ºC at 50ºC/min, hold 1 min, heat to -1.5ºC at 10ºC/min, hold ~90 s, cool to -60ºC at 130ºC/min. Ice was seeded during the -2ºC hold by moving the edge of the sample over a cold seeding block. Before initiating rapid cooling at 130ºC/min a field of view was randomly selected that contained a single cell pair (determined by visualization of two distinct nuclei by SYTO13 fluorescence) with intact cell membranes (determined by lack of ethidium homodimer fluorescence). IIF was identified as a directional wave with a time scale of ~3 ms (Stott, 2006). The temperature and location of IIF initiation were determined from frame by frame playback of the video. In some cases extracellular ice obscured the location of IIF initiation, preventing unambiguous classification of the IIF location into a category (i.e., cell-cell interface, perimeter, or interior). These cell pairs were excluded from analysis of the location of IIF initiation. PIP was identified as a darkening at the cell-cell interface with a time scale of approximately 50 ms, and the frame for initiation of PIP was determined by playback at ~200 frames per second. The persistence time of the singlet state was taken as the time between arrival of intracellular ice at the cell-cell interface in the first cell to freeze, and IIF in the second cell to freeze.

Analysis of State Transitions

For analysis of the rates of the state transitions depicted in Figure 1, the following strategy was used. For a general state transition between an initial state and a final state with a first-order rate coefficient *J*, the rate at which the final state is formed is proportional to the number of cell pairs in the initial state:

$$\frac{dN_f}{dt} = JN_i \tag{20}$$

Solving Eq. 20 for the time integral of the rate *J*, which is indicative of the likelihood that a given cell pair in the initial state will reach the final state in a time *t*, one obtains

$$\int_0^t Jdt = \int_0^{N_f(t)} \frac{dN_f}{N_i} \tag{21}$$

where N_i is the number in the initial state and N_f is the number that have passed from the initial state to the final state (i.e., the number of state transitions that have occurred). Since dN_f and N_i can only assume integer values, the integral in Eq. 21 can be replaced a trapezoidal integral approximation comprising a summation over the transitions between the initial and final states:

$$\int_0^t Jdt = \frac{1}{2}\sum_{k=1}^{N_f(t)}\left(\frac{1}{N_i\left(t_k^-\right)} + \frac{1}{N_i\left(t_k^+\right)}\right) \tag{22}$$

In Eq. 22, $N_i\left(t_k^-\right)$ is the number in the initial state before the k$^{\text{th}}$ state transition and $N_i\left(t_k^+\right)$ is the number in the initial state after the k$^{\text{th}}$ state transition. The time integrals associated with the state transitions shown in Figure 1 were calculated from experimental data using Eq. 22. For a small number of state transitions, $N_i\left(t_k^+\right)$ was zero, the reciprocal of which is undefined. In these instances, the left Riemann sum integral approximation was used:

$$\int_{t_k^-}^{t_k^+} J dt = \frac{1}{N_i\left(t_k^-\right)} \qquad [23]$$

Statistical Analysis

Unless otherwise noted, data are reported as averages and standard error of the mean. For pairwise comparison of the slopes of best-fit lines, two-tailed t-tests were used. For normally distributed data and equal variances, the data were analyzed by ANOVA, followed by Tukey’s tests. When either of these criteria was not met (i.e., normal distribution, equal variances), the data were analyzed using a nonparametric ANOVA (Kruskal-Wallis), followed by Dunn’s method for pairwise comparisons. For classification of events into categories (i.e., IIF location, incidence of PIP), the standard deviation was estimated as square root of the number of observations in each category, as expected for a homogeneous Poisson process. These frequency data were analyzed using χ^2 tests. Differences were considered to be significant at a confidence level of 95% ($p < 0.05$).

Results

We first examined the probability of IIF in MIN6 cell pairs during cooling at 130°C/min. As shown in Figure 2A, the cumulative IIF probability was similar for AS, AS+Ecad and AS+Cx cells (mean IIF temperature = 14.6±0.3°C, 13.2±0.4°C and -13.0±0.4°C, respectively), but WT cells underwent IIF at a significantly lower temperature ($p<0.05$, -23.2±0.4°C), indicating that intercellular junction protein expression affects IIF. Whereas the cumulative IIF probability is dependent on the rate of IIP, which is likely to be influenced intercellular junctions, the probability of the unfrozen state is not dependent on IIP. As shown in Figure 2B, intercellular junction protein expression affected the probability of the unfrozen state, yielding a significantly lower mean temperature for disappearance of the unfrozen state in WT cells (-22.5±0.6°C, $p < 0.05$) than in the genetically modified clones (14.0±0.4°C, 12.1±0.5°C and -12.3±0.5°C for AS, AS+Ecad and AS+Cx, respectively), indicating that the observed differences in the overall IIF probability cannot be attributed to differences in IIP kinetics.

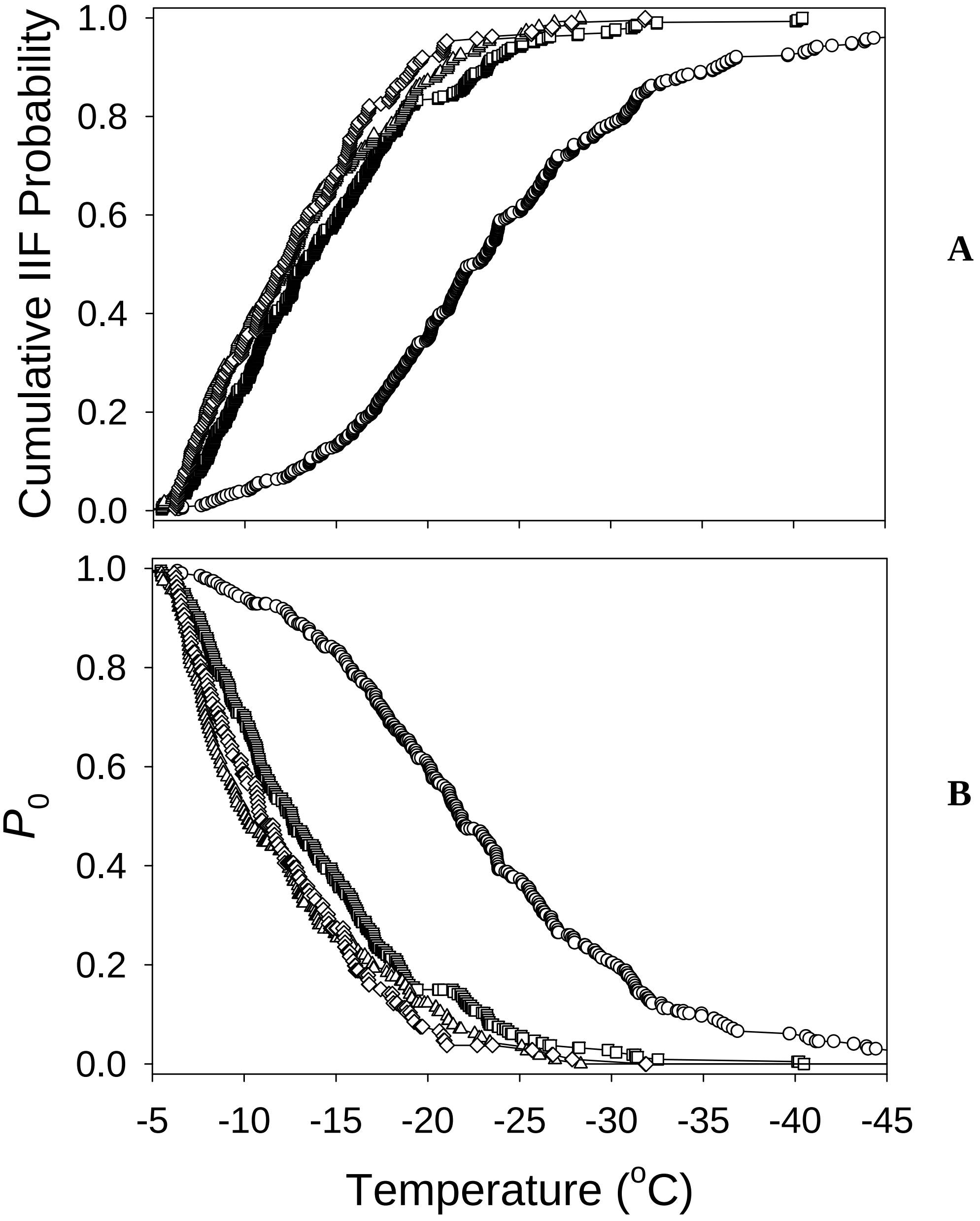

FIGURE 7.2. Cumulative IIF probability (A) and probability of the unfrozen state (B) during cooling to -60°C at 130°C/min for WT (circles), AS (squares), AS+Ecad (triangles) or AS+Cx cells (diamonds). Data represents 196, 213, 114, and 106 cell pairs for WT, AS, AS+Ecad, and AS+Cx cells, respectively.

To explore the reasons for the observed differences in IIF kinetics, we investigated PIP at the interface between adjoining cells, which was observed as a rapid (~50 ms) darkening, presumably due to scattering of transilluminated light upon formation of ice. The PIP event frequently preceded and colocalized with initiation of IIF. Figure 3 shows an example of PIP and IIF in a cell pair comprising AS cells. Although not depicted in Figure 3, multiple darkening events were observed at the cell-cell interface for this cell pair between -15.7°C and -16°C. Shortly afterward, IIF initiated at the site of PIP in the cell at the right, and at -16.05°C the semicircular ice crystal growth front can be observed. This was followed by initiation of IIF at the site of PIP in the cell at the left and subsequent intracellular ice growth, a snapshot of which is shown at -16.28°C.

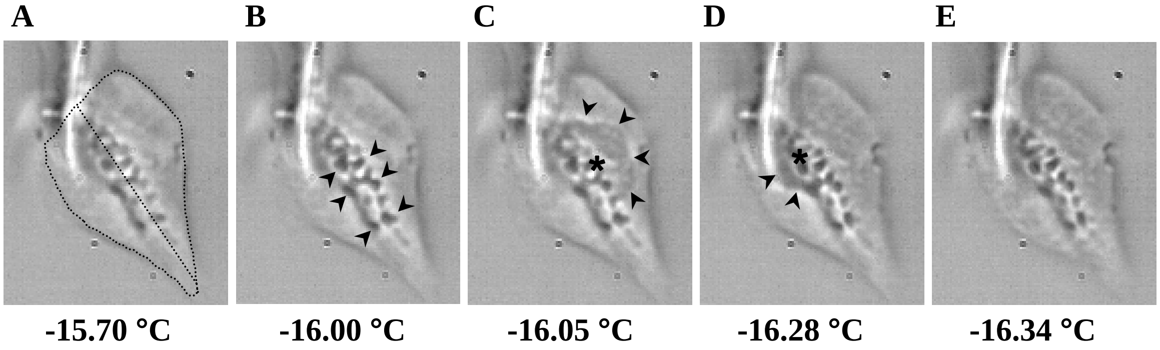

FIGURE 7.3. PIP and IIF in MIN6-AS pairs during cooling at 130°C/min. (A) Cell pair prior to IIF. The dotted line outlines the cells. (B) PIP at the cell-cell interface. (C, D) IIF initiation, indicated by the asterisks, at the site of PIP. (E) Cell pair after IIF.

To characterize the importance of PIP in MIN6 cell pairs, cryomicroscopy videos for approximately 100 cell pairs for each of WT, AS, AS+Ecad and AS+Cx cells were examined for the occurrence of PIP. As shown in Figure 4A, PIP occurred in 47% of WT cell pairs, whereas greater than 78% of cell pairs comprising AS, AS+Ecad and AS+Cx cells exhibited PIP. These differences in the incidence of PIP were statistically significant ($p < 0.001$), indicating that cell phenotype (i.e., intercellular junction protein expression) affects the frequency of PIP. In particular, AS, AS+Ecad and AS+Cx cells, which lack expression of the tight junction protein occludin, exhibited a significantly higher incidence of PIP than the WT cells ($p < 0.001$), which express normal levels of occludin.

In addition to the incidence of PIP, we determined the temperature at initiation of PIP. As shown in Figure 4B, the mean PIP temperature varied between -11.4°C for WT cells and -7.9°C for AS+Ecad cells, resulting in a statistically significant effect of intercellular junction protein expression on the mean PIP temperature ($p < 0.001$). Post-hoc tests revealed a significantly lower mean PIP temperature in WT cells (which express the tight junction protein occludin) than in AS, AS+Ecad or AS+Cx cells ($p < 0.05$), all of which lack occludin expression. The differences in PIP temperature between AS, AS+Ecad and AS+Cx cells was not statistically significant ($p > 0.1$).

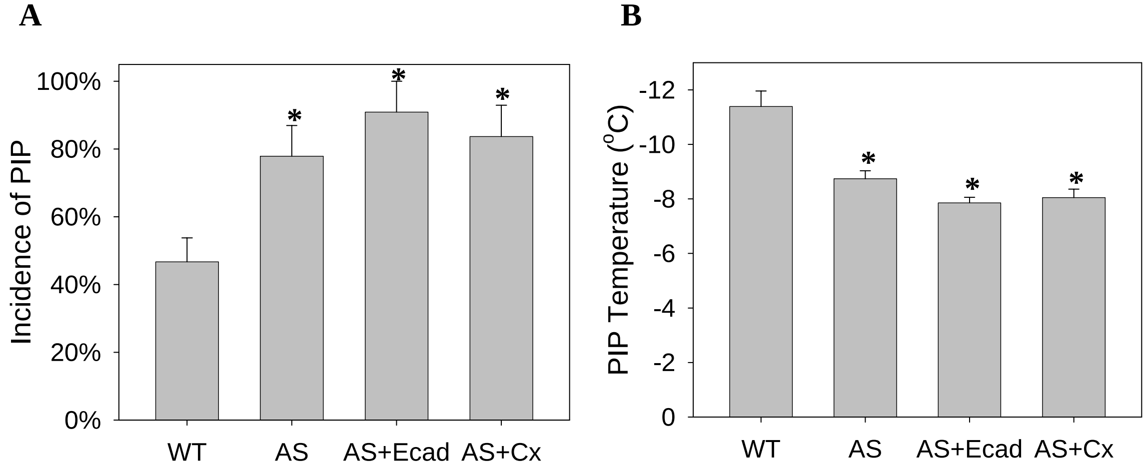

FIGURE 7.4. Incidence and temperature of PIP in cell pairs cooled to -60°C at 130°C/min. PIP observations were made in 92, 95, 110 and 98 cell pairs for WT, AS, AS+Ecad and AS+Cx cells, respectively. * indicates a statistically significant difference from the WT cells ($p < 0.001$).

We next examined the rate of PIP by analyzing the transition between state A and state B using Eq. 22 to determine the time integral of the PIP rate, which is plotted in Figure 5. A linear relationship between the time integral of J_{PIP} and temperature was observed between -6°C and -12°C, indicating a constant value of J_{PIP} in this temperature range. A linear fit to the data yielded $J_{PIP} = 0.11 \pm 0.004\ s^{-1}$, $0.47 \pm 0.006\ s^{-1}$, $0.85 \pm 0.008\ s^{-1}$ and $0.61 \pm 0.007\ s^{-1}$ for WT, AS, AS+Ecad and AS+Cx cells, respectively. Pairwise comparisons for J_{PIP} yielded statistically significant differences in all cases ($p < 0.001$), indicating a significant effect of intercellular junction protein expression on the rate of PIP. These data for the PIP rate (WT <AS < AS+Cx < AS+Ecad) are consistent with both the incidence and temperature of PIP.

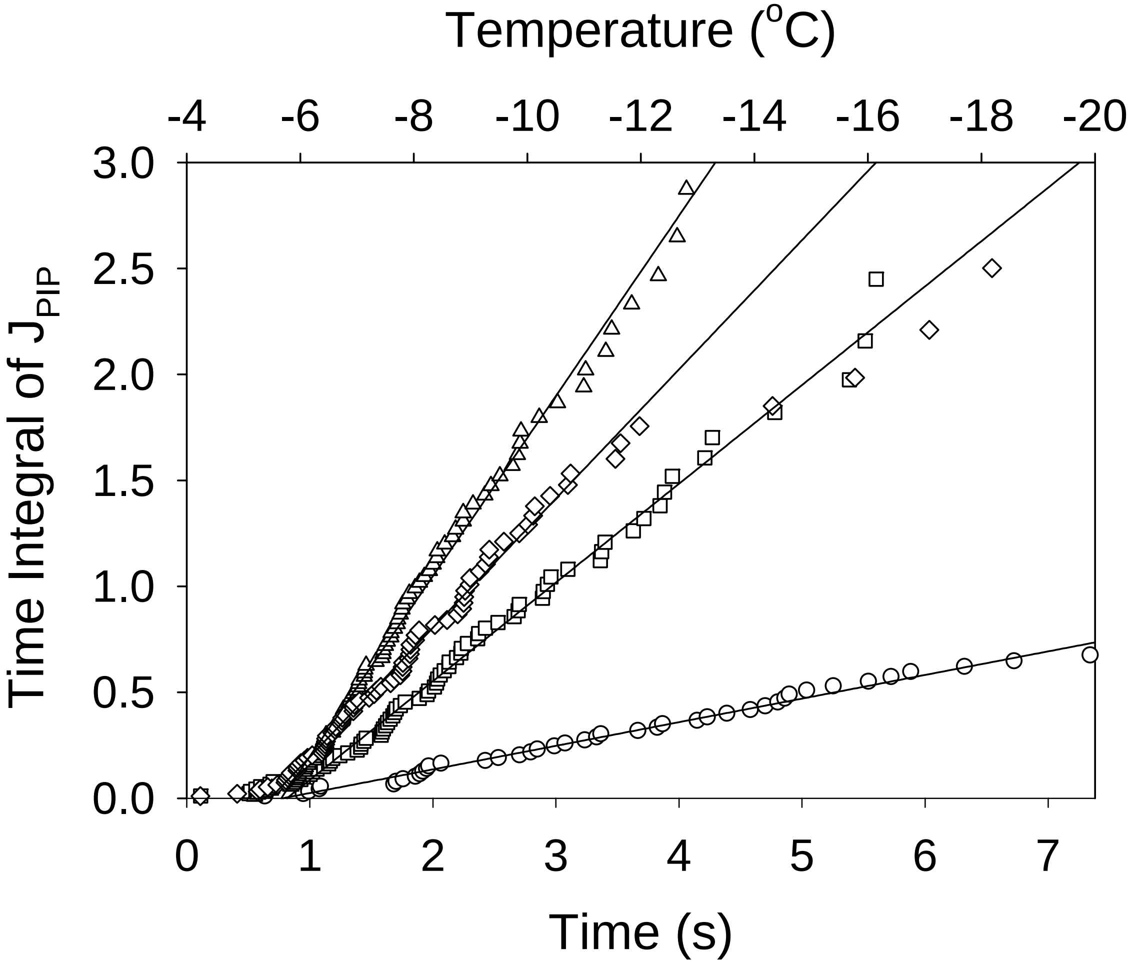

FIGURE 7.5. Time integral of the PIP rate (J_{PIP}) determined by examining the transition between state A and state B during cooling to -60°C at 130°C/min for cell pairs comprising WT (circles), AS (squares), AS+Ecad (triangles) or AS+Cx cells (diamonds). To approximate J_{PIP}, which is equal to the slope of the above plot, the data were fit to a linear model in the temperature range -6°C to -12°C (lines).

After examining the effect of intercellular junction protein expression on PIP, we next sought to determine the relationship between PIP and IIF. Figure 6 illustrates the spatial correlation between PIP and IIF. The location of IIF initiation was classified into three groups for the transition between state B and the singlet state: cell perimeter, cell-cell interface and cell interior. As shown in Figure 6, the proportion of IIF events that initiated at the interface between adjoining cells (i.e., the site of PIP) was significantly higher than the cell perimeter or the cell interior for all cell phenotypes ($p < 0.001$). However, the differences in IIF location between cell phenotypes was not statistically significant ($p = 0.09$).

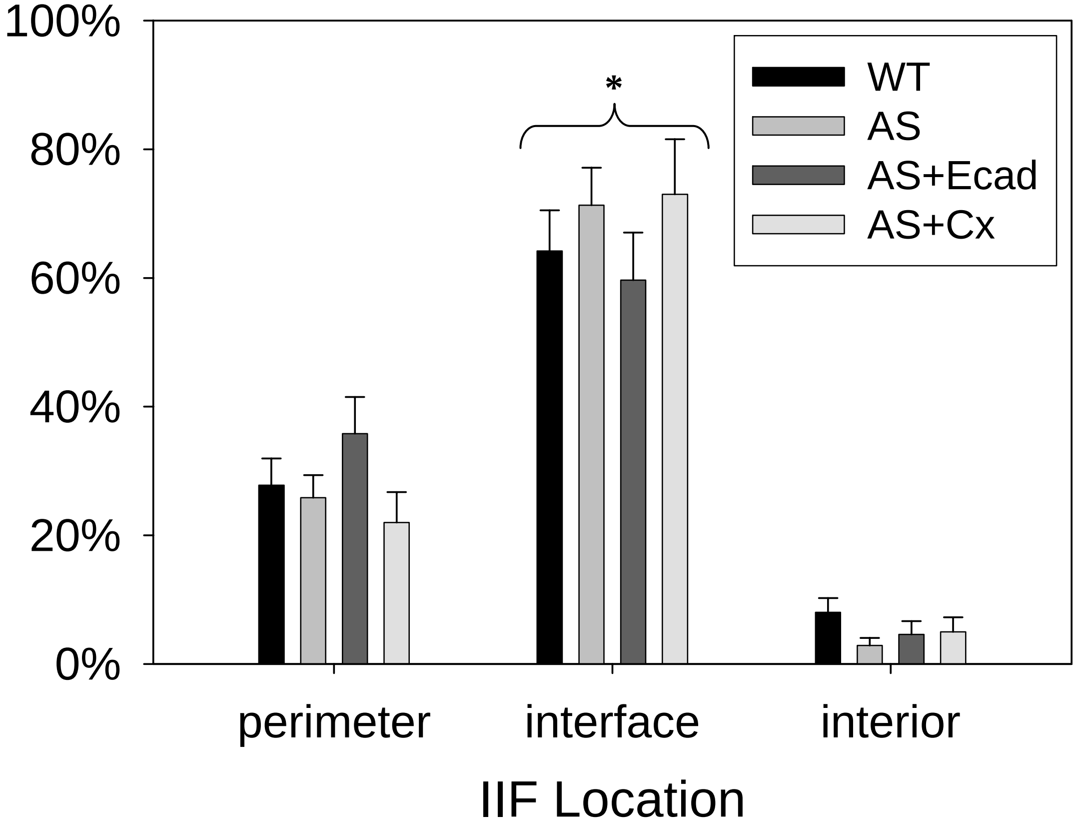

FIGURE 7.6. Location of IIF initiation during transition between state B and the singlet state (see Figure 1), indicating a significantly higher incidence of IIF initiation at the cell-cell interface for all MIN6 cell phenotypes ($p < 0.001$).

In addition to the spatial correlation between PIP and IIF, a temporal correlation was observed, as illustrated in Figure 7. Linear fits to the data yielded a statistically significant slope of approximately 1 for all cell phenotypes ($p < 0.05$), indicating a significant correlation between IIF temperature and PIP temperature. The majority of data points were above the line for concurrent IIF and PIP, resulting in a time difference between PIP and IIF that was significantly greater than zero for all cell phenotypes ($p < 0.001$), which indicates that PIP usually precedes IIF.

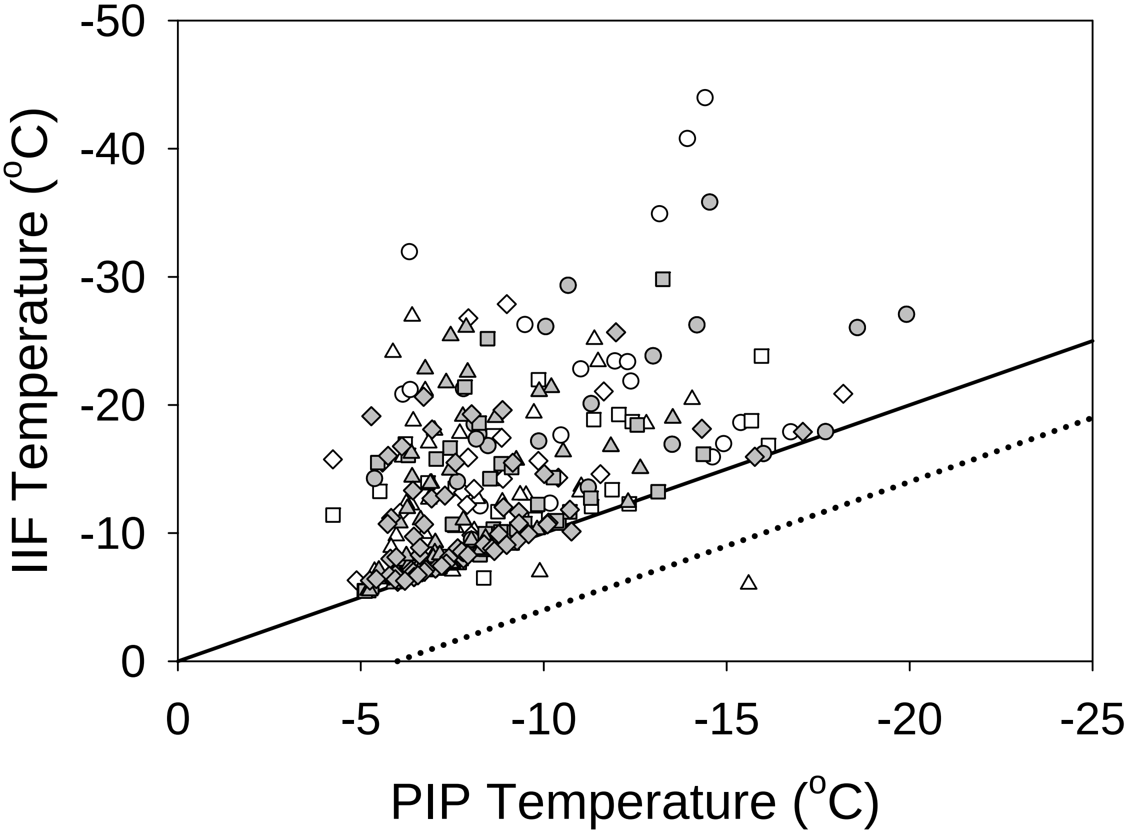

FIGURE 7.7. Temporal correlation between PIP and IIF during cooling to -60°C at 130°C/min for cell pairs comprising WT (circles), AS (squares), AS+Ecad (triangles) or AS+Cx cells (diamonds). The IIF temperature corresponds to transition between state B and the singlet state (see Figure 1). The gray symbols indicate IIF initiation at the cell-cell interface. The solid line shows concurrent PIP and IIF (i.e., y = x). Whereas video acquisition was stopped after IIF, the dotted line shows the average temperature at the end of video recording (i.e., on average, PIP events were only recorded above this line).

We next investigated the effect of intercellular junction protein expression on the rate of independent IIF (J_i) by examining the time between formation of state B and formation of the singlet state (i.e., the persistence time for state B). For a homogeneous Poisson process (i.e., constant J_i), the mean persistence time for state B is expected to be equal to the inverse of $2J_i$. Figure 8 shows the persistence time as a function of the PIP temperature. For all cell phenotypes, the slope of the best-fit line to the data was not significantly different from zero ($p > 0.1$), indicating that J_i is not strongly dependent on temperature between -5°C and -20°C. Thus, the persistence time data were pooled and compared by ANOVA, revealing a statistically significant effect of intercellular junction protein expression on the mean persistence time ($p < 0.001$). The mean persistence time for WT cells (5.2±0.7 s) was significantly higher ($p < 0.05$) than the persistence time for AS (1.9±0.3 s), AS+Ecad (2.4±0.3 s) and AS+Cx cells (2.1±0.3 s). Using these data, the rate of independent IIF was calculated to be $J_i = 0.10\ s^{-1}$, $0.26\ s^{-1}$, $0.21\ s^{-1}$ and $0.25\ s^{-1}$ for WT, AS, AS+Ecad and AS+Cx cells, respectively.

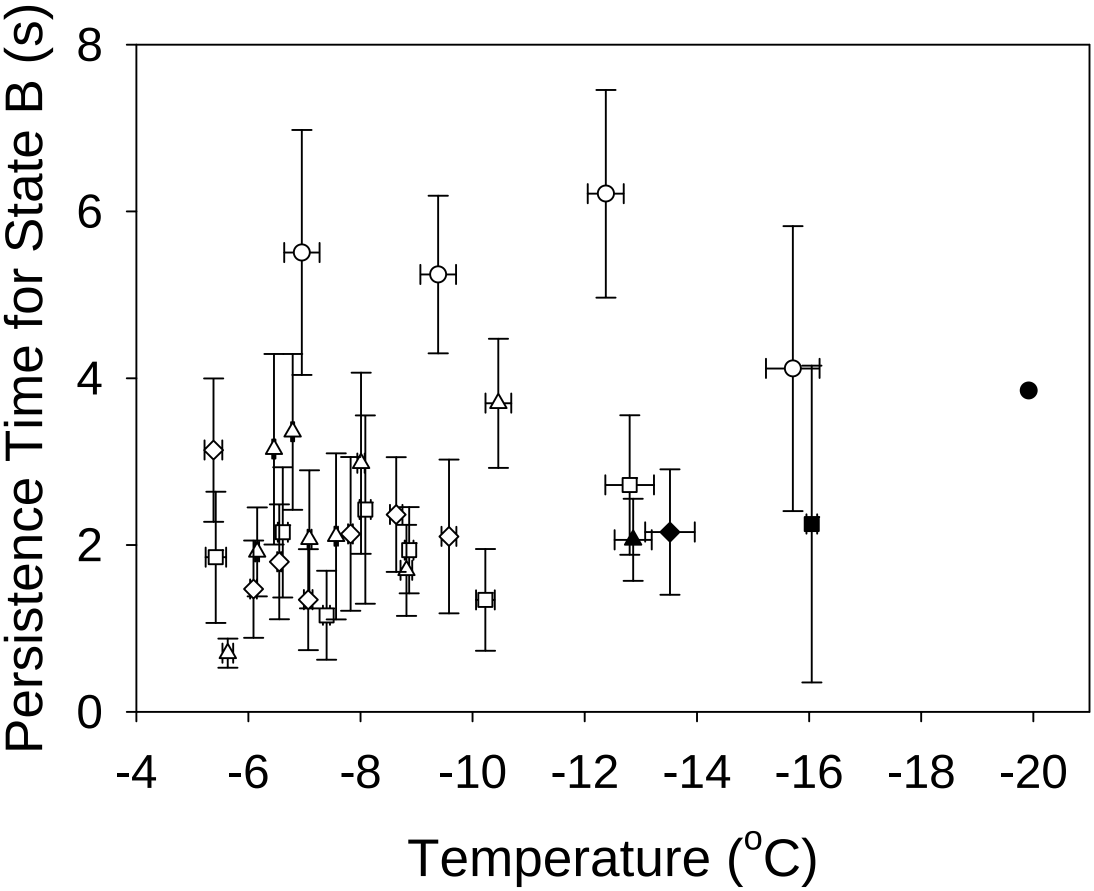

FIGURE 7.8. Persistence time of state B for WT (circles), AS (squares), AS+Ecad (triangles) or AS+Cx cells (diamonds) cooled to -60°C at 130°C/min. Persistence time data were paired with the corresponding temperature for transition between state A and state B, and pooled into groups of 10 samples (open symbols), or 1, 2, 6 or 9 samples (closed symbols, WT, AS, AS+Ecad or AS+Cx, respectively).

To further examine independent IIF, we determined the time integral of J_i by analyzing the transition between state B and the singlet state using Eq. 22. Figure 9 shows the time integral of J_i as a function of temperature, the slope of which is equal to J_i. Pairwise comparison of the slopes of the best-fit lines in the temperature range -6°C to -25°C revealed statistically significant differences in J_i for all combinations of cell phenotype, indicating that intercellular junction protein expression affects the rate of independent IIF. The value of J_i determined from the best-fit lines was the highest for AS cells ($0.30 \pm 0.008\ s^{-1}$), which have reduced expression of several intercellular junction proteins, and the lowest for WT cells ($0.093 \pm 0.005\ s^{-1}$), which express normal levels of intercellular junction proteins. Intermediate values of J_i were observed for AS+Ecad and AS+Cx cells ($0.20 \pm 0.004\ s^{-1}$ and $0.26 \pm 0.005\ s^{-1}$, respectively). The estimates for J_i determined from Figure 9 are very similar to the J_i values determined from the persistence time of state B (Figure 8), as shown in Table 1.

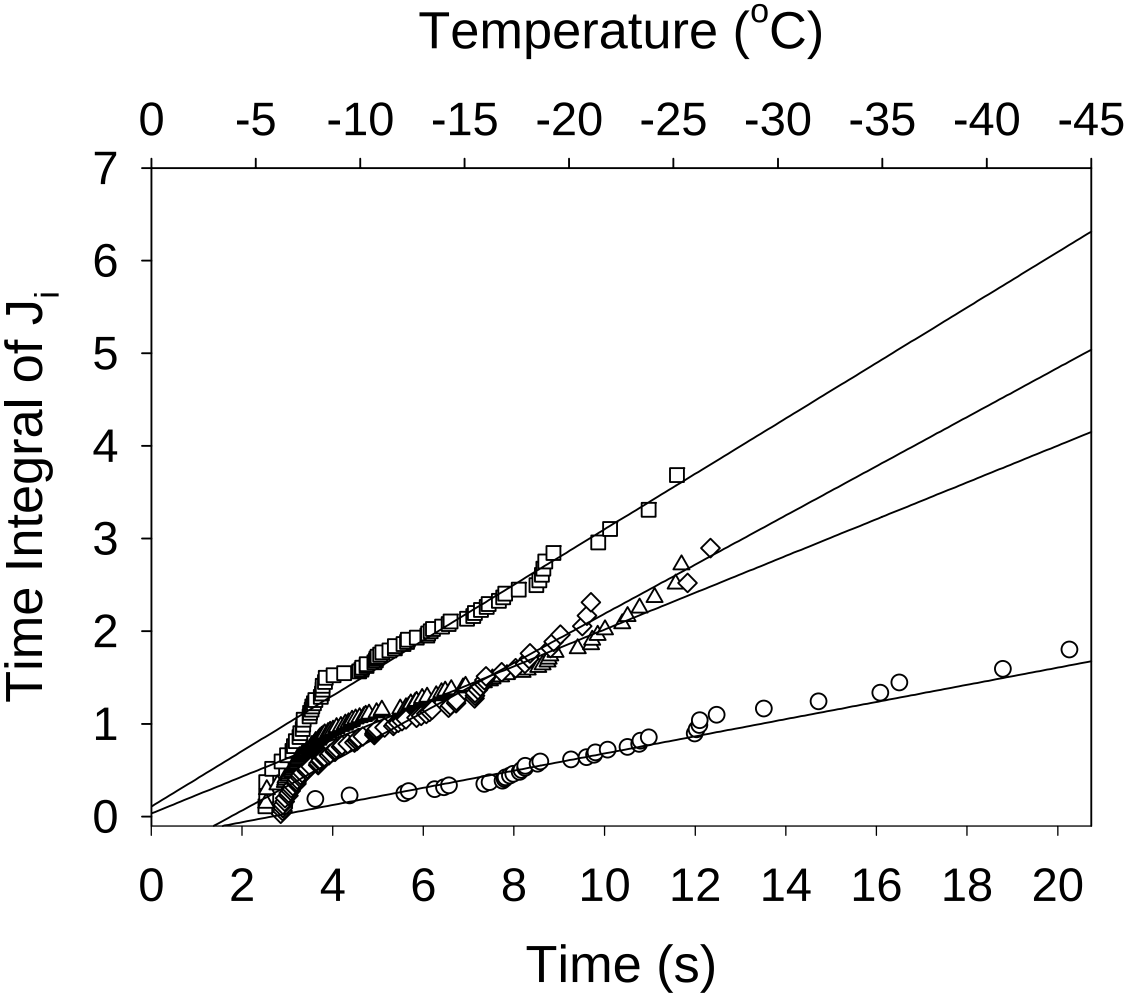

FIGURE 7.9. Time integral of the independent IIF rate (J_i) determined by examining the transition between state B and the singlet state during cooling to -60°C at 130°C/min for cell pairs comprising WT (circles), AS (squares), AS+Ecad (triangles) or AS+Cx cells (diamonds). To approximate J_i, which is equal to the slope of the above plot, the data were fit to a linear model in the temperature range -6°C to -25°C (lines).

TABLE 7.1. Rate of interaction independent IIF (J_i, s^{-1}).

Method	**WT**	**AS**	**AS+Ecad**	**AS+Cx**
J_i determined from Fig. 8	0.10	0.26	0.21	0.25
J_i determined from Fig. 9	0.093	0.30	0.20	0.27

We next sought to determine the effect of intercellular junction protein expression on IIP. Although Irimia and Karlsson (2002) estimated the rate of IIP by examining the reduction in the maximum probability of the singlet state ($P_{1,max}$) below 0.5, the IIF model presented herein contains an additional rate process (i.e., PIP) which may reduce $P_{1,max}$. Figure 10 shows theoretical predictions for $P_{1,max}$ as a function of $\bar{J}_i$ obtained using Eq. 16 and 17 for several values of the nondimensional propagation rate, α. As expected, for small $\bar{J}_i$, the values for $P_{1,max}$ match predictions using the model of Irimia and Karlsson (Eq. 18); for $\alpha = 0$, IIF in the cell pairs is uncorrelated and $P_{1,max} = 0.5$, but as the propagation rate increases, IIF becomes increasingly correlated and $P_{1,max}$ decreases. However, as $\bar{J}_i$ increases, the value of $P_{1,max}$ decreases below the predictions of Irimia and Karlsson's model. In fact, even in the absence of IIP, IIF events in the cell pairs can be highly correlated when $\bar{J}_i$ is large, resulting in a small value of $P_{1,max}$. Also shown in Figure 10 are theoretical predictions for the maximum probability of state B ($P_{B,max}$) obtained using Eq. 15. Since formation and consumption of state B are not dependent on the propagation rate, $P_{B,max}$ can be described by a single curve. For low $\bar{J}_i$, nearly all cell pairs in the ensemble undergo PIP (i.e., the cell pairs enter state B) before any appreciable consumption of state B can occur, resulting in a $P_{B,max}$ of approximately 1. In contrast, for large $\bar{J}_i$, cell pairs in state B are consumed more rapidly than they are formed, resulting in small values of $P_{B,max}$.

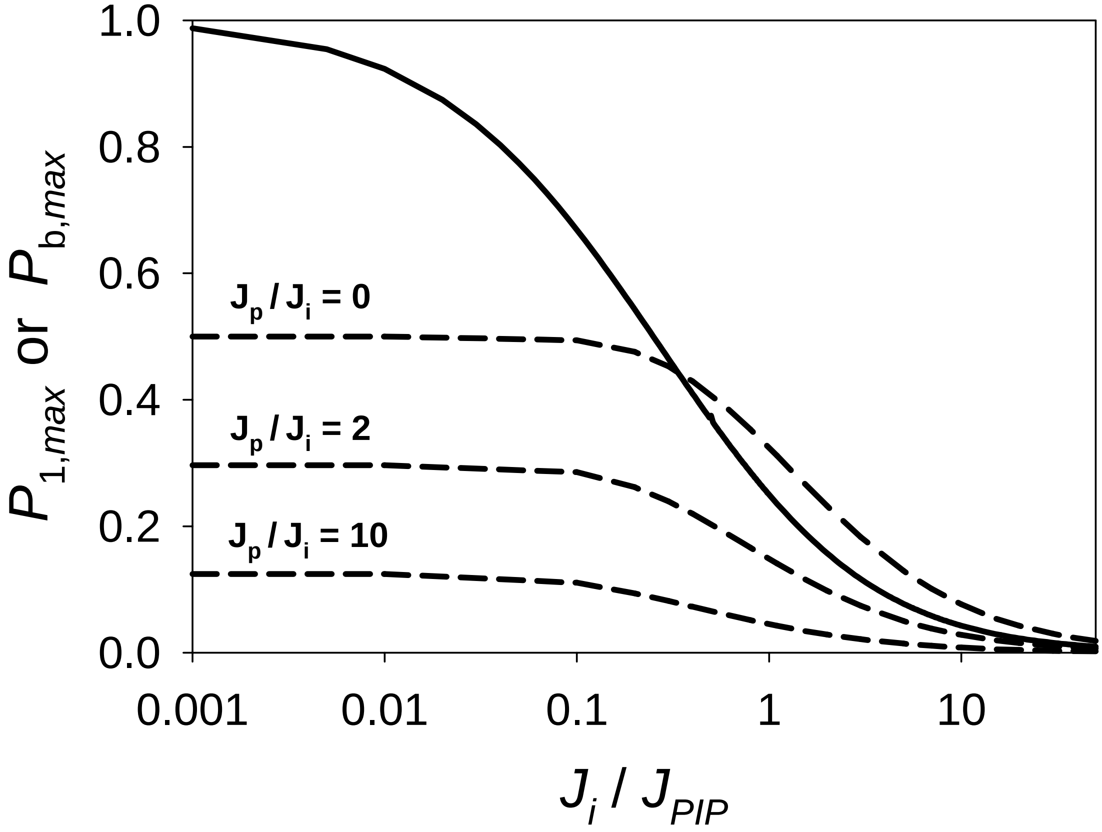

FIGURE 7.10. Theoretical predictions for the maximum singlet state probability ($P_{1,max}$, dashed lines) and the maximum probability of state B ($P_{B,max}$, solid line), assuming time-invariant values of $\bar{J}_i = J_i / J_{PIP}$ and $\alpha = J_p / J_{PIP}$.

To probe for the presence of IIP in the MIN6 cell pairs, we determined P_B and P_1 from the cryomicroscopy data, as shown in Figure 11. The values of $P_{B,max}$ determined from Figure 11A were 0.33, 0.28, 0.35 and 0.33 for WT, AS, AS+Ecad and AS+Cx cells, respectively. These experimental values for $P_{B,max}$ are consistent with predictions for $P_{B,max}$ using Eq. 15 in conjunction with the estimates for J_{PIP} and J_i from Figures 5 and 9, as shown in Table 2. Given the theoretical simulations presented in Fig. 10, one can use these measured values of $P_{B,max}$ to predict $P_{1,max}$ in the absence of IIP, which can then be compared with the experimentally measured value of $P_{1,max}$ to determine the presence (or absence) of IIP in the MIN6 cell pairs. As shown in Figure 11B, the experimental data yielded values for $P_{1,max}$ of 0.12, 0.14, 0.27 and 0.20 for WT, AS, AS+Ecad and AS+Cx cells, respectively. In Table 2, these values of $P_{1,max}$ are compared against predictions for $P_{1,max}$ in the absence of IIP. For all cell phenotypes, the predicted value of $P_{1,max}$ in the absence of propagation was higher than the experimentally measured value, which is indicative of the presence of IIP in the MIN6 cell pairs.

TABLE 7.2. Maximum probability of the singlet state and state B.

Method	**WT**	**AS**	**AS+Ecad**	**AS+Cx**
$P_{B,max}$ determined from experimental data for P_B (Fig. 11A)	0.33	0.28	0.35	0.33
$P_{B,max}$ predicted from the measured rates J_{PIP} and J_i (see Eq. 15)	0.29	0.31	0.5	0.39
$P_{1,max}$ determined from experimental data for P_1 (Fig. 11B)	0.12	0.14	0.27	0.20
$P_{1,max}$ predicted for $J_p / J_i = 0$ (Fig. 10)*	0.36	0.35	0.40	0.39

*The most conservative estimate for $P_{B,max}$ (i.e., the lowest) was used to estimate $P_{1,max}$.

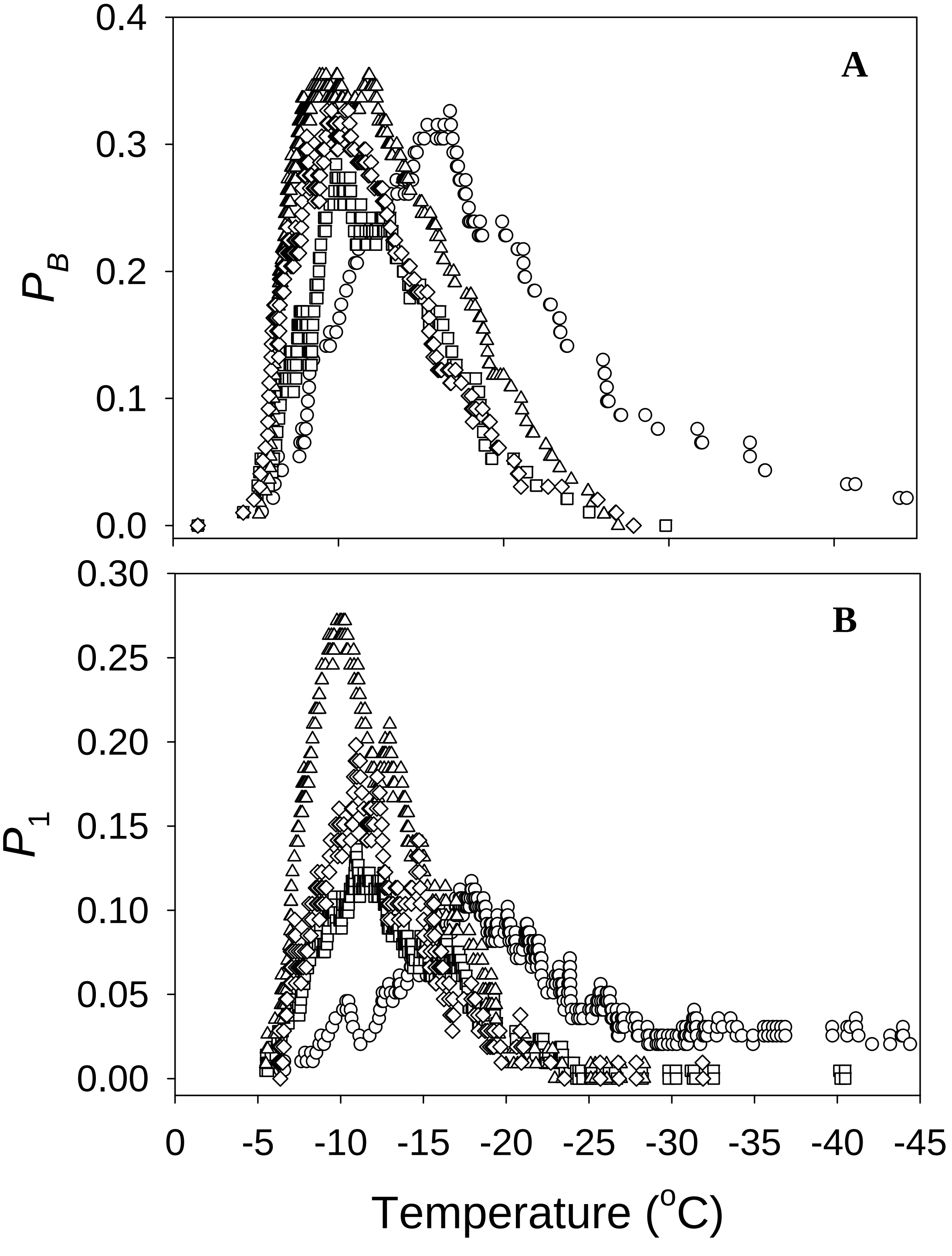

FIGURE 7.11. Probability of state B (A) and probability of the singlet state (B) for cell pairs comprising WT (circles), AS (squares), AS+Ecad (triangles) or AS+Cx cells (diamonds), cooled to -60°C and 130°C/min.

Further evidence for IIP in the MIN6 cell pairs is provided by the increase in the incidence of IIF initiation at the cell-cell interface after formation of the singlet state, as shown in Figure 12. For all cell phenotypes, the incidence of IIF initiation at the interface was significantly higher for formation of the doublet state than for formation of the singlet state ($p < 0.005$), which is consistent with the expected increase in IIF initiation at the interface because of intercellular ice propagation.

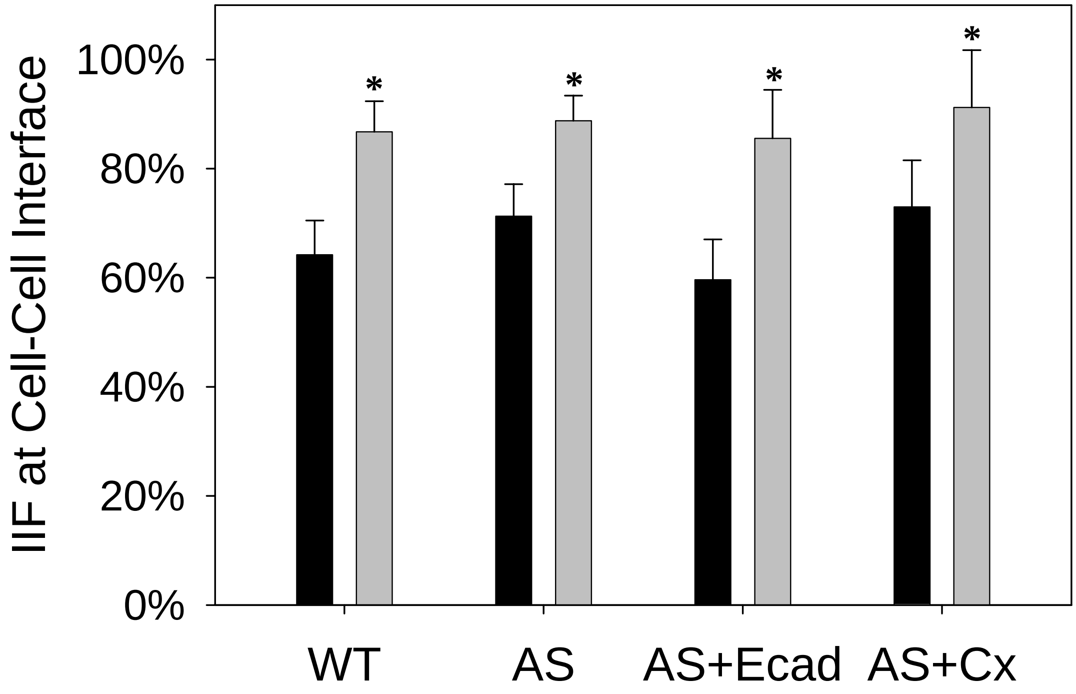

FIGURE 7.12. Incidence of IIF initiation at the cell-cell interface for the transition between the unfrozen state and the singlet state (black bars) and the transition between the singlet state and the doublet state (gray bars). * indicates a statistically significant difference ($p \leq 0.002$) within the given cell phenotype.

To explore the effect of intercellular junction protein expression on the rate of IIP, we quantified the persistence time of the singlet state (i.e., the time between formation of the singlet state and formation of the doublet state), which is expected to be inversely related to the sum of the propagation rate and the independent IIF rate. The singlet state persistence time is plotted against the temperature at formation of the singlet state in Figure 13. A significant increase in the persistence time with temperature was observed for all cell phenotypes ($p < 0.005$), resulting in approximately an order magnitude decrease in the persistence time between -5°C and -20°C. The mean persistence time was 0.57±0.1 s, 0.59±0.1 s, 1.1±0.2 s and 0.65±0.1 s for WT, AS, AS+Ecad and AS+Cx cells, respectively, resulting in temperature-averaged values for $J_i + J_p$ of 1.8 s^{-1}, 1.7 s^{-1}, 0.9 s^{-1} and 1.5 s^{-1}. Although there are apparent differences in the singlet state persistence time, these differences should be interpreted cautiously since the mean temperature for singlet state formation varies with cell phenotype (-22.4°C, -14.0°C, -12.1°C and -12.3°C for WT, AS, AS+Ecad and AS+Cx cells, respectively), and the persistence time has a strong dependence on temperature.

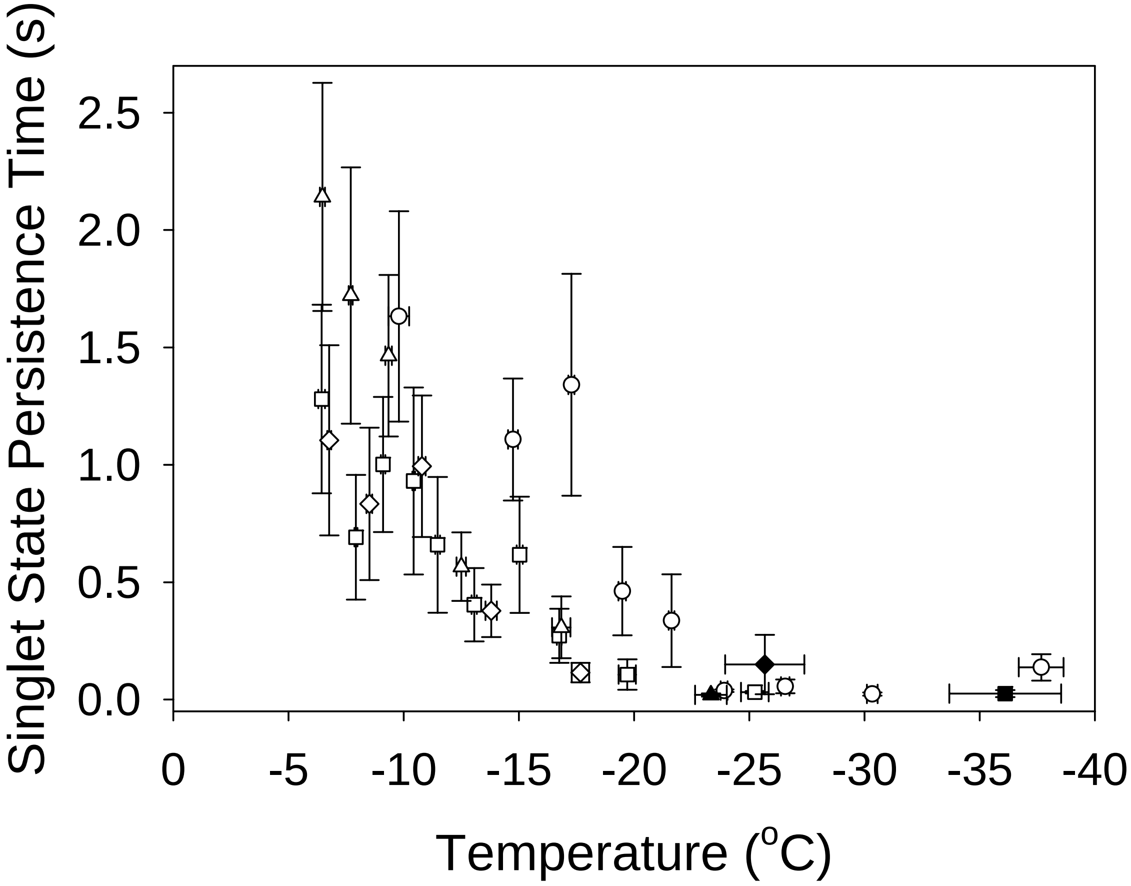

FIGURE 7.13. Singlet state persistence time for WT (circles), AS (squares), AS+Ecad (triangles) or AS+Cx cells (diamonds) cooled to -60°C at 130°C/min. Persistence time data were paired with the corresponding temperature for transition between state B and the singlet state, and pooled into groups of 20 samples (open symbols), or 4, 14, or 6 samples (closed symbols, AS, AS+Ecad or AS+Cx, respectively).

To further examine the effect of intercellular junction protein expression on IIP, we determined the time integral of the sum of the independent IIF rate and the propagation rate by analyzing the transition between the singlet state and the doublet state using Eq. 22. The resulting data are plotted in Figure 14A as a function of temperature. The best-fit line over the entire temperature range yielded $J_i + J_p = 1.1 \pm 0.03\ \mathrm{s}^{-1}$,

$2.2 \pm 0.06\ s^{-1}$, $1.4 \pm 0.06\ s^{-1}$ and $1.5 \pm 0.04\ s^{-1}$ for WT, AS, AS+Ecad and AS+Cx, respectively, which approximately matches the results obtained from Figure 13.

To isolate the effect of IIP, we subtracted Figure 9 from Figure 14A to obtain the time integral of J_p, which is plotted in Figure 14B. Gross examination of the time integral of J_p reveals similar propagation kinetics for all cell phenotypes, indicating that there is not a dramatic effect of intercellular junction protein expression on IIP. However, subtle differences between the cell phenotypes are evident. AS and AS+Ecad cells, both of which lack expression of Cx36, exhibited an in initially high J_p (as evidenced by the high slope between -5°C and -8°C), an intermediate region of low J_p (between -8°C and -18°C), followed by a sharp upturn in J_p at around -18°C. In contrast, WT and AS+Cx cells, which express normal levels of connexin-36, exhibited an approximately constant J_p over the entire temperature range, as evidenced by the linearity of the time integral of J_p in Fig. 14B.

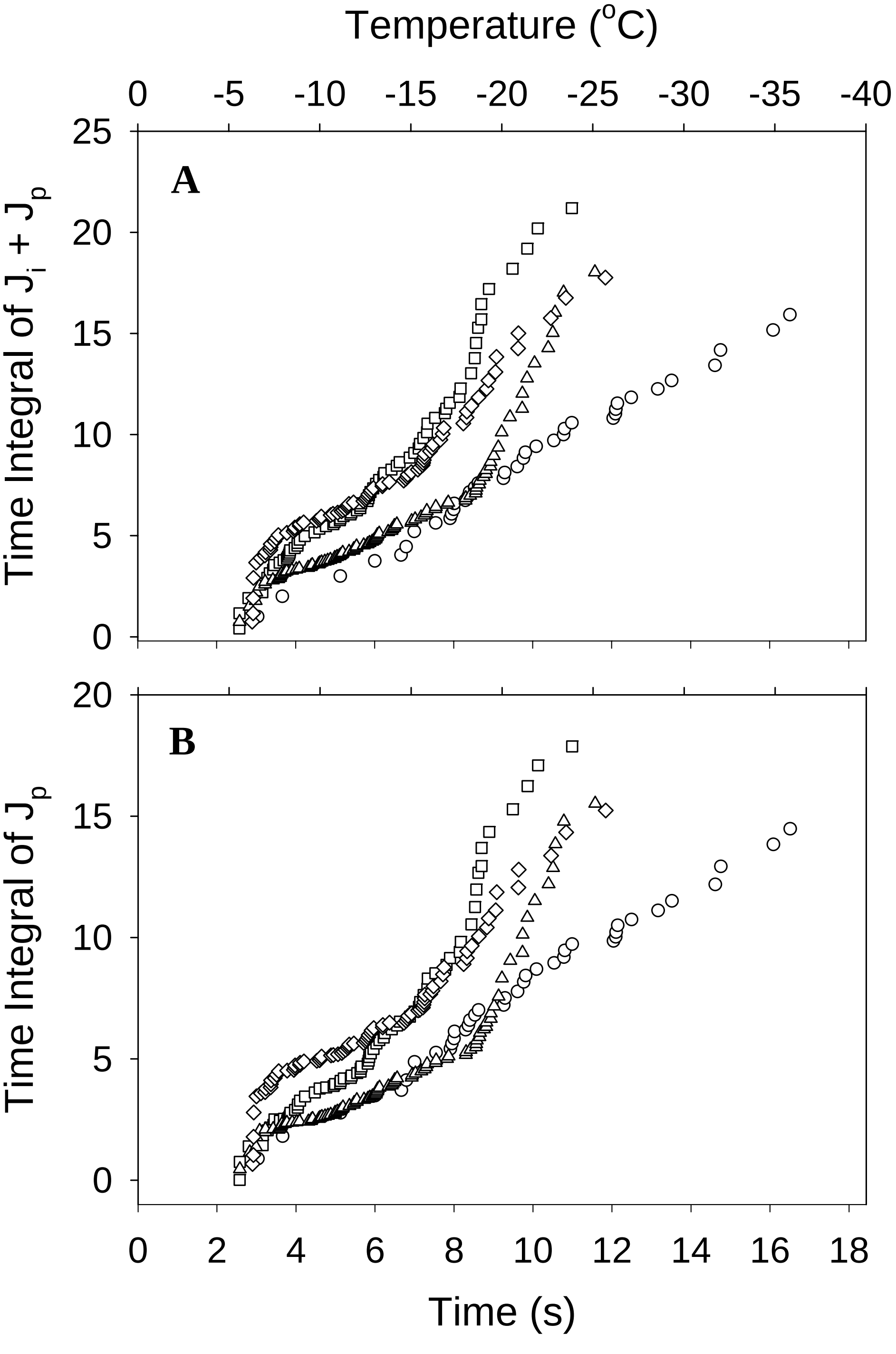

FIGURE 7.14. Time integral of the combined rate of independent IIF (J_i) and IIP (J_p), determined by examining the transition between the singlet state and the doublet state (A), and the time integral of J_p, determined by subtracting the data in Figure 9 from Figure 14A (B). Cell pairs comprising WT (circles), AS (squares), AS+Ecad (triangles) or AS+Cx cells (diamonds) were cooled to -60°C at 130°C/min.

Discussion

We have used genetically modified MIN6 cells expressing different levels of intercellular junction proteins to study the effect of intercellular junctions on IIF. We frequently observed penetration of extracellular ice into the paracellular space between adjoining cells, and incorporated this new phenomenon into a mathematical model describing the IIF states in cell pairs in terms of three stochastic rate processes: PIP, independent IIF, and IIP. The rate of PIP and independent IIF were both lower in WT cells than in genetically modified cells with impaired tight junctions (i.e., AS, AS+Ecad, and AS+Cx cells), suggesting that tight junctions are involved in both PIP and independent IIF. As a consequence of the decreased rate of PIP and independent IIF, WT cells exhibited a lower IIF temperature than the genetically modified clones lacking occludin expression, indicating that tight junctions may reduce the likelihood of IIF during cryopreservation. Although the rate of IIP was not dramatically affected by intercellular junction protein expression, subtle differences were observed suggesting that intercellular junctions influence IIP.

Although PIP at the cell-cell interface has not previously been reported, Stott (2006) observed PIP in the space between the basal cell membrane and the glass substrate. Stott (2006) showed that the PIP temperature was consistent with predictions using a model of ice growth in pores (Acker et al., 2001) with the pore dimensions approximated using a cell-substrate separation distance of 10-15 nm (Burmeister et al., 1994). For intercellular junctions, the relevant dimension is the separation distance between apposing membranes, which depends on the type of junction present. Tight junctions form an intimate connection between apposing membranes and contain aqueous pores approximately 0.5 nm in diameter (Watson et al. 2001), adherens junctions exhibit a membrane separation distance of approximately 25 nm (Zheng et al., 2006) and gap junctions have a membrane separation distance of about 3 nm (Sosinski and Nicholson, 2005). Assuming a contact angle of 0° (as did Stott, 2006) and isotonic solution in the paracellular space, these structures correspond with a ice penetration temperatures of about -3°C for adherens junctions, and < -25°C for tight junctions and gap junctions. However, as indicated by Acker et al. (2001), the contact angle may be much higher than 0° (e.g., 85°), resulting in a PIP temperature of about -10°C for tight junctions, and >-4°C for gap junctions and adherens junctions. Given that we observed PIP temperatures ranging between -4°C and -20°C, our results are consistent with the predictions of pore theory. Further support for describing PIP using pore theory is provided by the fact that the lowest PIP temperature occurred in cells expressing the tight junction protein occludin (i.e., WT cells), given that tight junctions have the smallest pore dimensions and the lowest expected ice penetration temperature.

We showed that PIP at the cell-cell interface generally preceded and colocalized with IIF, suggesting a causative relationship between PIP and IIF. Stott (2006) also observed a correlation between IIF and PIP, and hypothesized that PIP enabled a mechanical interaction between the cell membrane and the extracellular ice that ultimately led to membrane rupture and concomitant IIF. Several other researchers have suggested a link between mechanical interaction with the extracellular ice and cell damage. Erythrocytes were observed to be pushed into the channels between ice dendrites during directional solidification, resulting in cell deformation; the nature of this cell-ice interaction was related to cell survival (Ishiguro and Rubinsky, 1994). Hubel et al. (1992) observed similar results for B-lymphoblasts. Mazur et al. (2005) observed physical distortion of mouse oocytes after formation of extracellular ice, and suggested that this deformation was related to IIF. Given these findings, it is plausible that PIP at the cell-cell interface imparts a mechanical force to the cells, resulting membrane failure and subsequent IIF.

IIP was significant in all of the MIN6 clones, and the rate of IIP was not dramatically affected by intercellular junction protein expression, indicating that the mechanism of IIP cannot be entirely attributed to any of the proteins considered in this study (i.e., connexin-36, E-cadherin, and occludin). The most common explanation for the IIP phenomenon is ice growth through gap junction pores (Acker et al., 2001, Berger and Uhrik, 1996), but in MIN6 cells IIP appears to occur predominately via some other mechanism, as evidenced by the minimal effect of altering gap junction expression on the rate of IIP. Although we did not see a dramatic effect of gap junctions on IIP, Irimia and Karlsson (2002, 2005) observed a decrease in the rate of IIP of almost 80% in HepG2 cells after treatment with a gap junction blocker. However, Irimia and Karlsson (2005) point out that HepG2 cells exhibit minimal intercellular coupling via gap junctions (Yang et al., 2003), which suggests that the large reduction in the rate of IIP after treatment with gap junction blocker may be due to nonspecific effects. Although the role of gap junctions in IIP remains unclear, it is becoming increasingly evident that IIP can occur in the absence of gap junctions. Despite the overall similarity of the IIP rates between the MIN6 clones, there were subtle differences that may implicate intercellular junctions in the IIP process. As shown in Figure 14, cells lacking connexin-36 (i.e., AS and AS+Ecad) exhibited an IIP rate that was highly temperature dependent, with fast IIP below -8°C, slower IIP between -8°C and -18°C, and fast IIP below -18°C. In contrast, WT and AS+Cx cells exhibited an IIP rate that was approximately constant over the entire temperature range (as indicated by the linearity of the plot in Figure 14). Although it is difficult to draw conclusions about the mechanism of IIP from these results, intercellular junctions seem to be involved. Future work is necessary to elucidate the mechanism(s) of IIP.

Since cellular water transport is known to affect the kinetics of IIF, it is possible that the differences in IIF kinetics that we observed for the genetically modified MIN6 clones were related to differences in water transport kinetics. To address this possibility, we measured the water permeability for monolayers of WT and AS cells, as shown in the appendix. There were not significant differences in water permeability (see Figure 15), suggesting that the observed differences in IIF kinetics cannot be attributed to differences in cellular water transport. However, despite the similar permeabilities in WT and AS cells, predictions of cell dehydration during freezing yielded lower water content and supercooling for WT cells than for AS cells, particularly for temperatures less than -15°C (see Figure 16). Even so, the differences in supercooling were minimal for temperatures greater than -15°C, whereas the differences in the measured IIF kinetics were quite large in this temperature range, which suggests that observed differences in IIF kinetics were not caused by differences in cellular water transport.

Conclusions

The development of successful cryopreservation protocols for tissues will require an improved understanding of IIF, which has been shown to be enhanced in tissue by the presence of cell-cell interactions. We have used genetic engineering approaches to control the expression of intercellular junction proteins, enabling investigation of the molecular mechanisms of IIF associated with cell-cell contact. A new mechanism of IIF was observed, resulting from penetration of extracellular ice into the intercellular space. The likelihood of this PIP phenomenon and subsequent IIF was reduced in cells expressing the tight junction protein occludin, suggesting that tight junctions may protect cells in tissue from IIF. Although many researchers have attributed IIP to growth of ice through gap junction pores, we did not observe a reduction in the rate of IIP after removal of the gap junction protein connexin-36. However, the temperature-dependent IIP rate was affected by intercellular junction protein expression, indicating that intercellular junctions are involved in IIP. Future studies will be necessary to fully elucidate the mechanisms of IIP.

Appendix

To explore the possibility that the water membrane permeability for MIN6 cells was altered by transfection, we measured the permeability for WT and AS cells using a fluorescence quenching technique (Solenov et al., 2004; Chapter 5). Briefly, cell monolayers were incubated in 1.25 μg/ml calcein-AM solution for 15-20 min, and then exposed to hypertonic solution in a temperature-controlled flow chamber while monitoring the fluorescence intensity by digital video microscopy. The resulting data were fit to the following model of membrane water transport to determine the kinetic constant L_pA/V_{w0} (see Chapter 5):

$$\frac{d\left({}^{V_w}\!/_{V_{w0}} \right)}{dt} = \frac{L_p A}{V_{w0}} \left(\Pi_i - \Pi_e \right) \qquad [24]$$

where V_w is the osmotically active volume, L_p is the membrane water permeability, A is the cell surface area, Π is the osmotic pressure and the subscripts "0", "i" and "e" refer to isotonic, intracellular, and extracellular conditions, respectively.

The resulting values of L_pA/V_{w0} are displayed in an Arrhenius plot in Figure 15. The linearity of the data indicates that the temperature dependence of L_p is adequately described by the Arrhenius relationship:

$$L_p = L_{p,ref} \exp\left[\frac{E_a}{R}\left(\frac{1}{T_{ref}} - \frac{1}{T}\right)\right] \qquad [25]$$

where E_a is the activation energy, R is the ideal gas constant, T is the absolute temperature, and $L_{p,ref}$ and T_{ref} are the reference permeability and temperature, respectively. The best-fit lines were not significantly different, as indicated by the 95% confidence interval lines, yielding activation energies for water transport of $E_a = 45 \pm 4$ kJ/mol and $E_a = 51 \pm 3$ kJ/mol, and L_pA/V_{w0} values at 0°C of 9.3×10^{-9} Pa^{-1} s^{-1} and 6.7×10^{-9} Pa^{-1} s^{-1} for WT and AS cells, respectively.

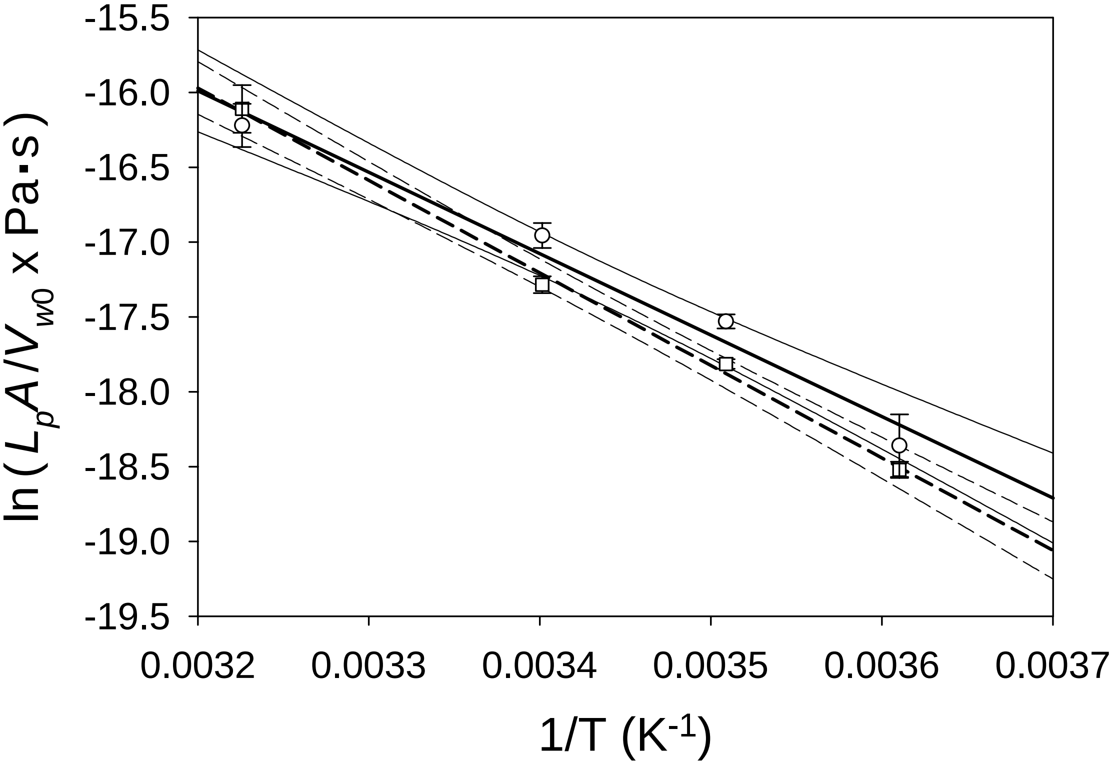

FIGURE 7.15. Arrhenius plot for monolayers of WT (circles) and AS cells (squares). Experiments were performed at 4, 12, 21 and 37°C, and best-fit lines and 95% confidence intervals are shown for WT (solid lines) and AS cells (dashed lines).

The data presented in Figure 15 were used to predict cellular dehydration during cooling from -1.5°C to -60°C at 130°C/min in the presence of extracellular ice (i.e., the cooling protocol used in the cryomicroscopy experiments), as shown in Figure 16. To make predictions using Eqs. 24 and 25, we assumed that the extracellular solution was in chemical equilibrium with ice, and the intracellular solution was ideal (Mazur, 1963), yielding:

$$\Pi_e = \frac{\Delta H_f}{v_w}\left(1 - \frac{T}{T_m}\right) \qquad [26]$$

and

$$\Pi_i = \frac{-RT}{v_w} \ln\left(\frac{V_w / V_{w0}}{V_w / V_{w0} + v_w M_0} \right) \qquad [27]$$

where ΔH_f = 6016.5 J/mol, T_m = 273.15 K and $v_w = 1.8 \times 10^{-5}$ m^3/mol are the heat of fusion, melting temperature and molar volume of pure water, respectively, and M_0 is the isotonic osmolarity. Using the best-fit lines from Figure 15 (E_a ± standard error), one obtains predictions for intracellular water content and supercooling that are quite different for WT and AS cells, despite the lack of a significant difference between the Arrhenius plots. This indicates that the extent of cellular dehydration during freezing is very sensitive to the membrane permeability parameters. In other words, although no statistically significant differences in water permeability were detected, it is possible that the MIN6 clones used in this study have slight differences in water permeability, resulting in different supercooling and water content during freezing. However, the supercooling predictions for WT and AS cells are very similar for temperatures above -15°C, suggesting that differences in IIF behavior in this regime cannot be attributed to differences in water transport kinetics.

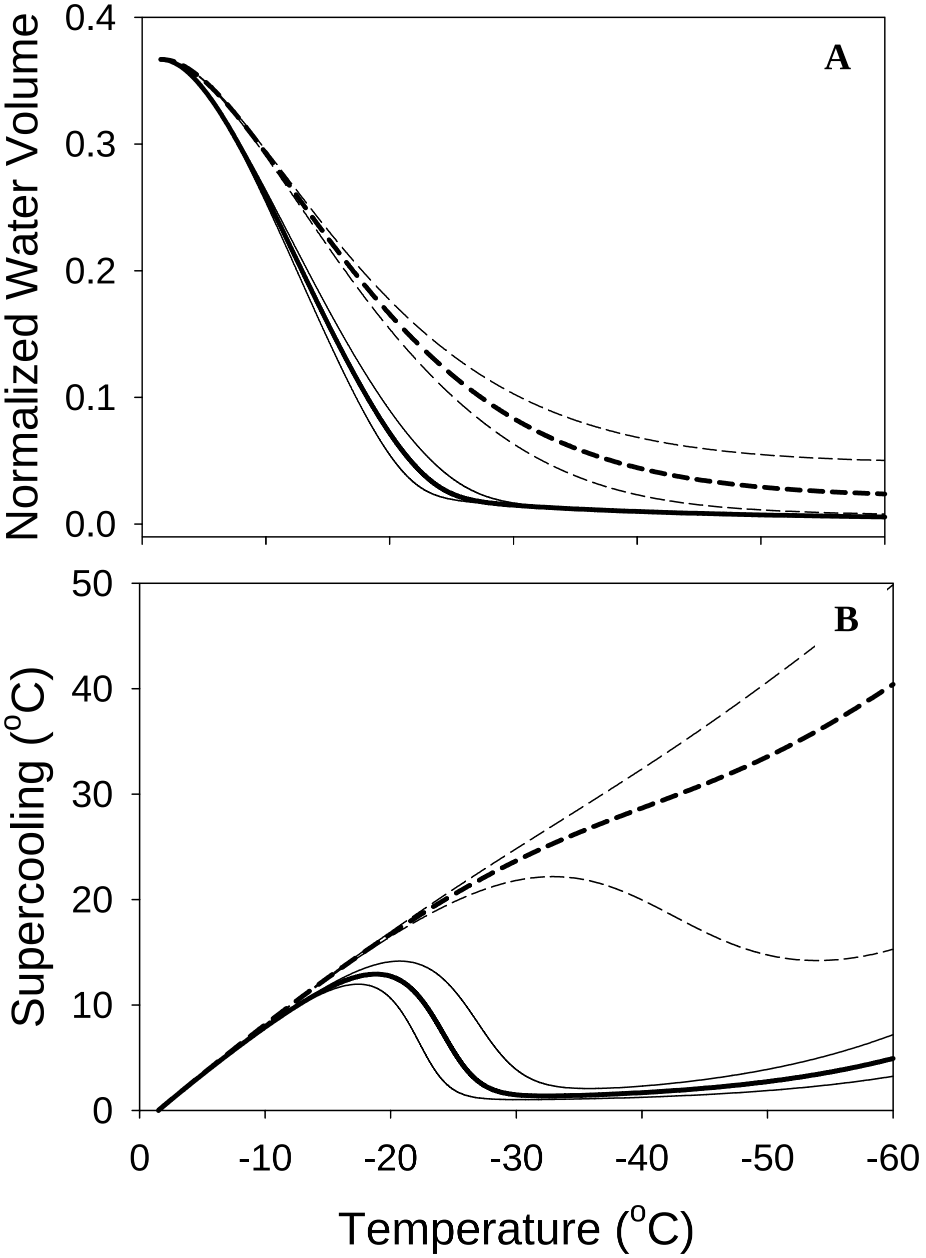

FIGURE 7.16. Predicted cellular water content and supercooling for WT (solid lines, $L_pA/V_{w0} = 9.3 \times 10^{-9}$ Pa^{-1} s^{-1} at 0°C, Ea = 45 ± 4 kJ/mol) and AS cells (dashed lines, $L_pA/V_{w0} = 6.7 \times 10^{-9}$ Pa^{-1} s^{-1} at 0°C, Ea = 51 ± 3) cooled from -1.5°C to -60°C at 130°C/min in the presence of extracellular ice.

CHAPTER 8

EFFECT OF CYTOPLASM VISCOSITY AND SUPERCOOLING ON INTRACELLULAR ICE FORMATION IN MICROPATTERNED CELL PAIRS

Introduction

The development of successful cryopreservation strategies for tissue is hindered by our inadequate understanding of intracellular ice formation (IIF) in tissue. Whereas the large majority of existing IIF data was determined in cell suspensions, there is evidence that the mechanisms of IIF in tissue and cell suspensions are different. Previous studies have shown an increased likelihood for IIF in single attached cells compared with cells in suspension (Acker and McGann, 2002; Irimia and Karlsson, 2002), suggesting that new IIF mechanisms exist in tissue as a result of cell-substrate connections. In addition to IIF associated with cell-substrate interactions, cell-cell interactions have been shown to influence IIF, resulting in an increased IIF probability for monolayers compared with single attached cells (Acker and McGann, 2002; Irimia and Karlsson, 2002). This increase in IIF probability has been attributed to propagation of ice between neighboring cells, which has been hypothesized to occur by growth of ice through gap junction pores (Acker et al., 2001; Berger and Uhrik, 1996; Irimia and Karlsson, 2002). However, this hypothesis does not entirely explain intercellular ice propagation, since evidence of propagation has been observed in cells lacking active gap junctions (Acker et al., 2001; Irimia and Karlsson, 2002; Chapter 7). Although the exact mechanisms of IIF associated with cell-substrate and cell-cell interactions are unknown, it is clear that these mechanisms of IIF are unique to tissue.

Whereas cryopreservation procedures are generally optimized by adjusting the cooling rate and the concentration of cryoprotectants (CPAs), the effect of these factors on the new IIF mechanisms in tissue is unknown since most studies of IIF in tissue are conducted for fast cooling rates in the absence of CPA. This gap in our current knowledge represents a significant obstacle to developing mathematical models of IIF that can be used for optimization of tissue cryopreservation protocols. Mathematical optimization strategies have been successful for cell suspensions (Karlsson et al., 1996) using models describing intracellular ice nucleation as a function of the thermodynamic state of the cell cytoplasm (temperature and composition). We have recently presented membrane permeability data for adherent tissue in the presence of CPA, enabling prediction of the thermodynamic state of the cytoplasm during tissue freezing (Chapter 6). However, the dependence of the tissue IIF kinetics on the thermodynamic state of the intracellular solution is unknown. In order to optimize tissue cryopreservation procedures based on IIF predictions, mathematical models describing IIF in tissue as a function of the thermodynamic state of the cytoplasm are necessary.

The goal of the present study was to determine the effect of the thermodynamic state of the cell cytoplasm on the kinetics of IIF in tissue. To facilitate analysis of the data, IIF was investigated in a model tissue system comprising a micropatterned cell pair. High-speed video cryomicroscopy was used to determine the temperature and intracellular location of IIF initiation in the cell pairs during freezing at several cooling rates in the presence of dimethyl-sulfoxide (Me_2SO). The IIF data were analyzed in terms of two stochastic rate processes: interaction independent IIF (i.e., IIF not dependent on the presence of internal ice in a neighboring cell) and intercellular ice propagation

(Irimia and Karlsson, 2002). The rates of independent IIF and intercellular ice propagation were determined as a function of the intracellular supercooling and viscosity by coupling the IIF data with predictions of membrane water transport during freezing.

Theoretical Background

Cellular Dehydration

During cryopreservation cells are exposed to conditions that result in osmotic transport of water across the cell membrane. As the extracellular ice phase grows, the solutes in the remaining unfrozen fraction become increasingly concentrated, causing an osmotic imbalance that drives water efflux from the cells. Water transport across the cell membrane can be described in terms of this gradient in osmotic pressure (Π), as follows (Karlsson et al., 1993; Mazur, 1963):

$$\frac{d\left(V_w / V_{w0}\right)}{dt} = \frac{L_p A}{V_{w0}}\left(\Pi^i - \Pi^e\right) \qquad [1]$$

where V_w is the osmotically active cell volume (i.e., the volume of cellular water that can be removed in the limit of infinite osmotic strength), A is the cell surface area, L_p is the membrane water permeability, the subscript "0" corresponds with an isotonic concentration of impermeable solutes, and the superscripts "*i*" and "*e*" denote intracellular and extracellular conditions, respectively. Although permeable cryoprotectants (CPAs) are frequently used in cryopreservation procedures, CPA transport is generally neglected such that Eq. 1 is sufficient to describe the membrane transport during freezing (Karlsson et al., 1993).

The osmotic pressure of the extracellular solution is assumed to be in chemical equilibrium with the ice, resulting in:

$$\Pi_e = \frac{\Delta H_f}{v_w}\left(1 - \frac{T}{T_m}\right) \qquad [2]$$

where $\Delta H_f = 6016.5$ J/mol, $T_m = 273.15$ K and $v_w = 1.8 \times 10^{-5}$ m^3/mol are the heat of fusion, melting temperature and molar volume of pure water, respectively.

Assuming an ideal intracellular solution, the intracellular osmotic pressure can be expressed as:

$$\Pi_i = \frac{-RT}{v_w}\ln\left(\frac{V_w / V_{w0}}{V_w / V_{w0} + v_w M_{s0} + v_w M_{a0}}\right) \qquad [3]$$

where R is the ideal gas constant, and M_{s0} is the isotonic osmolarity of impermeable solutes (e.g., salts), and M_{a0} is the CPA osmolarity corresponding with M_{s0}.

The temperature dependence of the membrane water permeability is given by the Arrhenius relationship:

$$L_p = L_{p,ref} \exp\left[\frac{E_{Lp}}{R}\left(\frac{1}{T_{ref}} - \frac{1}{T}\right)\right] \qquad [4]$$

where the $L_{p,ref}$ is the water permeability at the reference temperature, T_{ref}, and E_{Lp} is the activation energy for membrane water transport.

To fully describe membrane transport during freezing, the relationship between the temperature and the time is needed. For a linear cooling rate (B), one obtains:

$$\frac{dT}{dt} = -B \qquad [5]$$

Combining Eqs. 1-5, it is possible to predict the water content during freezing, from which several important characteristics of the intracellular solution can be obtained, such as the supercooling and viscosity. The intracellular supercooling (ΔT) can be predicted from the normalized cell water content using the following equation:

$$\Delta T = \left[\frac{1}{T_m} - \frac{R}{\Delta H_f} \ln\left(\frac{V_w / V_{w0}}{V_w / V_{w0} + v_w M_{s0} + v_w M_{a0}} \right) \right]^{-1} - T \qquad [6]$$

The intracellular viscosity can be predicted from the cell water content and the known initial concentrations of CPA and impermeable solutes. As described by Karlsson et al. (1993), the viscosity of the cytoplasm (η) can be approximated as the viscosity of a ternary solution of Me_2SO, NaCl and water, which can be characterized by the volume fraction of hydrated salt spheres (ϕ_{sph}), and the viscosity of the binary solution consisting of "free" water (i.e., water that is not incorporated into the hydrated salt spheres) and Me_2SO (η_{binary}):

$$\eta = \eta_{binary} \cdot \exp\left\{ \frac{2.5\phi_{sph}}{1 - 0.609375\phi_{sph}} \right\} \qquad [7]$$

The volume fraction of salt spheres can be expressed in terms of the normalized cell water content as follows:

$$\phi_{sph} = \frac{M_{s0}\left(v_s + h v_w\right)}{V_w / V_{w0} + v_s M_{s0} + v_a M_{a0}} \qquad [8]$$

where $v_s = 1.35 \times 10^{-5}$ m^3/osmole is the volume occupied by 1 osmole of NaCl, $h = 1$ is the number of water molecules in the hydration shell of a single NaCl molecule and $v_a = 7.13 \times 10^{-5}$ m^3/mol is the molar volume of Me_2SO. The viscosity of the binary water-Me_2SO solution is characterized by the Me_2SO mole fraction (x_a) and the temperature as follows:

$$\eta_{binary}(x_a, T) = \eta_A(T) + \frac{\eta_C(x_a)}{0.00248} \cdot \left[\eta_B(T) - \eta_A(T) \right] \qquad [9a]$$

$$\eta_A(T) = (6.6274 \times 10^{-7}) \cdot e^{2173.3/T} \qquad [9b]$$

$$\eta_B(T) = (3.0049 \times 10^{-7}) \cdot e^{2774.7/T} \qquad [9c]$$

$$\eta_C(x_a) = 0.1235x_a^6 - 0.4518x_a^5 + 0.6266x_a^4 - 0.3909x_a^3 + 0.0901x_a^2 + 0.0037x_a \qquad [9d]$$

The Me_2SO mole fraction can be expressed in terms of the normalized cell water content as follows:

$$x_a = \frac{M_{a0}}{(1/v_w)(V_w/V_{w0}) + M_{a0} - hM_{s0}} \qquad [10]$$

As shown above, it is possible to predict the normalized cell water content during freezing (Eqs. 1-5), from which the cytoplasm supercooling (Eq. 6) and viscosity (Eqs. 7-10) can be calculated. The only necessary cell-specific parameters are the permeability constant L_pA/V_{w0} and the activation energy for water transport E_{Lp}.

Intracellular Ice Formation

Although the exact mechanisms of IIF in tissue are not known, the IIF process can be modeled in terms of general rate processes without assuming an explicit dependence of the IIF rate on the thermodynamic variables of the system (i.e., temperature, solute concentrations). Irimia and Karlsson (2002) describe IIF in a two-cell system using two stochastic rate processes: interaction independent IIF, which describes any mechanism of IIF that does not depend on the presence of internal ice in an adjoining cell, and intercellular ice propagation, which describes any mechanism of IIF that requires the presence of internal ice in an adjoining cell. The two-cell system is characterized by three IIF states: the unfrozen state (i.e., neither cell contains intracellular ice), the singlet state (i.e., one of the two cells contains intracellular ice) and the doublet state (i.e., both cells contain intracellular ice). The probabilities of these IIF states is given in terms of the rate of independent IIF (J_i) and the rate of intercellular ice propagation (J_p) as follows:

$$\frac{dP_0}{dt} = -2J_i P_0 \qquad [11]$$

$$\frac{dP_1}{dt} = 2J_i P_0 - \left(J_i + J_p\right)P_1 \qquad [12]$$

$$P_2 = 1 - P_0 - P_1 \qquad [13]$$

where P_0, P_1 and P_2 are the probabilities of the unfrozen state, singlet state and doublet state, respectively. Rewriting Eq. 11 in terms of the non-dimensional time,

$$\tau = \int_0^t J_i dt\ , \qquad [14]$$

it is possible to obtain a solution for the probability of the unfrozen state:

$$P_0 = e^{-2\tau} \qquad [15]$$

In the case of negligible intercellular ice propagation, the probability of the singlet state is given as:

$$P_1 = 2e^{-\tau} - 2e^{-2\tau} \qquad [16]$$

Combining Eqs. 15 and 16, one can calculate the expected value of the singlet state probability in the absence of propagation using experimental data for the probability of the unfrozen state.

Materials and Methods

Micropatterning

Microscale features were patterned onto silicon wafers using photolithography techniques with microfiche as the photomask (Deng et al., 1999, 2000). The features were drawn in Autocad with dimensions 25 fold larger than the desired size of the final micropattern, and then printed onto high quality photo paper at a resolution of 1200 dpi. These printouts were optically reduced by a factor of 25 onto microfiche, which were used as the photomasks. Silicon wafers were spin-coated with SU-8 photoresist (Microchem) to a thickness of 7 μm, followed by hotplate bakes at 65°C, 95°C and 65°C for 2 min, 5 min and 2 min, respectively. The wafers were then exposed to UV light (9.65 mW/cm^2 at 405 nm) through the microfiche photomask for 16.5 s using an OAI mask aligner in contact mode. After exposure, the wafers were baked on a hotplate at 65°C, 95°C and 65°C for 1 min at each temperature. The light-exposed photoresist was developed in SU-8 developer (Microchem) for 1 min, rinsed in isopropyl alcohol for 1 min, dried with a nitrogen gun and baked on a hotplate at 95°C for 10 min.

The features on the silicon wafers were used to create molds comprising poly-dimethylsiloxane (PDMS, Sylgard 184, Superior Essex), which were then used to create non-adhesive agarose features on glass substrates (Nelson and Chen, 2002). Prior to creating PDMS molds, the wafers were exposed to tridecafluoro-1,1,2,2-tetrahydrooctyl-1-trichlorosilane (United Chemical Technologies) for 45 min under vacuum to prevent adhesion of the PDMS to the wafer. The PDMS elastomer and curing agent were thoroughly mixed at a ratio of 10:1, and poured over the wafers in a Petri dish to a thickness of approximately 5 mm. The Petri dish was exposed to vacuum to remove bubbles, and then cured in a dry heat oven for 6 hr at 65°C. After curing, the PDMS molds were removed from the wafer, cut to size, and inverted (features down) onto 12 mm diameter glass coverslips. A small volume of ethanol was wicked between the PDMS mold and the coverslip and allowed to evaporate for approximately 20 min. Agarose solution (aqueous solution containing 0.6 % w/v agarose and 40% v/v ethanol) was heated while stirring until the solution just began to boil, and then wicked between the PDMS mold and the coverslip. The agarose was allowed to dry for approximately 2 hr before removing the PDMS mold. The coverslip containing the agarose features was sterilized by exposure to 70% ethanol for 5 min, rinsed with phosphate buffered saline solution (PBS), and incubated in human plasma fibronectin solution (Invitrogen, 25 μg/ml in PBS) at 37°C for 1 hr. The coverslips were then rinsed and stored in PBS for up to 6 hr before cell seeding.

Cell Culture

Bovine pulmonary artery endothelial cells (BPAEC, Cambrex) were cultured in a 5% CO_2 environment at 37°C in tissue culture flasks containing MCDB 131 media (Mediatech) supplemented with 5% v/v fetal bovine serum (Sigma-Aldrich), 2 ng/mL basic human fibroblast growth factor (PeproTech), 10 ng/mL human epithelial growth factor (Invitrogen), 1 ng/mL vascular endothelial growth factor (Sigma-Aldrich), 2 ng/mL insulin-like growth factor-1 (Invitrogen), 0.001 mg/mL hydrocortisone (Sigma-Aldrich), 2 mM L-glutamine (Mediatech), 100 U/mL penicillin and 100 μg/mL streptomycin (Invitrogen), and 50 μg/mL ascorbic acid (Sigma-Aldrich). Media was changed every 2 days and passages were performed when the flasks reached a confluency of approximately 80% by exposure to trypsin-EDTA solution (Cambrex) for 5 min, as recommended by the vendor. For cryomicroscopy experiments, BPAEC cultures at passages 7-9 were suspended in media at a density of approximately 10^4 cells/mL, seeded onto the micropatterned coverslips, and cultured for 18-24 hr.

Cryomicroscopy

To prepare the BPAEC cultures for cryomicroscopy experiments, samples were incubated in culture media containing the membrane permeable nucleic acid stain SYTO13 (2 μM) and the membrane impermeable stain ethidium homodimer (10 μM) at 37ºC for 10 to 60 min. Immediately prior to freezing, glass coverslips were placed in Hepes buffered saline solution (Cambrex) containing 5% v/v Me_2SO for 2 min (which was sufficient to allow equilibration with the Me_2SO solution, see Chapter 6), and then dried by dragging the bottom of the coverslip across a Kimwipe and inverted onto a 16 mm coverslip on the temperature-controlled microscope stage.

Samples were observed during cooling using a high-speed video cryomicroscopy system consisting of a temperature-controlled microscope stage (FDCS 196, Linkam Scientific Instruments, Tadworth, Surrey, UK), an upright microscope (Eclipse ME600, Nikon) and a high-speed digital camera (Phantom v4.3 Vision Research, New Jersey, USA). Temperature was calibrated by measuring the melting point of purified water. Samples were visualized under Khöler illumination using a 50x objective with the microscope halogen lamp set to maximum light output. Images were acquired at 1000-4000 Hz with an exposure time of 143 μs, and video acquisition was stopped using the camera trigger after observing IIF. The depression of the camera trigger was detected using the pressure sensor of the temperature controller (TMS 94, Linkam), allowing synchronization of the temperature measurements with the video frames.

BPAEC cell pairs were subjected to the cooling protocols summarized in Table 1. Samples were cooled to T_{seed} and held for 1 min to permit seeding of extracellular ice, ramped at 5ºC/min to T_{hold} and held for 3-6 min to permit equilibration with the extracellular solution (equilibration was confirmed using predictions of cell membrane transport with the permeability parameters from Chapter 6), and then cooled at a rate *B* to -70ºC. Ice seeding was accomplished by moving the edge of the sample over a cold seeding block.

TABLE 8.1. Cooling protocols.

Protocol	**T_{seed} (°C)**	**T_{hold} (°C)**	***B* (°C/min)**
1	-5	-3	130
2	-5	-5	130
3	-5	-8.5	130
4	-5	-3	40
5	-5	-3	80

Before initiating cooling at *B*, a field of view was randomly selected that contained a single cell pair (determined by visualization of two distinct nuclei by SYTO13 fluorescence) with intact cell membranes (determined by lack of ethidium homodimer fluorescence) occupying a bowtie shaped pattern, as shown in Figure 1. IIF was identified as a directional wave with a time scale of ~3 ms (Stott, 2006). The temperature and location of IIF initiation were determined from frame by frame playback of the video.

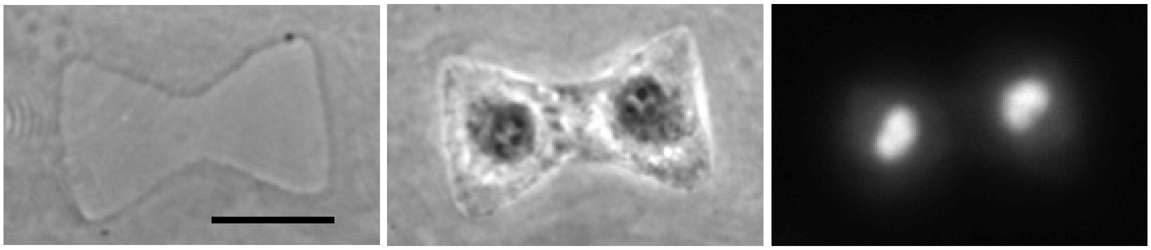

FIGURE 8.1. Phase contrast images of an empty agarose micropattern (left), and a micropattern containing two BPAEC (middle), as evidenced by Syto-13 nuclear staining (right). The scale bar represents 30 μm.

Analysis of IIF rates

For analysis of the rates of the state transitions described by Eqs. 11 and 12, the following strategy was used. For a general state transition between an initial state and a final state with a first-order rate coefficient *J*, the rate at which the final state is formed is proportional to the number of cell pairs in the initial state:

$$\frac{dN_f}{dt} = JN_i \qquad [17]$$

Solving Eq. 17 for the time integral of the rate *J*, which is indicative of the likelihood that a given cell pair in the initial state will reach the final state in a time *t*, one obtains

$$\int_0^t J dt = \int_0^{N_f(t)} \frac{dN_f}{N_i} \qquad [18]$$

where N_i is the number in the initial state and N_f is the number that have passed from the initial state to the final state (i.e., the number of state transitions that have occurred). Since dN_f and N_i can only assume integer values, the integral in Eq. 18 can be replaced a trapezoidal integral approximation comprising a summation over the transitions between the initial and final states:

$$\int_0^t J dt = \frac{1}{2} \sum_{k=1}^{N_f(t)} \left(\frac{1}{N_i(t_k^-)} + \frac{1}{N_i(t_k^+)} \right) \qquad [19]$$

In Eq. 19, $N_i(t_k^-)$ is the number in the initial state before the kth state transition and $N_i(t_k^+)$ is the number in the initial state after the kth state transition. The time integrals associated with the state transitions described by Eqs. 11 and 12 were calculated from experimental data using Eq. 19. For a small number of state transitions, $N_i(t_k^+)$ was zero, the reciprocal of which is undefined. In these instances, the left Riemann sum integral approximation was used:

$$\int_{t_k^-}^{t_k^+} J dt = \frac{1}{N_i(t_k^-)} \qquad [20]$$

The rates of the state transitions were determined from the time integrals using a linear fit to 15 consecutive data points. The rate of independent IIF was calculated by noting that the rate of the transition between the unfrozen state and the singlet state is equal to twice the independent IIF rate. Determination of the propagation was more complicated since the rate of the transition between the singlet and doublet states is equal to the sum of the independent IIF rate and the propagation rate. To isolate the effect of propagation, the independent IIF rate was subtracted from the data for the rate of the transition between singlet and doublet states.

Prediction of Cell Dehydration

Cell dehydration was predicted during freezing using Eqs. 1-5 with water transport parameters determined for BPAEC monolayers in a previous study (Chapter 6). We used an activation energy for water transport of 49 kJ/mol, and a reference water permeability parameter at 21°C of $L_pA/V_{w0} = 3.2 \times 10^{-8}$ Pa^{-1} s^{-1}.

Statistical Analysis

Unless otherwise noted, data are reported as averages and standard error of the mean. For normally distributed data and equal variances, the data were analyzed by ANOVA, followed by Tukey's tests. When either of these criteria was not met (i.e., normal distribution, equal variances), the data were analyzed using a nonparametric ANOVA (Kruskal-Wallis), followed by Dunn's method for pairwise comparisons. For classification of events into categories (i.e., IIF location), the standard deviation was estimated as square root of the number of observations in each category, as expected for a homogeneous Poisson process. These frequency data were analyzed using χ^2 tests. Differences were considered to be significant at a confidence level of 95% ($p < 0.05$).

Results

Figure 2 compares the kinetics of IIF in micropatterned BPAEC pairs subjected to the freezing protocols described in Table 1. The mean IIF temperature was -29.0±0.7°C, -33.9±0.8°C, -39.9±0.8°C, -26.6±0.8°C and -26.0±0.7°C for protocols 1, 2, 3, 4, and 5, respectively, revealing a significant effect of the cryopreservation protocol on the IIF temperature ($p < 0.05$). Pairwise comparisons yielded significantly lower IIF temperatures as the hold temperature decreased. However, the cooling rate did not significantly affect the IIF temperature.

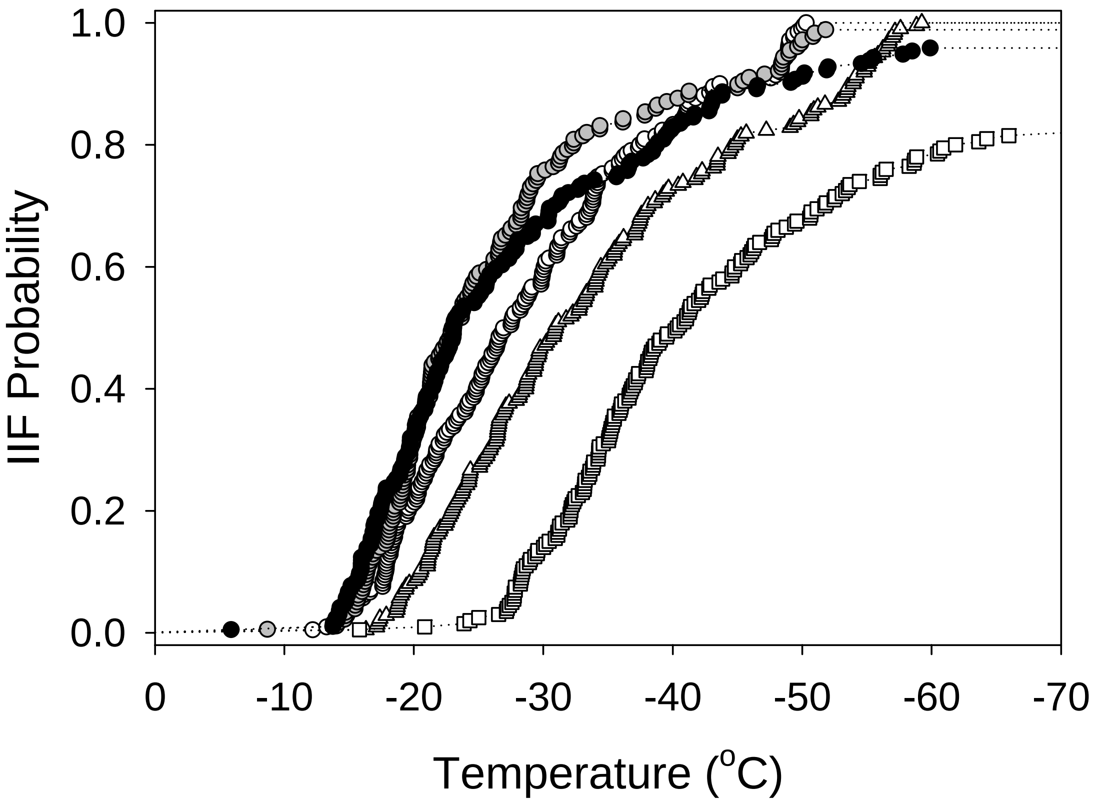

FIGURE 8.2. Effect of cryopreservation protocol on the cumulative probability of IIF. To investigate the effect of the hold temperature on IIF, cell pairs in the presence of 5% v/v DMSO were frozen at 130°C/min from holding temperatures of -3°C (open circles), -5°C (triangles) or -8°C (squares). To explore the effect of cooling rate on IIF, cell pairs were cooled at 80°C/min (gray circles) and 40°C/min (black circles) from a hold temperature of -3°C.

To facilitate investigation of the causes for the observed differences in IIF kinetics, we explored the mechanisms of IIF in the micropatterned BPAEC pairs by examining the location of IIF initiation, as summarized in Table 2. We classified IIF initiation sites into four categories: the cell perimeter, the cell interior, the cell-cell interface, and unknown. For the first cell in the pair to undergo IIF, the majority of IIF initiation sites were at the cell perimeter, indicating an IIF mechanism specific to this site for transition between the unfrozen state and the singlet state. In contrast, IIF initiation in the second cell occurred predominantly at the cell-cell interface, indicating an IIF mechanism specific to the interface for transition between the singlet and doublet states. These data are consistent with the presence of a propagative IIF mechanism that is only active when internal ice is present in a neighboring cell (i.e., the singlet state), causing a transition between independent IIF in the first cell to undergo IIF (yielding IIF at the cell perimeter) and intercellular ice propagation in the second cell to undergo IIF (yielding IIF at the cell-cell interface).

TABLE 8.2. IIF Location.

Protocol[a]	**1st or 2nd Cell to Freeze?**	**Perimeter (%)**	**Interface (%)**	**Interior (%)**	**Unknown (%)**
1	1st	69 ± 8	15 ± 4	6 ± 2	10 ± 3
	2nd	16 ± 4*	70 ± 8*	7 ± 3	8 ± 3
2	1st	67 ± 8	16 ± 4	11 ± 3	6 ± 2
	2nd	22 ± 5*	57 ± 7*	11 ± 3	9 ± 3
3	1st	46 ±7	26 ± 5	11 ± 4	18 ± 4
	2nd	18 ± 5*	55 ± 8*	5 ± 3	22 ± 5
4	1st	65 ± 8	26 ± 5	7 ± 3	2 ± 2
	2nd	29 ± 6*	52 ± 8*	11 ± 4	9 ± 3
5	1st	64 ± 9	26 ± 5	6 ± 3	5 ± 2
	2nd	18 ± 5*	71 ± 9*	7 ± 3	5 ± 2

[a] Cryopreservation protocols are given in Table 1.
* Indicates a significant difference from the 1st cell to freeze ($p < 0.05$).

Further evidence for the presence of intercellular ice propagation is obtained by examining the singlet state probability. As shown in Figure 3, the singlet state probability falls well below the predictions in the absence of propagation for all the cryopreservation protocols investigated, indicating that the IIF events in the cell pairs are correlated, most likely as result of intercellular ice propagation. These data for the probability of the singlet state, together with the IIF location results, justify the mathematical description of IIF in the cell pairs in terms of two rate processes: independent IIF and intercellular ice propagation.

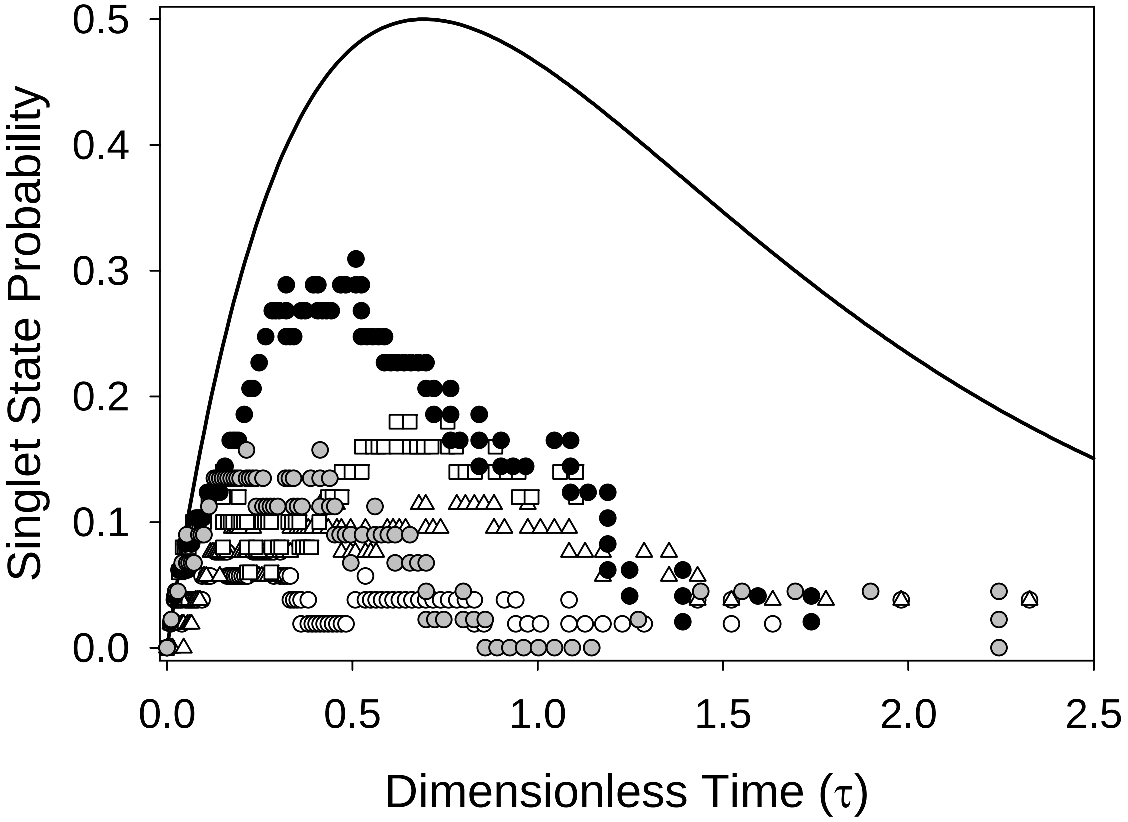

FIGURE 8.3. Effect of cryopreservation protocol on the singlet state probability. Cell pairs in the presence of 5% v/v DMSO were frozen at 130°C/min from hold temperatures of -3°C (open circles), -5°C (triangles) or -8°C (squares). Cell pairs were also cooled at 80°C/min (gray circles) and 40°C/min (black circles) from a hold temperature of -3°C.

To examine the effect of the freezing protocol on the kinetics of independent IIF, we determined the mean time after initiation of cooling for the transition between the unfrozen state and the singlet state (i.e., unfrozen state persistence time), as summarized in Table 3. Since the rate of this state transition is twice the independent IIF rate (see Eq. 11), the mean unfrozen state persistence time can be used as an indicator of the average independent IIF rate. The mean unfrozen state persistence time ranged between 6.5 s and 31.3 s, representing a significant effect of the freezing protocol on the unfrozen state persistent time, and indicating that the average rate of independent IIF is affected by the freezing protocol.

The effect of freezing protocol on the rate of intercellular ice propagation was examined using the singlet state persistence time, which is expected to be inversely related to the sum of the independent IIF and propagation rates (see Eq. 12). As shown in Table 3, the singlet state persistence time varied by more than an order of magnitude, resulting in a significant effect of the freezing protocol on the singlet state persistence time, and suggesting that the propagation rate is affected by the freezing protocol.

TABLE 8.3. Persistence time for the unfrozen state and the singlet state.

Protocol[*]	**Unfrozen State Persistence Time (s)**	**Singlet State Persistence Time (s)**
1	11.7 ± 0.5	0.7 ± 0.1
2	12.6 ± 0.5	1.7 ± 0.3 [a]
3	13.9 ± 0.5	2.0 ± 0.3 [a]
5	31.3 ± 1.6 [abc]	8.0 ± 1.1 [ab]
5	16.6 ± 0.8 [abd]	1.4 ± 0.3 [ad]

[*] Cryopreservation protocols are given in Table 1.
[a-d] Statistically significant difference from protocol 1, 2, 3 or 4, respectively.

Whereas the rates of independent IIF and intercellular ice propagation may be affected by the thermodynamic state of cytoplasm (temperature, composition), which changes throughout the freezing process, we predicted the changes in the cytoplasm composition using a model of cell dehydration (Eqs. 1-5). These numerical simulations were used to obtain the cell water content, intracellular supercooling and cytoplasm viscosity, as shown in Figure 4. All of the cryopreservation protocols resulted in a reduction in the cell water content during cooling, the magnitude of which was largest for the slowest cooling rate (40°C/min). These predictions of cell water content were used to determine the intracellular supercooling, which generally increased during the cooling process. For cooling at 130°C/min, the intracellular supercooling exhibited an approximately linear increase during cooling that was nearly consistent with the expectation for negligible water transport (i.e., for these protocols, the supercooling was not appreciably affected by membrane water transport). However, cooling at the slowest rate yielded an initial maximum in the supercooling of approximately 10°C, a reduction in supercooling to < 5°C, and finally a region of approximately linearly increasing supercooling. The cytoplasm viscosity increased by multiple orders of magnitude during cooling. The most dramatic changes in viscosity were observed for the slowest cooling rate, resulting in an increase of almost 3 orders of magnitude.

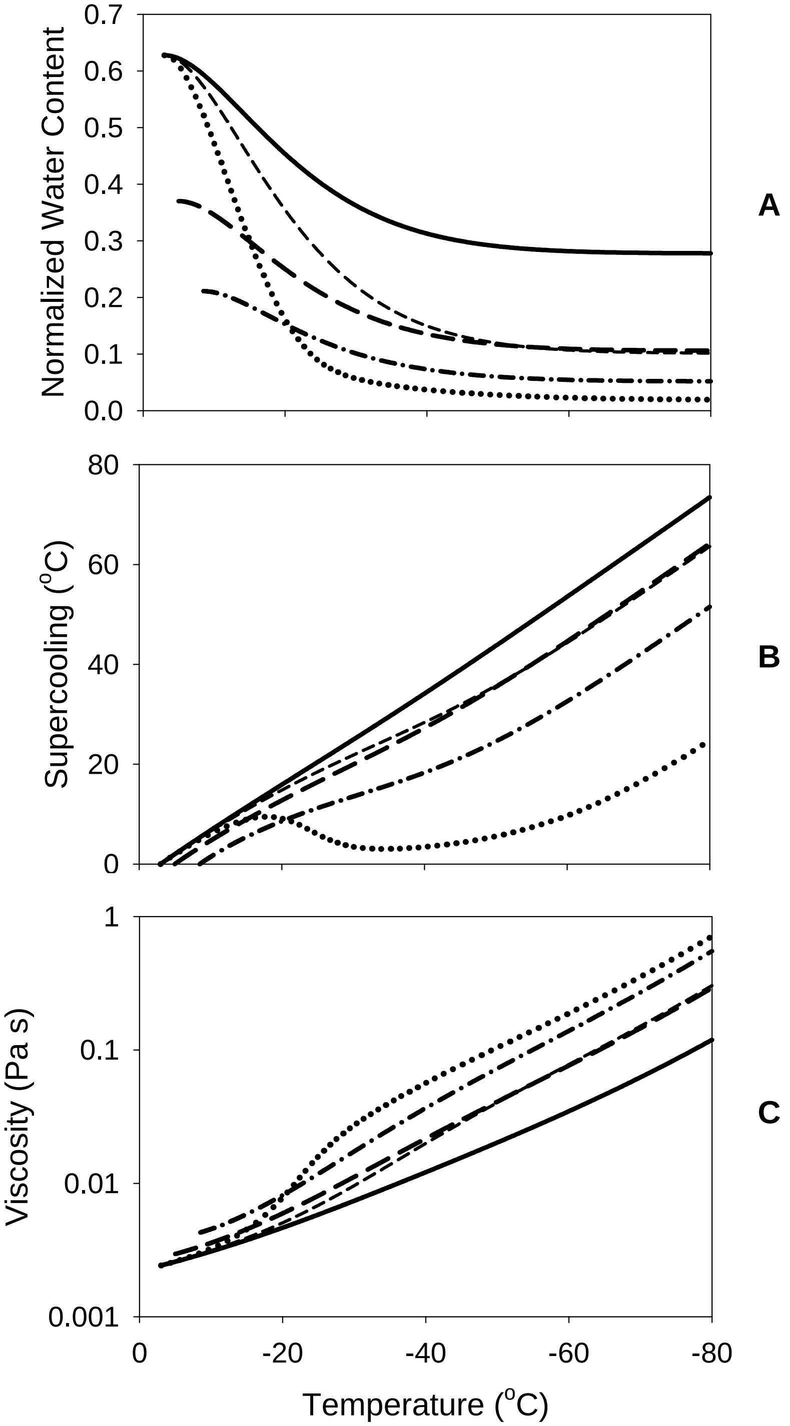

FIGURE 8.4. Predicted cellular water content (A, normalized to isotonic conditions), intracellular supercooling (B) and viscosity (C) during freezing. Cell pairs in the presence of 5% v/v DMSO were frozen at 130°C/min from hold temperatures of -3°C (solid lines), -5°C (long-dash) or -8°C (dash-dot). Cell pairs were also cooled at 80°C/min (short-dash) and 40°C/min (dotted lines) from a hold temperature of -3°C.

The cell dehydration predictions shown in Figure 4 were then used to examine the dependence of the rate of independent IIF on the intracellular supercooling and viscosity. Figure 5 illustrates the independent IIF rate as a function of viscosity and supercooling. To establish the dependence of the independent IIF rate on these parameters, the data for cell pairs cooled at 130°C/min (i.e., protocols 1-3) were fit to a power law function, yielding ($R^2 = 0.65$):

$$J_i = \left(2.143\times10^{-3}\right)\Delta T^{1.0975}\eta^{-0.0557} \qquad [21]$$

The exponent for the supercooling was significantly greater than zero, yielding an approximately linear dependence of the independent IIF rate on the supercooling. The exponent for the viscosity was significantly less than zero, which is consistent with a reduction in the independent IIF rate as the viscosity increases. However, the small magnitude of the exponent indicates that the independent IIF rate is not strongly dependent on viscosity.

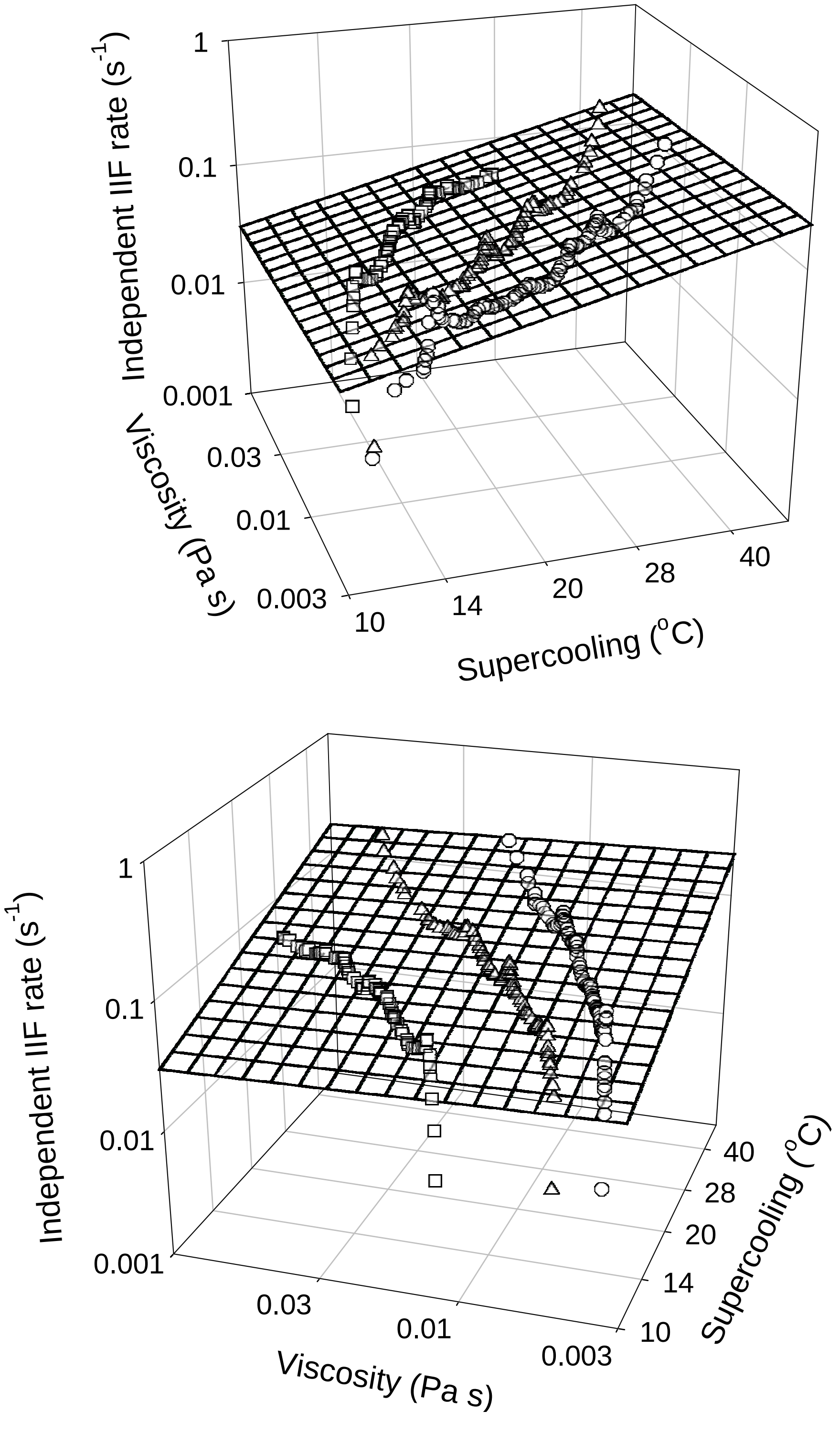

FIGURE 8.5. Effect of intracellular supercooling and viscosity on the independent IIF rate for cell pairs cooled at 130°C/min from hold temperatures of -3°C (circles), -5°C (triangles) and -8.5°C (squares). The mesh plot shows the best-fit power law function.

To validate the best-fit function describing the independent IIF rate as a function of supercooling and viscosity (Eq. 21), we compared the predicted independent IIF rate with experimental data for cooling rates of 40°C/min and 80°C/min, as shown in Figure 6. The predictions for the independent IIF rate approximately match the experimental data, correctly predicting the observed trend of decreasing independent IIF rate with decreasing cooling rate.

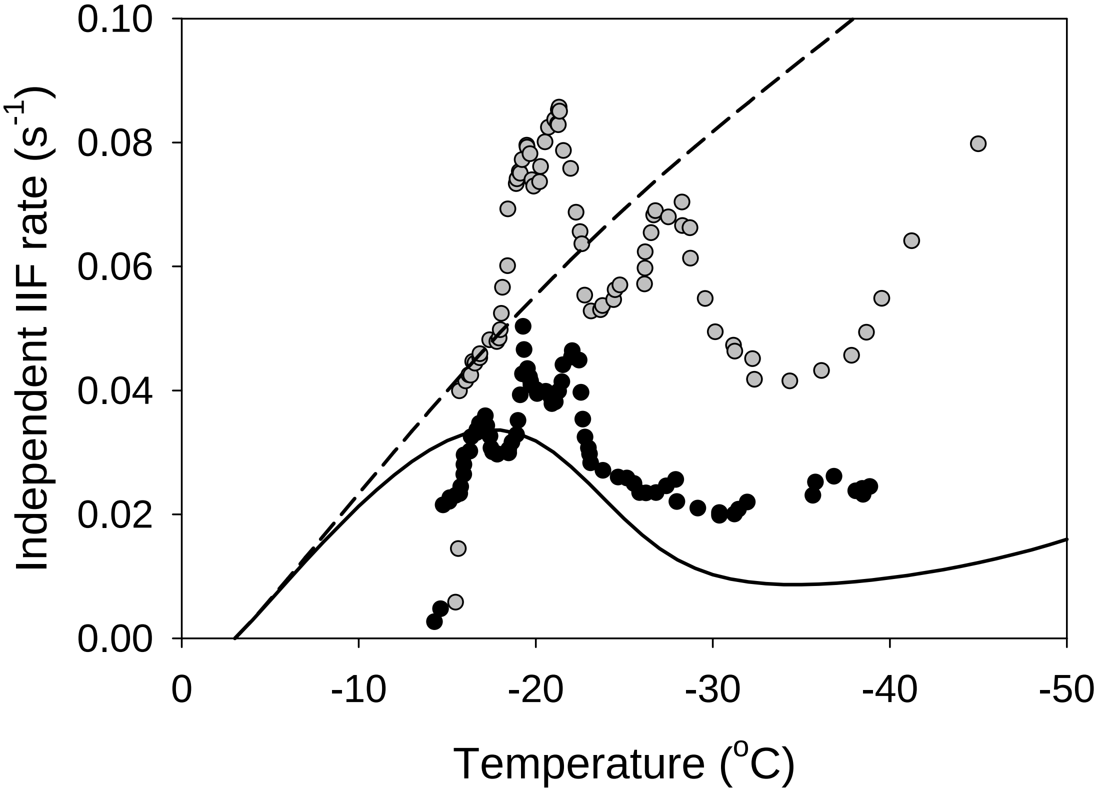

FIGURE 8.6. Validation of the best-fit model for the independent IIF rate. Experimental data and predictions are given for cell pairs cooled at 80°C/min (gray circles and short-dash, respectively) and 40°C/min (black circles and solid line, respectively).

Next, we evaluated the effect of intracellular supercooling and viscosity on the rate of intercellular ice propagation, as illustrated in Figure 7. The data for cell pairs cooled at 130°C/min were fit to a power law model, yielding the following best-fit equation (R^2 = 0.47):

$$J_p = \left(1.297 \times 10^{-3}\right)\Delta T^{0.7982}\eta^{-0.95} \qquad [22]$$

The exponents for both supercooling and viscosity were significantly different from zero, indicating a significant effect of both variables on the propagation rate. The propagation rate tended to increase with supercooling, as evidenced by the positive exponent, whereas the propagation rate tended to decrease as the viscosity increased, as evidenced by the negative exponent. The magnitude of the supercooling exponent was similar for both propagation and independent IIF, indicating a similar dependence of the rates of propagation and independent IIF on this variable. However, the exponents for the viscosity differed by more than two orders of magnitude, indicating that the propagation rate is more strongly dependent on the viscosity.

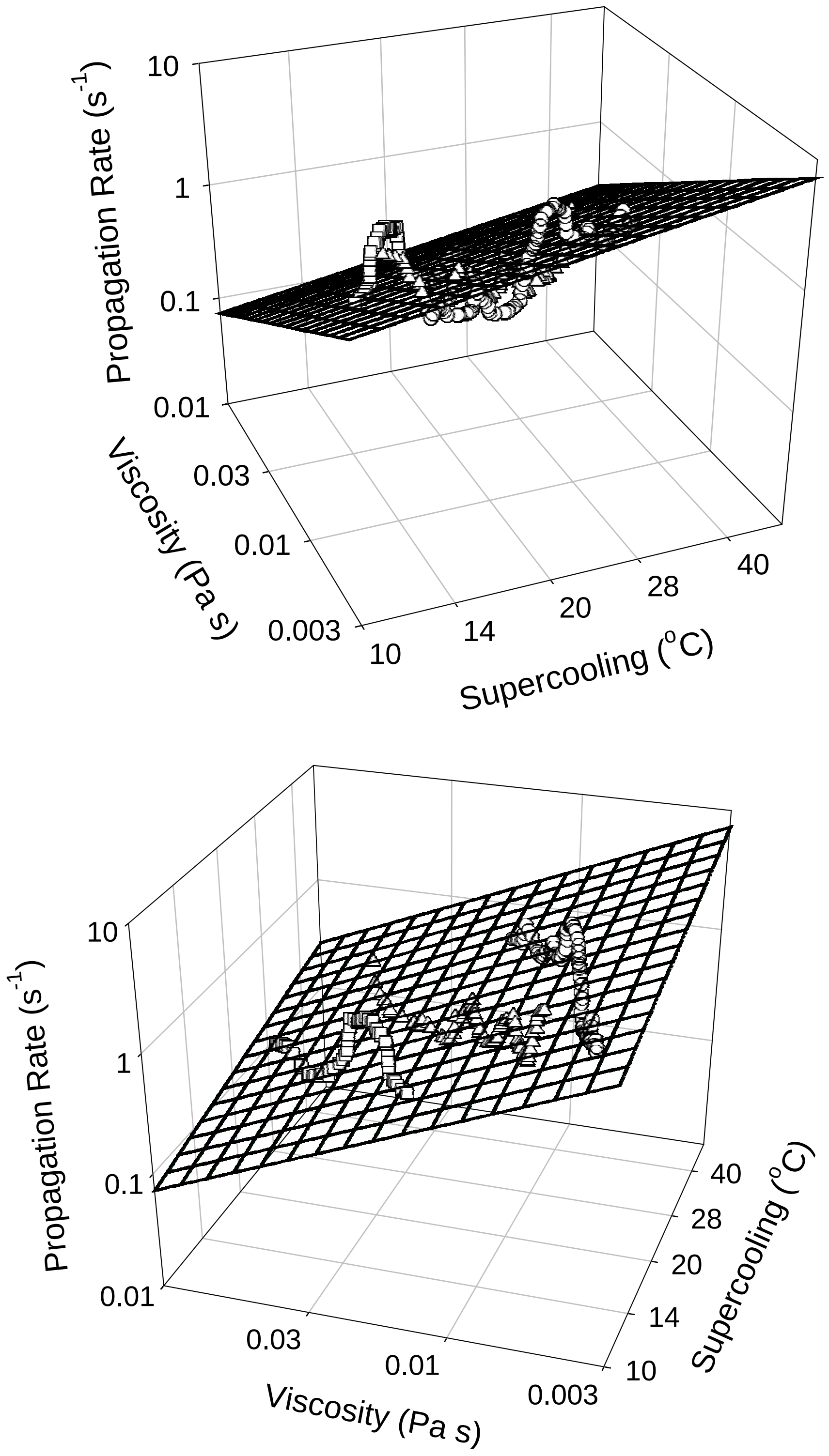

FIGURE 8.7. Effect of intracellular supercooling and viscosity on the propagation rate for cell pairs cooled at 130°C/min from hold temperatures of -3°C (circles), -5°C (triangles) and -8.5°C (squares). The mesh plot shows the best-fit power law function.

To validate the best-fit model for the propagation rate, experimental data for cooling rates of 40°C/min and 80°C/min were compared against model predictions, as shown in Figure 8. The data for cooling at 80°C/min approximately matches the model predictions, but cooling at 40°C/min yielded lower propagation rates than the predictions. Despite the deviations between the data and the model, the trend of decreasing propagation rate with decreasing cooling rate was correctly predicted by the model.

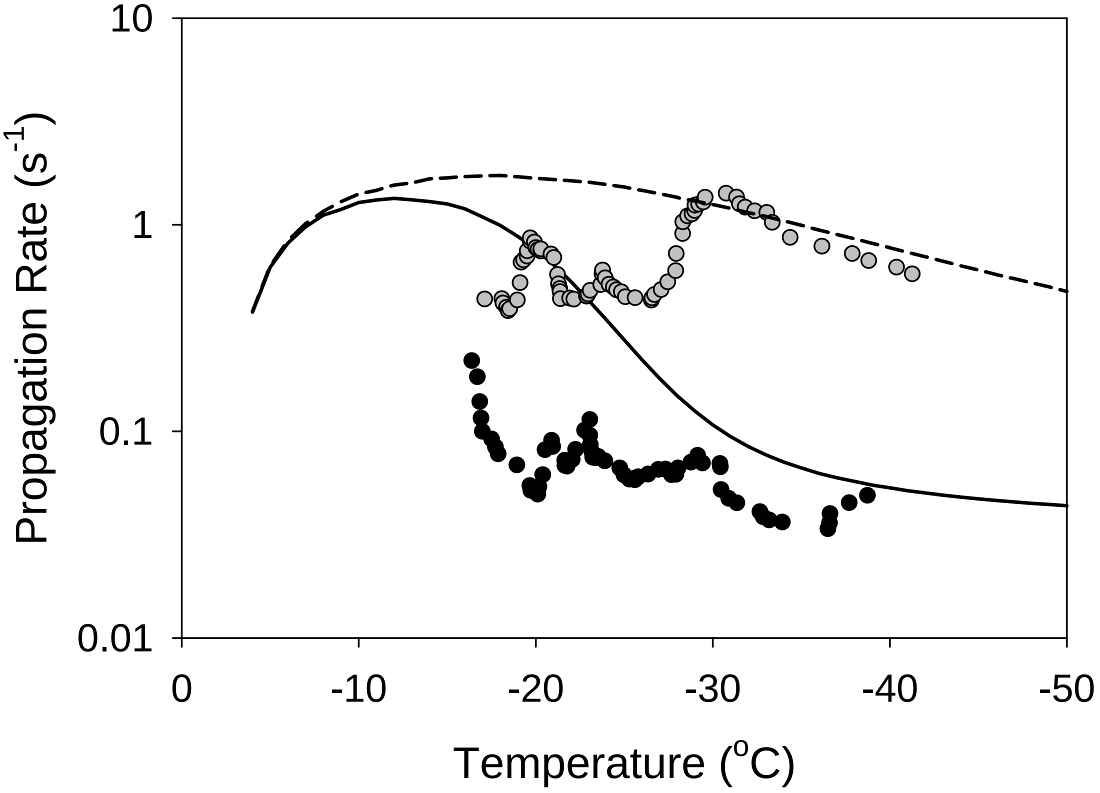

FIGURE 8.8. Validation of the best-fit model for the intercellular ice propagation rate. Experimental data and predictions are given for cell pairs cooled at 80°C/min (gray circles and short-dash, respectively) and 40°C/min (black circles and solid line, respectively).

Discussion

The purpose of this study was to investigate the effect of the intracellular supercooling and viscosity, variables that describe the thermodynamic state of the cytoplasm, on the kinetics of IIF in tissue. We showed that IIF in BPAEC pairs could be described in terms of independent IIF and intercellular ice propagation, and that the kinetics of these IIF mechanisms was influenced by the freezing protocol. To investigate the reasons for these differences, we determined the rates of independent IIF and propagation as a function of intracellular supercooling and viscosity. We fit a simple power law model to the data, revealing a significant effect of both supercooling and viscosity on the rates of independent IIF and intercellular ice propagation.

Despite the simplicity of the models for the rates of independent IIF and propagation, the model predictions approximately match the trends in the data, suggesting that these models can be used to aide in the design of cryopreservation procedures for tissue. The rates of independent IIF and propagation decreased as the cooling rate decreased, suggesting that the incidence of IIF can be reduced by reducing the cooling rate. This trend is consistent with the trend of increasing cell death with increasing cooling rate that has been observed for both tissue (Armitage and Juss, 1996; Merchant et al., 1996; Oegema et al., 2000; Pasch et al., 1999; Pegg, 2002) and cell suspensions (Mazur et al., 1972; Toner, 1993).

In this study we assumed that the kinetics of IIF in tissue could be determined given the thermodynamic state of the intracellular solution, an assumption that has proved to be valid for cell suspensions (Karlsson et al., 1993, 1994, 1996). The variables needed to describe the state of the cytoplasm are the temperature, the pressure (assumed to be atmospheric), the cell water content, and intracellular CPA content (the content of endogenous solutes is not a unique variable and can be determined from the water content and the CPA content). Whereas the thermodynamic state of the cytoplasm depends on three variables that change throughout the freezing process (temperature, water content, CPA content), we have only considered two quantities to characterize the state of the cytoplasm: the supercooling and the viscosity. This approach not only allowed simplification of the analysis (since only two variables were considered), but also permitted expression of the IIF rates in terms of more physically meaningful quantities, since the supercooling represents the thermodynamic driving force for formation of intracellular ice and the viscosity is expected to affect the kinetics of ice formation. However, because of the simplification involved in describing the thermodynamic state in terms of two variables (rather than three), it is possible that there are effects that we did not capture with our simple models. As more tissue IIF data becomes available, it may be possible to explore more thorough modeling approaches that include all of the necessary thermodynamic state variables.

The interpretation of the results in the present study is limited by the uncertainty in the predictions of the intracellular supercooling and viscosity as a function of temperature. Although we used *in situ* measurements of water transport kinetics in monolayers of BPAEC to obtain the permeability parameters used for these predictions (Chapter 6), the experiments were performed at suprazero temperatures and extrapolated to subzero temperatures, which can be associated with error (Rule et al., 1980). In addition, the predictions of cell water content are highly sensitive to the value of the activation energy, and as a consequence, slight error in estimates for the activation energy can lead to dramatic differences in the predicted supercooling and viscosity (Karlsson et al., 1993; Chapter 7).

In summary, we have demonstrated that the IIF kinetics in tissue constructs can be described as a function of the intracellular supercooling and viscosity, which are variables that can be modulated by the freezing protocol details, such as CPA concentration and cooling rate. We fit simple power-law models to the data for the rates of independent IIF and intercellular ice propagation, enabling prediction of IIF kinetics during tissue freezing. Despite the simple phenomenological nature of these models, the predictions match the expected trends in IIF kinetics, emphasizing the potential value of mathematical modeling approaches for cryopreservation protocol design. Future investigations of the physical mechanisms of IIF in tissue promises to lead to more accurate mechanistic models of the IIF process, which will ultimately lead to improved strategies for tissue cryopreservation.

CHAPTER 9

CONCLUSIONS

Cryopreservation is a critical technology for reducing the cost of medical therapies involving living cells or tissue (e.g., organ transplants), and for efficiently producing products containing living material (e.g., tissue-engineering products). However, current approaches for cryopreservation of tissue frequently result in unacceptable reductions in cell viability. The development of successful tissue cryopreservation strategies is hindered by an inadequate understanding of cell membrane mass transport and intracellular ice formation (IIF) in tissue. The goal of this research was to investigate membrane water transport and intracellular ice formation in tissue, towards the development of tissue cryopreservation strategies.

Whereas previous studies have suggested using the membrane permeability properties derived from cell suspensions to predict membrane mass transport during tissue cryopreservation (e.g., Ebertz and McGann, 2002), there is evidence in the literature that the membrane permeability in intact tissue differs from that of the corresponding cell suspension (Bischof, 2000; Yarmush et al., 1992). With the goal of determining a strategy for obtaining the permeability parameters necessary to predict membrane mass transport during tissue freezing, we measured the membrane permeability in both monolayers and suspensions comprising two different cell types (bovine pulmonary artery endothelial cells and MIN6 cells, a mouse β-cell line), using a recently developed fluorescence quenching technique (Solenov et al., 2004) and the well-known electronic cell sizing method, respectively. We made significant improvements to both the fluorescence quenching technique and the electronic sizing method, leading to more accurate membrane permeability measurements. Comparison between monolayers and suspensions revealed differences in membrane mass transport kinetics, resulting in differences in the predictions of membrane mass transport during freezing. Thus, the practice of using permeability properties derived from cell suspensions as a tool for designing tissue cryopreservation procedures is not adequate, and *in situ* permeability measurement methods such as the fluorescence quenching technique are needed.

Although we obtained membrane permeability data in cell monolayers, our ultimate objective is to develop cryopreservation procedures for three-dimensional tissue. We posit that the membrane permeability properties of cells within a three-dimensional tissue can be more accurately approximated using the membrane permeability properties of cell monolayers than the corresponding cell suspensions. The cell isolation process (chemical and mechanical disaggregation to form a cell suspension) was shown to alter the membrane permeability properties, illustrating that the permeability properties of cell suspensions are poor indicators of the permeability in intact tissue. Furthermore, monolayers exhibit many of the physical characteristics of three-dimensional tissue that may affect the membrane permeability, such as cell-matrix interactions, cell-cell interactions and an organized cytoskeleton. To test the validity of using the membrane permeability properties of cell monolayers to predict membrane mass transport in three-dimensional tissue, direct measurement of the membrane permeability in three-dimensional tissue will be required. However, convenient techniques for measurement of the permeability in three-dimensional tissue are currently not available.

An accurate description of cell membrane mass transport in three-dimensional tissue will require modeling of mass transport in the interstitial space, as well as mass transport across the cell membrane. Although the membrane permeability properties that we measured for cell monolayers can be used to predict membrane mass transport, additional tissue-specific parameters are needed to describe mass transport in the interstitial space. For example, transport in pancreatic islets has been described using a network thermodynamic model, which employs tissue-specific interstitial diffusion parameters to characterize mass transport in the interstitial space, and membrane permeability parameters to characterize mass transport across the cell membrane (de Freitas et al., 1997).

Although the mechanisms of IIF in cell suspensions are relatively well understood, new IIF mechanisms exist in tissue that are only recently being investigated. Since several researchers have observed enhanced IIF kinetics associated with cell-cell interactions, we have investigated the effect of the architecture of the cell-cell interface on IIF using genetically modified cells expressing different levels of intercellular junction proteins. We observed a new phenomenon in these cells – penetration of extracellular ice into the paracellular space at the cell-cell interface – and showed that this phenomenon was spatially and temporally correlated with IIF, suggesting a causative link between interaction with the extracellular ice and subsequent IIF. In genetically modified cells lacking the tight junction protein occludin, the temperature and incidence of paracellular ice penetration and IIF were reduced, suggesting that tight junctions may protect cells during freezing by preventing penetration of extracellular ice into the cell-cell interface.

Our observation of paracellular ice penetration at the cell-cell interface, coupled with the recent observation of penetration of extracellular ice between the basal cell membrane and the glass substrate (Stott, 2006), point towards potential strategies for reducing IIF in tissue by blocking cell-ice interactions at the cell-cell and cell-substrate connections. There are several potential approaches for blocking cell-ice interactions. It may be possible to sterically prevent cell-ice interactions by modifying the cell surface using, for example, poly-ethylene glycols (Kellem et al., 2003). Additionally, because our results suggest that tight junctions reduce the likelihood of paracellular ice penetration, it may be possible to prevent damaging cell-ice interactions by transient expression of proteins involved in tight junctions.

In cell suspensions, IIF has been shown to be linked to the extent of cell membrane water transport during freezing, leading to models describing IIF in terms of the cytoplasm composition and temperature (Karlsson et al., 1996). However, the dependence of IIF in tissue on these factors is not known since most studies of IIF in tissue have used fast cooling rates (i.e., precluding membrane water transport). We measured the kinetics of IIF in tissue constructs comprising two cells during cooling at various rates in the presence of CPA, revealing that the rates of independent IIF and propagation are positively correlated with the intracellular supercooling and negatively correlated with the viscosity. We determined simple phenomenological models for the rates of independent IIF and propagation, and showed that the model predictions match the trends in the experimental data. Using these models, it is possible to predict IIF as a function of protocol parameters that are controllable experimentally (e.g., cooling rate, CPA concentration), representing an important step towards designing tissue cryopreservation protocols using mathematical models.

Although the IIF data in the present study was obtained using tissue constructs comprising two cells, the IIF rate processes that we investigated (i.e., independent IIF and propagation) can be used to predict IIF in larger tissues. The results reported by Irimia and Karlsson (2005) provide evidence of the potential for using experiments with two cell constructs to describe IIF in larger tissues. They demonstrated that IIF in linear arrays comprising four cells could be predicted using the rates of independent IIF and propagation measured using two cell constructs. Assuming that the rates of independent IIF and propagation that we measured in two-cell constructs can be extended to larger tissues, the modeling approach presented here can be used to predict the kinetics of IIF in larger tissues, given the spatial arrangement of the cells in the tissue. Future studies are necessary to test the accuracy of model predictions for larger tissues against experiment measurements of IIF.

By studying IIF and membrane mass transport in tissue constructs, we obtained an improved understanding of the tissue cryopreservation process, which may lead to the development of new strategies for the cryopreservation of tissue. We determined the membrane permeability parameters necessary for predicting cell membrane transport in tissue constructs, and we developed phenomenological models for the rates of independent IIF and intercellular ice propagation in terms of the cytoplasm supercooling and viscosity, which vary during cooling because of membrane water transport. Using coupled models describing membrane water transport and the kinetics of IIF in tissue, it may be possible to optimize the cooling procedure and CPA concentration by predicting conditions that avoid IIF. Furthermore, we identified a new IIF mechanism associated with penetration of extracellular ice into the cell-cell interface, and showed that loss of the tight junction protein occludin was associated with an enhanced IIF probability. These data suggests that it may be possible to reduce the likelihood of IIF by blocking cell-ice interactions at the cell-cell interface, representing a new strategy for tissue cryopreservation.

REFERENCES

(1996). CRC Handbook of Chemistry and Physics, 77th edn (CRC Press).

Acker, J., Pasch, J., Heschel, I., Rau, G., and McGann, L. (1999a). Comparison of optical measurement and electrical measurement techniques for the study of osmotic responses of cell suspensions. Cryo Letters *20*, 315-324.

Acker, J.P., Elliott, J.A., and McGann, L.E. (2001). Intercellular ice propagation: experimental evidence for ice growth through membrane pores. Biophys J *81*, 1389-1397.

Acker, J.P., Larese, A., Yang, H., Petrenko, A., and McGann, L.E. (1999b). Intracellular ice formation is affected by cell interactions. Cryobiology *38*, 363-371.

Acker, J.P., and McGann, L.E. (1998). The role of cell-cell contact on intracellular ice formation. Cryo Letters *19*, 367-374.

Acker, J.P., and McGann, L.E. (2002). Innocuous intracellular ice improves survival of frozen cells. Cell Transplant *11*, 563-571.

Adams, R.B., Voelker, W.H., and Gregg, E.C. (1967). Electrical counting and sizing of mammalian cells in suspension: an experimental evaluation. Phys Med Biol *12*, 79-92.

Adams, S.L., Kleinhans, F.W., Mladenov, P.V., and Hessian, P.A. (2003). Membrane permeability characteristics and osmotic tolerance limits of sea urchin (Evechinus chloroticus) eggs. Cryobiology *47*, 1-13.

Agca, Y., Liu, J., Mullen, S., Johnson-Ward, J., Gould, K., Chan, A., and Critser, J. (2005a). Chimpanzee (Pan troglodytes) spermatozoa osmotic tolerance and cryoprotectant permeability characteristics. J Androl *26*, 470-477.

Agca, Y., Mullen, S., Liu, J., Johnson-Ward, J., Gould, K., Chan, A., and Critser, J. (2005b). Osmotic tolerance and membrane permeability characteristics of rhesus monkey (Macaca mulatta) spermatozoa. Cryobiology *51*, 1-14.

Aggarwal, S., Diller, K., and Dawidson, I. (1986). Microscopic response of dog pancreas beta-cells to freezing and osmotic stresses. Cryo Letters *7*, 218-225.

Altamirano, J., Brodwick, M.S., Alvarez-Leefmans, F.J. (1998). Regulatory Volume Decrease and Intracellular Ca2+ in Murine Neuroblastoma Cells Studied with Fluorescent Probes. J Gen Physiol *112*, 145-160.

Anderson, E.C., Petersen, D.F., and Tobey, R.A. (1970). Density invariance of cultured Chinese hamster cells with stage of the mitotic cycle. Biophys J *10*, 630-645.

Armitage, W., and Juss, B. (1996a). The influence of cooling rate on survival of frozen cells in monolayers and in suspensions. Cryo Letters *17*, 213-218.

Armitage, W.J. (1986). Effect of solute concentration on intracellular water volume and hydraulic conductivity of human blood platelets. J Physiol *374*, 375-385.

Armitage, W.J., and Juss, B.K. (1996b). Osmotic response of mammalian cells: effects of permeating cryoprotectants on nonsolvent volume. J Cell Physiol *168*, 532-538.

Balasubramanian, S.K., Bischof, J.C., and Hubel, A. (2006). Water transport and IIF parameters for a connective tissue equivalent. Cryobiology *52*, 62-73.

Bell, G.I., and Anderson, E.C. (1967). Cell growth and division. I. A mathematical model with applications to cell volume distributions in mammalian suspension cultures. Biophys J *7*, 329-351.

Ben-Sasson, S., Patinkin, D., Grover, N.B., and Doljanski, F. (1974). Electrical sizing of particles in suspensions. IV. Lymphocytes. J Cell Physiol *84*, 205-214.

Benson, C.T., Liu, C., Gao, D.Y., Critser, E.S., Benson, J.D., and Critser, J.K. (1998). Hydraulic conductivity (Lp) and its activation energy (Ea), cryoprotectant agent permeability (Ps) and its Ea, and reflection coefficients (sigma) for golden hamster individual pancreatic islet cell membranes. Cryobiology *37*, 290-299.

Benson, C.T., Liu, C., Gao, D.Y., Critser, E.S., and Critser, J.K. (1993). Determination of the osmotic characteristics of hamster pancreatic islets and isolated pancreatic islet cells. Cell Transplant *2*, 461-465.

Berg, R. (1992). Sample concentration in particle size analysis. American Laboratory *February*, 83-84.

Berger, W.K., and Uhrik, B. (1996). Freeze-induced shrinkage of individual cells and cell-to-cell propagation of intracellular ice in cell chains from salivary glands. Experientia *52*, 843-850.

Berner, J.-L., Gervais, P. (1993). A New Visualization Chamber to Study the Transient Volumetric Response of Yeast Cells Submitted to Osmotic Shifts. Biotechnology and Bioengineering *43*, 165-170.

Bischof, J.C. (2000). Quantitative measurement and prediction of biophysical response during freezing in tissues. Annu Rev Biomed Eng *2*, 257-288.

Brodkey, R.S. (1995). The Phenomena of Fluid Motions, 4 Rev edn (Dover Publications).

Brown, M.S. (1980). Freezing of nonwoody plant tissues. IV. Nucleation sites for freezing and refreezing of onion bulb epidermal cells. Cryobiology *17*, 184-186.

Burmeister, J.S., Truskey, G.A., Yarbrough, J.L., and Reichert, W.M. (1994). Imaging of cell/substrate contacts on polymers by total internal reflection fluorescence microscopy. Biotechnol Prog *10*, 26-31.

Calabrese, A., Caton, D., and Meda, P. (2004). Differentiating the effects of Cx36 and E-cadherin for proper insulin secretion of MIN6 cells. Exp Cell Res *294*, 379-391.

Calabrese, A., Zhang, M., Serre-Beinier, V., Caton, D., Mas, C., Satin, L.S., and Meda, P. (2003). Connexin 36 controls synchronization of Ca2+ oscillations and insulin secretion in MIN6 cells. Diabetes *52*, 417-424.

Capo-Aponte, J.E., Iserovich, P., Reinach, P.S. (2006). Characterization of Regulatory Volume Behavior by Flourescence Quenching in Human Corneal Epithelial Cells. J Membrane Biol *207*, 11-22.

Crowe, W.E., Altamirano, J., Huerto, L., and Alvarez-Leefmans, F.J. (1995). Volume changes in single N1E-115 neuroblastoma cells measured with a fluorescent probe. Neuroscience *69*, 283-296.

Deng, T., Tien, J., Xu, B., and Whitesides, G.M. (1999). Using patterns in microfiche as photomasks in 10-mu m-scale microfabrication. Langmuir *15*, 6575-6581.

Deng, T., Wu, H., Brittain, S.T., and Whitesides, G.M. (2000). Prototyping of masks, masters, and stamps/molds for soft lithography using an office printer and photographic reduction. Anal Chem *72*, 3176-3180.

Devireddy, R.V., and Bischof, J.C. (1998). Measurement of water transport during freezing in mammalian liver tissue: Part II--The use of differential scanning calorimetry. J Biomech Eng *120*, 559-569.

Ebertz, S.L., and McGann, L.E. (2004). Cryoprotectant permeability parameters for cells used in a bioengineered human corneal equivalent and applications for cryopreservation. Cryobiology *49*, 169-180.

Echevarria, M., Verkman, A.S. (1992). Optical measurement of osmotic water transport in cultured cells. J Gen Physiol *99*, 573-589.

Elmoazzen, H.Y., Chan, C.C., Acker, J.P., Elliott, J.A., and McGann, L.E. (2005). The effect of cell size distribution on predicted osmotic responses of cells. Cryo Letters *26*, 147-158.

Farinas, J., Kneen, M., Moore, M., Verkman, A.S. (1997). Plasma Membrane Water Permeability of Cultured Cells and Epithelia Measured by Light Microscopy with Spatial Filtering. J Gen Physiol *110*, 283-296.

Farinas, J., Simanek, V., Verkman, A.S. (1995). Cell Volume Measured by Total Internal Reflection Microfluorimetry: Application to Water and Solute Transport in Cells Transfected with Water Channel Homologs. Biophysical Journal *68*, 1613-1620.

Farinas, J., Verkman, A.S. (1996). Cell volume and plasma membrane osmotic water permeability in epithelial cell layers measured by interferometry. Biophys J *71(6)*, 3511-3522.

Farmer, R.E., and Macey, R.I. (1970). Perturbation of red cell volume: rectification of osmotic flow. Biochim Biophys Acta *196*, 53-65.

Fedorow, C., McGann, L.E., Korbutt, G.S., Rayat, G.R., Rajotte, R.V., and Lakey, J.R. (2001). Osmotic and cryoprotectant permeation characteristics of islet cells isolated from the newborn pig pancreas. Cell Transplant *10*, 651-659.

Gao, D.Y., Chang, Q., Liu, C., Farris, K., Harvey, K., McGann, L.E., English, D., Jansen, J., and Critser, J.K. (1998). Fundamental cryobiology of human hematopoietic progenitor cells. I: Osmotic characteristics and volume distribution. Cryobiology *36*, 40-48.

Gilmore, J.A., Du, J., Tao, J., Peter, A.T., and Critser, J.K. (1996). Osmotic properties of boar spermatozoa and their relevance to cryopreservation. J Reprod Fertil *107*, 87-95.

Gilmore, J.A., McGann, L.E., Liu, J., Gao, D.Y., Peter, A.T., Kleinhans, F.W., and Critser, J.K. (1995). Effect of cryoprotectant solutes on water permeability of human spermatozoa. Biol Reprod *53*, 985-995.

Hamann, S., Herrara-Perez, J., Bundgaard, M, Alvarez-Leefmans, F., Zeuthen, T. (2005). Water permeability of Na+ -K+ -2CL- cotransporters in mammalian epithelial cells. J Physiol *568*, 123-135.

Hamann, S., Kiilgaard, J., la Cour, M., Prause, J.U., Zeuthen, T. (2003). Cotransport of H+, lactate, and H2O in porcine retinal pigment epithelial cells. Experimental Eye Research *76*, 493-504.

Hamann, S., Kiilgaard, J., Litman, T., Alvarez-Leefmans, F. J., Winther, B..R., Zeuthen, T. (2002). Measurement of Cell Volume Changes by Fluorescence Self-Quenching. Journal of Fluorescence *12*, 139-145.

Hayashi, H., Inoue, K., Shinohara, S., Gu, Y.J., Setoyama, H., Kawakami, Y., Yamasaki, T., Cui, W.X., Kinoshita, N., Imamura, M., *et al.* (1998). New approach by tissue engineering for extended selective transplantation with a pancreatic B-cell line (MIN6). Transplant Proc *30*, 83-85.

Helleman, P.W. (1990). More about coiincidence loss and reference methods. Phys Med Biol *35*, 1159-1162.

Helleman, P.W., and Benjamin, C.J. (1969). The Toa micro cell counter. II. A study of the occurrence of 'coincidence loss'. Scand J Haematol *6*, 128-132.

Hempling, H.G. (1977). The permeability of the lymphocyte membrane: applying a particle size analyzer and a hybrid computer to measure rapid changes in cell volume. Acta Cytol *21*, 96-100.

Hempling, H.G., and White, S. (1984). Permeability of cultured megakaryocytopoietic cells of the rat to dimethyl sulfoxide. Cryobiology *21*, 133-143.

Herve, J.C., Bourmeyster, N., and Sarrouilhe, D. (2004). Diversity in protein-protein interactions of connexins: emerging roles. Biochim Biophys Acta *1662*, 22-41.

Hing, W., Poole, C., Jensen, C., & Watson, M (2000). An integrated environmental perfusion chamber and heating system for long-term high resolution imaging of living cells. Journal of Microscopy *1999, Pt 2*, 90-95.

Hoffman, J.D. (2001). Numerical Methods for Engineers and Scientists, 2nd Edition edn (CRC).

Hubel, A., Cravalho, E.G., Nunner, B., and Korber, C. (1992). Survival of directionally solidified B-lymphoblasts under various crystal growth conditions. Cryobiology *29*, 183-198.

Hunt, C.J., Armitage, S.E., and Pegg, D.E. (2003). Cryopreservation of umbilical cord blood: 1. Osmotically inactive volume, hydraulic conductivity and permeability of CD34(+) cells to dimethyl sulphoxide. Cryobiology *46*, 61-75.

Irimia, D., and Karlsson, J.O. (2002). Kinetics and mechanism of intercellular ice propagation in a micropatterned tissue construct. Biophys J *82*, 1858-1868.

Irimia, D., and Karlsson, J.O. (2005). Kinetics of intracellular ice formation in one-dimensional arrays of interacting biological cells. Biophys J *88*, 647-660.

Ishiguro, H., and Rubinsky, B. (1994). Mechanical interactions between ice crystals and red blood cells during directional solidification. Cryobiology *31*, 483-500.

Kaplan, D., Bungay, P., Sullivan, J., Zimmerberg, J. (1996). A rapid-flow perfusion chamber for high-resolution microscopy. Journal of Microscopy *181*, 286-297.

Karlsson, J.O. (2004). Theoretical analysis of unidirectional intercellular ice propagation in stratified cell clusters. Cryobiology *48*, 357-361.

Karlsson, J.O., Cravalho, E.G., Borel Rinkes, I.H., Tompkins, R.G., Yarmush, M.L., and Toner, M. (1993). Nucleation and growth of ice crystals inside cultured hepatocytes during freezing in the presence of dimethyl sulfoxide. Biophys J *65*, 2524-2536.

Karlsson, J.O., Cravalho, E.G., and Toner, M. (1994). A model of diffusion-limited ice growth inside biological cells during freezing. J Appl Phys *75*, 4442-4455.

Karlsson, J.O., Eroglu, A., Toth, T.L., Cravalho, E.G., and Toner, M. (1996). Fertilization and development of mouse oocytes cryopreserved using a theoretically optimized protocol. Hum Reprod *11*, 1296-1305.

Karlsson, J.O., and Toner, M. (1996). Long-term storage of tissues by cryopreservation: critical issues. Biomaterials *17*, 243-256.

Kellam, B., De Bank, P.A., and Shakesheff, K.M. (2003). Chemical modification of mammalian cell surfaces. Chem Soc Rev *32*, 327-337.

Levin, M., Verkman, A.S. (2004). Aquaporin-Dependent Water Permeation at the Mouse Ocular Surface: In Vivo Microfluorimetric Measurements in Cornea and Conjunctiva. Investigative Ophthalmology and Visual Science *45*, 4423-4432.

Lewis, S.M., England, J.M., and Kubota, F. (1989). Coincidence correction in red blood cell counting. Phys Med Biol *34*, 1239-1246.

Liu, B., and McGrath, J.J. (2006). Effects of two-step freezing on the ultra-structural components of murine osteoblast cultures. Cryo Letters *27*, 369-374.

Liu, C., Benson, C.T., Gao, D., Haag, B.W., McGann, L.E., and Critser, J.K. (1995). Water permeability and its activation energy for individual hamster pancreatic islet cells. Cryobiology *32*, 493-502.

Liu, J., Zieger, M.A., Lakey, J.R., Woods, E.J., and Critser, J.K. (1997). The determination of membrane permeability coefficients of canine pancreatic islet cells and their application to islet cryopreservation. Cryobiology *35*, 1-13.

Lovelock, J.E. (1953). The mechanism of the protective action of glycerol against haemolysis by freezing and thawing. Biochim Biophys Acta *11*, 28-36.

Maranon, I.M., Gervais, P., Molin P. (1997). Determination of Cells' Water Membrane Permeability: Unexpected High Osmotic Permeability of Saccharomyces cerevisiae. Biotechnology and Bioengineering *56*, 63-70.

Mazur, P. (1963). Kinetics of Water Loss from Cells at Subzero Temperatures and the Likelihood of Intracellular Freezing. J Gen Physiol *47*, 347-369.

Mazur, P. (1984). Freezing of living cells: mechanisms and implications. Am J Physiol *247*, C125-142.

Mazur, P. (1990). Equilibrium, quasi-equilibrium, and nonequilibrium freezing of mammalian embryos. Cell Biophys *17*, 53-92.

Mazur, P., Leibo, S.P., and Chu, E.H. (1972). A two-factor hypothesis of freezing injury. Evidence from Chinese hamster tissue-culture cells. Exp Cell Res *71*, 345-355.

Mazur, P., Seki, S., Pinn, I.L., Kleinhans, F.W., and Edashige, K. (2005). Extra- and intracellular ice formation in mouse oocytes. Cryobiology *51*, 29-53.

McCaa, C., Diller, K.R., Aggarwal, S.J., and Takahashi, T. (1991). Cryomicroscopic determination of the membrane osmotic properties of human monocytes at subfreezing temperatures. Cryobiology *28*, 391-399.

McGann, L.E., Kruuv, J., and Frey, H.E. (1972). Repair of freezing damage in mammalian cells. Cryobiology *9*, 496-501.

McGann, L.E., Stevenson, M., Muldrew, K., and Schachar, N. (1988). Kinetics of osmotic water movement in chondrocytes isolated from articular cartilage and applications to cryopreservation. J Orthop Res *6*, 109-115.

McGann, L.E., Turner, A.R., and Turc, J.M. (1982). Microcomputer interface for rapid measurements of average volume using an electronic particle counter. Med Biol Eng Comput *20*, 117-120.

McGrath, J.J. (1988). Membrane Transport Properties. In Low Temperature Biotechnology: Emerging Application and Engineering Contributions, J. McGrath, and K. Diller, eds. (New York: American Society of Mechanical Engineers), pp. 273-331.

McGrath, J.J. (1997). Quantitative measurement of cell membrane transport: technology and applications. Cryobiology *34*, 315-334.

McGrath, J.J., Gao, J.T., Benson, C.T., Critser, E.S., and Critser, J.K. (1992). Coupled Transport Across the Murine Oocyte Plasma Membrane: Water and Cryoprotective Agents. In The 28th National Heat Transfer Conference and Exhibition (San Diego, CA, AMSE), pp. 1-13.

Merchant, F.A., Diller, K.R., Aggarwal, S.J., and Bovik, A.C. (1996). Viability analysis of cryopreserved rat pancreatic islets using laser scanning confocal microscopy. Cryobiology *33*, 236-252.

Merryman, H.T. (1968). Modified model for the mechanism of freezing injury in erythrocytes. Nature London *218*, 333-336.

Miyazaki, J., Araki, K., Yamato, E., Ikegami, H., Asano, T., Shibasaki, Y., Oka, Y., and Yamamura, K. (1990). Establishment of a pancreatic beta cell line that retains glucose-inducible insulin secretion: special reference to expression of glucose transporter isoforms. Endocrinology *127*, 126-132.

Morton, K.W. (1996). Numerical Solution of Convection-Diffusion Problems, 1st edn (Chapman & Hall).

Muallem, S., Zhang, B., Loessberg, P, Star, R. (1992). Simultaneous Recording of Cell Volume Changes and Intracellular pH or

Ca2+ Concentrations in Single Osteosarcoma Cells UMR-106-01. The Journal of Biological Chemistry *267*, 17658-17664.

Muldrew, K., Liang, S., Liu, Z., and Wan, R. (2001). Kinetics of osmotic water movement from rabbit patellar tendon and medial collateral ligament fibroblasts. Cryo Letters *22*, 329-336.

Munson, B.R., Young, D.F., and Okiishi, T.H. (1998). Fundamentals of Fluid Mechanics (John Wiley & Sons Inc).

Nelson, C.M., and Chen, C.S. (2002). Cell-cell signaling by direct contact increases cell proliferation via a PI3K-dependent signal. FEBS Lett *514*, 238-242.

Oegema, T.R., Jr., Deloria, L.B., Fedewa, M.M., Bischof, J.C., and Lewis, J.L. (2000). A simple cryopreservation method for the maintenance of cell viability and mechanical integrity of a cultured cartilage analog. Cryobiology *40*, 370-375.

Olson, J.E., Sankar, R., Holtzman, D., James, A., and Fleischhacker, D. (1986). Energy-dependent volume regulation in primary cultured cerebral astrocytes. J Cell Physiol *128*, 209-215.

Pasch, J., Schiefer, A., Heschel, I., and Rau, G. (1999). Cryopreservation of keratinocytes in a monolayer. Cryobiology *39*, 158-168.

Pazhayannur, P.V., and Bischof, J.C. (1997). Measurement and simulation of water transport during freezing in mammalian liver tissue. J Biomech Eng *119*, 269-277.

Pegg, D.E. (2002). Cryopreservation of vascular endothelial cells as isolated cells and as monolayers. Cryobiology *44*, 46-53.

Petrunkina, A.M., and Topfer-Petersen, E. (2000). Heterogeneous osmotic behaviour in boar sperm populations and its relevance for detection of changes in plasma membrane. Reprod Fertil Dev *12*, 297-305.

Pisani, J., and Thomson, G. (1971). Coincidence errors in automatic particle counters. Journal of Physics E: Scientific Instruments *4*, 359-361.

Raat, N.J., De Smet, P., van Driessche, W., Bindels, R.J., and Van Os, C.H. (1996). Measuring volume perturbation of proximal tubular cells in primary culture with three different techniques. Am J Physiol *271*, C235-241.

Rajotte, R.V. (1999). Islet cryopreservation protocols. Ann N Y Acad Sci *875*, 200-207.

Rich, G.T., Sha'afi, I., Romualdez, A., and Solomon, A.K. (1968). Effect of osmolality on the hydraulic permeability coefficient of red cells. J Gen Physiol *52*, 941-954.

Rosenberg, H.M., and Gregg, E.C. (1969). Kinetics of cell volume changes of murine lymphoma cells subjected to different agents in vitro. Biophys J *9*, 592-606.

Rule, G.S., Law, P., Kruuv, J., and Lepock, J.R. (1980). Water permeability of mammalian cells as a function of temperature in the presence of dimethylsulfoxide: correlation with the state of the membrane lipids. J Cell Physiol *103*, 407-416.

Saadoun, S., Papadopoulos, M., Hara-Chikuma, M., Verkman, A.S. (2005). Impairment of angiogenesis and cell migration by targeted aquaporin-1 gene disruption. Nature *434*, 786-792.

Scheiwe, M.W., and Korber, C. (1983). Basic investigations on the freezing of human lymphocytes. Cryobiology *20*, 257-273.

Sheetz, M.P. (2001). Cell control by membrane-cytoskeleton adhesion. Nat Rev Mol Cell Biol *2*, 392-396.

Sikdar, S., and Webster, S. (1980). Coulter particle counting at high counting rates. Journal of Physics E: Scientific Instruments *13*, 1075-1077.

Sinclair, W.K., and Ross, D.W. (1969). Modes of growth in mammalian cells. Biophys J *9*, 1056-1070.

Sipe, C.R., Chanana, A.D., Cronkite, E.P., Joel, D.D., and Schiffer, L.M. (1966). Studies on lymphopoiesis. VII. Size distribution of bovine thoracic duct lymphocytes. Proc Soc Exp Biol Med *123*, 158-161.

Smith, D.J., Josephson, S.J., Bischof, J.C. (1997). A model of cryosurgical destruction in AT-1 prostate tumor based on cellular damage mechanisms. Trans AmSoc Mech Eng *HTD-355/BED-37*, 149-150.

Smith, D.J., Pham, L., and Bischof, J.C. (1998a). The Effect of Dimethysulfoxide on the Water Transport Response of Rat Liver Tissue During Freezing. Cryo-Letters *19*, 343-354.

Smith, D.J., Schulte, M., and Bischof, J.C. (1998b). The effect of dimethylsulfoxide on the water transport response of rat hepatocytes during freezing. J Biomech Eng *120*, 549-558.

Solenov, E., Watanabe, H., Manley, G.T., and Verkman, A.S. (2004). Sevenfold-reduced osmotic water permeability in primary astrocyte cultures from AQP-4-deficient mice, measured by a fluorescence quenching method. Am J Physiol Cell Physiol *286*, C426-432.

Sonnentag, T., Siegel, W.K., Bachmann, O., Rossmann, H., Mack, A., Wagner, H.J., Gregor, M., Seidler, U. (2000). Agonist-induced cytoplasmic volume changes in cultured rabbit parietal cells. Am J Physiol Gastronintest Liver Physiol *279*, G40-G48.

Sosinsky, G.E., and Nicholson, B.J. (2005). Structural organization of gap junction channels. Biochim Biophys Acta *1711*, 99-125.

Srinivas, S., Bonanno, J. (1997). Measurement of changes in cell volume based on fluorescence quenching. the American Physiological Society, C1405-1414.

Srinivas, S., Bonanno, J., Lariviere, E., Jans, D., Van Driessche, W. (2003). Measurement of rapid changes in cell volume by forward light scattering. Eur J Physiol *447*, 97-108.

Stott, S. (2006). Kinetic study of intracellular ice formation in micropatterned endothelial cell cultures using high speed video cryomicroscopy. (Ph.D. Thesis, Georgia Institute of Technology).

Stuckey, I.H., and Curtis, O.F. (1938). Ice Formation and the Death of Plant Cells by Freezing. Plant Physiol *13*, 815-833.

Takamatsu, H., Komori, Y., Zawlodzka, S., Motoo, G. (2004). Quantitative Examination of a Perfusion Microscope for the Study of Osmotic Response of Cells. Journal of Biomechanical Engineering *126*, 402-409.

Tauc, M., Le Maout, S., Poujeol, P. (1990). Flourescent video-microscopy study of regulatory volume decrease in primary culture of rabbit proximal convoluted tubule. Biochimica et Biophysica Acta *1052*, 278-284.

Toner, M. (1993). Nucleation of ice crystals inside biological cells. In Advances in Low Temperature Biology, P. Steponkus, ed. (London, JAI Press Ltd.), pp. 1-51.

Toner, M., Cravalho, E.G., and Karel, M. (1990). Thermodynamics and kinetics of intracellular ice formation during freezing of biological cells. J Appl Phys *67*, 1582-1593.

Toupin, C.J., Le Maguer, M., and McGann, L.E. (1989). Permeability of human granulocytes to water: rectification of osmotic flow. Cryobiology *26*, 431-444.

Tsuruta, T., Ishimoto, Y., and Masuoka, T. (1998). Effects of glycerol on intracellular ice formation and dehydration of onion epidermis. Ann N Y Acad Sci *858*, 217-226.

Watson, C.J., Rowland, M., and Warhurst, G. (2001). Functional modeling of tight junctions in intestinal cell monolayers using polyethylene glycol oligomers. Am J Physiol Cell Physiol *281*, C388-397.

Weiser, M.G. (1987). Size referenced electronic leukocyte counting threshold and lysed leukocyte size distribution of common domestic animal species. Vet Pathol *24*, 560-563.

Westring, D.W., Ladinsky, J.L., and Feick, P. (1969). The volume distribution of human lymphocytes. Proc Soc Exp Biol Med *131*, 1077-1083.

Woods, E.J., Liu, J., Derrow, C.W., Smith, F.O., Williams, D.A., and Critser, J.K. (2000). Osmometric and permeability characteristics of human placental/umbilical cord blood CD34+ cells and their application to cryopreservation. J Hematother Stem Cell Res *9*, 161-173.

Woods, E.J., Liu, J., Gilmore, J.A., Reid, T.J., Gao, D.Y., and Critser, J.K. (1999). Determination of human platelet membrane permeability coefficients using the Kedem-Katchalsky formalism: estimates from two- vs three-parameter fits. Cryobiology *38*, 200-208.

Wu, W.T., Lyu, S.R., and Hsieh, W.H. (2005). Cryopreservation and biophysical properties of articular cartilage chondrocytes. Cryobiology *51*, 330-338.

Wynn, E., and Hounslow, M. (1997). Coincidence correction for electrical-zone (Coulter-counter) particle size analysers. Powder Technology *93*, 163-175.

Yang, H., Jia, X., Ebertz, S., and McGann, L.E. (1996). Cell junctions are targets for freezing injury. Cryobiology *33*, 672-673.

Yang, J., Ichikawa, A., and Tsuchiya, T. (2003). A novel function of connexin 32: marked enhancement of liver function in a hepatoma cell line. Biochem Biophys Res Commun *307*, 80-85.

Yarmush, M.L., Toner, M., Dunn, J.C., Rotem, A., Hubel, A., and Tompkins, R.G. (1992). Hepatic tissue engineering. Development of critical technologies. Ann N Y Acad Sci *665*, 238-252.

Zelenina, M., Brismar, H. (2000). Osmotic water permeability measurements using confocal laser scaning microscopy. Eur Biophys J *29*, 165-171.

Zheng, K., Trivedi, M., and Siahaan, T.J. (2006). Structure and function of the intercellular junctions: barrier of paracellular drug delivery. Curr Pharm Des *12*, 2813-2824.

Zieger, M.A., Tredget, E.E., and McGann, L.E. (1996). Mechanisms of cryoinjury and cryoprotection in split-thickness skin. Cryobiology *33*, 376-389.